

CALIBRATION OF HIGH-PRECISION FLEXURE PARALLEL ROBOTS

THÈSE N° 3712 (2006)

PRÉSENTÉE LE 22 DÉCEMBRE 2006

À LA FACULTÉ DES SCIENCES ET TECHNIQUES DE L'INGÉNIEUR
Laboratoire de systèmes robotiques 2
SECTION DE MICROTECHNIQUE

ÉCOLE POLYTECHNIQUE FÉDÉRALE DE LAUSANNE

POUR L'OBTENTION DU GRADE DE DOCTEUR ÈS SCIENCES

PAR

Nuno Ricardo FAZENDA CARRIÇO

ingénieur physicien diplômé EPF
de nationalité portugaise

acceptée sur proposition du jury:

Prof. M.-O. Hongler, président du jury
Prof. R. Clavel, directeur de thèse
Dr I. Beltrami, rapporteur
Dr M. Bierlaire, rapporteur
Dr F. Meli, rapporteur



ÉCOLE POLYTECHNIQUE
FÉDÉRALE DE LAUSANNE

Lausanne, EPFL
2007

à Léa,

à mes parents,

à memória dos meus avós Josefa e Guilhermino

*“As far as the laws of mathematics refer to reality,
they are not certain, and as far as they are certain,
they do not refer to reality.”*

Albert Einstein
(1879 – 1955)

Abstract

Calibration of High-Precision Flexure Parallel Robots

Over the last decades, calibration techniques have been widely used in robotics since they represent a cost-effective solution for improving the accuracy of robots and machine-tools. They only involve software modification without the necessity of revising the robot design or tightening the manufacturing tolerances.

The goal of this thesis is to propose a procedure that guides the engineer through the calibration of a given multi-DOF flexure parallel robot within sub- μm accuracy. Two robots having 3 and 6 degrees of freedom have been considered as a case-study throughout the work.

As in any calibration procedure, the work has been conducted on three different fronts: measurement, data processing and validation. The originality of this thesis in respect to published material lies in these three points.

Measurements were carried out in a chamber inside which the measuring environment was protected against mechanical and thermal perturbations. In particular, the temperature variations experienced by the different parts of the measuring loop during a typical measurement session were stabilized within less than $\pm 0.1\text{ }^{\circ}\text{C}$.

Proposed procedures allow the collection of reliable sets of data on the two robots. Delicate aspects of practical implementation are discussed. In particular, the problem of collecting a complete set of 6D data within accuracies in the nanometre range, for which there is still a lack of standard equipment, is solved using a procedure comprising several steps and making use of existing instrumentation.

Suggestions for future investigations are given, regarding either long-term research problems or short-term industrial implementation issues.

Data processing was performed using two different techniques in order to reach absolute accuracies after calibration better than $\pm 100\text{ nm}$ for translations and $\pm 3\text{ arcsec}$ for rotations ($\pm 0.3\text{ arcsec}$ inside a more restricted range of $\pm 0.11^{\circ}$).

The first method is called the “model-based approach” and requires the use of a known analytical relationship between the motor and operational coordinates of the robot. This relationship involves a certain number of parameters that can be related to the geometry of the robot (physical models) or simply mathematical coefficients of an approximating mathematical function (behavioural models). In the case of high-precision multi-DOF flexure parallel robots, we show that polynomial-based behavioural models are preferable to physical models in terms of accuracy for data processing tasks.

In the second method, called the “model-free approach”, the user does not need to model explicitly the main error sources (or their effect) affecting the robot accuracy. A model-free approach has been implemented using *Artificial Neural Networks*. We show that, using a heuristic search based on a decision-tree, the architecture of a network with satisfactory prediction capability can be found systematically. In particular, this algorithm can find a network able to predict the direct correspondence between the motor and operational coordinates (within the desired accuracy) without the help of the Inverse Geometric Model of the robot, i.e. even if the nominal geometry of the robot being calibrated remains unknown. This result contradicts conclusions reported by previous researchers.

It is claimed that any robot (not necessarily a high-precision flexure parallel mechanism) can be calibrated by means of a “neural approach” in which the architecture of an appropriate network is determined with the help of our algorithm. Two examples (other than the robots measured in this thesis) are given to illustrate this universality.

In the last part of this work, we provide a feasibility study on the use of indentation, a technique traditionally used for material testing, as a *validation procedure* to assess the accuracy of the calibrated degrees of freedom.

The industrial interest of this technique lies in the fact that the robot is asked to execute similar motions to those involved in a real micro-machining operation.

Key-words: *robot calibration, sub- μm accuracy, flexure parallel robots, neural networks, indentation.*

Étalonnage de robots parallèles de haute précision à articulations flexibles

Dans les dernières décennies, les techniques d'étalonnage ont connu un succès fulgurant en robotique. Elles sont en effet une solution attractive pour améliorer la précision d'un manipulateur industriel donné puisqu'elles ne demandent qu'une modification au niveau du logiciel.

Le but de cette thèse est de proposer une procédure visant à guider l'ingénieur dans l'étalonnage des robots parallèles de précisions sub- μm à articulations flexibles et ayant plusieurs degrés de liberté. Deux robots à 3 et 6 degrés de liberté sont pris comme cas d'étude.

Comme dans n'importe quelle procédure d'étalonnage, le travail a été conduit sur plusieurs fronts: procédés de mesure, traitement de données et validation. L'originalité de cette thèse réside dans ces trois aspects.

Les *mesures* ont eu lieu à l'intérieur d'une chambre visant à garantir une bonne isolation mécanique et thermique de l'environnement métrologique. En particulier, les variations de température subies par les différentes parties de la boucle de mesure pendant la durée d'une mesure typique, ont été stabilisées avec une tolérance meilleure que $\pm 0.1^\circ\text{C}$.

Des procédures ont été proposées permettant l'acquisition de données fiables sur les deux robots. Les aspects délicats liés à l'implémentation pratique de ces procédures sont discutés. En particulier, le problème de l'acquisition de mesures 6D avec des précisions nanométriques (pour lequel il n'y a toujours pas d'équipement standard) est résolu par l'intermédiaire d'une procédure en plusieurs étapes et faisant intervenir des instruments existants.

Des suggestions sont formulées pour la suite des travaux soit sur le long terme, au niveau de la recherche fondamentale, soit dans une perspective d'implémentation industrielle à court terme.

Deux techniques ont été proposées pour le *traitement des données* permettant d'atteindre des précisions absolues après étalonnage meilleures que $\pm 100\text{ nm}$ pour les translations et $\pm 3\text{ arcsec}$ pour les rotations ($\pm 0.3\text{ arcsec}$ à l'intérieur d'une plage plus restreinte de $\pm 0.11^\circ$).

La première méthode requiert un modèle analytique décrivant la correspondance entre les coordonnées articulaires et les coordonnées opérationnelles du robot. Ce modèle fait intervenir un certain nombre de paramètres pouvant être liés à la géométrie du robot (modèles à représentation physique) ou simplement des coefficients d'une fonction mathématique (modèles de comportement). Dans le cas des robots parallèles à articulations flexibles, il a été démontré que des modèles de comportement basés sur des fonctions polynomiales priment sur des modèles à représentation physique en termes de précision dans le traitement de données.

Dans une deuxième approche, l'utilisateur n'a pas besoin de modéliser explicitement les différentes sources d'erreur (ou leur effet). Une approche de ce type a été implémentée en utilisant des *réseaux de neurones artificiels*. On démontre qu'une heuristique de type « arbre de décision » permet de déterminer systématiquement l'architecture d'un réseau pouvant fournir une précision satisfaisante au problème. En particulier, il est possible d'obtenir un réseau pouvant prédire la correspondance directe entre coordonnées opérationnelles et articulaires avec la précision escomptée sans l'aide du modèle géométrique inverse du robot, c'est-à-dire même en ne connaissant pas a priori la géométrie nominale du robot à étalonner. Ce dernier résultat contredit les résultats obtenus par d'autres chercheurs.

Il est dit que tout robot (pas nécessairement un robot parallèle de haute précision à articulations flexibles) peut être étalonné par le biais d'une « approche neuronale » dans laquelle l'architecture d'un réseau approprié est déterminée par l'algorithme proposé. Cette universalité est illustrée sur 2 exemples autres que les robots mesurés dans ce travail.

Dans la dernière partie de cette thèse, on fait une étude de faisabilité sur l'utilisation de l'indentation, une technique employée traditionnellement dans la caractérisation des propriétés mécaniques des matériaux, en tant que *procédé de validation* pour contrôler la qualité de l'étalonnage effectué.

L'intérêt industriel de cette technique réside dans le fait que le robot y exécute des mouvements semblables à ceux qu'il serait amené à faire lors d'un procédé typique de micro-usinage.

Mots clés: *étalonnage de robots, précision sub- μm , robots parallèles à articulations flexibles, réseaux de neurones, indentation.*

Acknowledgements

Research is team work. This thesis would not have been possible without the help of many persons whom I would like to thank.

First and foremost, I would like to express my deepest gratitude to *Professor Dr Reymond Clavel*, my thesis advisor for his inspiring guidance, encouragement and suggestions throughout this research. He spent a considerable amount of his time in helping me at every stage of this work. I am also indebted to him for creating numerous opportunities for me to learn and grow as an engineer and researcher.

Thanks finally for having given me the opportunity to accomplish this work in such a stimulating working environment.

I would like to acknowledge the members of my thesis jury for having agreed to examine this contribution: they are *Prof. Dr Max-Olivier Hongler*, *Dr Ivano Beltrami*, *Prof. Dr Michel Bierlaire* and *Dr Felix Meli*.

Among the industry partners of the project, particular thanks are due to *Dr Ivano Beltrami*, Head of the research department at AGIE S.A., for the many discussions we had concerning calibration, temperatures, cubes and models. Thanks for having helped me in maintaining this work ‘usable’ for industrial purposes.

I am also extremely grateful to *Dr Felix Meli* from the Swiss Federal Office of Metrology and Accreditation (METAS) for his precious advices and the insightful discussions we had concerning high-precision metrology. I cannot count how many times he has lent us the METAS autocollimator.

Thanks also to *Dr Jean-François Willemin* from IMT Masken und Teilungen AG as well as to *Mr Stefano Bottinelli* and *Mr Yann Mabillard* from MECARTEX for their valuable comments during project reviews.

My heartfelt thanks go to *Mr Stéphane Rossopoulos*, my project colleague, for fruitful discussions and for sharing with me his extensive experience in industry. Many ideas, concepts and systems reported in this thesis come from the work of Stéphane. Moreover, the careful proofreading and astute technical comments he made on the dissertation draft helped me to smooth out many rough edges in this thesis.

Thanks also to *Dr Tiavina Niaritsiry*, my project colleague, for his friendship and help throughout hard periods. Tiavina was actually the original developer of the temperature regulation system used in this work.

Throughout the research period, many students made a direct or indirect contribution to this work in the context of internships, semester or master projects. They are: *Mr Emanuele Lubrano*, *Mr Christian Fischer*, *Mr Manuel Saglini*, *Mr Niklaus Hügi*, *Mr Alexei Kounine*, *Mr Mario Greber* and *Mr Olivier Blanc*.

I would like to thank all these people and especially *Mr Emanuele Lubrano* with whom I had the opportunity to work for almost 2 years. He is the author of much software used for the work reported in this thesis.

Special thanks are due to *Dr Mohamed Bouri*. Without Dr Bouri's PC-based control system, none of the robots studied in this thesis could actually work. Thanks also to his ever-willingness in helping me during the many "out-of-control" situations (sometimes during the week-end!).

I am also grateful to *Dr Sébastien Gautsch* from SAMLAB (CSEM) for the great deal of patience he had in performing the measurements of the positions of the indents. Advices coming from his direct boss, *Prof. Dr Urs Stauffer*, were also much appreciated.

During my stay at the LSRO, I will not forget the colleagues with whom I shared many enjoyable discussions during coffee breaks: they are *Dr Jean-Marc Breguet*, *Dr Rodolfo Rabe*, *Ms Mélanie Dafflon*, *Dr Patrick Helmer*, *Dr Guy Ramel* (from ASL), *Mr Robert Dünsch*, *Mr Benoît Lorent*, *Mr François Barrot* (from LSRO 1) and *Mr Willy Maeder*.

During my stay at the LSRO, the invaluable advices concerning administrative issues coming from *Mrs Heidi Banz* and *Mrs Anne Remillet-Schaller* were greatly appreciated.

I also gratefully acknowledge the *Swiss Federal Commission for Technology and Innovation* (CTI) for the financial support of this work under the TOP NANO 21 program (projects N° 5625.1 and 7027.1).

Thanks also to *Mrs Pamela Jones* and *Mr Hans-Jakob Reichen* for the careful proofread of the thesis draft (English correction).

Last but not least, I would like to express my most sincere appreciation and love to *Léa Müller*, for providing me with continuous affection and motivation throughout this work, and my parents, *Maria Filomena Chapeleira Fazenda* and *Sebastião António Pires Carriço*: *YOU* made this.

List of acronyms

ANN	Artificial Neural Network(s)
DOF	degree(s) of freedom
EDM	Electro-Discharge Machining
IGM	Inverse Geometric Model
LASER	Light Amplification by Stimulated Emission of Radiation
LSRO	Laboratoire de Systèmes Robotiques (<i>Laboratory of Robotic Systems – EPFL</i>)
METAS	Metrologie und Akkreditierung Schweiz (<i>Swiss Federal Office of Metrology and Accreditation</i>)
NN	Neural Network(s)
ppm	part per million
RWT	Rotations without translations
SEM	Scanning Electron Microscope
TWR	Translations without rotations

Table of contents

Chapter 1 – Introduction	1
1.1. – General introduction	1
1.2 – Preliminaries and definitions	1
1.2.1 – <i>Flexure parallel robots</i>	1
1.2.2 – <i>Accuracy, resolution and repeatability</i>	4
1.3. – Robot calibration	5
1.3.1 – <i>Kinematic models</i>	5
1.3.2 – <i>Sources of inaccuracy</i>	7
1.3.3 – <i>Steps in a calibration procedure</i>	8
1.4 – Contributions of this work	9
1.4.1 – <i>Goal of this work</i>	9
1.4.2 – <i>Original contributions</i>	9
1.5 – Multidisciplinarity of the related research	10
1.6 – Structure of the report	11
 Chapter 2 – Literature survey	 13
2.1 – Kinematic modelling	13
2.1.1 – <i>Modelling geometric parameters</i>	13
2.1.2 – <i>Modelling non-geometric parameters</i>	13
2.1.3 – <i>Model-free techniques</i>	14
2.2 – Measurements	14
2.2.1 – <i>Traditional systems</i>	14
2.2.2 – <i>Recent developments in 3D nano-metrology</i>	15
2.3 – Identification issues	15
2.4 – Methods used for parallel robots	16
2.4.1 – <i>Open-loop methods</i>	16
2.4.2 – <i>Closed-loop methods</i>	17
2.4.3 – <i>Implicit-loop methods</i>	17
2.4.4 – <i>Screw-axis methods</i>	17
2.4.5 – <i>Self-calibration methods</i>	17
2.5 – Conclusion	18

PART I – DATA COLLECTION

Chapter 3 – Development of a measuring system 21

3.1 – Introduction	21
3.1.1 – <i>Challenges in performing measurements within sub-μm accuracy</i>	21
3.1.2 – <i>Goal of this work and chapter outline</i>	21
3.2 – Measuring devices used and their sources of inaccuracy	22
3.2.1 – <i>Laser interferometer</i>	22
3.2.2 – <i>Laser displacement sensors</i>	27
3.2.3 – <i>Electronic autocollimators</i>	28
3.3 – Regulation of the measuring environment	32
3.3.1 – <i>Introduction and motivation</i>	32
3.3.2 – <i>Temperature regulation system</i>	33
3.3.3 – <i>Results of temperature regulation</i>	36
3.4 – General points observed for the data collection	41
3.4.1 – <i>Automation of the measurement procedure</i>	41
3.4.2 – <i>Averaging the vibrations due to the robot position regulation</i>	44
3.4.3 – <i>Correction of the thermal drift</i>	44
3.4.4 – <i>Other issues</i>	46
3.5 – Conclusion	49

Chapter 4 – Measuring the 3 and the 6-DOF robots 51

4.1 – Introduction	51
4.1.1 – <i>Chapter outline</i>	51
4.1.2 – <i>Terminology and convention</i>	51
4.2 – Measuring the 3-DOF robot	52
4.2.1 – <i>Measuring protocol</i>	52
4.2.2 – <i>Residual passive angular variations and their effect</i>	54
4.2.3 – <i>Measurement results</i>	57
4.3 – Measuring the 6-DOF robot	63
4.3.1 – <i>Measuring protocol</i>	63
4.3.2 – <i>Absolute reference frame</i>	74
4.3.3 – <i>Delicate aspects</i>	76
4.3.4 – <i>Measurement results</i>	78
4.4 – Conclusion	85

PART II – DATA PROCESSING

Chapter 5 – Model-based approach to pose correction 89

5.1 – Introduction	89
5.2 – Towards behavioural models	90
5.2.1 – <i>The case of elementary flexures</i>	90
5.2.2 – <i>The case of the 3-DOF robot</i>	91
5.3 – Using polynomial functions for pose correction	94
5.3.1 – <i>Literature review</i>	94
5.3.2 – <i>Using multi-variable polynomials for pose correction</i>	95
5.4 – Correcting the pose of the 3-DOF robot	98
5.4.1 – <i>Working with measurement data</i>	98
5.4.2 – <i>Working with simulation data</i>	100
5.5 – Correcting the pose of the 6-DOF robot	103
5.5.1 – <i>Working with measurement data</i>	103
5.5.2 – <i>Working with simulation data</i>	107
5.6 – Industrial success of the model-based approach	110
5.7 – Conclusion	111

Chapter 6 – Model-free approach to pose correction 113

6.1 – Introduction	113
6.2 – What is a Neural Network?	114
6.2.1 – <i>A brief remind on the theory of Neural Networks</i>	114
6.2.2 – <i>Using Neural Networks in function approximation problems</i>	116
6.3 – Using Neural Networks in robot calibration	120
6.3.1 – <i>Literature review</i>	120
6.3.2 – <i>Using Neural Networks in robot calibration</i>	122
6.3.3 – <i>Directions for future investigations</i>	127
6.4 – Correcting the pose of the 3-DOF robot	128
6.4.1 – <i>Working with measurement data</i>	128
6.4.2 – <i>Working with simulation data</i>	130
6.5 – Correcting the pose of the 6-DOF robot	133
6.5.1 – <i>Working with measurement data</i>	133
6.5.2 – <i>Working with simulation data</i>	136
6.6 – Universality of the proposed method	140
6.6.1 – <i>Test with another flexure parallel robot</i>	140
6.6.2 – <i>Test with a “non-flexure” parallel robot</i>	140
6.7 – Conclusion	141

PART III – QUALITY CONTROL

Chapter 7 – Indentation as a verification tool 145

7.1 – A technique traditionally used for material testing	145
7.2 – The indentation experiment	146
7.3 – Measuring the position of the indents	147
7.3.1 – <i>Measurement procedure</i>	150
7.3.2 – <i>Uncertainty budget and estimation of the measurement accuracy</i>	151
7.4 – Measurement results	151
7.4.1 – <i>1D comparison before/after calibration</i>	151
7.4.2 – <i>2D errors in the indent positions for the calibrated robot</i>	152
7.4.3 – <i>“Indirect” verification of the 3rd degree of freedom</i>	153
7.5 – Conclusion	154

Chapter 8 – General conclusion 155

8.1 – Summary	155
8.1.1 – <i>Measurements</i>	155
8.1.2 – <i>Data processing</i>	158
8.1.3 – <i>Verification procedures</i>	159
8.2 – Suggestions for future research	159
8.2.1 – <i>New research challenges</i>	159
8.2.2 – <i>Towards industrial implementation</i>	161
8.3 – Concluding remark	165

APPENDICES

Appendix A – Measuring instrumentation	169
A.1 – <i>SIOS</i> [®] SP 2000 laser interferometer	169
A.2 – <i>Keyence</i> [®] LC 2420/2430 laser displacement sensors	171
A.3 – <i>Newport</i> [®] LDS 1000 electronic autocollimator	171
A.4 – On the concepts of linearity and sampling frequency	172
A.5 – On the use of the <i>Keyence</i> [®] sensors in our 6D measuring procedure	174
 Appendix B – Effect of the residual passive angular variations on the calibration of the active DOF of the 3-DOF robot	 179
B.1 – Preliminary analysis in the 2D case	179
B.2 – General case in 3D	180
B.3 – Sensitivity analysis	182
 Appendix C – Remarks on the application of our 6D calibration protocol in real industrial operations	 185
C.1 – Preliminary: geometric decomposition of a 6D motion	185
C.2 – Remarks on the use of our 6D calibration protocol in future 6D industrial applications.....	186
 Appendix D – Calibration of High-Precision Flexure Parallel Robots: View of the different phases of the procedure	 189
D.1 – General overview	189
D.2 – Phase 0: basic decisions before calibration	190
D.3 – Phase 1: preparation of the measurements	191
D.4 – Phase 2: data collection	192
D.5 – Phase 3: data processing	193
D.6 – Phase 4: verification of the calibration conformity	195
 Glossary	 197
 References	 205
 Curriculum Vitae	 215

Chapter 1 – Introduction

1.1 – General Introduction

A common way to improve the accuracy of a given manipulator is through *hardware* modification, i.e. revising the robot mechanical structure or design (by proposing, for example, new joint concepts) and imposing tighter tolerances in manufacturing the robot parts. However, the manufacturing costs associated with this solution will be very high if the accuracy requirements are beyond certain levels.

It has been acknowledged that a more cost-effective solution is to build a manipulator with relaxed tolerances and to modify the mathematical model in the controller so that the *software* compensates for the actual inaccuracy of the robot. *Robot calibration* is the process of enhancing the accuracy of a given manipulator through software modification. Notice that calibration acts only on the active (or actuated) degrees of freedom of the manipulator, leaving the passive degrees of freedom to the care of the designer¹.

Calibration can be carried out at two different levels. Static calibration refers to the identification of accurate models covering all the physical properties and effects that influence the static (time invariant) positional accuracy of the manipulator. Dynamic calibration deals with the identification of models describing motion characteristics of the manipulator (forces, actuator torques, accelerations) and dynamic effects that occur on a manipulator such as friction and link stiffness.

This work is concerned with the static and load-invariant calibration of a certain class of robots.

1.2 – Preliminaries and definitions

This section introduces a few terms and definitions that are essential for a proper understanding of the work discussed in this report.

The robots considered as a case-study in this thesis are also presented.

1.2.1 – *Flexure parallel robots*

(a) – Parallel robots

The majority of today's industrial robots are serial manipulators. Usually, such robots have a large workspace and high dexterity but suffer mainly from their relatively low accuracy and structural stiffness due to their open-loop structure.

Over the last 20 years, attention has been given to parallel robots [Mer00]. A *parallel robot* is a closed-loop mechanism in which the mobile platform is connected to the base by at least 2 serial kinematic chains (legs).

Parallel mechanisms present themselves as feasible alternatives to their serial counterparts in situations where the demand for high speed, accurate motion and dynamic loading outweighs those for workspace and dexterity.

One of the most famous examples of parallel mechanisms is the 6 degree of freedom Stewart platform [Ste65], consisting of 6 variable-length legs connected at one end to a fixed base by U-joints and at the other end to a moveable plate by ball joints (**Figure 1.1a**). Originally proposed

¹ As we will see in this thesis, on the calibration of the 3-DOF robot, passive degrees of freedom (angular variations) influence the reading of the active degrees of freedom and, therefore, impose an attainable limit for calibration. Consequently, we believe that, in terms of absolute attainable performances in a calibration procedure (only limited by the measuring instrumentation), it is desirable to work with 6-DOF manipulators where all the degrees of freedom are active.

as a flight simulator platform, this mechanism has served, since then, in many other applications such as robotic assembly [MCa79], satellite tracking [Afz89] and also as a machine-tool [Rat85 and Sti95].

After the first ideas of parallel manipulators by Stewart, Clavel proposed in the late 80s the famous Delta structure (**Figure 1.1b**) as a base for a family of machines dedicated to high-speed operations [Cla91].

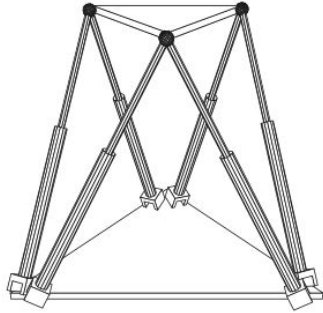


Figure 1.1a – The Stewart platform

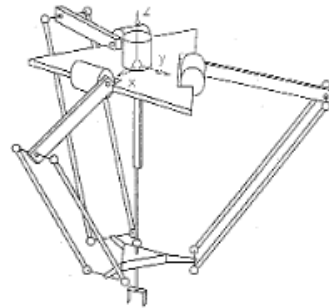


Figure 1.1b – The Delta 4 robot.

Today, the use of parallel manipulators can be found in many different applications, from haptic controllers, force/torque sensors, surgical instrumentation to machine tools.

(b) – Flexure parallel robots

The use of flexure hinges (**Figure 1.2**) as a building block for the design of new robotic parallel mechanisms has recently attracted attention in the research community [Hen00].

In fact, the use of this type of structure allows the design of joints able to provide motions without dry friction, backlash, wear or mechanical play and with no need for lubrication. Thus, flexure mechanisms can produce highly repeatable motions (at the nanometre range).

These advantages, together with vacuum and clean room compatibilities, explain the recent use of flexure parallel robots as ultra-precision manipulation systems in various fields such as optical fibre coupling, micro-grippers, scanning electron microscopy, micromachining and microlithography and, more recently, nano-metrology [Ryu 97, Glö00, Jos02, Mel03, Yi03, Cul04, Cul04b and Jos05].

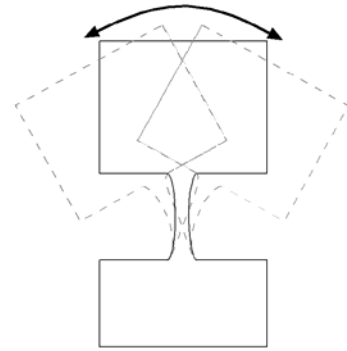


Figure 1.2 – Flexure hinge.

The main drawback of this type of manipulators lies however in their often limited workspace.

(c) – Presentation of the robots studied in this work

Two robots recently designed at the EPFL's *Laboratory of Robotic Systems* (LSRO), a 3-DOF and a 6-DOF mechanism, are taken as a case-study throughout this thesis.

■ 3-DOF robot

The first robot considered is a parallel kinematic mechanism called “Delta Cube” [Bac01 and Bac03] with 5 loops and 3 kinematic chains able to provide pure translational motions along the 3 directions of the Cartesian space (X, Y and Z).

Each kinematic chain consists of a translational stage made of 4 flexure hinges (**Figure 1.3a**) followed by a space parallelogram made of 4 pairs of flexure hinges at 90° (**Figure 1.3b**).

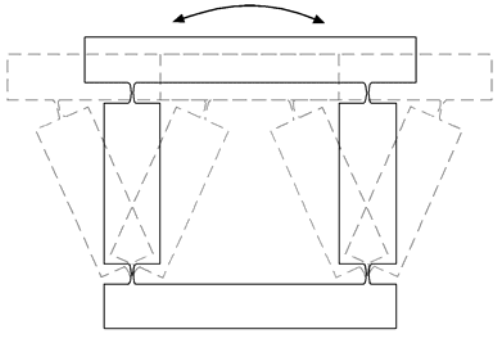


Figure 1.3a – Translational stage made of 4 flexure hinges.

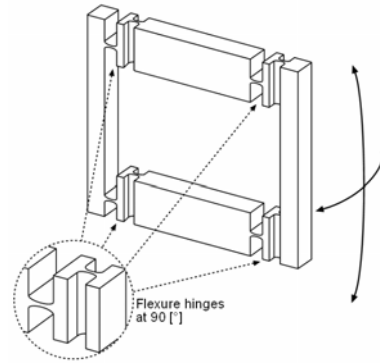


Figure 1.3b – Space parallelogram in the 3-DOF robot.

Thanks to *Heidenhain*^{®2} nanometer resolution linear encoders measuring the displacement of the translational stages, the robot is able to perform highly-repeatable 3D motions with a resolution of 10 nm over the workspace $4.0 \times 4.0 \times 4.0 \text{ mm}^3$ ($\pm 2 \text{ mm}$ along each axis).

Figure 1.4 shows a schematic view of the robot kinematic structure.

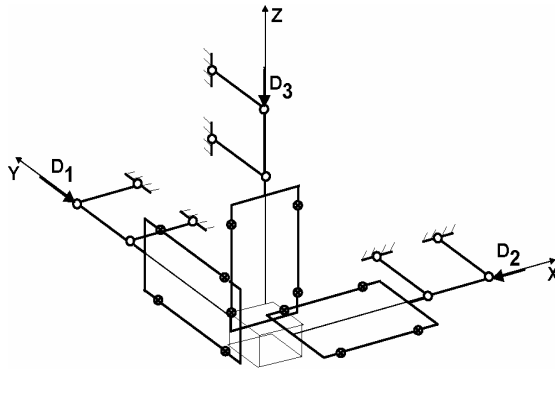


Figure 1.4a – Arrangement of the different joints in the “Delta Cube II” robot.

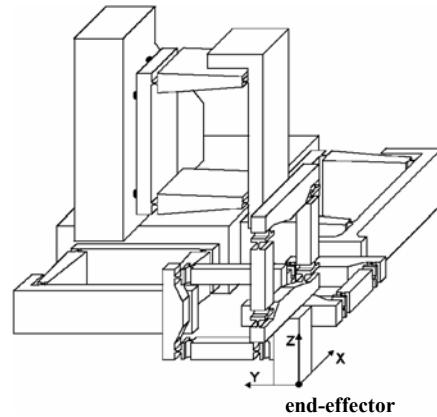


Figure 1.4b – Representation of the Delta Cube II.

■ 6-DOF robot

The most complex structure considered in this thesis is a parallel mechanism called “Sigma 6” [Hel06] having 3 degrees of freedom in translation (X , Y , Z) and 3 degrees of freedom in rotation (θ_X , θ_Y , θ_Z).

The robot, whose structure bears a resemblance to the Stewart platform, is composed of 6 kinematic chains.

Like the 3-DOF robot, each kinematic chain is made of a 4-flexure translational stage (**Figure 1.3a**) and a connecting rod made of 2 pairs of flexure hinges at 90° placed serially with a torsion bar allowing a passive rotation of the joint around its own axis (**Figure 1.5**).

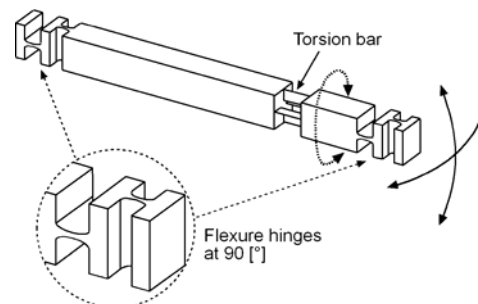


Figure 1.5 – Connecting rod composing each kinematic chain of the 6-DOF robot (and placed after the translational stage).

² *Heidenhain*[®] (Schweiz) AG, Vieristrasse 14 CH-8603 Schwerzenbach, Switzerland.

Again, the displacement of the prismatic joints is achieved with the help of *Heidenhain*[®] nanometer resolution linear encoders. This gives the robot a resolution of 10 nm and 0.25 μ rad (~ 0.05 arcsec) in translations and rotations, respectively, over its 6D workspace³: 7.0 mm x 7.0 mm x 7.0 mm x 7.0 mm x 7.0 mm x 7.0 mm.

The kinematic structure of this robot is illustrated in **Figures 1.6a** and **1.6b**.

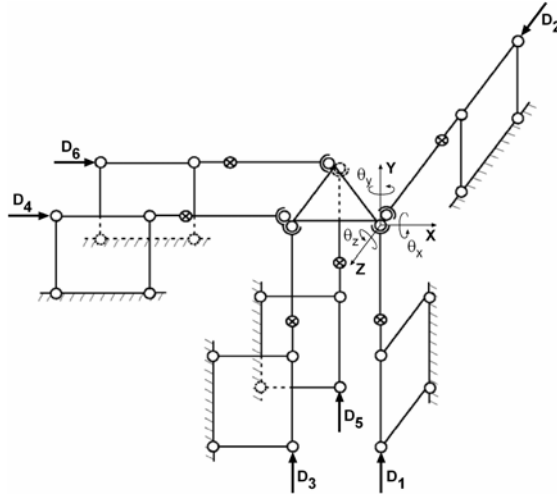


Figure 1.6a – Arrangement of the different types of joints in the “Sigma 6” mechanism.

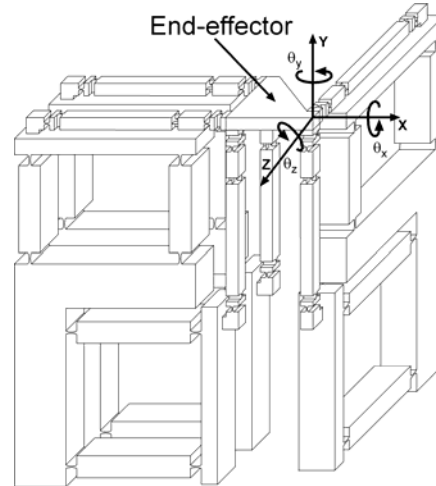


Figure 1.6b – Representation of the “Sigma 6” robot.

1.2.2 – Accuracy, resolution and repeatability

Accuracy, *resolution* and *repeatability* are all terms that characterize the positioning capability of a given robot.

Resolution is the finest incremental motion that can be achieved by the robot in the operational space. It is dependent on the joint type, encoders and the robot structure.

Repeatability is the robot’s capability to return to a previously taught pose⁴.

A poor repeatability is the result of *non-deterministic effects* arising for example from the measurements (e.g. accuracy of measurement devices or errors due to the operator) or errors in the robot (e.g. joint friction or backlash in the kinematics, joint servo and actuator systems).

Resolution and repeatability are characteristics that are hardware determined and cannot be changed easily.

Accuracy refers to the difference between a nominal pose (never taught before) that ideally has to be reached by the robot and the actual attained pose.

Accuracy depends on *systematic effects*, such as errors in the robot structure (e.g. errors due to manufacturing tolerances) or errors in the model used for motion control. A detailed discussion of the sources of inaccuracy of a robot will be given in the next section.

While repeatability can be improved mainly through hardware modification of the robot components, accuracy⁵ can be improved by means of software procedures to be included in the controller.

³ Actually, the workspace of this robot is not a 6D hyper-cube. However, the discussion of the real workspace is beyond the scope of this thesis.

⁴ Metrologists are often interested in two particular types of repeatability (especially if the measurements are concerned with nanoscale dimensions): the *reproducibility* and the *traceability*.

The former includes the measurement errors occurring when the same experiment is repeated a large number of times in the same conditions. The latter refers to an unbroken chain of measurements relating the reading of an instrument to a known standard.

⁵ In practice, the repeatability defines, together with resolution, the limit of the accuracy that can be reached through calibration.

For a better understanding of the difference between accuracy and repeatability, an analogy is established with a shooter in **Figure 1.7**.

High repeatability is of prime importance for a variety of robotic applications such as pick-and-place. In these operations, the robot is guided through the required poses (with the help of a teach pendant) and the corresponding joint coordinates are recorded. During actual operations, the robot “plays back” the recorded joint coordinates.

On the other hand, tasks involving off-line programming (e.g. computer-integrated manufacturing), in which the robot is controlled by a supervisory computer, depend on the manipulator’s accuracy.

When an absolute frame (that always stays at the same place) is defined, we might need to reach some position in respect to that frame. This frame defines an *absolute accuracy*.

In some applications like micro- or nano-manipulation, we may only need to position a given object within a certain distance in respect to some relative frame (e.g. using visual sensor-feedback), even if the absolute position of the frame changes in time (e.g. because of temperature gradients). In this case, we are dealing with *relative accuracy*⁶.

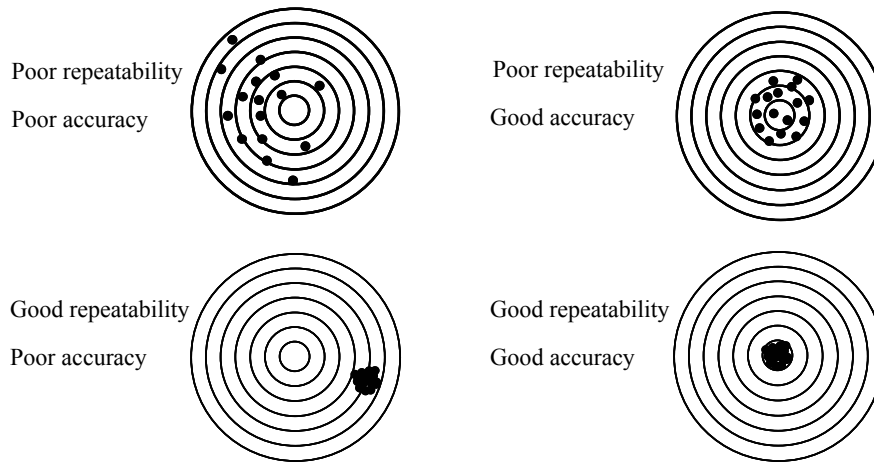


Figure 1.7 – Repeatability and accuracy of a shooter evaluated from the observation of different shooting targets.

In the past, several researchers [Ack85 and Vuk95] have proposed different sub-classifications for these terms (such as “internal accuracy” and “uni-path pose repeatability”).

The reader is however referred to the standard mathematical definitions of robot pose accuracy and repeatability recently given by the International Standards Organization – ISO 9283 (1998).

1.3 – Robot calibration

1.3.1 – Kinematic models

The desired locations of a robot end-effector are normally specified in Cartesian space, while these locations are achieved by controlling the joint variables in the robot’s joint space.

⁶ Some authors consider relative accuracy and repeatability to be equivalent terms. However, in this thesis, this distinction is maintained, in accordance with the above definitions.

The purpose of a **geometric model** is to relate the joint displacements to the pose⁷ of the end-effector. The absolute accuracy of the robot depends of course on how accurately this model reflects the actual robot.

For a given set of joint coordinates, the **direct** (or **forward**) **model** consists of solving the geometric model for the corresponding set of end-effector coordinates, whereas the **inverse model** gives, for a given set of end-effector coordinates, the corresponding joint coordinates. In general, for parallel robots, the analytical computation of the inverse model is always easier than the one of the forward model. For the latter, iterative approaches can be found in the literature [Mer00 and Hes95].

The kinematic models adopted for the control of a given parallel robot are usually simple and based on several simplifying assumptions such as a perfect parallelism between successive joint axes or the absence of manufacturing errors in the robot geometry. These models are called **nominal models**.

The goal of calibration is to replace these nominal models by a more accurate description of the relationship between joint and end-effector coordinates.

Different types of approach can be used to find this accurate description. Throughout this thesis, we propose the 2 following approaches: the *model-based* and the *model-free* approaches.

■ In the **model-based approach**, the relationship between these coordinates is provided through an analytical model.

This model has a given number of *parameters*. In the calibration procedure, these parameters have to be determined by means of an optimization algorithm applied to a cost function properly defined⁸.

This model can be a *physical model* if it is the result of a detailed physical representation, taking into account the main sources of inaccuracy (for example, length variations of the different robot arms). The model can also be a *behavioural model* if it is extracted from a previous observation of the kinematic behaviour of the robot over its workspace.

Chapter 5 is concerned with a model-based approach.

■ In the **model-free approach**, the relationship between the end-effector coordinates and the corresponding joint coordinates is fully or partly produced in a 'black-box' method.

This means that the robot user does not have to formulate *a priori* any analytical model for correcting the errors in the robot pose. All the “intelligence” of finding an appropriate model is delegated to the approach itself.

A model-free technique is reported in Chapter 6.

The main advantage of the model-free approach over the model-based method is evident⁹. In fact, in the former, the user does not have to provide knowledge about the main sources of inaccuracy affecting the robot pose.

We believe that this advantage is of extreme importance in the case of flexure parallel robots, for which the number of physical parameters increases exponentially with the complexity of the robot kinematic structure. In fact, for this type of robots, only simulation models (e.g. *Finite Element models*) can provide some insight on this question – however, in simulation, much time is needed to analyze the effect of each source of inaccuracy. Moreover, the accuracy of the absolute values of the obtained simulation results is often uncertain since they are strongly related to several computational issues such as type of element, number of elements, degree of meshing, etc. A recent dissertation presented at the LSRO was dedicated to the study, using

⁷ Throughout this thesis, the term **pose** means position and orientation. It refers, therefore, to 6 degrees of freedom (= 3 translations + 3 rotations).

⁸ In general, this cost function is defined, for a given set of joint coordinates, as the error between the pose predicted by the model used to control the robot and the real pose (determined with the help of external measuring devices).

⁹ A detailed comparison between these two methods is provided in **section D.5 of Appendix D**.

Finite-Element simulation, of the sources of inaccuracy for a particular class of flexure parallel robots [Nia06].

However, the main drawback of the model-free approach lies in the difficulty of finding appropriate functions that perform the approximation of a given set of input-output pairs within the desired accuracy without falling into overfit¹⁰.

As we shall see in Chapter 2, the different calibration approaches found so far in the literature rely mostly on model-based approaches with physical models.

1.3.2 – Sources of inaccuracy

Researchers have been working to identify the static sources of inaccuracy in robot operations for many years.

The literature has basically defined 2 different kinds of error sources. These are often called *geometric* and *non-geometric* (or sometimes *kinematic* and *non-kinematic*). To these two categories, we will add a third one that will be critical in our work.

■ **Geometric errors** are deviations that are constant for all robot configurations. It is well known that, due to manufacturing tolerances, the geometry of robotic manipulators does not match exactly the design goals. This may cause, for example, small changes in the link lengths of the robot which, in turn, cause positional changes of the robot end-effector. Moreover, geometric errors can also come from the assembly of the different robot components (e.g. misalignments between joint axes).

Since these errors have a systematic nature, they can be compensated (of course, as long as they are controllable – see the footnote in page 1) by means of proper modifications of the kinematic model and through a calibration procedure.

■ **Non-geometric errors** are dependent on the robot configurations.

Errors occurring in the motion transmission between the different joints, such as friction, wear and backlash are the ones most commonly cited in the literature.

Additionally, deflections in robot links may also be a source of errors. Non-geometric effects can also be at the joint level (e.g. electrical zeroes of the joint encoders do not generally coincide with the mechanical zeroes of the joints themselves) or in the control procedure (e.g. finite resolution of joint encoders, steady-state control errors).

■ **Working conditions** in which the robot is operating (or calibrated) can also have a major influence on its static positioning accuracy.

In many situations, robots are operating under unsteady environments caused by heat generation from a variety of sources (local sources like drive motors and transmission devices or variations in the ambient temperature). Temperature gradients are responsible for a significant amount of deformation within the components of the machine structure.

Moreover, it is known from the basic theory of mechanisms that static loads applied to the end-effector (such as gravity and contact forces) can cause non-negligible deflections depending on the magnitude, orientation and point of application of these loads.

A schematic list of the different sources of inaccuracy mentioned above is shown in **Figure 1.8**.

The discussion on the relative importance of each source of inaccuracy has been extensively debated in the literature. Some authors considered only geometric errors for calibration, considering non-geometric factors to be random (and therefore not subjected to software improvement); others have proposed, in addition to geometric defects, non-linear analytical descriptions of the non-geometric errors based on experimental observations.

¹⁰ *Overfitting* is a key issue in classical approximation problems. This term will be explained and illustrated in Chapters 5 and 6.

For a discussion of the importance of the different sources of inaccuracy in the case of high-precision flexure parallel robots, the reader is referred to the work of Niaritsiry [Nia06].

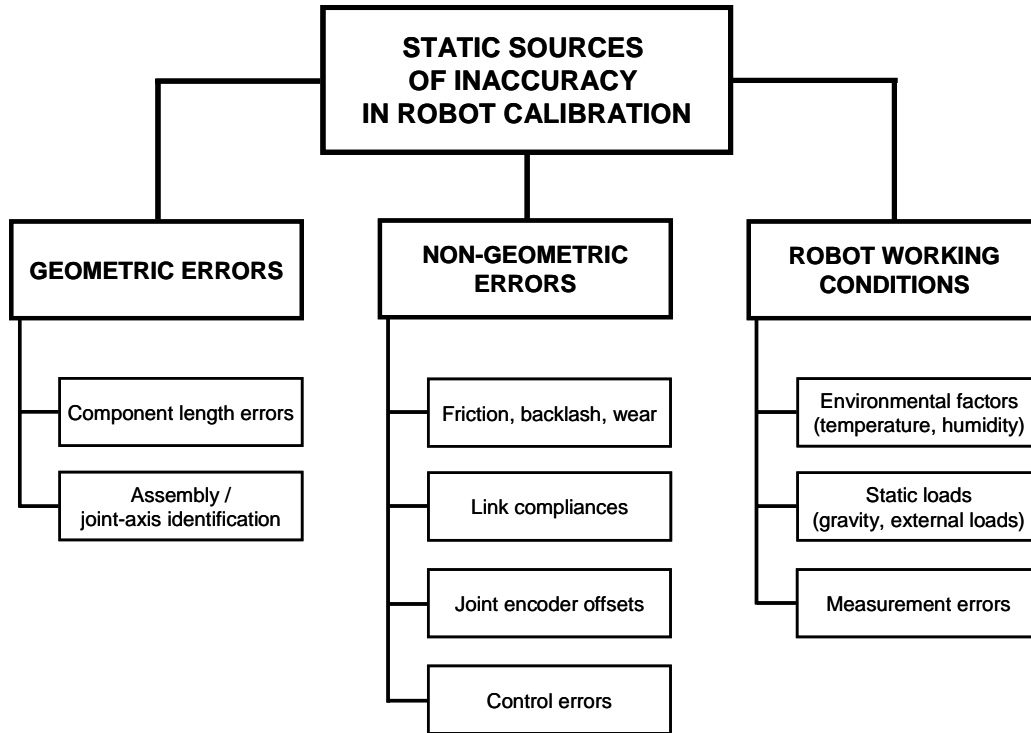


Figure 1.8 – Sources of inaccuracy commonly considered in static robot calibration problems.

1.3.3 – Steps in a calibration procedure

In general, a robot calibration procedure encompasses 4 distinct actions¹¹, none of which is trivial: (1) modelling, (2) measurement, (3) identification and (4) correction.

Modelling refers to the choice of a functional relationship between the joint variables and the resulting pose of the end-effector. The model selected should contain the factors considered to be significant in contributing to accuracy.

In the next step, physical data is collected from *measurements* of the robot which has to be calibrated. This data contains information relating the input of the model to the output.

The mathematical process of using the data collected to *identify* the coefficients of the model is the third step in calibration.

Finally, the *correction* step is intended to implement the new model in the position control software of the robot.

In this work, research will be conducted on all the phases mentioned above.

¹¹ A fifth action is actually considered in this thesis: *validation* (chapter 7). As long as time and costs can afford this additional step, we believe that validation procedures (ideally close to the application for which the robot will be used) should be included, especially when accuracies in the sub- μm range are involved.

1.4 – Contributions of this work

1.4.1 – Goal of this work

From a general point of view, we can say that:

The general goal of this work is, through 2 case-studies, to propose a methodology for the calibration of any multi-DOF high-precision flexure parallel robot.

In order to reach this global objective, two different goals were considered:

- From the *experimental* point of view, the challenge of this work is to calibrate a 3-DOF and a 6-DOF high-precision flexure parallel robot in order to reach absolute accuracies in the order of ± 100 nm and ± 1 arcsec for translations and rotations, respectively;
- From the *theoretical* point of view, the main goal of this work is to propose different mathematical tools and discuss their use in data processing tasks so that the correction of the errors in the robot pose yields maximum accuracy.

1.4.2 – Original contributions

To the best of our knowledge, **this thesis is the first to address the calibration of multi-DOF high-precision flexure parallel robots within the sub- μ m accuracy range.**

The original contributions of this work are both experimental and theoretical:

■ Original contributions from the experimental point of view

1. The problem of collecting a reliable set of 6D data within sub- μ m accuracy does not have, so far, a standard commercial solution.

In this thesis, we provide an answer to this problem by means of an innovative protocol comprising several steps which make use of existing instrumentation.

2. Two high-precision flexure parallel robots with 3 and 6-DOF were calibrated within accuracies better than ± 100 nm for translations (both robots) and ± 3 arcsec for rotations (± 0.3 arcsec inside a more restricted range of $\pm 0.11^\circ$).

3. We provide a feasibility study on the use of indentation, a technique widely used for material testing, as a validation procedure to assess the accuracy of the calibrated degrees of freedom within the sub- μ m accuracy range.

The industrial interest of this technique lies in the fact that the robot is asked to execute motions similar to those involved in a real micro-machining operation.

■ Original contributions from the theoretical point of view

1. We propose the use of *behavioural models* for correcting the errors in the pose of high-precision flexure parallel robots. These models have rarely been used so far by previous researchers, who preferred to use models involving parameters directly related to the geometry of the manipulators under calibration.

We prove that multi-variable polynomials, which are amongst the oldest approaches to global fitting techniques, can provide better accuracy than classical kinematic models based on a physical representation.

2. Using either a model-based or a model-free approach, we demonstrate that it is possible to calibrate high-precision flexure parallel robots even if the sources of inaccuracy are not modelled (because they cannot be identified or because they are difficult to model directly) and also if the *nominal* geometry of the robot being calibrated is not known. We believe that this is a major result which refutes conclusions drawn by previous researchers.

3. Despite the fact that the use of neural networks in robot calibration problems is not new, no author so far has proposed a systematic methodology for finding the architecture (number of hidden layers and number of neurons in the hidden layers) of a network able to correct the pose of a given robot within a desired accuracy.

We solve this problem by means of a heuristic based on a decision-tree search. For the two robots studied, we show that this algorithm can always find a satisfactory solution for the error compensation independently of the configuration used for the data processing tasks.

We claim that this algorithm can find an appropriate network for the calibration of any robot. Two examples (other than the robots measured in this thesis) are given to illustrate this universality.

1.5 – Multidisciplinary of the related research

The current work deals with a multidisciplinary research field in which 4 different domains are interacting: *robotics*, *function approximation*, *3D/6D nano-metrology* and *material testing* – see **Figure 1.9**.

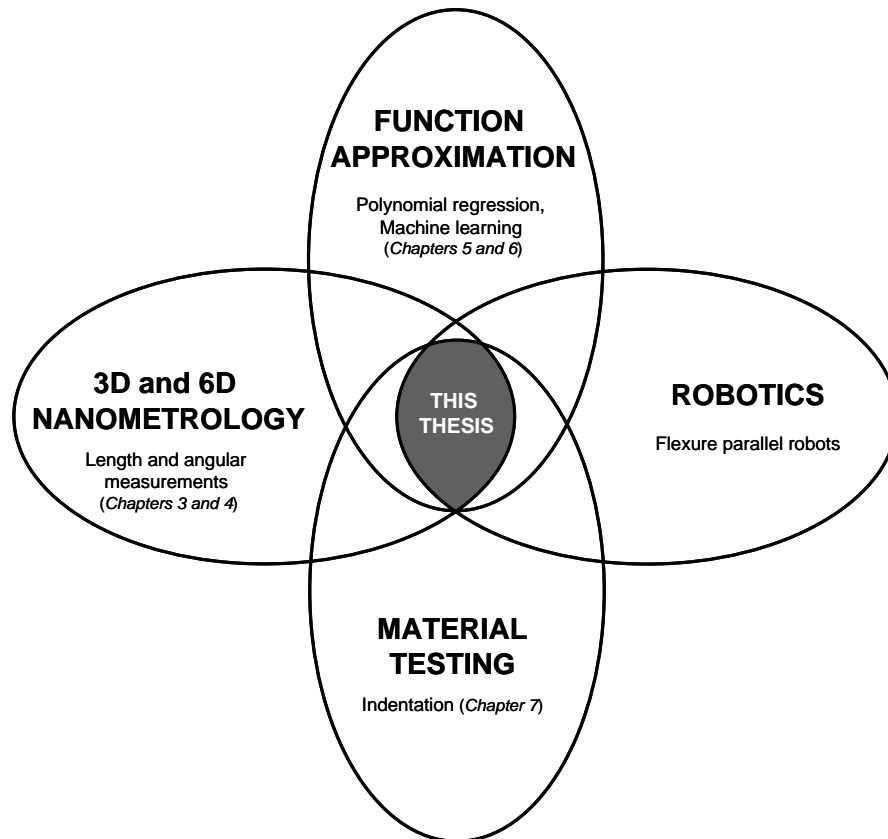


Figure 1.9 – Different domains interacting with the research related to this thesis.

This report should be regarded as a user's guide for practitioners who wish to solve a new engineering problem by making use of well-established tools from these 4 different elementary fields.

In other words, this document has been written in order to help the engineer in performing the calibration of a given high-precision multi-DOF flexure parallel robot throughout the procedure¹². The focus was therefore on the description of a global methodology rather than the presentation of measurement details or extensive mathematical developments.

1.6 – Structure of the report

The structure of the report is as follows:

- **Chapter 2** outlines a *literature survey* of past work on robot calibration. Experimental devices and techniques used in this field as well as the different theoretical methods used so far to process the data are briefly described;

- Experimental issues are discussed in **Chapters 3 and 4**. Since this thesis deals with measurements within the sub- μm accuracy domain, much attention has been paid to the instrumentation used and to the way *measurements* have been performed. The delicate aspects of the measuring procedures are pointed out and solutions are proposed for overcoming these difficulties in order to obtain the most accurate data;

- **Chapter 5** focuses on a *model-based approach to calibration*. We show that *behavioural models* and, in particular, multi-variable polynomials, are well adapted for the correction of errors in the pose of multi-DOF high-precision flexure parallel robots within accuracies approaching the motion resolutions. Computer simulations and experimental studies are conducted on the 2 robots. Results are presented and discussed;

- **Chapter 6** presents a *model-free approach to calibration*. Our goal is to provide some insight into how *artificial neural networks* can be used to calibrate a given flexure parallel robot. In particular, we propose an algorithm to find the architecture of a network for correcting the pose of any robot within the desired accuracy. The robustness of this neural approach is tested through simulation and experimental data on the 2 robots;

- In **Chapter 7**, we demonstrate the feasibility of the use of *indentation*, a technique traditionally employed for determining the mechanical properties of different materials, to assess the accuracy of the calibrated degrees of freedom. The industrial interest of this technique lies in the fact that the robot is asked to execute motions similar to those involved in a real machining operation;

- Finally, **Chapter 8 concludes this report**. A summary of the important contributions of the thesis is given and suggestions for future research in this field are outlined.

¹² Though the methods presented in this thesis were originally developed for high-precision flexure parallel robots, we believe that they can be applied to any other robot.

Chapter 2 – Literature Survey

Robot calibration is a research area that has grown considerably over the last twenty years. This is evidenced by a large number of publications, including textbooks [Moo91 and Ber93] and survey papers [Rot87 and Hol88].

This chapter is organized in two parts. The **first part** (comprising **sections 2.1, 2.2 and 2.3**), concerns the calibration of any robot and reviews the main axes of research in this discipline by identifying the key contributions made so far in each one. In the **second part (section 2.4)**, we shall focus on the methods used specifically for the calibration of parallel mechanisms.

2.1 – Kinematic modelling

Static robot calibration requires the use of parametric models of the manipulator kinematics, to find the true mapping between the joint configurations and the poses of the end-effector.

It has been reported [Eve87, Moo91] that accurate robot kinematic models for the purpose of calibration need to fulfil the properties of *completeness*, *proportionality* and *equivalence*. A kinematic model is said to be complete if all the kinematic properties of the manipulator are represented by corresponding independent model parameters. Proportionality implies that a small change in the actual robot structure will result in a correspondingly small change in its parameters. Equivalence refers to the ability of transforming the parameters of one model to different model descriptions.

2.1.1 - *Modelling geometric parameters*

In the earliest robot calibration works, researchers made systematic use of the Denavit-Hartenberg (D-H) parameterisation [Den55] in which the manipulator kinematics is modelled by composing elementary link models in a serial way. These link models use only four geometric parameters per link to describe the relative displacement between coordinate frames of neighbouring links.

However, Mooring [Moo83] and Hayati [Hay83] reported independently that D-H models did not fulfil the requirements of completeness and proportionality for robots having parallel or near-parallel consecutive joint axes and proposed a modification to the former by introducing an extra parameter.

During the 1980's, many researchers came with their own model variants. In fact, the number of models almost equalled the number of researchers. An excellent review of these different models, categorized into 4-, 5- and 6-link parameter models is given by Hollerbach [Hol88].

2.1.2 – *Modelling non-geometric parameters*

Non-geometric effects are usually modelled by adding extra terms to the overall geometric model of the manipulator. The analytical formulation of these terms is often inspired by prior experimental observations.

Vincze [Vin94] stated that non-geometric effects are mainly due to joint related characteristics and used a linear joint-dependent model for their correction.

Alternative and more sophisticated joint-dependent formulations were also applied by Whitney [Whi86], Everett [Eve93] and Vincze [Vin96 and Vin99].

2.1.3 – Model-free techniques

Due to the complexity of the structure of many multi-DOF mechanisms, alternative modelling approaches proposed to approximate the error rather than modelling explicitly the different errors sources.

In fact, different well-established tools coming from the function approximation theory were used for this purpose, such as splines [Dor93, Hüg05 and Bla06], polynomial functions (see **section 5.3.1** for a brief review) and artificial neural networks (see **section 6.3.1** for a detailed review of this issue).

In comparison to models making use of parameters directly related to the physical representation of the robot being calibrated, it should be noted that very few papers in the literature make use of model-free techniques.

2.2 – Measurements

2.2.1 – Traditional systems

Different measurement systems have been used so far for robot calibration tasks. The main differences are in the measurement method (contact or non-contact), the number of captured DOF (from 1 to 6), accuracy and costs [Hol96].

Typical measurement devices for robot calibration are wire potentiometers [Jeo98], telescopic ball systems measured by radial distance transducers (LVDT) [Gos93], interferometers [Cha87, Ali03, Tan93], ultrasonic systems [Ber93b], proximity sensors, imaging laser tracking systems [Vin94b, New00, Bai03b and Sch93], single and stereo camera systems [Zhu96], magnetic trackers, theodolites [Zhu95, Bes99 and Fra99], cable driven systems, ball-bars and other systems traditionally used for machine-tool inspection [Cau96].

Interesting brief reviews of metrology techniques for robot calibration can be found in [Par87, Now88 and Kyl95].

Figure 2.1 represents one of the first 6D-measuring devices, due to R. H. McEntire [ME76], which makes use of an arrangement of three pairs of dial gauges to mutually-orthogonal sides of a cube held in the end-effector of the robot. Notice that complete information can be deduced from the dial gauges, on both the position and orientation of the cube in respect to the Cartesian reference coordinate frame.

Several variants of this system (for example, using a 3-2-1 gauge configuration instead of the traditional 2-2-2) have been used for robot calibration such as in [Per98].

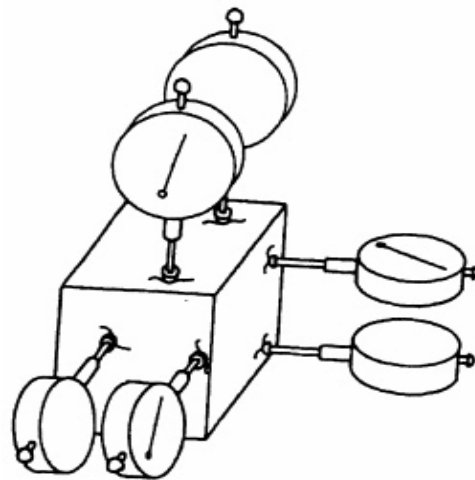


Figure 2.1 – Pose-measuring system proposed by McEntire [ME76] and making use of dial gauges measuring the faces of a cube placed on the robot end-effector.

Finally, in recent years, there has been an extensive development of vision-based robot pose measurement methods [Zhu94 and Zhu96]. Two main configurations can be found depending on whether the CCD camera is kept in a stationary configuration (fixed in the robot environment) or if it is mounted on the robot end-effector (“eye-on-hand” configuration).

2.2.2 - Recent developments in 3D nano-metrology

Existing robot calibration works have so far only dealt with accuracies down to the μm range.

In fact, very few metrology systems are able to provide measuring uncertainties in the nanometre range over a range of several tens of millimetres.

Recent advances in 3D nano-metrology include the development of a so-called *Nano-Positioning and Nano-Measuring Machine* by Manske and co-workers [Man05], now commercialized by SIOS [SIO] (see **Figure 2.2** below), as well as a new $\mu\text{-CMM}$ machine by METAS [MET] with a claimed overall measuring accuracy of less than 30 nm over a range of 90 mm x 90 mm x 90 mm.

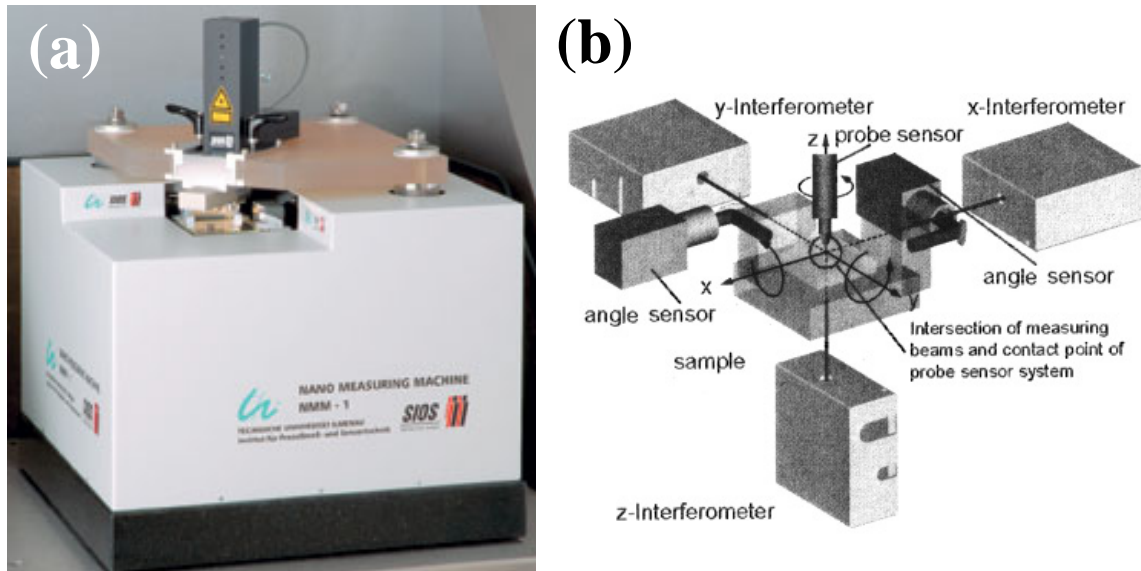


Figure 2.2 – The *Nano-Positioning and Nano-Measuring Machine* (NMM-1) commercialized by SIOS® Meßtechnik GmbH.

The manufacturer announces a measuring accuracy of less than 10 nm over a measuring range of 25 mm x 25 mm x 5 mm.

(a): Photographic view of the overall measurement system (b): Set-up of the Abbe error free arrangement in the three coordinates measured and contributing partly to the accuracy performances of the machine.

2.3 – Identification issues

Numerical methods used for model parameter identification are at the core of most robot calibration techniques. Procedures in which model parameters are calculated from several measured robot end-effector poses require numerical optimization methods.

Several issues related to the identifiability of model parameters have been addressed so far by robot calibration researchers.

A major problem highlighted in the literature is *parameter redundancy* [Eve88, Moo89]. In such a case, there are more parameters in the model than necessary for model completeness, hence the model is not minimal. It has been recognized that redundant parameters do not increase the

accuracy of a model but rather cause problems in the identification phase since it leads to a linear dependency in the columns of the Jacobian.

Another problem which has been the object of several investigations is the selection of poses that have to be measured for obtaining “optimal” results during the identification phase. Different indices have been developed in order to evaluate the degree of “observability” in the identification of a given parameter for a specific end-effector pose [Men88, Bor89, Dri90, Kha91, Dan02, Hua03 and Dan05].

2.4 – Methods used for parallel robots

In this section, we will adopt the classification originally proposed by Hollerbach in [Hol96], (applicable to serial and parallel manipulators) to identify the different methods applied so far for the calibration of closed-chain structures.

According to this author, calibration methods usually fall into one of the following categories:

- open-loop methods;
- closed-loop methods;
- implicit-loop methods;
- screw-axis methods;
- self-calibration methods.

Notice that the distinction between some of the methods is often small and arbitrary. For example, a given open-loop method may constrain some degrees of freedom, and also measure others, thus mixing open and closed-loop methods. In addition, parallel structures have a mixture of sensed and unsensed joints, the latter being formally not different from the task kinematics of passive joints for closed-loop methods.

2.4.1 – *Open-loop methods*

The most common and widely used calibration method is the open-loop method, in which a manipulator is placed in a number of poses and the complete or partial end-effector pose is measured. The term “open-loop” refers in fact to an end-point that is positioned freely in space. In general, this method tends to be used for the calibration of serial mechanisms rather than parallel ones.

Examples of these are:

- the work of Koseki [Kos98] considering the calibration of a 6-legged parallel arm by means of a laser tracking coordinate-measuring system;
- the work of Besnard and Khalil [Bes99] in which a Stewart platform is calibrated with the help of two inclinometers;
- the calibration of a Stewart platform using pose measurements obtained by a single theodolite by Zhuang [Zhu95].

2.4.2 – Closed-loop methods

As opposed to the classical open-loop method, the closed-loop method does not require an external measurement system. For serial mechanisms, calibration is achieved by sensing joint angles only, by attaching the end-effector to the environment in order to form a mobile closed-kinematic chain.

Bennett and Hollerbach [Ben91] used the closed-loop method to calibrate manipulators formed into mobile closed-kinematic chains.

Everett and Lin [Eve88b] considered the kinematic calibration of a five-bar actuated joint mechanism. Their approach was based on a constrained optimization technique involving a large number of redundant parameters, the constrained equations arising from the fact that the closed-loop had to remain closed for all the configurations.

Finally, extensions of the closed-loop method to multiple closed-loop systems have been considered in [Eve93b and Nah94].

2.4.3 – Implicit-loop methods

In an implicit-loop method, the error enters the kinematic loop equation implicitly, rather than being the explicit output of a conventional input – output formulation. The main advantage is that difficult-to-model error sources, such as input noise and backlash, can be included in the merit function to be optimized.

Wampler and Hollerbach [Wam95] used the implicit-loop method in order to demonstrate a unified formulation on the self-calibration of both serial and parallel robots. Their paper included an application to two 6-DOF mechanisms.

Vischer [Vis96] has also made use of the implicit-loop technique for the calibration of a Delta parallel structure.

2.4.4 – Screw-axis methods

The basic principle of screw-axis methods is slightly different from that of kinematic-loop methods. In fact, each axis is now identified independently as a screw. The major advantage lies in the fact that kinematic parameters can be identified without the need for solving a non-linear optimization problem.

The most commonly known variant is called Circle Point Analysis (CPA). It consists of measuring the end-point position by acting on a different joint at a time. It can then be regarded as an open-loop method with this particular pose selection.

Examples of the application of the CPA technique can be found in [Sul01 and Abd00].

2.4.5 – Self-calibration methods

Self-calibration is similar to the closed-loop method, except that additional sensor data is often used to facilitate the calibration; hence, it may be viewed as a variant of the closed-loop method.

This method has the potential for removing the dependence on any external pose-sensing information and has the capability of producing accurate measurement data over the entire workspace of the system with a fast measuring rate. Moreover, it is completely non-invasive.

Probably for these reasons, self-calibration methods are gaining popularity among researchers working with the calibration of parallel robots, as can be seen by the number of papers based on this particular method [Zhu97, Zhu98, Not95, Mas93 and Iur99].

2.5 – Conclusion

We shall retain three main conclusions from this chapter:

- the great majority of the mechanisms studied in the literature present a serial structure. In fact, due to their inherent complexity, arising from the coupling between different degrees of freedom, parallel structures have received much less attention;
- so far, the models used for parameter identification purposes have tried to provide a realistic representation of the robot being calibrated, in order to be able to include the highest number of physical error sources. Very few authors have regarded calibration as a pure function approximation problem;
- to the best of our knowledge, the problem of calibrating multi-DOF parallel structures (or even a serial mechanism) within accuracies in the nanometre range has not been considered so far by any author. It is still a domain mainly reserved to metrologists, rather than roboticists.

DATA COLLECTION

Chapter 3 – Development of a measuring system

3.1 – Introduction

3.1.1 – *Challenges in performing measurements within sub- μm accuracy*

At the sub- μm range, it is well known that performing accurate measurements requires not only expensive instrumentation but also skilled operators. In fact, at that level of accuracy a great deal of time and effort has to be dedicated not only to fine adjustments of the measuring devices themselves but also to the regulation of the working environment, since there is a strong dependency of the signal-to-noise ratio on external perturbations such as **temperature variations** and vibrations.

Moreover, a market review of high-precision measuring instrumentation has shown that there is no standard solution to measure the six degrees of freedom (three translations + three rotations) simultaneously within absolute accuracies of the order of $\pm 10\text{ nm}$ and $\pm 0.1\text{ arcsec}$ for translations and rotations, respectively.

Notice, however, that commercial solutions for measuring translations or rotations (separately) are common. Examples of these are *laser interferometers* (for distances) and *autocollimators* or *angular interferometers* (for angles).

3.1.2 – *Goal of this work and chapter outline*

As was mentioned in **Chapter 1**, the goal of this thesis is not to introduce innovations in the nano-metrology research field. Our goal is rather to bring knowledge of state-of-the-art nano-metrology methods and instrumentation into robotics.

Therefore, instead of developing a new measuring method or instrument (which would be the subject of a metrology dissertation), *we propose to use existing high-precision instrumentation for the measurement of angles and distances and to focus on defining measurement protocols specifically adapted to the needs of our robots.*

The goal of this chapter is to provide the roboticist with knowledge of how to plan and perform reliable measurements with sub- μm accuracy. Of course, if even more accuracy is sought, a specific metrological development should be done, preferably in (or in strong cooperation with) a metrology institution.

This chapter is organized as follows. In **section 3.2**, we present the main properties of the state-of-the-art instrumentation used in our work, as well as the error sources to be controlled or compensated for in order to optimize the accuracy of the reading of the instruments. Since temperature variations (together with vibrations) are the main error source to be dealt with at the sub- μm accuracy range, **section 3.3** deals with the development of a thermal insulation chamber inside which measurements were carried out. Finally, **section 3.4** discusses some general points to observe in order to collect reliable data from any multi-DOF high-precision flexure parallel robot.

The reader is also referred to **Chapter 4** in which we describe the work accomplished specifically on the 3 and 6-DOF robots.

3.2 – Measuring devices used and their sources of inaccuracy

In this section, we present the different measuring devices used to collect data from our robots.

The translational motions were measured perpendicularly to the surfaces of a mirror cube (mounted on the robot end-effector) using a *laser interferometer*.

Angular measurements were carried out using *electronic autocollimators*. Depending on the magnitude of these angles, the measurements were performed either on the surfaces of the mirror cube or on the faces of polygon prisms.

In addition to the above devices (sufficient for the calibration of the 3-DOF robot), three *laser high-precision absolute displacement sensors* are also required for the calibration of the 6-DOF robot.

In this section, focus is on the description of the different error sources and the necessary adjustments that have to be made in order to guarantee accurate measurements with the above measuring devices.

As a supplement to this section, the reader is also referred to **Appendix A** for a brief description of the basic operating principles of the instruments.

3.2.1 – Laser interferometer

(a) Instrument properties

All translational motions were measured using a *SIOS*^{®1} SP 2000 laser interferometer. **Table 3.1** below summarizes the main properties of this device.

PROPERTY	VALUE
Laser wavelength	$\lambda \sim 633 \text{ nm}$
Laser wavelength stability	$\leq 2 \times 10^{-8} \text{ (0.02 ppm)}$
Laser wavelength uncertainty ²	10^{-6} (1 ppm)
Measurement resolution	$\lambda/512 \sim 1.24 \text{ nm}$
Measurement range	$0 \dots 2'000 \text{ mm}$
Maximum tolerated tilt-angle (external reflector)	$\pm 2 \text{ arcmin}$
Maximum tolerated scanning rate (for fringe counting)	$600 \text{ mm} \cdot \text{s}^{-1}$
Laser output power	2 mW

Table 3.1 – Main properties of the *SIOS*[®] SP 2000 laser interferometer used in our experiments [SIO2].

¹ *SIOS*[®] Meßtechnik GmbH – Am Vogelherd 46 D-98693 Ilmenau, Germany.

² The value of this parameter is actually not specified by *SIOS*[®]. The value indicated herein corresponds to a typical situation of an interferometer before calibration.

(b) Sources of inaccuracy

■ Alignment errors

• Cosine errors

Cosine error is a measurement error caused by an angular misalignment between the laser beam and the axis of motion of the displacement being measured – **Figure 3.1**.

Cosine error degrades the signal received by the receiver and, more importantly, reduces the accuracy of the measurement because the actual target displacement is not measured.

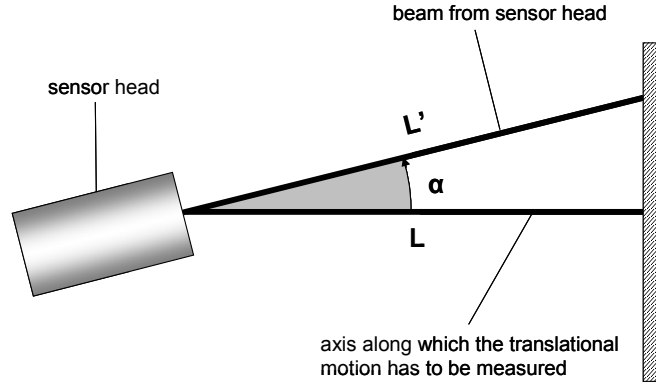


Figure 3.1 – Illustration of the *cosine error*.

If we let L be the distance to be measured and α the angular misalignment between the axis to be measured and the incident beam, then the measurement error ΔL arising from this effect and corrupting the measurement reading is given by:

$$\Delta L = L' - L = L \cdot [\cos(\alpha) - 1] \quad (\text{eq. 3.1})$$

In our case, the maximum value of this error is less than $\pm 1 \text{ nm}$ since L is, in general, less than 5 mm and $\alpha_{\max} = 120 \text{ arcsec}$ (as specified in **Table 3.1**).

• Abbe errors

Abbe errors result from an offset between the measurement laser beam and the axis of motion of the target – **Figure 3.2**.

The residual systematic error in the measurement reading due to an offset of the beam exiting the sensor head relative to the measurement axis is³:

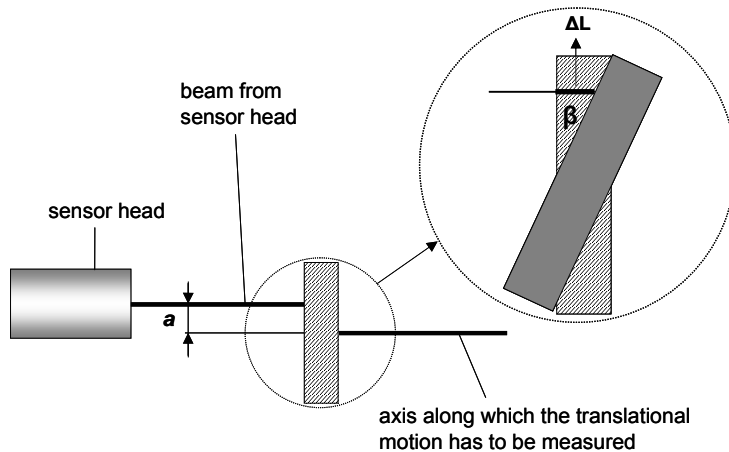


Figure 3.2 – Illustration of the *Abbe error*.

where a is the offset of the beam exiting the sensor head relative to the measurement axis (called “Abbe offset”) and β is mirror tilt angle (see **Figure 3.2**).

³ Some authors consider the expression of the Abbe errors to be rather $\Delta L = a \cdot \sin(\beta)$, depending on the definition of a . In our case, since the angle β is very small, the use of this alternative expression provides the same error value.

Positioning the beam as close as possible to the axis of motion will reduce the Abbe error⁴.

• When collecting the data from the 3-DOF robot, Abbe errors could be up to $\pm 50 \text{ nm}$, assuming Abbe offsets up to $\pm 1 \text{ mm}$ and parasitic angular variations up to $\pm 10 \text{ arcsec}$.

• In the case of the 6-DOF robot, Abbe errors are negligible ($< \pm 2 \text{ nm}$) since angular variations of the external mirror (in respect to its initial orientation) when measuring with interferometer are in this case less than $\pm 0.3 \text{ arcsec}$.

■ Dependence of the laser wavelength on environmental factors

Laser wavelength varies with the refractive index of ambient air, which in turn varies with temperature, barometric pressure and humidity. The relation between these properties of air and its refractive index is expressed by the *Edlen equation*.

Table 3.2 gives the numerical values of the variation of the laser wavelength in respect to variations in the environmental factors (temperature, pressure and relative humidity).

<i>Errors in environmental factors</i>	<i>Relative errors in λ</i>	<i>Maximum ranges of environmental factors</i>
Temperature: $\pm 0.3 \text{ }^{\circ}\text{C}$	$\pm 2.8 \times 10^{-7}$	$20 \text{ }^{\circ}\text{C} \pm 10 \text{ }^{\circ}\text{C}$
Pressure: $\pm 50 \text{ Pa}$	$\pm 1.4 \times 10^{-7}$	$101.325 \pm 20 \text{ KPa}$
Relative humidity: $\pm 3 \text{ \%}$	$\pm 0.3 \times 10^{-7}$	$10 \text{ \%} - 90 \text{ \%}$

Table 3.2 – Influence of the environmental factors on the laser wavelength (according to Edlen equation and manufacturer data [SIO2]) in the case of the SIOS® SP 2000 laser interferometer.

According to the values reported in **Table 3.2**, we can see that:

• A variation in the temperature of the ambient air of $1 \text{ }^{\circ}\text{C}$ leads to a variation in the laser wavelength of approximately 10×10^{-7} . The corresponding measurement uncertainty over a given measuring path L will then be $\varepsilon = 0.1 \times 10^{-5} \times L$.

Example: if $\Delta T = 1 \text{ }^{\circ}\text{C}$ and $L = 100 \text{ mm} \rightarrow \varepsilon = 100 \text{ nm}$

• A variation in the barometric pressure of $4'000 \text{ Pa}^5$ leads to a variation in the laser wavelength of approximately 1×10^{-5} . The corresponding measurement uncertainty over a given measuring path L will then be $\varepsilon = 1 \times 10^{-5} \times L$.

Example: if $\Delta P = 4'000 \text{ Pa}$ and $L = 100 \text{ mm} \rightarrow \varepsilon = 1 \text{ }\mu\text{m}$

• A variation in the relative humidity of 1 \% leads to a variation in the laser wavelength of approximately 0.1×10^{-7} . The corresponding measurement uncertainty over a given measuring path L will then be $\varepsilon = 0.1 \times 10^{-7} \times L$.

Example: if $\Delta H = 1 \text{ \%}$ and $L = 100 \text{ mm} \rightarrow \varepsilon = 1 \text{ nm}$

We can see that temperature and pressure are the main factors to be corrected for performing accurate measurements with the laser interferometer. A pressure transducer and a temperature sensor (precision Pt-100-thermistor) are used to correct⁶ the laser wavelength periodically (every 10 seconds).

⁴ Notice that the interferometer reading can be corrected for Abbe errors as long as the corresponding Abbe offset and tilt are known. A correction of this type has been performed in the case of the 3-DOF – see **section 4.2.2** and **Appendix B**.

⁵ $4'000 \text{ Pa}$ is an extreme value corresponding to a storm.

⁶ Measuring resolutions of these sensors are $0.02 \text{ }^{\circ}\text{C}$ and 7 Pa [SIO2]. Ideally, the correction of the laser wavelength has to take into account the interferometer's dead path and the distance to be measured, represented respectively by l and d in **Figure A.1** in **Appendix A**. However, in our case, since the value of the dead path remains unknown the correction of the wavelength is only performed on d .

Correction of humidity has not been performed as the variations in the relative humidity during a measuring period are typically within $\pm 5\%$ (which, in our case, brings an error of ± 5 nm).

■ Expansions of the interferometer's dead path

During a measuring session, the interferometer's dead path may experience expansions. These expansions are mainly related to variations in the **temperatures** T_i of the different materials taking part in the measuring loop between the splitter and the object, according to a well known linear law:

$$l = l_0 + \sum_i a_i \cdot \Delta T_i \quad (\text{eq. 3.3})$$

where $a_i = l_{0,i} \cdot \alpha_i$, $\Delta T_i = T_i - T_{i,0}$ and α_i are the thermal expansion coefficients of the materials.

These temperature variations ΔT_i are mainly due to variations in the temperature of the air surrounding each material (convection-based heat transfer).

The dead path may also experience expansions in respect to **humidity** due to the presence of hydrophilic materials such as glue.

In a first approximation, this expansion is linear in respect to the humidity variation ΔH :

$$l = l_0 + b \cdot \Delta H \quad (\text{eq. 3.4})$$

In order to evaluate the relative importance of humidity and temperature variations in the expansions of the interferometer's dead path, a simple test was carried out (**Figure 3.3**).

In our test, the *SIOS*[®] interferometer, mounted over a block of aluminium ($\alpha_{Al} \sim 21 \cdot 10^{-6} / ^\circ\text{C}$) was reading the position of a mirror cube.

The measurements were taken inside a polystyrene box (protecting the measuring environment from air currents and other transient disturbances).

Every minute, the reading of the interferometer was recorded. For every measurement, variations in the temperature of the interferometer T_I , in the temperature of the environment T , in the humidity of the environment H and in the temperature of the aluminium block T_B (in which the interferometer and the mirror were mounted) were also recorded.

Ten measurement sessions lasting 24 h each were performed.

A linear least-squares regression was then achieved with the data recorded in order to determine the different expansion coefficients of equations 3.3 and 3.4.

The expression describing the expansion of the interferometer's dead path was therefore:

$$\Delta d = 423.4598 \frac{\text{nm}}{^\circ\text{C}} \Delta T_B + 709.9946 \frac{\text{nm}}{^\circ\text{C}} \Delta T_I - 801.0895 \frac{\text{nm}}{^\circ\text{C}} \Delta T - 17.6994 \frac{\text{nm}}{\%} \Delta H \quad (\text{eq. 3.5})$$

Again, the results of this test showed the **importance of temperature monitoring and correction in order to obtain reliable measurements with sub- μm accuracy**.

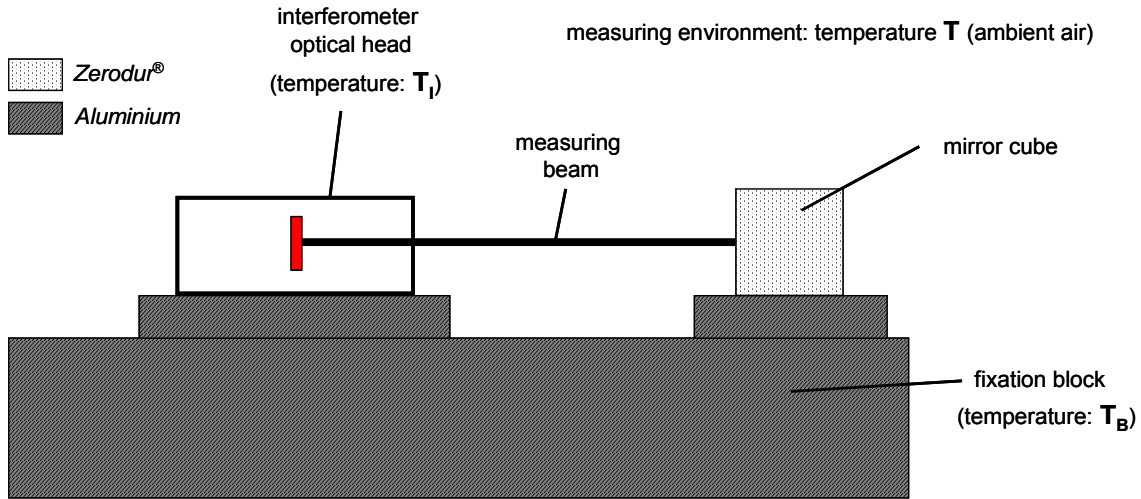


Figure 3.3 – Set-up used to evaluate the expansion of the interferometer's dead path in respect to the temperature and humidity.

■ “Beam break”

Laser interferometers are devices based on *incremental counting*. Therefore, the distances are always measured in a relative mode. This means that at the beginning of the measurement, after the reflecting surface is set orthogonal to the beam, the interferometer reading is set to zero and measurements are carried out relatively to this position.

The major inconvenient of this incrementally-based operating principle lies in the fact that, if the orthogonality between the incident and reflected beams goes (statically or dynamically) out of the tolerated range (± 120 arcsec in the case of the *SIOS*[®] SP 2000), the previous reference position in respect to which the reading was being achieved is lost – “*beam break*”. This causes the subsequent readings to be radically shifted by an unknown offset.

In our case, this issue was particularly important when measuring the translations of the 6-DOF robot – see **paragraph (a)** of **section 4.3.3**.

■ Other issues

In order to maximize the accuracy of the reading, the following points were observed during the measurements with the *SIOS*[®] interferometer [SIO2]:

- Surfaces with high *reflectivity* (better than 90 %) and *flatness* (better than $\lambda/20 \sim 30$ nm) were used for the measurements⁷. In addition, they were properly cleaned with acetone and kept free of dust, dirt and fingerprints at all times;
- *All interconnecting cables* (in particular the fiberoptic cable used to conduct the beam from the He-Ne laser housed in the power supply/signal analyzer unit to the sensor head) *were securely clamped down and free from tensions and stresses during all measurement sessions* as their influence could be critical;
- The accuracy of the interferometer measurements is critically dependent upon the sensor mount and mechanical relaxations in the screwed parts. To avoid errors arising from mechanical stresses, measurements started at least one day after mounting the optical head. Moreover, the temperature regulation period made this “mechanical stabilization” easier⁸.

⁷ The description of the mirror cube used for our measurements will be given in **section 4.2.1 – paragraph (a)**.

⁸ Together with proper mounts, temperature cycles can be used for the suppression of mechanical stresses from a given fixation.

3.2.2 – Laser displacement sensors

(a) Instrument properties

Three *Keyence*^{®,9} laser displacement sensors (based on the optical triangulation principle – see **section A.2** of **Appendix A**) were used only for the calibration of the 6-DOF robot¹⁰. **Table 3.3** lists the main properties of these sensors [KEY].

PROPERTY	VALUE	
	<i>Model LC-2420</i>	<i>Model LC-2430</i>
Optical source	Semi-conductor laser $\lambda \sim 670$ nm	
Measurement resolution	10 nm	20 nm
Measurement range	± 0.2 mm	± 0.5 mm
Linearity ¹¹	± 100 nm	± 250 nm
Sampling frequency	50 KHz	
Operating distance (to target)	10 mm	30 mm
Laser output power	1.9 mW	

Table 3.3 – Main properties of the *Keyence*[®] LC laser displacement sensors [KEY].

Despite their poor linearity and range, the major advantage of these laser sensors in respect to the interferometer lies in the fact that they provide an absolute reading, which excludes any “beam break” issue. Therefore, even if the measurand goes out of range and back again into the reading zone, the sensor will provide an absolute value corresponding to the final position of the target.

(b) Sources of inaccuracy

As in the case of any high-precision optical instrument for measuring distances, **alignment errors** and **temperature variations** are key factors determining the accuracy of the reading of the *Keyence*[®] sensors.

Note also that, in our case, the measuring beam is not reflected on a planar external mirror, as an ideal measuring configuration would require. Instead, the reflection is rather performed on a steel mirror sphere (diameter = 15 mm) mounted on the robot end-effector.

This sphere therefore had to be kept free of dirt and dust and the beam had to be previously adjusted in such a way that the intensity of the received signal was maximized – **Figure 3.4**.

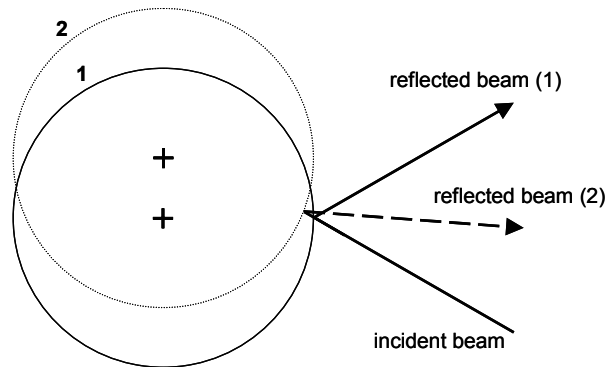


Figure 3.4 – “Bad reflection” of the laser beam at the sphere’s surface, decreasing the signal intensity and therefore the measurement accuracy.

⁹ *Keyence*[®] AG Schweiz, Schönenwerdstr. 7, CH-8902 Urdorf Switzerland.

¹⁰ See **section 4.3.1 – paragraph (c)**.

¹¹ The term “linearity” is explained in **Appendix A** and illustrated schematically in **Figure A.4** of this Appendix.

It is very important for the reader to note that these sensors were not used to actually perform measurements of distances¹² but rather as “zero detectors” i.e. only for adjusting the robot end-effector, through a closed-loop action, to a position for which the three sensors read “zero” simultaneously¹³.

Therefore, the particular configuration in which these sensors are used (reflection on a spherical surface) as well as the possible orthogonality errors between the three corresponding optical heads when fixed in their mount are not critical issues in our case.

3.2.3 – Electronic autocollimators

(a) Instrument properties

All angular measurements were performed using two *Newport*[®],¹⁴ LDS 1000 electronic autocollimators (**Figure 3.5**). **Table 3.4** lists the main properties of this device [LDS].

PROPERTY	VALUE
Laser wavelength	$\lambda \sim 670 \text{ nm}$
Measurement resolution	$\sim 0.02 \text{ arcsec}$
Measurement range	$\sim \pm 412 \text{ arcsec}$
Sampling frequency	2'000 Hz
Beam diameter	31 mm
Peak power	0.9 mW

Table 3.4 – Main properties of the *Newport*[®] LDS 1000 electronic autocollimator [LDS].

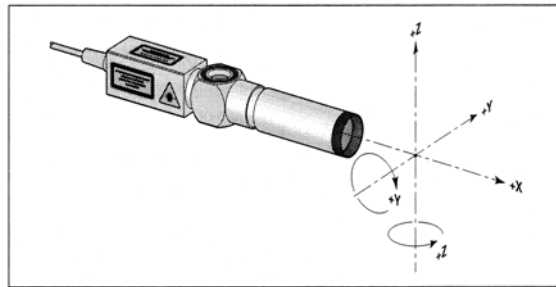


Figure 3.5 – Reading angular variations with the autocollimator.

Angular variations within the range of the autocollimators were measured on the surfaces of a precision **mirror cube**¹⁵.

Measurement of “large angles” (up to $\pm 3^\circ$) covering the angular workspace of the robot were performed with the help of **polygon prisms**¹⁶ previously calibrated by METAS¹⁷ within $\pm 0.5 \text{ arcsec}$ – **Figure 3.6**.

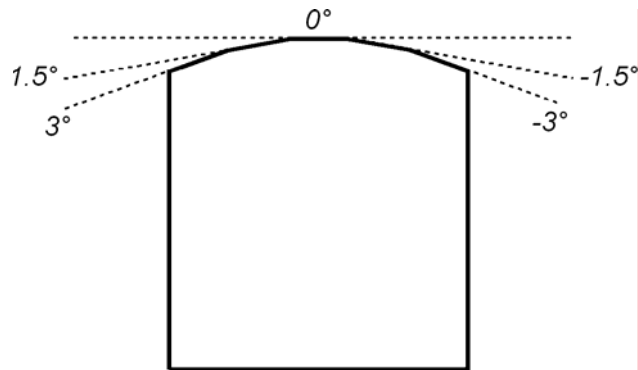


Figure 3.6 – Polygonal prism used for the measurement of “large angles” with the *Newport*[®] LDS autocollimator.

¹² The *SIOS*[®] interferometer was the device used for that purpose.

¹³ The reader is referred to **section A.5 of Appendix A** for additional information on this point.

¹⁴ *Newport*[®] GmbH, Guerickeweg 7, D-64291 Darmstadt, Germany.

¹⁵ The description of the characteristics of the mirror cube will be given in **section 4.2.1 – paragraph (a)**.

¹⁶ The dimensions of the polygon prisms were approximately equal to those of the mirror cube. Polygons with the same dimensions but having a higher number of faces could be used in the future – however, the accuracy of the corresponding measurements may be decreased drastically, according to what will be discussed in **paragraph (b)** of this section.

¹⁷ METAS: Swiss Federal Office of Metrology and Accreditation, Lindenweg 50 CH-3003 Wabern, Switzerland.

(b) Sources of inaccuracy

According to the manufacturer, the accuracy of the autocollimators is mainly influenced by the factors mentioned below.

■ Reduced size of the measuring beam

In order to test the influence of the size of the measuring beam, the test described hereafter was carried out.

A large number (> 500 points) of angular variations were measured in two different configurations: first, with the mirror cube (measuring surface: $30 \times 30 \text{ mm}^2$) and, second, with the central facet of the polygonal prism¹⁸ (measuring surface: $25 \times 3 \text{ mm}^2$).

The difference between the angular variations read by the autocollimator corresponding to the two different configurations revealed differences up to $\pm 2 \text{ arcsec}$ – **Figure 3.7**. This value can be explained by the reduction of the measuring surface used for the reflection of the laser beam.

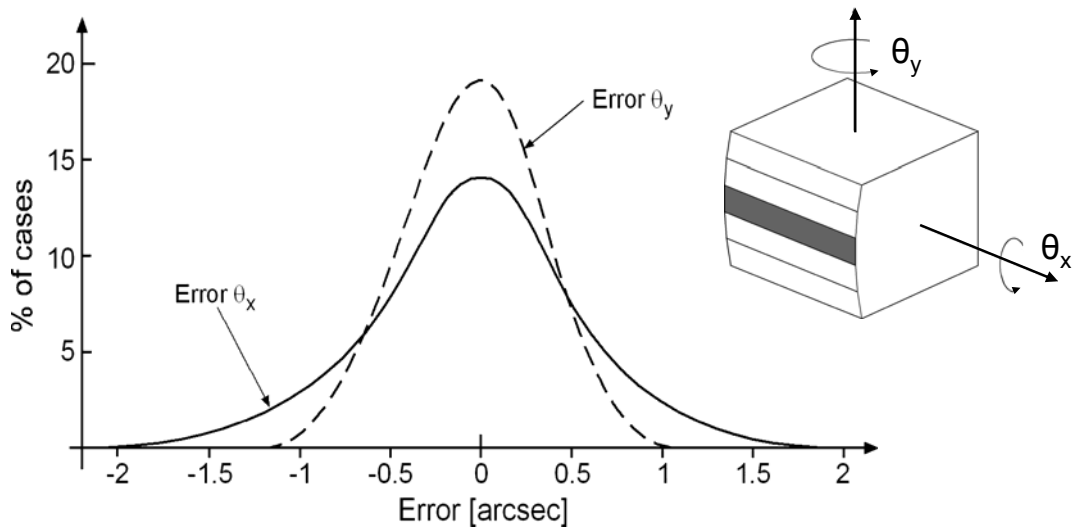


Figure 3.7 – Effect reducing of the reflecting surface on the measuring accuracy of the Newport® LDS autocollimator.

In addition to the previous parameter, it was also noticed that, for a given reduced measuring surface, differences in the reading were observed if different regions of the primary autocollimator beam were used for the measurements.

This situation is illustrated in **Figure 3.8** in which three different regions of the beam were used to read the angular variations on a surface with a restricted aperture.

Experiments showed that, for a reading aperture of $20 \text{ mm} \times 5 \text{ mm}$ and a distance $L = 8 \text{ mm}$ (see **Figure 3.8**), the reading differences could be up to $\pm 1 \text{ arcsec}$.

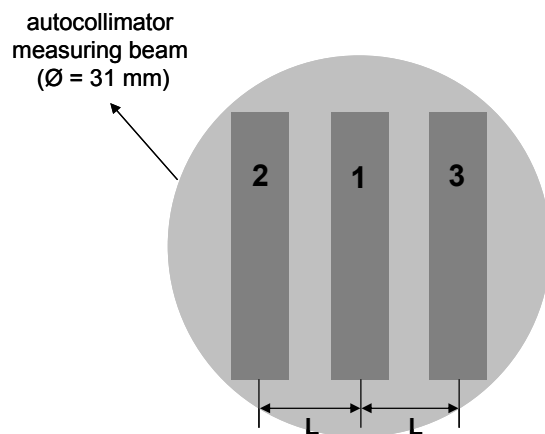


Figure 3.8 – Illustration of a displacement of the reflecting surface when performing measurements with the autocollimator.

¹⁸ The borders of the reflecting surfaces had to be covered since they could also influence the reading accuracy. Errors arising from border effects are particularly important in the case of medium and low quality mirrors.

We believe that the reason for this effect probably lies in the *lack of homogeneity of the autocollimator's measuring beam*. Measurements on mirrors presenting poor surface flatness may also bring additional error.

■ Temperature

According to *Newport*[®] [LDS], variations in the environmental temperature may cause differences in the reading of approximately 0.15 % / °C. In our case, this temperature effect is negligible since our measuring environment is thermally-regulated and stabilized.

Moreover, as opposed to the above measuring devices, *the reference position has proved to experience almost no angular drifts relatively to the temperature variations during the measurements (after the transient drifts occurring immediately after the optical head is fixed in its corresponding mount)*.

■ Operating distance

The manufacturer claims that large distances (> 1 m) can lead to variations of up to 0.2 arcsec·m⁻¹ due to atmospheric turbulence in the vicinity of the measuring bench.

Again, in our case, operating distances are generally less than 80 mm which makes this effect completely negligible.

(c) Calibration and use of the autocollimators

Before starting our measurements, the two electronic autocollimators were calibrated at METAS. At the end of this calibration, two important characteristics were known for each autocollimator:

- the *linearity* of the device¹⁹ (correspondence between the real value and the value indicated by the device) was calibrated within ± 0.16 arcsec;
- the orientation of the *auxiliary axis* of measurement (angle α in **Figure 3.9**) was calibrated within $\pm 0.01^\circ$.

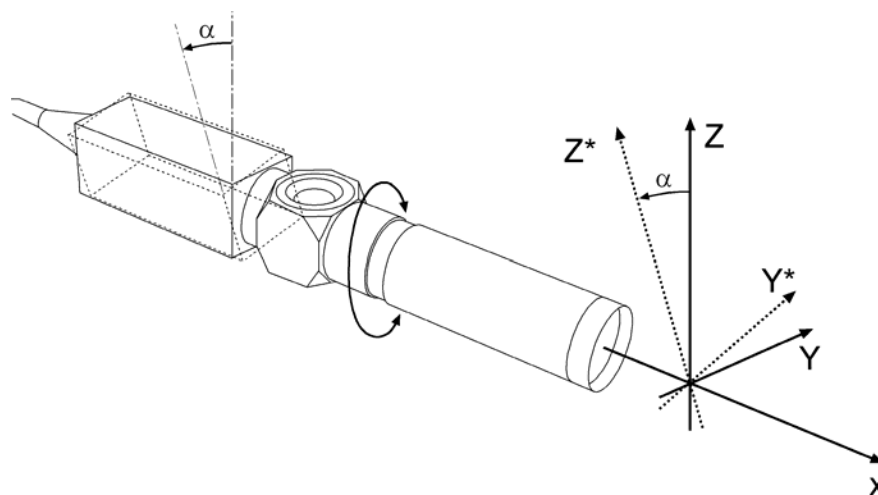


Figure 3.9– Illustration of the adjustment of the auxiliary axis (angle α) before a measurement session with the LDS autocollimator.

¹⁹ Before calibration, typical non-linearity values of the autocollimators could be up to ± 10 arcsec (full-scale). The definition of linearity is given in **Appendix A** and is illustrated in **Figure A.4** of this Appendix.

The purpose of the calibration of the auxiliary axis was, as far as possible, to align the “internal axes” of the autocollimator with the axes of our reference frame (in order to avoid “crosstalk” effects). **Figure 3.9** illustrates the adjustment of this so-called auxiliary axis (angle around X-axis in this figure).

The effect of a misalignment of this auxiliary axis could be observed when performing measurements with two autocollimators since there is a **redundant reading** for this particular measurement configuration (angle around the vertical axis).

In order to evaluate this effect, the situation illustrated in **Figure 3.10** was tested experimentally with the autocollimator **LDS 1** reading θ_x^{20} and $\theta_{z,1}$, while autocollimator **LDS 2** was reading θ_y and $\theta_{z,2}$. The auxiliary axis of **LDS 1** was adjusted to the value provided by METAS, while the auxiliary axis of **LDS 2** was set to different orientations, α , relatively to its corresponding METAS calibration value.

The difference $\Delta = \theta_{z,1} - \theta_{z,2}$ was then recorded for different orientations α and different consign values $\theta_{z,1} = \theta_z$ measured by **LDS 1** (assumed to provide a correct reading of θ_z).

Figure 3.11 reports this difference, observed to be up to ± 6 arcsec.

A proper adjustment of the auxiliary axes of the two autocollimators within $\pm 0.01^\circ$ performed with the help of a *Shaevitz*[®] **inclinometer** led to differences less than ± 0.2 arcsec in the redundant reading over the entire measuring range.

The analysis of the difference between the two readings of this angle can thus be used to detect whether the internal axes of the two autocollimators are properly aligned with the axes defined by the surfaces of the mirror cube²¹.

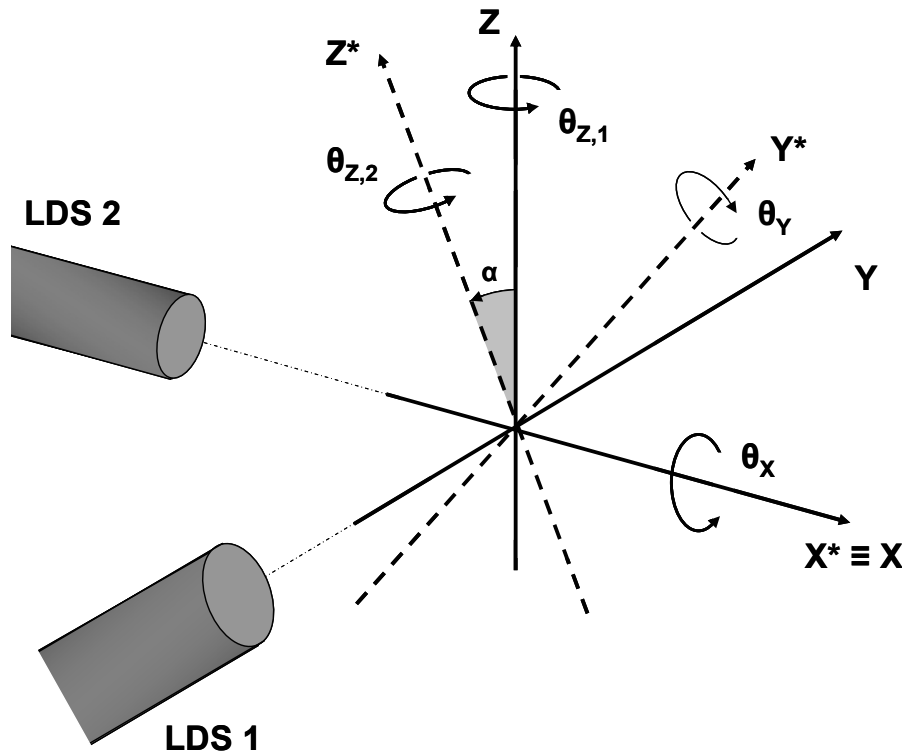


Figure 3.10 – Measurements with the two autocollimators **LDS 1** and **LDS 2**, with a misalignment of the auxiliary axis of **LDS 2**.

²⁰ Actually, “LDS 1” reads $-\theta_x$ instead of θ_x .

²¹ This adjustment will be particularly important for the measurements on the 6-DOF robot – see **section 4.3.1**.

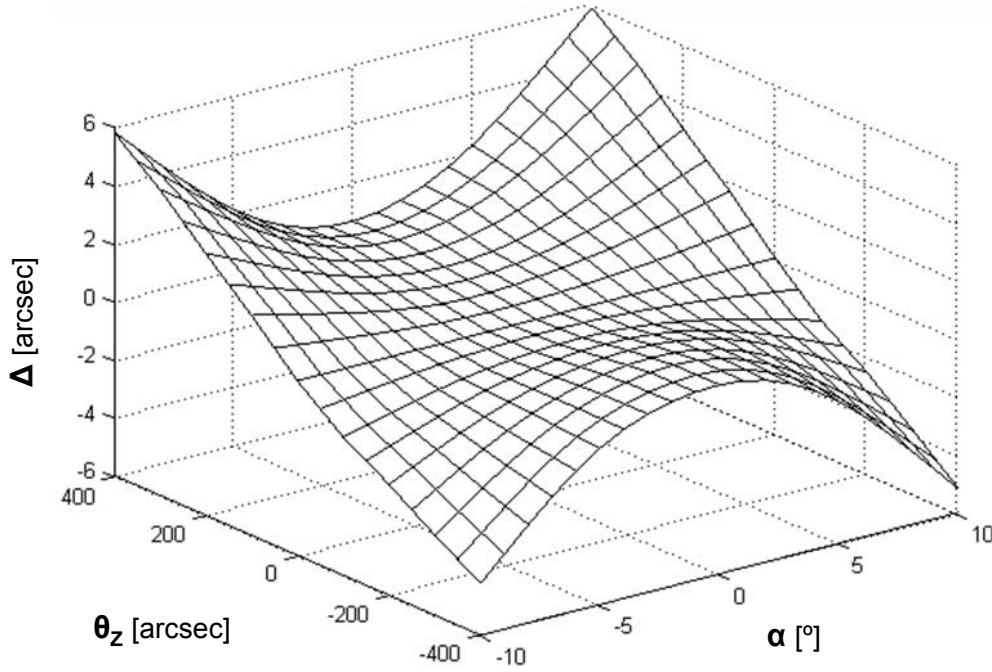


Figure 3.11 – Difference Δ in the redundant reading as a consequence of a misalignment of the autocollimator's auxiliary axis (configuration of **Figure 3.10**).

3.3 – Regulation of the measuring environment

3.3.1 – Introduction and motivation

As mentioned in the previous section, devices able to provide reliable measurements at the sub- μm range are, in general, strongly influenced by **temperature variations**. We have seen, for example, that temperature variations influence the reading of the *SIOS*[®] laser interferometer in two ways: (1) by expanding the interferometer dead path and (2) by changing the laser wavelength.

In addition to this, temperature variations may also influence the robot itself, by changing its geometric dimensions. Simple calculations indicate that a steel bar with a length of 200 mm undergoes an expansion of approximately 18 nm if its temperature varies by 0.01 °C. Since the geometric dimensions of the two robots studied in this thesis are in the order of 200 x 200 x 200 mm³ and the thermal expansion coefficient of their material (titanium alloy) is of the same order of magnitude as that of steel²², it is desirable to perform the measurements in an environment having a temperature varying less than ± 0.1 °C if we want to get an absolute measuring accuracy below ± 100 nm.

In reality, the two previous effects are, in general, coupled in such a way that it is almost impossible to distinguish the contribution of each effect to the drift indicated by the measuring device²³.

²² The thermal expansion coefficient of the titanium alloy is $\alpha_{\text{Ti6Al4V}} \sim 8.9 \cdot 10^{-6} / ^\circ\text{C}$.

²³ If the measuring devices are operating in a **differential mode** (e.g. 2-beam interferometer with 1 beam reading the surface of a fixed reference frame) the effect of the expansion of the interferometer's dead path can be fully suppressed. Unfortunately, for economic reasons, this solution could not be adopted.

In order to reduce the impact of temperature variations on the accuracy of a given high-precision flexure parallel robot, the following solutions can be adopted:

1. use materials with very low thermal expansion coefficients, such as *Invar*[®] or *Superinvar*[®];
2. work or measure inside a thermally-regulated environment in which the temperatures of the robot and of the different parts involved in the measuring/working loop are stabilized within a tolerance better than ± 0.1 °C;
3. introduce a real-time correction on the robot geometric model describing the different thermal expansions on the basis of a permanent reading of the temperatures of the relevant parts (robot + measuring/working loop).

Despite its simplicity, the first solution is often impracticable since it requires materials that are usually very expensive and/or difficult to manufacture. In addition, such materials may not have a mechanical behaviour (e.g. fatigue) adapted to achieve some particular kinematic functions (such as a translational stage).

The second solution is a more cost-effective approach. The goal here is to insulate the measuring/working environment from external disturbances and guarantee a stable and homogeneous distribution of the different temperatures. Therefore, the overall drift (robot + measuring/working loop) of the reference position is reduced without the need for determining the exact contribution of each part.

The most attractive solution from the industrial point of view is obviously the third one. This approach aims to guarantee accuracies within the sub- μm range for robots operating in unsteady industrial conditions, without having to insulate and/or stabilize the robot and its measuring/working environment. However, the difficulty of this approach lies in the fact that, in this case, gradients can occur, creating complex and non-linear behaviour coming from almost everything (robot, measuring loop, measuring instruments, industrial application, ...) Processing the overall signal in order to separate each relevant contribution and extracting robust and highly accurate predictive models will be a task of tremendous complexity.

In this thesis, we adopted the second solution (*temperature regulation*) by performing the measurements inside a thermal insulation chamber, leaving the thermal calibration (third solution) to future investigations²⁴. In **section 3.3.2** we present the thermal insulation chamber used, its active elements and the principle adopted for regulating the temperature. **Section 3.3.3** shows the results of the temperature regulation during the experiments conducted on the two robots and the improvement in respect to a non-regulated situation.

3.3.2 – *Temperature regulation system*

(a) Design of a thermal insulation chamber²⁵

As mentioned above, our main concern is to regulate and stabilize the temperatures of the robot being calibrated and that of the measuring environment.

When a robot is being calibrated, several heat sources have to be considered for a proper dimensioning of the system regulating the temperatures:

- the motors imposing the required displacements in the translational stages of the robot;
- the measurement devices used to collect the data.

²⁴ See **section 8.3.2 – paragraph (a).**

²⁵ The thermal insulation chamber used in this thesis was originally developed by Fischer [Fis03] and Niaritsiry [Nia06].

The design of our thermal insulation chamber aimed to answer the following requirements:

1. *thermal requirements:*

- insulation against external thermal disturbances (human operators, instrumentation);
- homogeneous temperature distribution inside the insulated environment;
- evacuation of the heat produced by the robot motors and measurement devices;
- possibility of regulating the temperature of the measuring environment.

2. *mechanical requirements:*

- avoid a rigid contact between the robot and the insulation system in order to suppress the propagation of vibrations;
- flexibility in mounting the active elements of the regulation in order to be able to test different scenarios (and therefore to find the best configuration for the regulation) for each of the two robots;
- practical requirements: sufficient space inside for the robot and different measuring devices, easy to open for eventual adjustments.

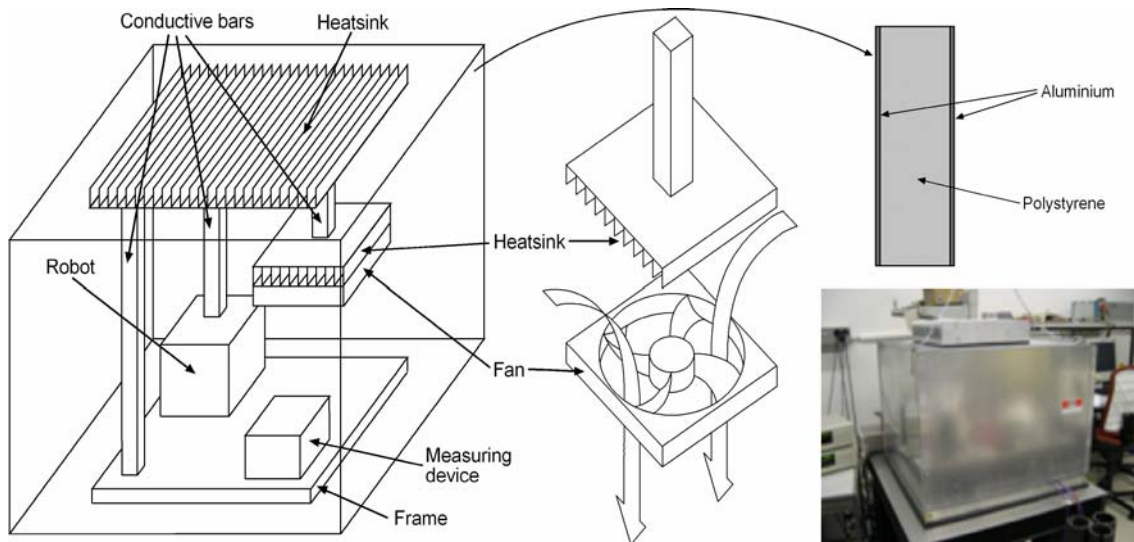


Figure 3.12 – The thermal chamber: scheme showing the main functional parts and photographic view.

In order to provide an answer to these requirements, the cost-effective solution described below has been developed.

The robot and all the measurement devices were mounted inside a 600 mm x 600 mm x 600 mm chamber with walls (thickness = 40 mm) made of polystyrene (very small thermal conductivity) for efficient insulation against thermal variations occurring outside the measuring environment. Both interior and exterior parts of the chamber walls are covered with aluminium (thickness = 2 mm) in order to create a homogeneous temperature distribution inside the box (inside walls) and to stiffen the outside structure (exterior walls).

The heat produced by the robot motors and the measurement instruments is evacuated with the help of *Peltier cells* (**Figure 3.13**) mounted between a conductive material (aluminium bars) linked to the part whose temperature is to be controlled and a heat sink connected to the external environment. A fan²⁶ system is used to maintain the temperature of the air inside the chamber homogeneous and constant throughout the regulation period.

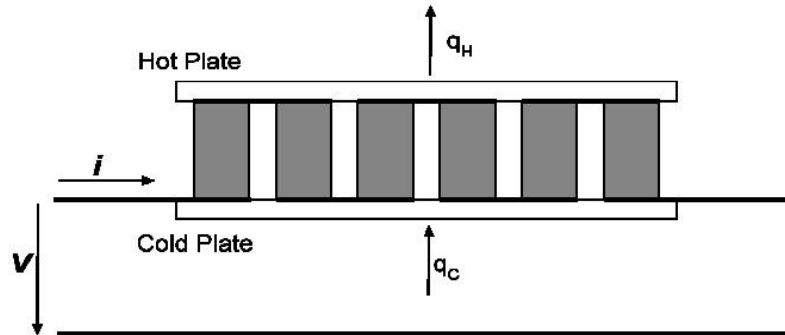


Figure 3.13 – Functional representation of a *Peltier cell*, the active element in our temperature regulation system.

The system can be opened from outside for easy access to the chamber inside. In order to complete the thermal and mechanical (protection against vibrations) insulation, the contact between the walls closing the thermal chamber and the *Newport*[®] anti-vibration table (on which the robot and the measurement devices are fixed) is made of rubber²⁷.

Figure 3.12 provides a schematic view of the different components inside the thermal chamber and a photographic view of the outside part (mounted in the *Newport*[®] table). In order to dimension the elements taking part in the thermal chamber, the thermal modelling was achieved by means of an equivalent electrical circuit analogy.

(b) Temperature regulation

Inside the thermal chamber, the different temperatures are acquired analogically with the help of Pt 1000 differential resistor temperature sensors²⁸ (model CRZ 2010-1) connected to a *Keithley*[®] 2700 multimeter. These sensors are placed in order to monitor all the parts involved in the measurement (robot structure, measuring devices, robot fixation frame, fixation of the measurement devices, ambient air). The readings are then converted into digital values in order to be processed by a computer.

Using a P-I-D closed-loop regulation law (implemented in *LabView*[®]) and taking into account the readings of the different temperatures, the computer calculates the currents to be supplied to the Peltier cells.

In order to stabilize the robot to a certain temperature consign, at least 6 – 8 hours are typically required. This thermal stabilization must, of course, also be active during the entire measurement phase, because the robot motors and the measuring devices will produce heat.

Figure 3.14 provides a schematic view of the overall temperature-regulation system.

²⁶ A laminar air flow has to be maintained in order to avoid turbulences in the air surrounding the robot. These turbulences could disturb our measurements by influencing the instrument readings and creating vibrations in the measuring environment.

²⁷ In addition to this, a mechanical decoupling between the different parts of the chamber is also suitable in order to minimize the influence of external vibrations on our measurements completing, therefore, the mechanical insulation of our measuring environment. Example: the conductive bars may be attached to the measuring frame by means of copper braids.

²⁸ These sensors were used because of their high sensitivity and low drift.

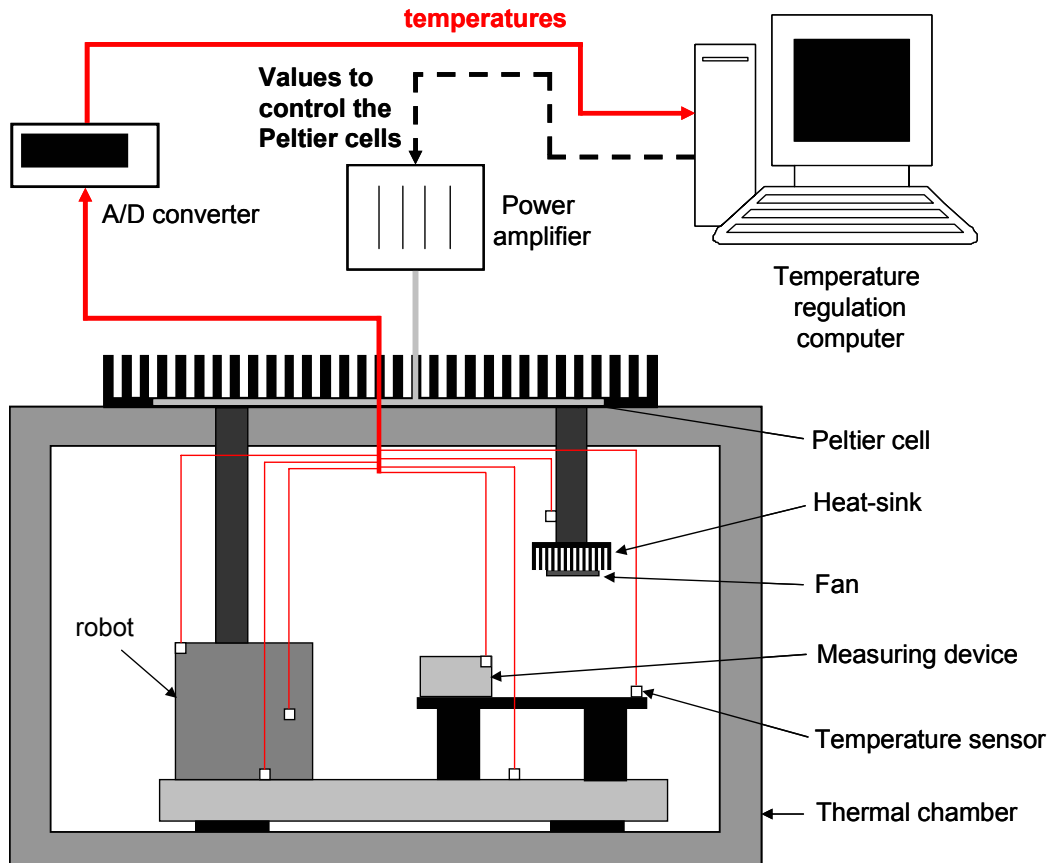


Figure 3.14 – General overview of the temperature regulation system.

3.3.3 – Results of temperature regulation

(a) Preliminaries

Two different heat transfer mechanisms are responsible for the temperature variations experienced by the robot mechanical parts:

- *conduction effect*: coming from temperature variations in the motors used to impose the displacement to the translational stages (and therefore attached to them) of each kinematic chain;
- *convection effect*: coming from temperature variations occurring in the ambient air surrounding the robot structure.

A recent work [Nia06] proved through experiments and simulations that a temperature variation in the motors has almost no influence on the temperature of the robot mobile structure. The heat transfer through conduction can thus be considered negligible.

Consequently, temperature variations suffered by the robot structure are almost exclusively attributable to variations in the temperature of the ambient air (convection).

As we shall see in paragraphs (b) and (c), *this observation was used to actually achieve the temperature regulation on both robots.*

(b) Experiments conducted on the 3-DOF robot

For the measurements of the 3-DOF robot, the different materials involved in the measuring loop were a titanium alloy (robot mobile structure), steel²⁹ (robot frame) and aluminium³⁰ (frame on which the measuring instruments were fixed) – **Figure 3.15**.

Different scenarios were tested experimentally for the temperature stabilization in the case of the 3-DOF robot.

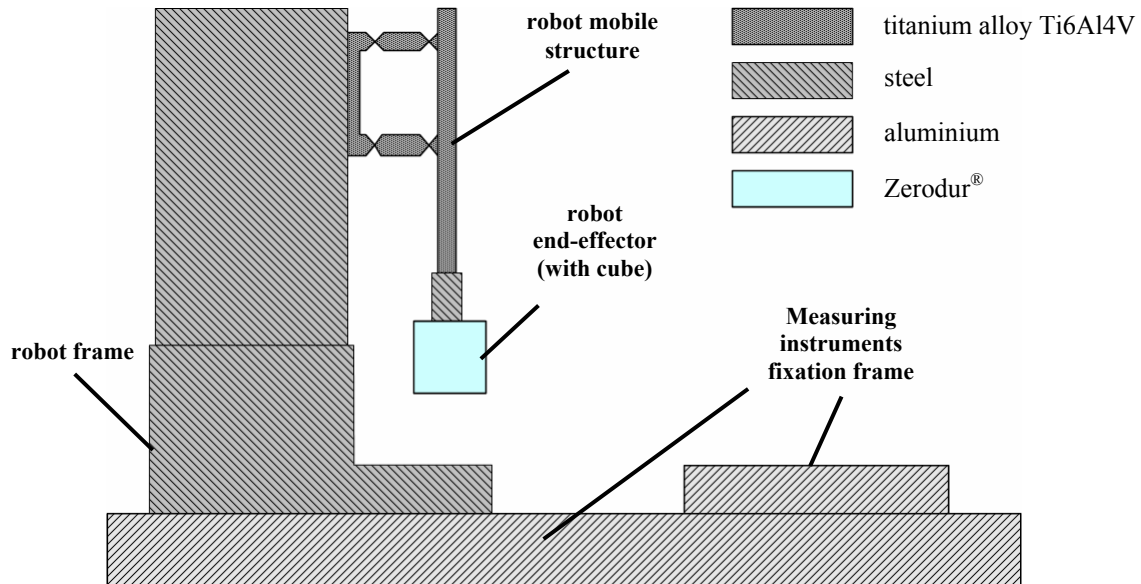


Figure 3.15 – Different materials involved in the measuring loop of the 3-DOF robot.

In fact, starting from a redundant number of Peltier elements (3 for the motors, 1 for the robot frame and the fixation frame of the measurement devices, 1 for robot mobile structure and the ambient air), different tests were carried out in order to determine the configuration having the minimum number of Peltier cells able to perform the desired temperature regulation.

The final configuration adopted had three Peltier cells³¹. A first Peltier regulates the temperature of the robot frame. A second Peltier regulates the temperature of the frame on which the measurement devices are fixed in order to guarantee a homogeneous distribution of the temperatures of the different materials inside the chamber³². The last Peltier regulates the temperature of the robot mobile structure through a regulation of the temperature of the air inside the chamber.

The reason for using the temperature of the ambient air inside the thermal chamber to perform the actual regulation is clear from the graphs in **Figure 3.16**. In fact, it was observed that the robot mobile structure, due to its small thermal inertia, has a temperature that follows closely the temperature of the ambient air surrounding the robot.

²⁹ Steel and titanium have very similar thermal expansion coefficients.

³⁰ Steel would clearly be a better choice here. However, at the beginning of the project, we wanted to increase the value of the expansion in the interferometer dead path, for study purposes – therefore, we decided to use aluminium, which has a higher thermal expansion coefficient: $\alpha_{Al} \sim 21 \cdot 10^{-6} / ^\circ C$.

³¹ These three Peltiers had of course the same temperature consign for the regulation: generally 25 °C.

³² The goal of an ideal temperature regulation is to set all the temperatures to the same consign value. However, when performing the measurements, since periodic returns to the reference position are done to correct the static part of the temperature drift (and the residual dynamic thermal drift after temperature stabilization), the only temperature that has actually to be set to the consign value is that of the robot mobile structure, since in this work the goal is to calibrate the two robots always for the same (stable) temperature. See **section 3.4.4** for a detailed discussion about strategies for the correction of thermal drift.

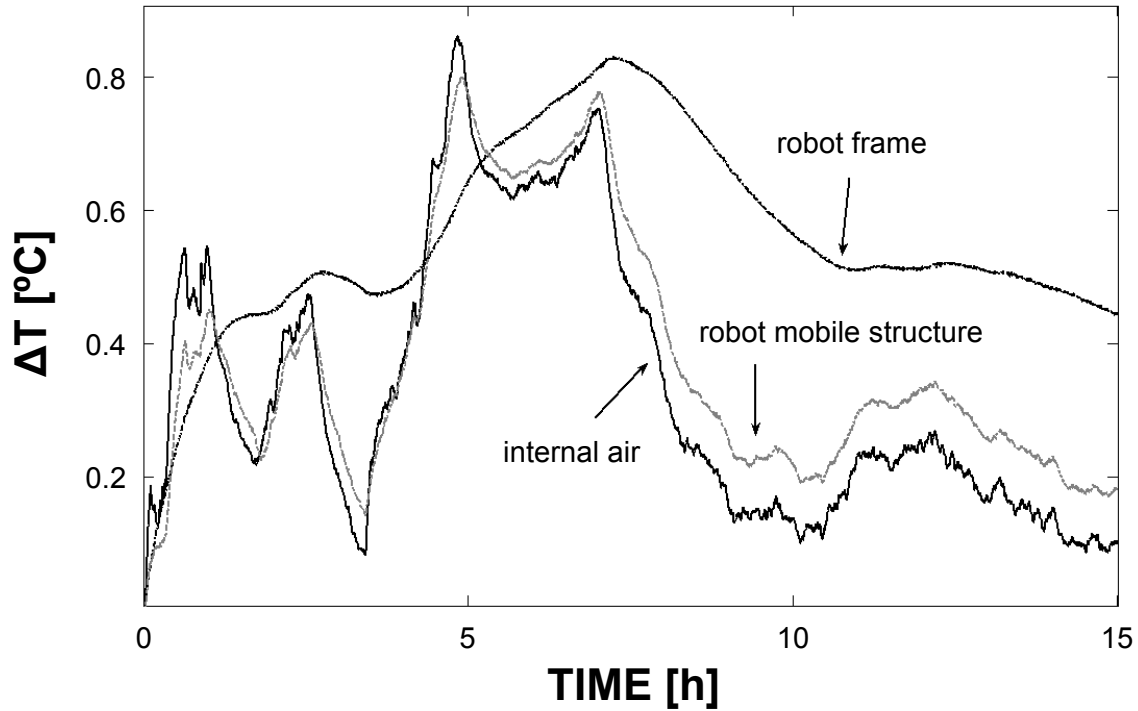


Figure 3.16 – Variations of the temperatures of the robot mobile structure, robot frame and the ambient air surrounding the robot structure in a situation without temperature regulation. Due to its small thermal inertia, the robot mobile structure follows very closely the temperature of the ambient air, whereas the robot frame, thanks to its large mass, has a thermal inertia much larger.

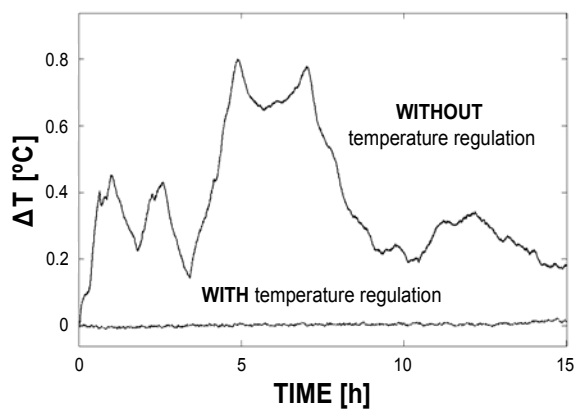


Figure 3.17a – Comparison of the variation of the temperature of the mobile structure of the 3-DOF robot in a situation with and without temperature stabilization.

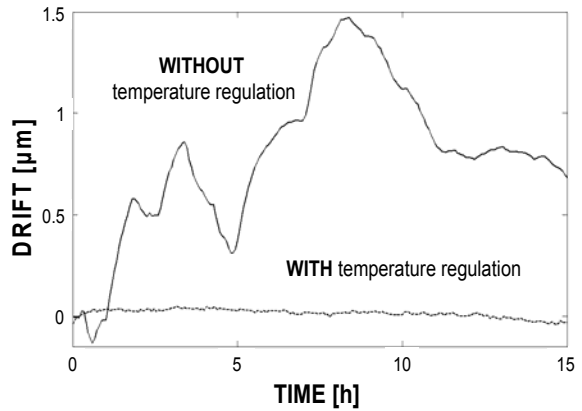


Figure 3.17b – Comparison of the variation of the drift of the reference position (read by the interferometer) of the 3-DOF robot in a situation with and without temperature stabilization (corresponding to the situations of **Figure 3.17a**).

A clear consequence of this temperature stabilization achieved can be observed by examining the values indicated by the *SIOS*[®] laser interferometer³³ when the robot end-effector returned periodically to the reference position, after the temperatures were stable.

In **Figures 3.17a** and **3.17b**, we present the variation of the temperature of the robot mobile structure and the corresponding drift of the reference position (as seen by the laser interferometer) in situations with and without temperature regulation.

³³ As already mentioned in **section 3.2.3**, typical angular drifts of the reference position (read by the two autocollimators) were observed to be very small (less than ± 0.15 arcsec).

(c) Experiments conducted on the 6-DOF robot

Figure 3.18 shows the different materials involved in the measuring loop of the 6-DOF robot. As opposed to the 3-DOF robot, the measuring loop is now much longer and almost exclusively made of materials with the same temperature expansion coefficient.

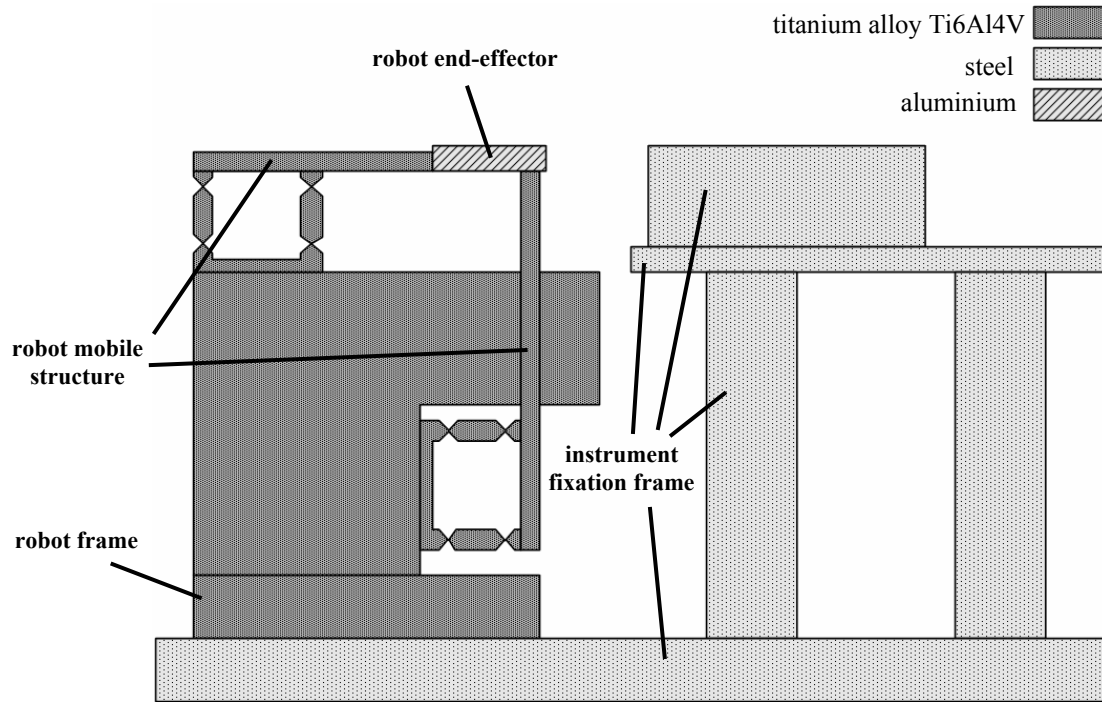


Figure 3.18 – Different materials involved in the measuring loop of the 6-DOF robot (general configuration). During our experiments, the robot end-effector was kept in aluminium since it was originally manufactured from this material. As mentioned previously, in the future, steel or titanium is preferable in order to guarantee a homogeneous thermal behaviour for the robot.

In the case of the 6-DOF robot, after testing several scenarios, the configuration adopted for the temperature regulation system had two Peltier cells regulating the temperature of the air inside the chamber (and, therefore, the temperature of the robot mobile structure) and two fans. These two fans were necessary since the frame on which the measuring instruments were fixed was limiting the air circulation inside the whole chamber.

The main difference compared with the set-up of the 3-DOF robot lies in the fact that *only the temperature of the robot mobile structure was used for the regulation*³⁴.

This means that every time a new temperature regulation run was launched, only the temperature of the robot mobile structure was actively stabilized and set to the consign value (in our case: 25 °C). Measurements have shown that this regulation also yielded stability in the non-regulated temperatures (robot frame, instrument fixation frame, internal air).

Figures 3.19 and **3.20** report the variations of the different temperatures involved in the measuring loop and the corresponding drift of the reference position (as seen by the laser interferometer) occurring in typical measurement situations with/without temperature stabilization.

³⁴ Using this simplified configuration made the regulation strategy (in particular finding the appropriate P-I-D values) easier.

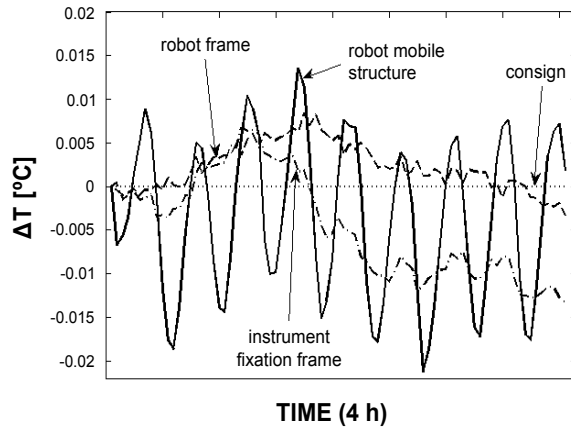


Figure 3.19a – Typical variation over a 4-hour period of the temperatures of the different parts involved in the measuring loop in a situation **with temperature regulation**.

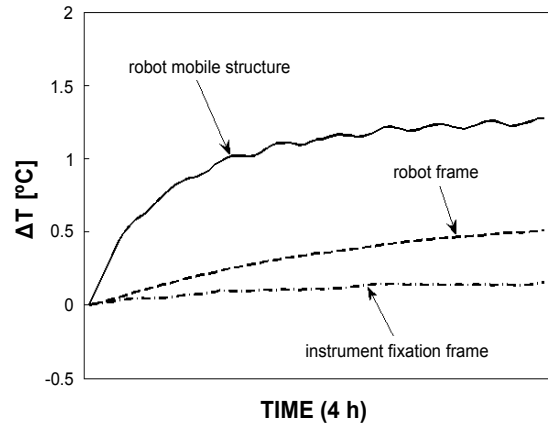


Figure 3.19b – Typical variation over a 4-hour period of the temperatures of the different parts involved in the measuring loop in a situation **without temperature regulation**.

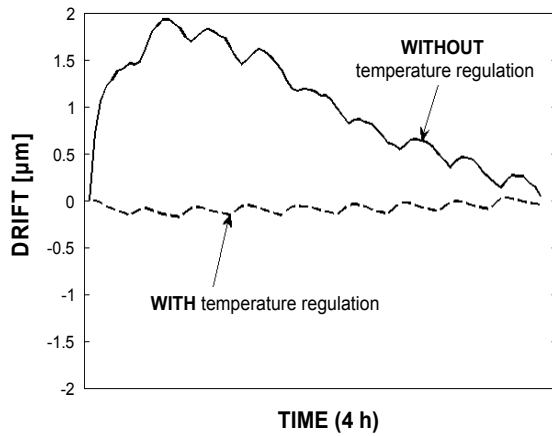


Figure 3.20a – Typical evolution of the drift of the robot reference position in the situations **with/without temperature regulation**.

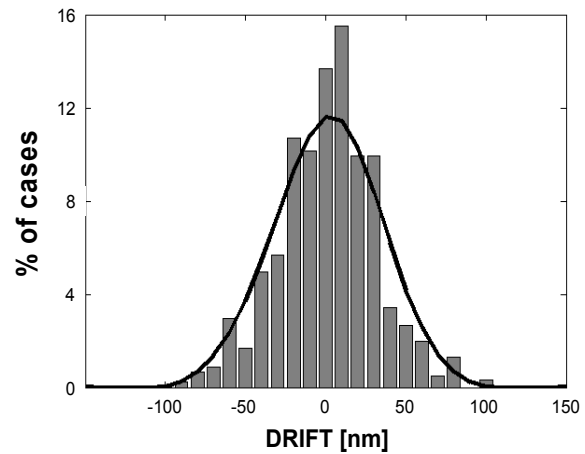


Figure 3.20b – Histogram of the drift (case of Figure 3.20a) of the robot reference position as seen by the laser interferometer during a measurement session **with temperature regulation**.

In order to see the real cumulative influence (robot + measurement system) of the temperature, a simple test was carried out by successively stabilizing the robot structure at 26 °C and then at 25.5 °C, starting from 25 °C. The drift of the reference position was then reported in respect to the value at 25 °C.

Results of this test are shown in **Figure 3.21**. As we can see, a variation of 1 °C inside the thermal chamber yielded a drift of the reference position of approximately 1.5 μm.

As mentioned previously, this drift is the result of two effects: (1) expansions of the robot mechanical parts and (2) expansion of the interferometer's dead path.

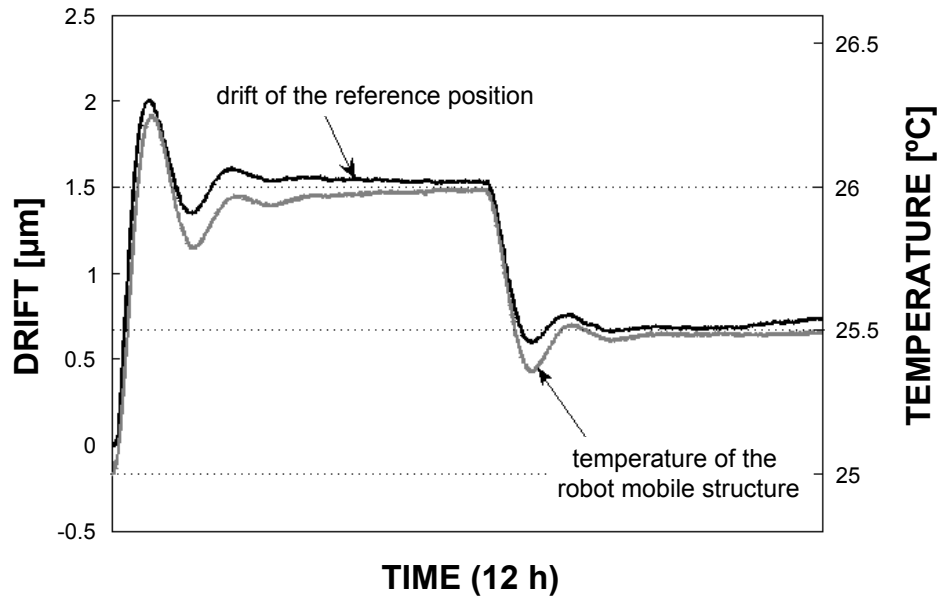


Figure 3.21 – Time evolutions of the drift of the reference position and the temperature of the robot mobile structure, as seen by the laser interferometer.

3.4 – General points observed for the data collection

In this section, we discuss general issues to be considered in order to optimize the accuracy of the measurement data acquired from any high-precision flexure parallel robot being calibrated.

3.4.1 – *Automation of the measurement procedure*

From the beginning of the project, we decided to automate the data acquisition procedure as far as possible for the following reasons:

- random errors coming from human operators are suppressed;
- “large” sets of data could be collected for data processing tasks;
- the actual measurements could be carried out during periods with minimal external disturbances (nights or week-ends). Weekdays could therefore be used for adjustments only.

A great deal of time and effort was then dedicated to the development of such an automated measuring system, briefly described below. **Figure 3.22** shows a schematic overall view of our system.

Three computers were used in our system:

- *robot control computer*: real-time computer with appropriate software and hardware for controlling the robot being measured;
- *temperature stabilization computer*: computer managing the regulation of the temperatures inside the thermal chamber. It is connected to a *Keithley*® 2700 multimeter

(A/D and D/A conversion cards installed in the computer) through RS-232C and to the Peltier cells system;

■ *measurement computer*: equipped with the necessary software for reading the measurement devices (also connected through RS-232C).

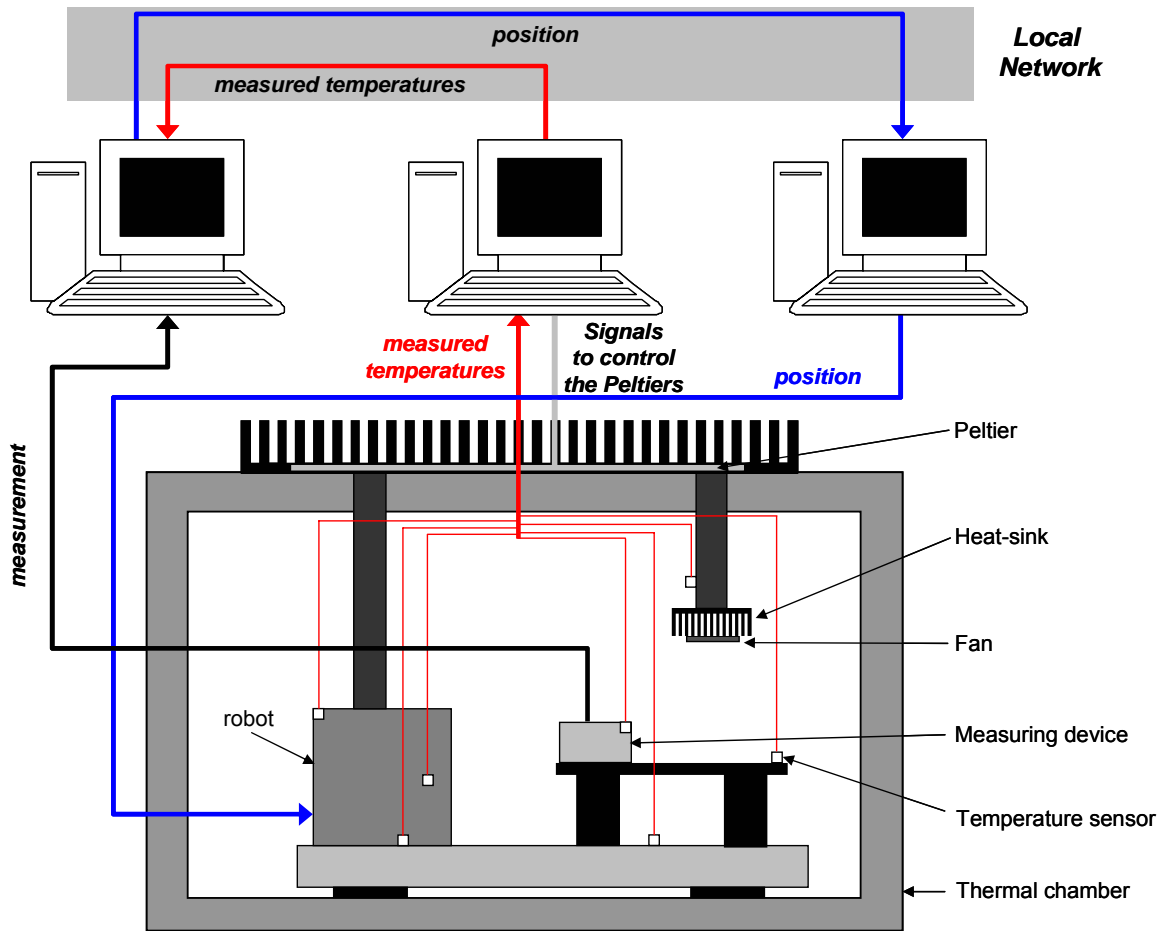


Figure 3.22 – General schematic view of the overall data acquisition system

The measurement computer is the central piece of our system. It is actually connected to the two other computers through TCP/IP. Its main function is to manage throughout the entire measuring procedure the time used to move the robot and the time used for the actual measurement.

Once the temperatures are set to their consign values and their variations are within ± 0.01 °C, the measurement computer sends to the control computer the order to move to a given position (in motor or operational coordinates). After giving this order, the measurement computer waits for a certain amount of time.

The *waiting time*³⁵ comprises the time required for the control computer to process the previous order, the time needed to actually reach the desired position and some additional margin time. At the end of this waiting time, the measurement computer will then trigger the measurement – see Figure 3.23.

³⁵ This waiting time was set to the time needed by the robot to go from one extreme position of the working space to another.

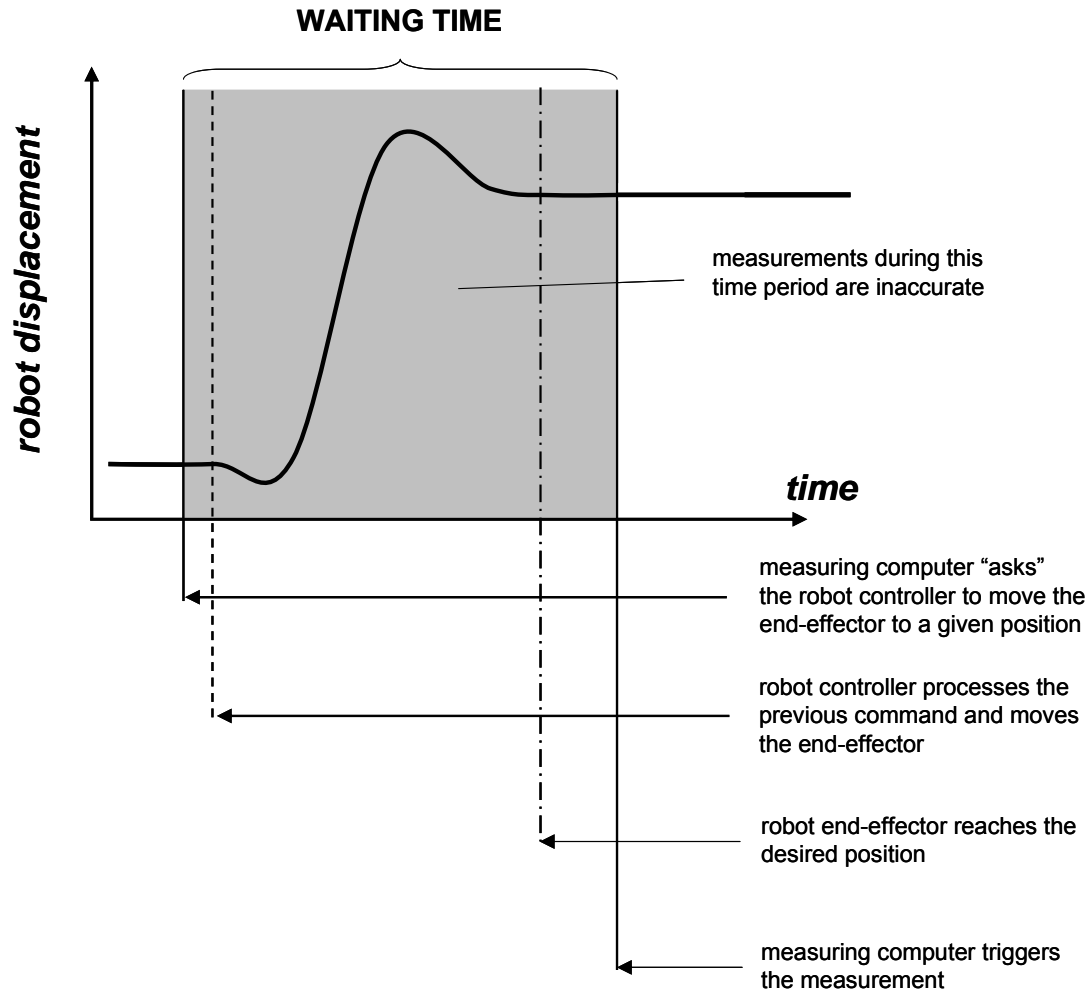


Figure 3.23 – Different times involved during a given measurement. In our case, typical values of the waiting time (comprising the four actions mentioned above) were between 10 and 15 seconds.

The measurement period in which the instruments are reading will last for a few seconds and the value actually stored for data processing is an average of a certain number of raw values sampled at a given frequency³⁶.

Finally, at the end of this measurement time, the measurement computer sends to the control computer a new order to move the robot end-effector to another position to be measured.

The result of a given measurement session is a text file with the time, the positions visited by the robot throughout the measurement procedure, the corresponding reading values of the measurement devices and the different temperatures read at the time of the measurement.

³⁶ The determination of the correct sampling frequency will be discussed in **section 3.4.2**.

3.4.2 – Averaging the vibrations due to the robot position regulation

When a given position is reached by the robot, there are always dynamic vibrations around the nominal values imposed by the motors. In our case, due to the robot position regulation, these vibrations were approximately ± 50 nm. In order to increase the accuracy of our measurements, the effect of these vibrations had to be suppressed.

For this purpose, the robot was moved to a number of different locations in its workspace (typically, positions at the boundaries of the workspace) and, for each location, the raw values indicated by the measurement device were recorded for a period of a few minutes by setting the sampling frequency of the instrument to its maximum value.

The frequency content of the robot position regulation signal was then determined from the previous record. The peak corresponding to the highest frequency in that spectrum was used to determine the minimum sampling frequency that had to be used in order to average all the oscillations around the position to be measured³⁷.

When the robot was set to a given position, 4 averaged values were determined as the result of 4 successive measurement times. The measurement value taken for data processing was the average of these 4 values. A final verification of the reliability of the data acquired during a given measurement session then consisted of analyzing the dispersion between these 4 values and the final averaged value. Typical dispersions were less than ± 5 nm for translations and less than ± 0.1 arcsec for rotations (**Figure 3.24**).

3.4.3 – Correction of the thermal drift

Despite the use of a temperature stabilization system, we have seen in **section 3.3** that there is still a drift³⁸ of up to 50 – 100 nm, coming from residual variations in the different temperatures of the measuring loop.

In order to correct the effect of this drift, periodic returns to the robot reference position³⁹ were performed so that the readings of the measurement devices could be updated by subtracting the relative displacement of the reference position. The correction of this drift was mainly important for the devices measuring translations since, as was mentioned previously, there were almost no angular drifts in our measurements.

Several strategies for correcting a given measurement reading for the thermal drift can be used:

- using *only the reading corresponding to the previous return to the reference position* (this correction can be performed in “real-time”);
- *on the basis of the two readings of the reference position before and after the position to be measured*, using a linear⁴⁰ piecewise correction (this correction can only be performed after the measurements are finished).

³⁷ The *Nyquist principle* states that the sampling frequency must be at least twice the frequency of the original signal. Aspects related to signal sampling are discussed in **Appendix A – section A.4**.

³⁸ The main part of this drift is attributed to the residual temperature variations (**section 3.4.4**). However, mechanical relaxations in screwed fixations could also be at the origin of this drift.

³⁹ This so-called “reference position” is generally the position of the robots immediately after initialization. An exception to this general rule exists, however, in the 3rd phase of the calibration procedure for the 6-DOF robot (“rotations without translations”): in this case, the reference position is, for each centre of rotation, the position of the sphere corresponding to the “pure translational” displacement of the robot performed at the beginning of the closed-loop – see **section 4.3.1 – paragraph (c)**.

⁴⁰ When the temperatures are already stabilized and if the time between two consecutive returns is under a certain threshold (typically 3-5 minutes), the drift can be approximated using a simple linear piecewise function – see **Figure 3.25**.

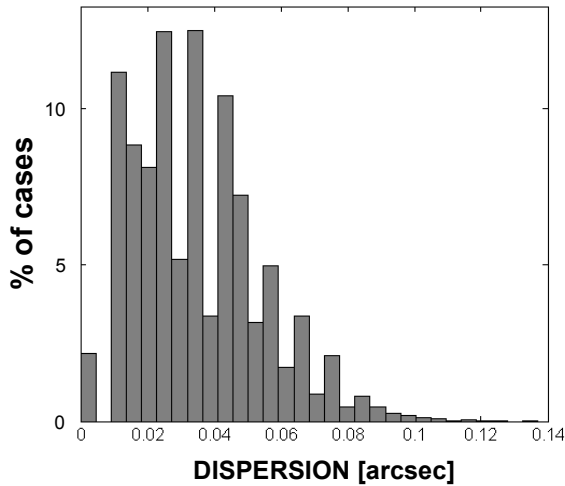


Figure 3.24a – Histogram of the dispersion between the four filtered values measured for a given robot position and the corresponding averaged value (taken for subsequent pose correction tasks) – case of the **angles**.

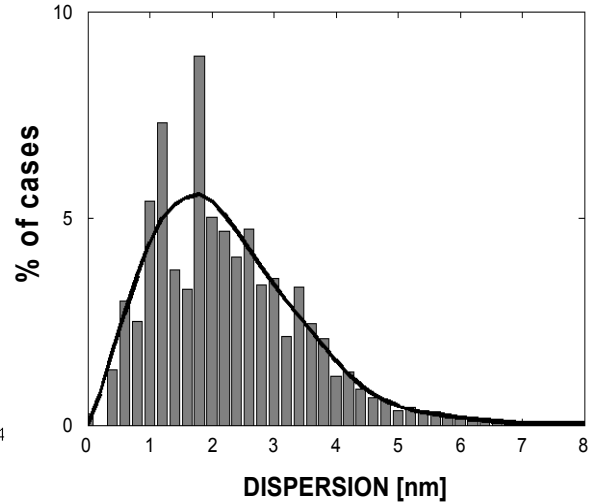


Figure 3.24b – Histogram of the dispersion between the four filtered values measured for a given robot position and the corresponding averaged value (taken for subsequent pose correction tasks) – case of the **translations**.

The second strategy proved to be more efficient and brought more accurate results for the data processing part.

The **time between two returns to the reference position** is actually a compromise between:

- *measuring time*: increasing the number of returns to the reference position will increase the overall measuring time, which in turn will generate additional costs from the industrial point of view;
- *quality of the temperature stabilization*: increasing the number of returns to the reference position will increase the number of end-effector motions. This will generate additional heat and may cause difficulties in maintaining, through the entire measurement period, a very good stability in the temperatures of all the parts involved in the measuring loop.

As a result of the previous compromise, typical time between two successive returns to the reference position was approximately 5 minutes.

Figure 3.25 shows a typical evolution of the drift of the reference position reading over a 5-minute period for three different measurement sessions occurring: **(a)** – outside the thermal chamber; **(b)** – inside the thermal chamber and without temperature regulation; **(c)** – inside the thermal chamber and with temperature regulation.

This figure shows the clear advantage of insulating the metrological environment against exterior perturbations. In fact, when the measuring environment is protected, the reference position only drifts up to ± 10 nm (instead of almost ± 200 nm in the non-protected environment). However, the clear advantage of the temperature regulation situation over the non-regulated situation cannot be seen in this figure since it is only effective over larger periods of time (at least 20 minutes).

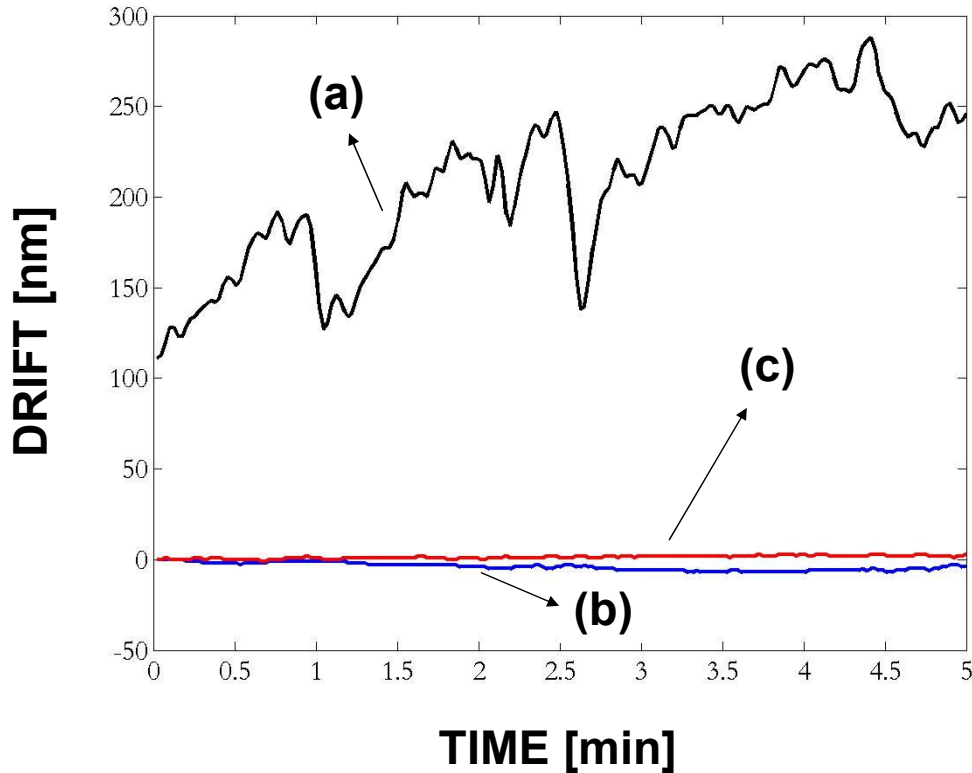


Figure 3.25 – Evolution of the drift of the reference position (as seen by the laser interferometer) during a 5-minute-period when the measurements are performed (a): outside the thermal chamber, (b): inside the thermal chamber but without temperature regulation and (c): inside the thermal chamber and with temperature regulation. The curve (a) was shifted for clarity purposes.

3.4.4 – Other issues

(a) Absolute reference frame

A prior and essential step before the calibration of any high-precision flexure parallel robot is to define the absolute reference frame in respect to which data will be reported⁴¹ (and therefore, in respect to which the robot will be calibrated).

In our case, due to the absence of any object defining accurately the directions and the location of this frame, we usually employed precision objects (such as mirror cubes) mounted on the robot end-effector to define the absolute frame. In addition, the positions of the robots immediately after initialization were used to define the origins of the frames (because of the excellent repeatability of flexure robots). The exact definitions of the absolute frames used for the calibration of the 3 and 6-DOF robots will be given in **sections 4.2.1 (a)** and **4.3.2**.

Notice that if the robot is calibrated in a given frame, it will of course be calibrated in respect to any other frame, provided that the relationship between these two frames is known precisely.

In future industrial applications, the absolute frame should preferably be defined already during the robot design stage, taking also into account the application for which the robot will be used. For example, an external absolute frame could be defined with the help of an additional mirror

⁴¹ Notice that *strictu sensu* absolute frames do not exist. As our cube frame is attached to the robot, we work somehow in a relative mode. However, as the temperature variations are within ± 0.01 °C the drift of our frame during the calibration lies in a few tens of nm.

cube firmly attached to the frame of the robot; the positions of the robot end-effector would then be measured in respect to that frame⁴².

(b) Robot initialization

When the robot is powered up, the initialization procedure requires the translational stages of each kinematic chain to touch their mechanical stops before actually going to their reference positions (this reference position is actually indicated physically in the *Heidenhain*[®] glass rules so that it can be recovered within nanometre repeatability over several initializations of the robot).

Depending on the speed at which the mechanical stop is actually touched, this procedure may generate small variations in the robot geometry (assembly between the robot parts). These variations may in turn not only deteriorate the quality of the measurements during a calibration procedure (if the calibration has several phases like that of the 6-DOF robot, for which the robot has to be initialized again) but also the quality of the previous calibration (supposing that the robot is being used in an industrial context).

Therefore, it was decided to initialize the robot only once, at the beginning of the procedure.

(c) Contact with the robots

Due to the presence of different assembled parts in the robot structure, the two robots studied in this thesis were found to be very delicate. Therefore, any mechanical contact or manipulation of their structure had to be avoided as much as possible during and after a calibration session in order for the calibration to be effective.

(d) Load of the end-effector

The algorithm used to regulate the position of the robot makes use of a P-I-D control law. The adjustment of these P, I and D parameters is to be performed in accordance with the load (magnitude and centre of mass) on the robot end-effector.

Therefore, changing the load without re-tuning the previous regulation parameters⁴³ may critically increase the oscillations in the robot position regulation up to several μm for some positions which may significantly influence the measurements.

For this reason, we decided always to work with an end-effector having the same load in the same centre of mass.

According to what has been said in the previous paragraph and as long as practice allows this to happen, *it is recommended to use end-effector mounts with the object(s) necessary for calibration (e.g.: the mirror cube in the case of the 3-DOF robot) and those required for the actual industrial application fixed simultaneously.*

⁴² Doing so would however introduce practical problems with the instrumentation used throughout this work, for example, in the case of distances (1-beam interferometer). Working with 2-beam interferometers would permit the use of such an external reference frame. See **Figure 8.2** in chapter 8.

⁴³ Particular care has to be paid if the end-effector mounts during the calibration and the utilization periods are different (as is currently the case for the 3-DOF robot, used as a μ -EDM machine by our industrial partner)

(e) Visual control

From the beginning of our measurements, we found that the data acquired from the robots varied quite smoothly over their entire workspace, since the motions of flexure parallel robots are free of friction or hysteresis⁴⁴.

This fact was often used as a supplementary mechanism for fault detection, especially for debugging purposes throughout the development of the data acquisition system – **Figure 3.26**.

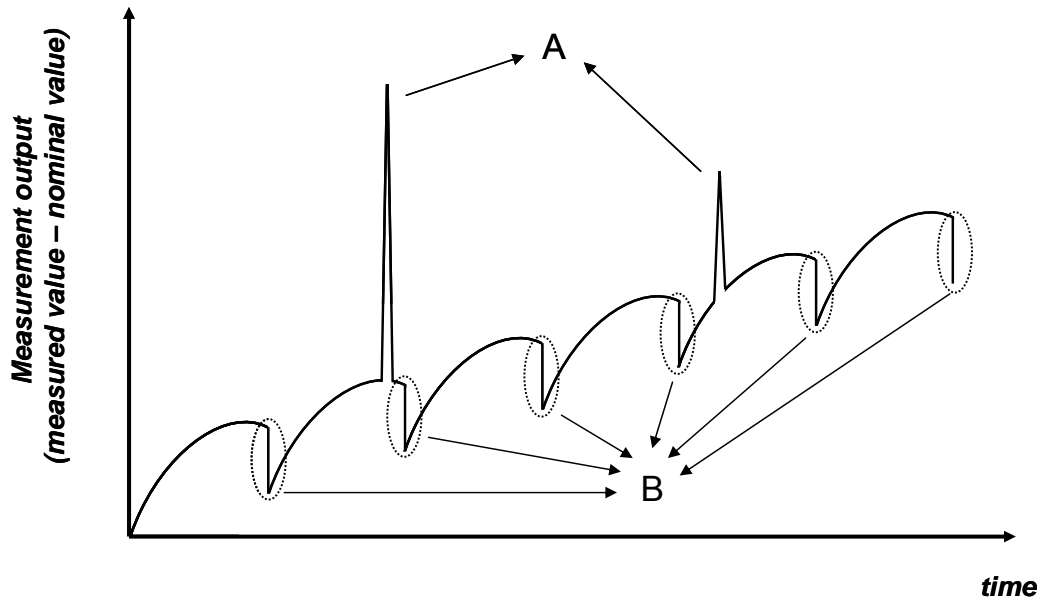


Figure 3.26 – Detection of errors in a measurement procedure on the basis of a visual inspection of the measured values. Spikes “A” revealed problems occurring during the measurement session, whereas “B” are discontinuities wanted during the measurements (returns to the reference position).

⁴⁴ As mentioned in section 1.2.1 – paragraph (b).

3.5 – Conclusion

Measuring high-precision flexure parallel robots within absolute accuracies in the sub- μm range is not a trivial task. It requires not only expensive instrumentation but also regulation and stabilization of the metrological environment.

The goal of this chapter was to provide the roboticist with a guide for the development of a measuring system for collecting reliable data from a given high-precision multi-DOF flexure parallel robot. Delicate aspects of practical implementation were pointed out.

■ The major parameter affecting the accuracy of our robots (and measurements) has proved to be **temperature variations** experienced by the robot mobile structure (closely following those of the ambient air). In order to limit to a few tens of nanometres the influence of this parameter on the accuracy of the robot, it is desirable to insulate the measuring environment from external disturbances by working inside a *thermal chamber*.

The purpose of this chamber is to regulate and stabilize (better than $\pm 0.1\text{ }^{\circ}\text{C}$) the temperature variations of the robot mobile structure and those of the materials forming the measuring loop. As a consequence of this, the thermal drift observed in the measurements of distances over “long” periods of time (minimum 10 h) could be reduced by a factor of at least 20 compared with a non-regulated situation (in laboratory conditions: stability of $\pm 1\text{ }^{\circ}\text{C}$).

In addition, the chamber also provides a mechanical insulation of the metrological environment.

■ In order to guarantee the reliability of the measurements, the **data acquisition system** should ideally be automated in order to avoid human intervention as far as possible (thus reducing random errors), reduce costs and, lastly, to be able to collect large amounts of data.

Special attention should be paid to the following issues:

- the definition of the *absolute reference frame* in respect to which the measurements are collected is of major importance. This frame has preferably to be considered during the robot design stage and also to be in relation with the robot’s industrial application;
- *thermal drifts* can be cancelled by returning periodically to the robot reference position;
- the sampling frequencies of the measuring instruments have to be set to values higher than the Nyquist limit;
- the robot end-effector has to be maintained with the same load in the same centre of mass during and after calibration;
- manipulation or contact of the robot parts has to be avoided as much as possible during and after calibration since it may have a significant influence on accuracy.

Chapter 4 – Measuring the 3 and 6-DOF robots

4.1 – Introduction

4.1.1 – Chapter outline

The goal of this chapter is to provide a description of the work accomplished on the 3 and 6 DOF robots.

Measuring protocols are proposed in order to “map” as much as possible the workspace of the robots. These protocols were developed and implemented in accordance with the general issues outlined in the previous chapter. Thus, *this chapter should be regarded as a follow-up of Chapter 3.*

Section 4.2 presents the work conducted on the 3-DOF robot. **Section 4.3** deals with the work accomplished on the 6-DOF robot.

The latter is the key part of this chapter as we report an original solution to a problem for which there is still a lack of standard equipment on the market: the measurement of translations combined with rotations (6D) at the sub- μm accuracy range.

4.1.2 – Terminology and convention

We would like to draw the reader’s attention on the following issues, which are necessary for a proper understanding of the work exposed in this chapter (in particular **section 4.3**).

(a) Terminology

- The term “**pose**” will be used to describe a set of 6 D operational coordinates ($X \ Y \ Z \ \theta_x \ \theta_y \ \theta_z$) characterizing the position and orientation of the robot end-effector in the Cartesian space.
- The terms “**position**” and “**orientation**” will be applied to designate, respectively, the translational ($X \ Y \ Z$) and the angular (or rotational) coordinates ($\theta_x \ \theta_y \ \theta_z$) of a given pose ($X \ Y \ Z \ \theta_x \ \theta_y \ \theta_z$).

(b) Convention on geometric modelling

The *fixed-frame convention* was adopted for the representation of the 6D pose.

According to this convention, the pose ($X \ Y \ Z \ \theta_x \ \theta_y \ \theta_z$) corresponds to the following geometric operations (performed in the order specified):

- three translations ($X \ Y \ Z$) in respect to a fixed absolute reference frame;
- three rotations ($\theta_x \ \theta_y \ \theta_z$) around the corresponding axes of a frame having:
 - the same directions as the fixed absolute reference frame;
 - a new origin at ($X \ Y \ Z$) from the one of the absolute frame (translated origin).

This convention was chosen attending to the limitations of our measuring devices (see **section 4.3.2**).

4.2 – Measuring the 3-DOF robot

4.2.1 – Measuring protocol

(a) – Cube and absolute frame

■ Mirror cube

For the calibration of the 3-DOF robot, a $30 \times 30 \times 30 \text{ mm}^3$ high-precision mirror cube¹ was mounted on the robot end-effector and the three translations (X, Y, Z) were measured along three functional surfaces using the laser interferometer (Figure 4.1).

The cube was made of Zerodur® and had Al-coated measuring surfaces with a reflectivity better than 90 %. In addition, the flatness of each measuring surface was better than $\lambda/20$ ($\sim 32 \text{ nm}$) in their $20 \text{ mm} \times 20 \text{ mm}$ central area (only this area was used for measuring the different degrees of freedom).

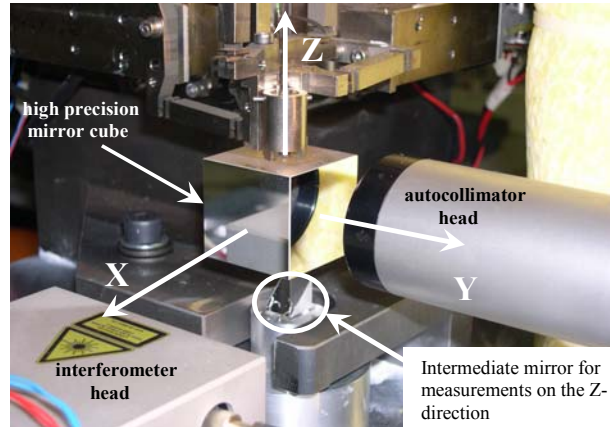


Figure 4.1 – Photographic view of the measuring devices reading a mirror cube mounted on the end-effector of the 3-DOF robot.

In addition, the errors² in the orthogonality between the different functional surfaces of the cube were reported within ± 1 arcsec by the cube manufacturer³.

■ Definition of the absolute reference frame

At the beginning of our project, the robot had been designed without any object to define accurately the directions and origin of the absolute frame in respect to which the operational coordinates of the end-effector were reported.

Ideally, a first mirror cube should be fixed to the robot frame and act as external absolute reference and a second cube should be attached to the end-effector⁴. The relative orientation of the second cube in respect to the first one should then be known accurately, so that the robot end-effector displacements could be measured in respect to the fixed external frame.

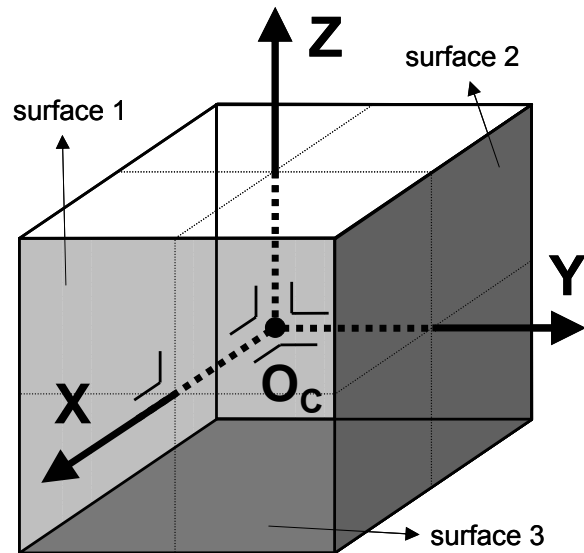


Figure 4.2 – Definition of the **absolute reference frame** in respect to which the measurements of the 3-DOF robot were collected.

¹ We have chosen 30 mm since this value corresponds approximately to the diameter of the autocollimator beam.

² These errors could go up to ± 16 arcsec. If not corrected, an error of ± 16 arcsec could corrupt the reading of the translation up to approximately $\pm 150 \text{ nm}$.

³ WZW – Optic AG, Mülhsteinstrasse 12 CH – 9436 Balgach, Switzerland.

⁴ See Figure 8.2 of Chapter 8 for a schematic illustration of this differential operating mode.

Unfortunately, due to a lack of appropriate instrumentation (such as a 2-beam interferometer), measurements could not be performed in this “ideal way” (differential mode).

It was therefore decided to use a single mirror cube permanently attached to the robot end-effector and to adopt a certain number of conventions in order to define our **absolute reference frame** in respect to which the measurements of the 3-DOF robot were collected and, therefore, in respect to which the robot was calibrated.

The absolute reference frame (**Figure 4.2**) is then considered to be a virtual frame with the following characteristics:

- the origin is the *centre of the mirror cube when the robot is in the reference position*⁵. For this particular position, we have: $(q_1 \ q_2 \ q_3) = (X \ Y \ Z) = (0 \ 0 \ 0)$.

- the directions are defined as follows: *the vector normal to the surface of the cube used to measure the translations along X-direction is adopted as absolute X-direction.*

The two vectors perpendicular to the surfaces used for the measurements of the translations along Y and Z axes, and corrected for the known orthogonality errors in respect to the first surface, are the actual absolute Y and Z directions.

In practice, *the measurements performed on the different surfaces of the cube were transformed into measurements performed in respect to the absolute frame by means of simple geometry.*

(b) – Set of positions measured during a calibration session

The positions for which the end-effector coordinates were measured during calibration correspond to regular displacements in all the three motor coordinates⁶. In order to avoid any contact with the robot mechanical stops during the measurements, the workspace “explored” was limited⁷ to $3.6 \times 3.6 \times 3.6 \text{ mm}^3$.

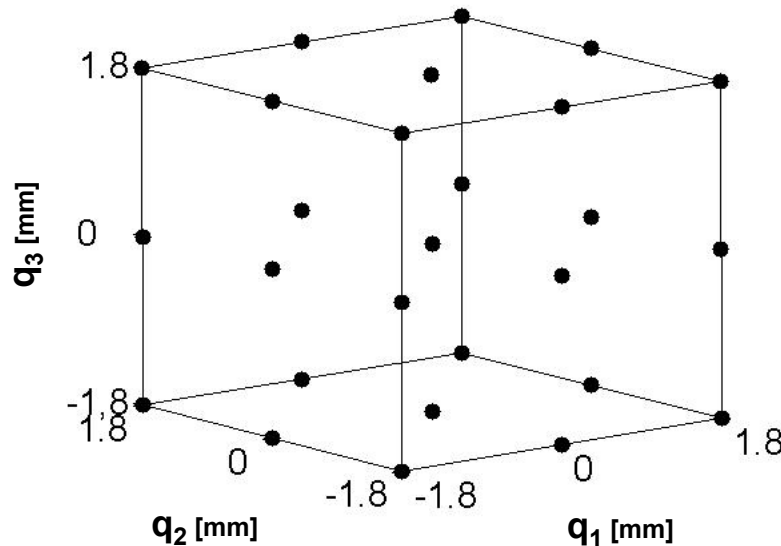


Figure 4.3 – Illustration of a few positions (uniformly distributed) measured during the calibration of the 3-DOF robot (reduced data set). These positions have been imposed (and reported) in the **motor coordinates**. Notice that positions uniformly distributed in ideal operational coordinates (inputs of the perfect IGM), rather than in motor coordinates, could also be measured and used for future data processing tasks.

⁵ The position of the robot end-effector immediately after initialization is called “reference position”.

⁶ In the case of the 6-DOF robot, notice that positions corresponding to regular displacements in motor coordinates could not be measured due to a lack of instrumentation able to measure the 6 D at the same time – see **section 4.3**.

⁷ Instead of the claimed workspace of $4 \times 4 \times 4 \text{ mm}^3$.

Figure 4.3 represents a number of positions (in motor coordinates) measured one after another during a calibration session. Notice that, for clarity purposes, this figure represents only a reduced set of positions ($3 \times 3 \times 3 = 27$), whereas the data set measured during a real calibration session comprised in fact $19 \times 19 \times 19 = 6'859$ positions (regular steps of 0.2 mm between neighbouring positions, in all the 3 directions).

4.2.2 – Residual passive angular variations and their effect

This section reports an important observation made at the beginning of our experimental work on the 3-DOF robot: the existence of residual passive (non-controllable) angular variations experienced by the end-effector throughout the workspace.

These angles influence the calibration of the active DOF of the robot (and, more generally, 3-DOF robots of the “Delta Cube” family). A recently completed Ph.D. work [Nia06] proposes methods for minimizing these angular variations through improvement of the robot design parameters.

(a) – Residual passive angular variations and causes

Recent simulation studies using Finite-Element models [Nia06], confirmed by experimental data, have shown that the motions along the different degrees of freedom (translations X, Y and Z) are affected by **residual passive angular variations** (roll, pitch, yaw) of systematic nature around the different axes of translation – **Figure 4.4a**.

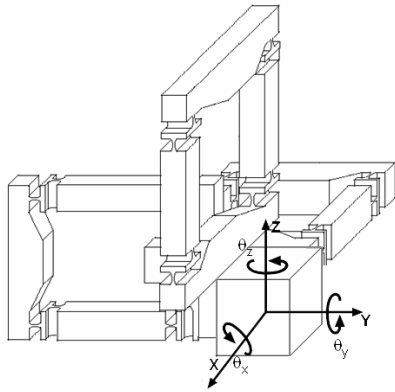


Figure 4.4a – Passive residual angular variations (roll - θ_x , pitch - θ_y and yaw - θ_z) suffered by the robot end-effector.

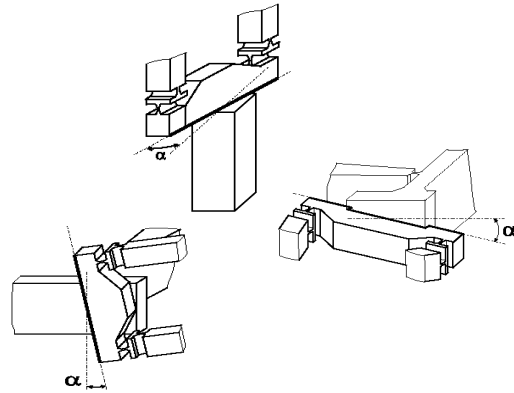


Figure 4.4b – Illustration of different assembly errors generating angular variations, according to [Nia06].

These variations are caused by a certain number of error sources (geometric errors due to manufacturing tolerances, assembly errors, etc) acting in a separate or coupled way.

Among the factors acting in a separate way and according to Niaritsiry's work, *assembly errors*⁸ (represented by the angles α in **Figure 4.4b**) in the attachment of the space parallelograms to the translational stage of the same kinematic chain, or to the end-effector, seem to be the main source of these angular variations.

⁸ Assembly errors may be suppressed using a monolithic design. However, this solution is impracticable due to its prohibitive cost.

According to this author, for a displacement of 2 mm of a given translational stage, the maximum angular variation experienced by the end-effector of a 3-DOF robot (with the same geometric dimensions as the Delta Cube II) is approximately 8 % of this assembly angle α (see **Figure 4.4b**). Example: if $\alpha = 0.1^\circ$ then these angular variations can be up to $\pm 0.008^\circ \sim \pm 30$ arcsec.

Measurements of roll (θ_x), pitch (θ_y) and yaw (θ_z) were performed using autocollimators. If no special care was taken in assembling the robot parts, angular variations up to ± 100 arcsec⁹ could take place¹⁰.

After a reassembly (acting on the fixation between the translational stages and the space parallelogram for each kinematic chain) of the robot parts guided by the indications of the autocollimators, angular variations could be limited to approximately ± 10 arcsec. **Figure 4.5** shows the variation of the angle θ_x within the workspace of the robot after this slight assembly readjustment.

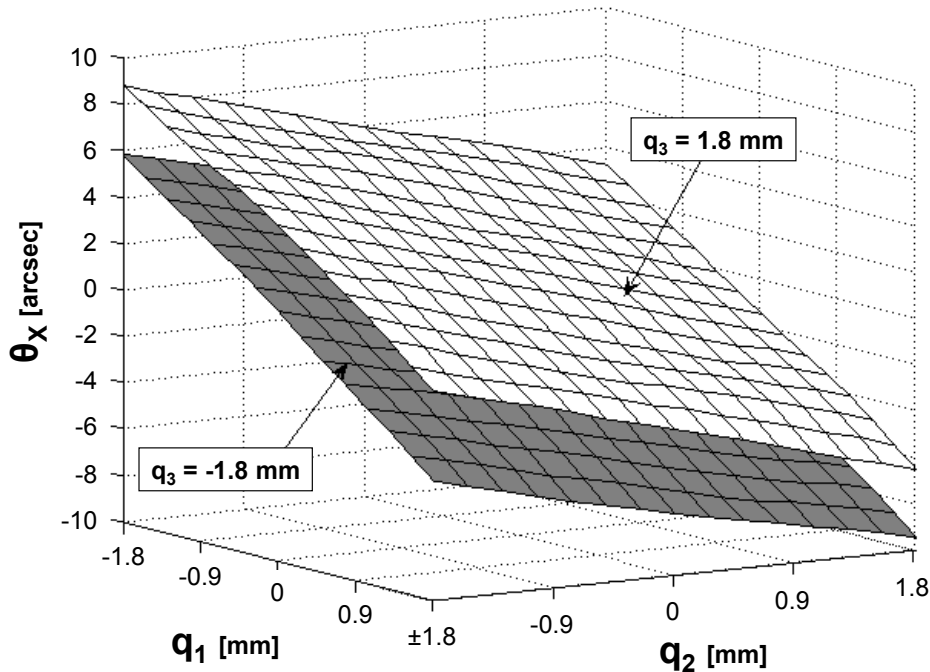


Figure 4.5 – Variation of the **roll** (θ_x) experienced by the robot end-effector in the articular space. This situation occurs after a slight readjustment of the robot assembly. **Pitch** (θ_y) and **yaw** (θ_z) had similar profiles and varied within the same range (i.e. max. ± 10 arcsec).

This figure also shows that these angular variations are relatively smooth, which makes them easily predictable for any position (q_1, q_2, q_3) of the robot workspace.

Simple linear laws of the type $\theta = A \cdot q_1 + B \cdot q_2 + C \cdot q_3$ could be used to predict these angular variations with an accuracy better than ± 0.2 arcsec over the entire robot workspace.

⁹ An angular variation of 100 arcsec would corrupt the reading of a translation of 1.8 mm up to approximately 900 nm.

¹⁰ We have also noticed that mounting/unmounting operations could also modify the range of these angular variations. It is quite difficult to provide an accurate estimation of this effect. Special care should then be taken if tools have to be mounted/unmounted on the robot end-effector several times between two calibration sessions.

Reliable calibration of the 3-DOF robot therefore requires:

- *before measuring the active DOF*: a readjustment of the assembled robot parts in order to minimize the residual angular variations (passive DOF) corrupting the reading of the translational motion of the end-effector over the robot workspace;
- *after measuring the active DOF*: the measurements of the translations performed on the surfaces of the mirror cube have to be corrected for the residual angular variations (measured with the help of autocollimators) and possible orthogonality errors between the surfaces of the cube, so that the coordinates of the centre of the cube (functional point to be calibrated) can be known.

The reader is referred to **Appendix B** in which we provide analytical expressions relating the position of the centre of the cube to the measurements performed on the surfaces of the cube.

(b) – Attainable limit in the calibration of the active DOF

Having regard to the expressions derived in section **B.2** of **Appendix B**, and assuming that:

- the residual passive angular variations experienced by the robot end-effector were within ± 10 arcsec;
- the orthogonality of the cube and the angular variations detected in the end-effector throughout all the robot workspace could be known/predicted within ± 1 arcsec and ± 0.2 arcsec, respectively;
- during our measurements, the interferometer's laser spot could be adjusted to the centre of the corresponding cube's surface¹¹ within ± 1 mm,

the maximum value of the error¹² due to angular effects that cannot be corrected in the calibration of the active DOF of the robot (practical attainable limit in the calibration) is approximately ± 50 nm.

¹¹ Adjusting the measuring spot to the centre of the cube within tolerances in the order of ± 0.2 mm may be possible without significant additional costs. However, this was not implemented since, according to the expressions reported in **Appendix B**, sub-mm tolerances do not improve significantly the accuracy of our measurements.

¹² This value does not include errors due to the accuracy of the measuring instrument and typical alignment effects such as those discussed in **section 3.2.1**.

4.2.3 – *Measurement results*

The goal of this section is to provide a complete accuracy portrait of the 3-DOF robot before calibration on the basis of the data collected.

We shall also try to provide an explanation for the error profiles presented.

However, as we shall see in Chapters 5 and 6, the calibration of this robot can still be performed on the basis of the measurement results obtained, even without knowing the reasons for their particular shape¹³.

In fact, a successful calibration of this 3-DOF robot (at the sub- μm range) only requires the minimization of the angular variations accompanying the translational motions of the end-effector (see **section 4.2.2**).

We would also like to re-alert the reader to the fact that *before calibration there is no object that unambiguously defines the **absolute frame** in respect to which the motions of the robot end-effector have to be measured and thus calibrated*¹⁴.

The measurement results corresponding to the errors of the robot before calibration are in fact reported in respect to an absolute frame defined by the surfaces of a mirror cube attached to the end-effector.

If this cube is removed from the end-effector and re-attached, the directions of the axes of the new absolute frame will be different. Consequently, the measurements of the same positions will, most probably, not give the same output.

Example: a difference of 5° between two attachments of the mirror cube on the end-effector (see, in particular, the angle around Z-axis as shown in **Figure 4.1**) can lead to a difference of up to $1.8 \cdot (1 - \cos(5^\circ)) \approx \pm 6.85 \mu\text{m}$ between two measurements of the same robot operational positions.

Figure 4.6 reports, for each direction of the absolute frame, the differences between the real operational coordinates measured by the interferometer and the consign values imposed by the ideal IGM.

The histograms of **Figure 4.6** provide information on the statistical distribution of the robot errors before calibration (number of positions measured = 6'859).

As can be seen, the values of these histograms are roughly symmetric in respect to the origin, which is due to the symmetry of the robot kinematic structure (see **Figure 1.4b** – page 1/3).

In fact, the actual axis of symmetry of the previous histograms is not exactly at $0 \mu\text{m}$ but rather at approximately $0.5 \mu\text{m}$. We believe that this offset can be attributed to the displacement (not considered by the ideal IGM controlling the robot motions) experienced by the centre of rotation of the different flexures during their motion¹⁵.

¹³ In practice, it is almost impossible (or possible, but at prohibitive costs) to measure the different dimensions of the robot in order to validate the arguments proposed in this section as the explanation for the error profiles.

Moreover, measuring the errors in the assembly of the different parts of the robot would also be completely useless since regular re-assemblies are probably necessary for different reasons (minimization of the angular variations, transport of the robot,...).

¹⁴ This means that, before calibration and *strictu sensu*, the IGM imposes displacements along directions that are not physically defined.

¹⁵ In fact, flexures do not behave like “perfect pivots” as assumed by the ideal IGM. The displacement of this so-called “instantaneous centre of rotation” has been studied by several researchers, including Bacher [Bac03] – see **section 5.2.1**.

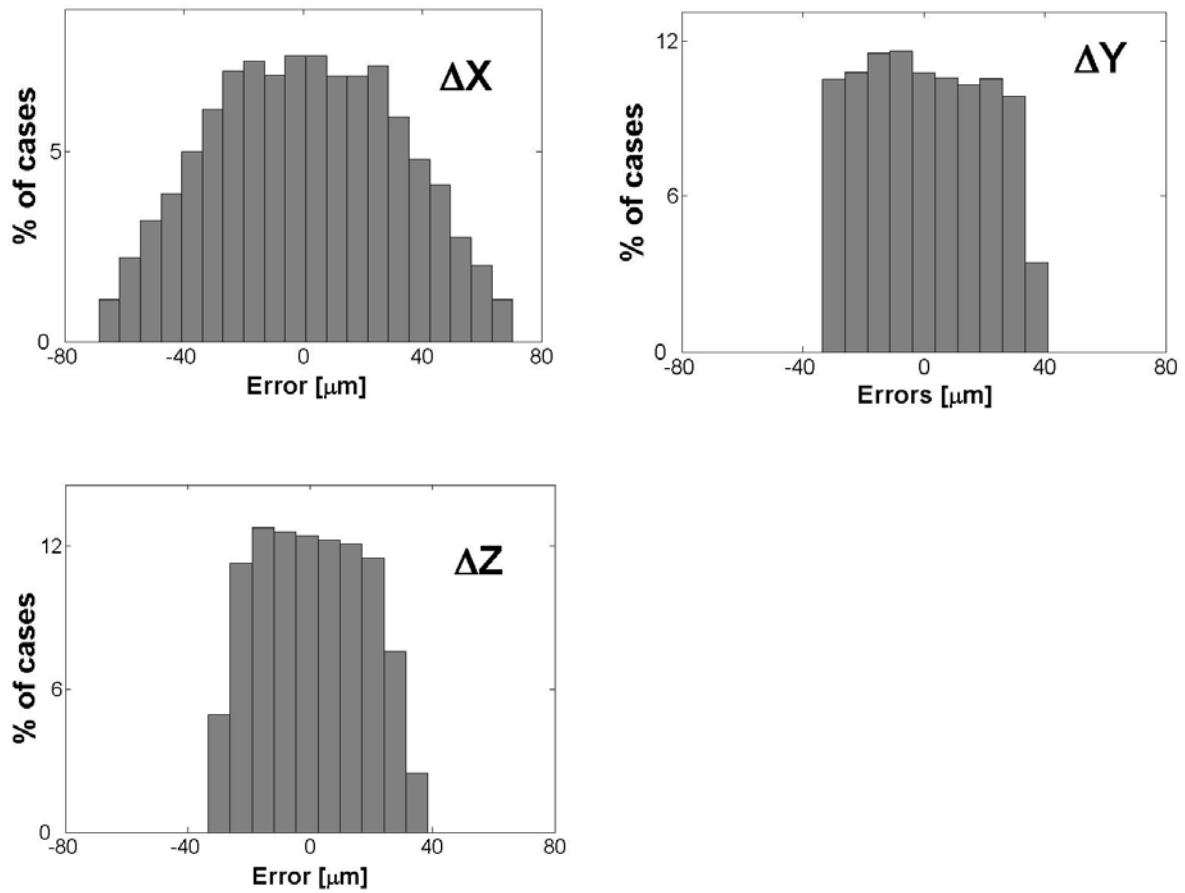


Figure 4.6 – Histogram of the errors (= measured operational coordinate – imposed operational coordinate, according to the ideal IGM) before calibration. The three graphs have been represented with the same scale in X-axis for comparison purposes.

In order to relate the measurement errors to the geometry of the robot, a full 3D representation is required. We propose to use *error isosurfaces* for this purpose. These are surfaces formed by the 3D coordinates for which the error under observation has some value of interest.

Figure 4.7 shows this isosurface representation of the errors (reported also in respect to the operational coordinates) along each direction.

The first important conclusion that can be drawn from the graphs of **Figure 4.7** is the fact that, for each direction, the error remains almost unchanged in respect to displacements along the direction being measured. Example: ΔX does not vary significantly in respect to X , ΔY in respect to Y and ΔZ in respect to Z .

This is due to the fact that, in this case, the accuracy is mainly determined by the excellent linear relative positioning accuracy of the *Heidenhain*[®] rules used to impose the displacements in the translational stage of the kinematic chain corresponding to the direction being measured.

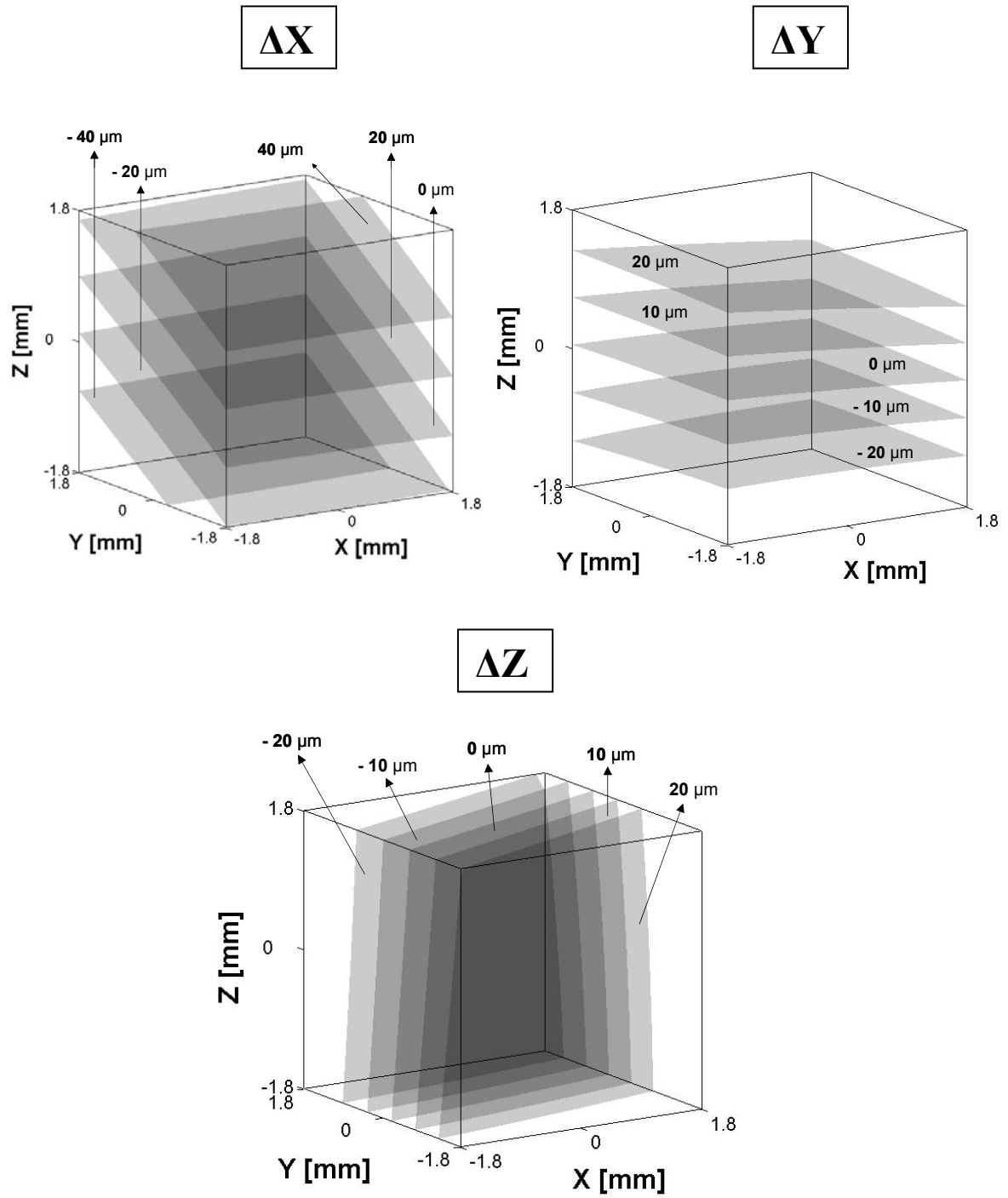


Figure 4.7 – Error isosurfaces of the 3-DOF robot **before calibration** in the operational workspace (and corresponding to the histograms of **Figure 4.6**).

Before going into a detailed explanation of the differences between the graphs of **Figure 4.7**, it is convenient to draw the reader's attention to the two following effects that may possibly explain a dependency of the error measured along one particular direction in respect to the two displacements taking place in the other directions (not being measured):

1) as we have said, the robot “internal frame”¹⁶ (for which the directions can NOT be defined physically) is always different from the frame used for calibration (defined by the surfaces of the mirror cube – see **paragraph (a)** of **section 4.2.1**).

As a consequence of this, the three original displacements controlled by the ideal IGM (in respect to the robot “internal frame”) will be mixed up when reported in the calibration frame. Therefore, the ideal IGM will not be able to correct residual motions measured in the calibration frame since the relationship between these two frames always remains unknown;

2) the space parallelograms of the different kinematic chains of the robot are never in their “ideal configuration” when the robot is in its reference position (**0 0 0**) – see **Figure 4.8**. This “real configuration” can be caused by the following reasons:

- the two parallel arms of the translational stages may not be in their ideal theoretical position when the robot is in the reference position (as a consequence of non-perfect referencing in the robot initialization procedure);
- the fixation of a given space parallelogram to its corresponding translational stage (or to the end-effector) may not be perfect. This is either the result of the finite assembly tolerances or the consequence of the readjustment performed in order to suppress the angular variations in the motions of the end-effector (see **section 4.2.2**).

As a consequence of this non-ideal initial configuration, the space parallelogram will no longer execute a trajectory that is perfectly symmetric in respect to the theoretical direction, as assumed by the IGM – see **Figure 4.8bis**. Therefore, the IGM will not be able to compensate accurately the residual displacements occurring along that vertical direction (Z-axis in **Figure 4.8bis**).

In order to evaluate the real influence of this second effect, let us suppose that $\alpha = 0.5^\circ$ (see **Figures 4.8** and **4.8bis** – “ α ” can also be seen as the angle between the two tangents to the two circular trajectories (1) and (2) at their middle points).

For a 1.8 mm stroke, this angle will cause a residual displacement in the vertical motion (Z-axis of **Figure 4.8bis**) of $1.8 \cdot \sin(\alpha) \approx 15.7 \mu\text{m}$.

When compared to the influence of the first effect given in the example of page 57 ($\pm 6.85 \mu\text{m}$, as a result of a 5° difference between two frames), we can see that **the second effect clearly prevails**¹⁷.

¹⁶ This “internal frame” would actually be a Cartesian frame defined by the perfectly orthogonal directions of the axes of motion of the three different translational stages.

Since this condition is never met in practice, it will always be impossible to define physically this so-called “internal frame”.

¹⁷ *Strictu sensu*, these two effects cannot be compared. However, from a practical point of view, we can consider that aligning the axes of the calibration frame with those of the robot “internal frame” (1st effect) within $\pm 5^\circ$ corresponds approximately to the same probability of having the space parallelograms with an initial orientation in the order of 0.5° (2nd effect).

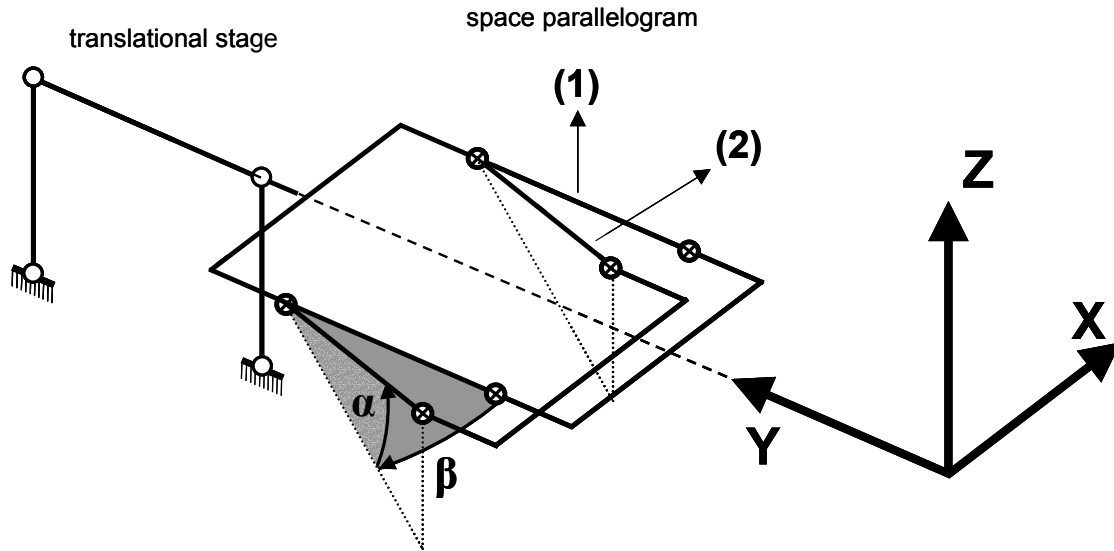


Figure 4.8 – “Real configuration” (2) of a given space parallelogram (case of the kinematic chain along Y-axis) of the 3-DOF robot at the robot reference position (0 0 0) versus its “ideal configuration” (1). The magnitudes of angles α and β were exaggerated in this figure for clarity purposes.

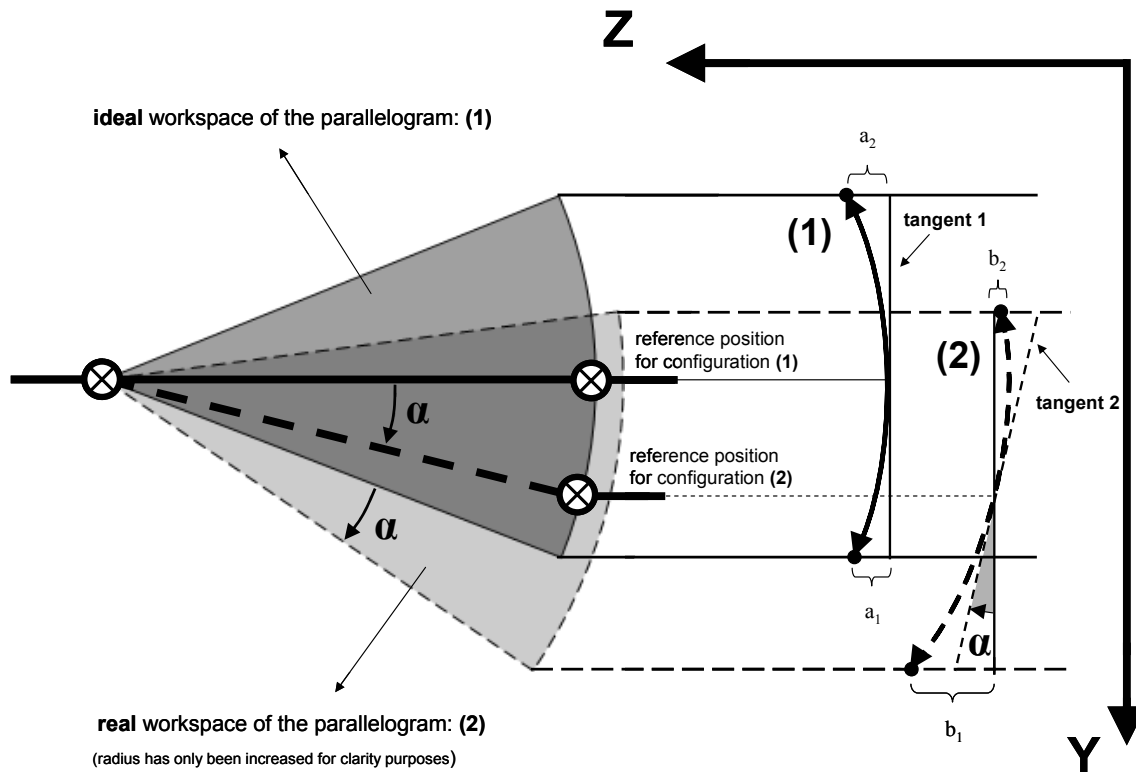


Figure 4.8bis – Trajectory executed by the space parallelogram if the latter is not in a perfect horizontal configuration at the robot reference position (0 0 0) (shifted by an offset α).

The position of the parallelogram can be controlled through a displacement imposed along the Y-axis. Residual displacements along Z-axis corresponding to different positions of the parallelogram (different Y displacements) are compensated by the IGM. Configuration (1) corresponds to a perfectly symmetric trajectory in respect to Z-axis ($a_1 = a_2$). The ideal IGM will then be able to predict the Z-displacements for every Y-displacement in a way that ΔZ will actually not vary in respect to Y-axis.

This is not the case for a real configuration (2) in which the trajectory of the parallelogram is no longer symmetric in respect to Z-axis ($b_1 \neq b_2$).

If we assume that the particular profiles of the graphs of **Figure 4.7** are exclusively the consequence of the second effect, then they can be explained as follows¹⁸:

- the dependency of ΔY in respect to Z coordinate is the consequence of the parallelogram of chain Y having an initial orientation of approximately 1.3° in the YZ-plane¹⁹.
 - an angle of similar magnitude in the YZ-plane for the initial configuration of the parallelogram of chain Z explains the dependency of ΔZ in respect to Y coordinate.
 - the dependency of ΔX in respect to both Y and Z coordinates can be explained by the fact that, in the chain X^{20} , two angles (in the XZ-plane and in the XY-plane) are corrupting the initial configuration of the corresponding parallelogram.
- The presence of two angles in this case may also explain why the values of ΔX vary in a range that is almost twice as high as that of ΔY and ΔZ – see **Figure 4.6**.

¹⁸ From the graphs of **Figure 4.7**, we can see that the dependency of a given error along a given direction in respect to the displacements in the remaining directions is linear at least in the first-order approximation (at the μm range). This is due to the fact that in our case only small angles are involved.

¹⁹ $1.3^\circ \approx \arcsin(40 \mu\text{m} / 1.8 \text{ mm})$. $\pm 40 \mu\text{m}$ is the maximum value taken by ΔY and ΔZ (see **Figure 4.6**) and $\pm 1.8 \text{ mm}$ is the maximum stroke for each direction of motion.

²⁰ The difference between chain X and the remaining kinematic chains of this robot lies in the attachment of the space parallelogram to the corresponding translational stage – see **Figure 1.4a** page 3.

4.3 – Measuring the 6-DOF robot

As we have mentioned previously, the main difficulty we had to face in the calibration of the 6-DOF robot lies in the fact that current high-precision metrology techniques can still not offer a standard device able to measure (within accuracies in the nanometre range) translations combined with rotations.

If we take the example of the *SIOS*[®] interferometer reading the displacements of a reflecting mirror, it is in fact well known that, when an angular variation with a magnitude over a certain threshold occurs (± 120 arcsec), the beam is lost. Even if this tilt angle is within the tolerated range, the angular variation will still have an influence on the distance measured by the beam (as in the case of the 3-DOF robot – see **section 4.2.2** and **Appendix B**).

4.3.1 – Measuring protocol

In order to collect a full set of 6D data (having translations combined with rotations) using the measuring devices presented in **section 3.2** (without a specific metrological development), we propose to use an original measuring protocol described in this section.

In this protocol, the 6D problem is divided into two separate 3D problems (translations + rotations), for which standard measuring devices are currently available²¹. An additional step is required at the end of these two 3D calibrations in order to obtain the full 6D data.

Notice that the extrapolation of 6D information from the two separate 3D data, without the additional merging step, is not possible.

This is due to the fact that our data processing approach implies that corrected poses can only be obtained if they are inside the workspace “mapped” during the measuring phase.

(a) – **Phase 1 : Calibration of the robot angular motions**

At the beginning of the procedure, a mirror cube was mounted on the robot end-effector.

As in the case of the 3-DOF robot, the surfaces of the cube were then used to define the directions of the absolute reference frame in respect to which the data was collected²².

Two electronic autocollimators were then fixed in order to read the three angles (θ_x , θ_y , θ_z) defining the orientation of the cube (and therefore the orientation of the end-effector), as shown in **Figure 4.9**.

Before starting the measurements, *the “internal axes” of the autocollimators were aligned with the axes of the absolute frame.*

To do so, their auxiliary axes were adjusted (as reported in **section 3.2.3 – paragraph c**) and their measuring beams were set orthogonally to the corresponding cube surface²³ (using *Newport*[®] precision LDS-SLXY mounts). This adjustment was important since the readings of the two autocollimators could then be used to recover the orientations of the absolute frame, if the cube had to be removed from the end-effector (case of the “large angles” measured in the polygon prisms).

²¹ In reality, current angular measuring devices still cannot cover the robot workspace (several °) while maintaining resolutions better than 0.1 arcsec.

²² The axes of this absolute frame are defined in the same way as in the case of the 3-DOF robot (see **paragraph a – section 4.2.1**). However, the origin of the frame is defined in a different way.

The complete definition of the absolute frame will be given in **section 4.3.2**.

²³ This alignment could be done within ± 1 arcsec.

The measurements could then start. The set of positions measured in this phase comprised positions of the robot workspace for which the 6 operational coordinates ((X, Y, Z, θ_x , θ_y , θ_z) as imposed by the ideal IGM²⁴) varied uniformly. Obviously, only the 3 angular operational coordinates θ_x , θ_y and θ_z could be measured in this phase.

“Small angles” i.e. within the range of the autocollimators (approx. ± 412 arcsec, see **Table 3.4**) were measured directly on the surfaces of the cube, while “large angles” (up to $\pm 3^\circ$) were measured on the faces of calibrated polygon prisms²⁵ (see **Figure 3.6**).

The data collected in this phase was then processed using one of the methods presented in Chapters 5 and 6. For the next steps of the calibration, *the robot end-effector was therefore able to execute angular motions with correct magnitudes throughout the entire workspace*. Hereafter, the model controlling these motions will be called **MODEL 1**.

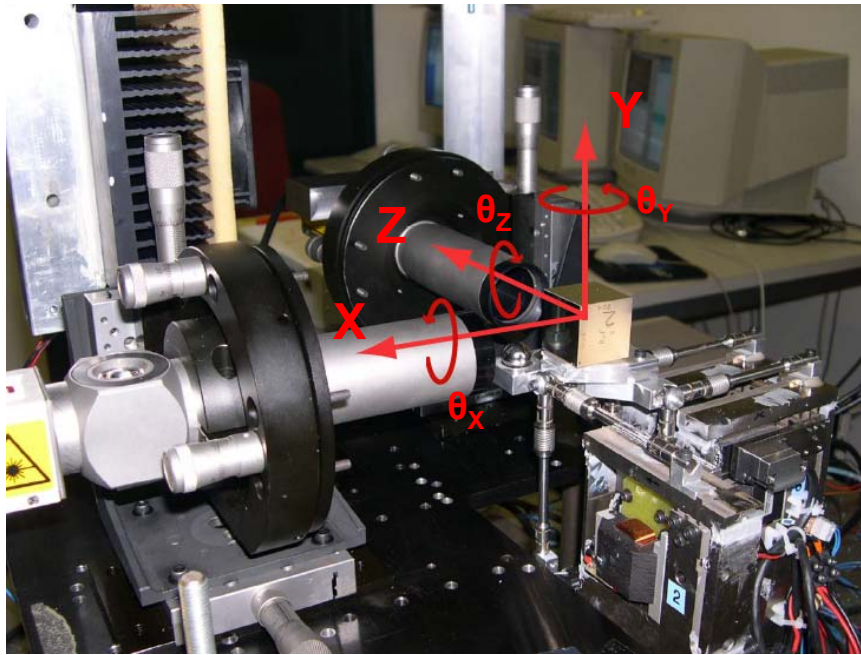


Figure 4.9 – Measuring the angular motions of the 6-DOF robot with two autocollimators. This figure reports the case of the “small angles” measured directly on the surfaces of the mirror cube.

In order to read “large angles” the cube had to be removed from the end-effector and a polygon prism had to be mounted at the same place. We used three different polygon prisms (one for each direction) and the measurements were carried out in a “serial way”.

This figure reports a frame X-Y-Z, with an origin at the centre of the cube, used to perform the measurements corresponding to phases 1 and 2. The **absolute frame** in respect to which the 6D data will be reported at the end of phase 3 has the same directions but a different origin. The reader is referred to **section 4.3.2** in which this aspect will be clarified.

(b) – Phase 2: Calibration of the robot translational motions

This phase was called “**translations without rotations**” (TWR) since it consisted of calibrating the translational degrees of freedom of the robot, after suppressing the angular variations on the end-effector motions.

Two different tasks have to be executed in this phase.

²⁴ Data processing techniques will be presented in **Chapters 5** and **6**.

²⁵ In the case of “large angles”, since the cube had to be removed from the end-effector (and replaced by polygon prisms), the adjusted autocollimators were then used to define the orientations of the absolute frame. Therefore, and despite the absence of the cube, the central facet of the polygon could be aligned to the directions of the absolute frame.

■ The **first task** is the suppression of the angular variations. Two solutions can be used to accomplish this task:

1. using **MODEL 1**, obtained in the previous phase;
2. using a **closed-loop** between the robot and the two autocollimators.

The first solution is certainly the fastest one and, therefore, the more cost-effective one. The second solution, slightly more accurate than the first one²⁶, is interesting in cases where we are only interested in the calibration of the robot translational motions (i.e. using the 6-DOF robot as a “perfect” 3D translator)²⁷.

Here, the focus is on the second solution (closed-loop), since the first solution is trivial. In the lines below, we report an algorithm summarizing the different actions involved in a typical closed-loop for suppressing the angular variations.

For clarity purposes, we define the following two parameters:

- **N** = *number of poses for which the rotations have to be suppressed (poses of STEP 1)*. At the end of the algorithm, it will also be the number of the “pure-translational” poses;
- **ϵ_{rot}** = *threshold below which rotations are considered to be suppressed*.

TWR algorithm – Suppression of the angular variations

STEP 0: The end-effector moves to the robot reference pose (**0 0 0 0 0 0**).
The readings of the two autocollimators for this position are recorded and, thereafter, *all angular measurements are performed relatively to this reference position*.

FOR i = 1 to N

STEP 1: The end-effector moves to a given pose with the following coordinates (according to the ideal IGM): (**X_i Y_i Z_i 0 0 0**).

STEP 2: The two autocollimators read the real orientations of the end-effector for that particular pose:
(**$\theta_{X, \text{residual}}$ $\theta_{Y, \text{residual}}$ $\theta_{Z, \text{residual}}$**).

STEP 3: **IF** (**$\|\theta_{X, \text{residual}}\| < \epsilon_{\text{rot}}$ and $\|\theta_{Y, \text{residual}}\| < \epsilon_{\text{rot}}$ and $\|\theta_{Z, \text{residual}}\| < \epsilon_{\text{rot}}$**)
the coordinates of this pose are recorded
(i.e. we consider that the angular variations are suppressed)

ELSE
a new pose is generated with the following coordinates (according to the ideal IGM):
(**X_i Y_i Z_i - $\theta_{X, \text{residual}}$ - $\theta_{Y, \text{residual}}$ - $\theta_{Z, \text{residual}}$**)

END i = i + 1 (i.e. go to a new pose in STEP 1)

²⁶ Best angular accuracies for the first solution are within ± 0.3 arcsec (best accuracy obtained for MODEL 1). For the second solution, angular accuracies lie within ± 0.02 arcsec (resolution of the autocollimators).

An angular variation of 0.3 arcsec would corrupt the reading of a 2 mm translation of only ± 3 nm.

²⁷ In these particular cases, such calibration may be performed using the second solution, which then becomes a separate 3D problem, rather than being part of a complete 6D calibration procedure.

Figure 4.11 represents the coordinates of a few positions measured in this phase (corresponding to STEP 1 in the TWR algorithm). Notice however that the number of positions corresponding to a real measurement session was at least $9 \times 9 \times 9 = 729$ (X, Y and Z varied regularly between -2 mm and +2 mm by steps of 0.5 mm).

Figures 4.10a and **4.10b** report respectively the influence of the threshold ϵ_{rot} on the average number of iterations and the influence of this threshold and of the number of poses on the total measurement time. Up to 900 poses, **Figure 4.10b** shows that, for a fixed number of poses to be corrected, imposing strict correction thresholds ϵ_{rot} does not have a major impact on the overall measuring time.

■ The **second task** is the measurement of the translations corresponding to the poses obtained at the end of the TWR algorithm. These measurements are accomplished with the help of the SIOS® laser interferometer.

Measurements along X- and Z- axes were performed on the surfaces of the cube (see example of **Figure 4.12**), whereas those along Y-axis require an auxiliary mirror.

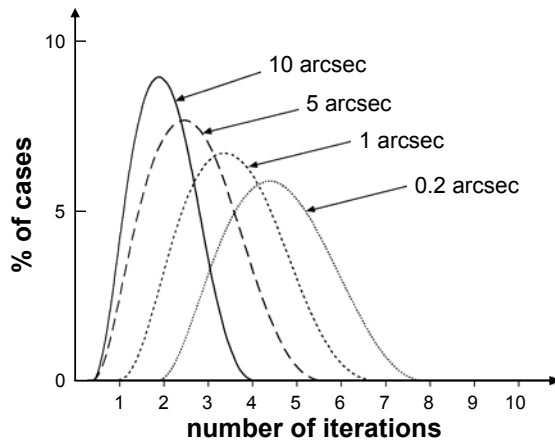


Figure 4.10a – Histogram of the number of iterations in respect to the threshold ϵ_{rot} adopted for the TWR closed-loop (measured on 729 points).

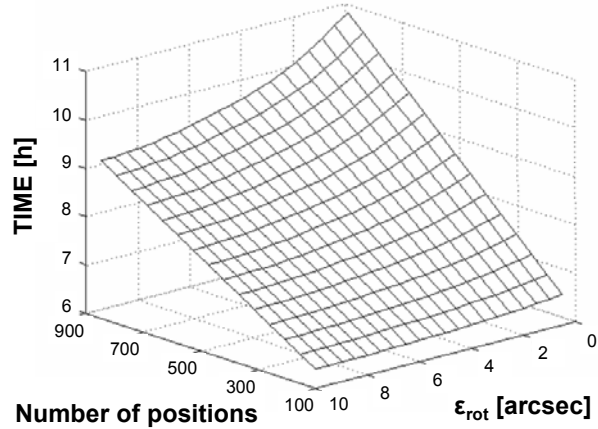


Figure 4.10b – Influence of the threshold ϵ_{rot} and the number of positions on the time required to perform the TWR closed-loop.

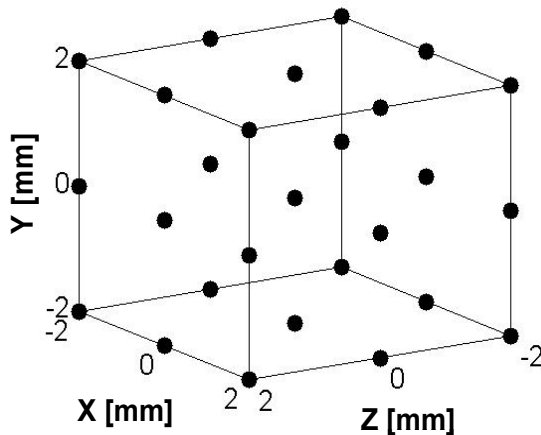


Figure 4.11 – Illustration of some positions used in STEP 1 of the TWR algorithm (reduced data set).

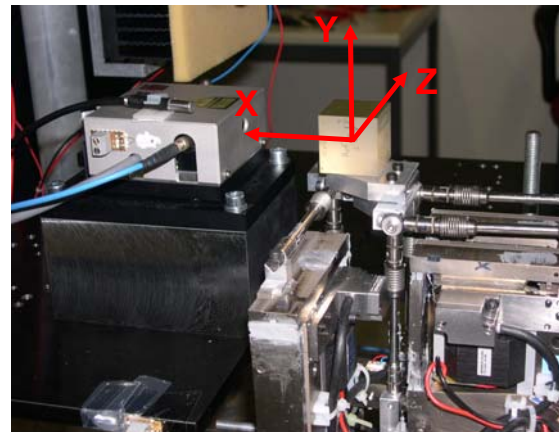


Figure 4.12 – Measuring the value of the translations along X-direction of the “pure-translational” points resulting from the TWR algorithm.

The collected data is then processed using one of the methods presented in Chapters 5 and 6. For the next steps of the calibration, *the robot end-effector could then be moved in a “pure-translation” way over the entire workspace.*

The model controlling these motions will be called **MODEL 2**.

(c) – Phase 3: Obtaining the full 6D data (translations combined with rotations)

In **phase 3**, the two 3D calibrations performed in phases 1 and 2 are merged in order to produce the 6D data that could not be measured directly (translations combined with rotations).

This phase consists roughly of performing rotations of known magnitude around different fixed centres of rotation with imposed translational coordinates.

Three Keyence® LC laser displacement sensors, having their optical heads mounted on an orthogonal frame²⁸, were reading the position of a 15 mm-diameter mirror sphere²⁹ mounted on the robot end-effector – Figure 4.13.

For each new centre of rotation a certain number of adjustments and operations were necessary before the measurements could actually start. The following procedure describes these actions.

Translations combined with rotations – preliminary adjustments

STEP 1: Using MODEL 2, the end-effector moves to the desired (or nominal) centre of rotation (example: **(1.6 1.6 1.6 0 0 0)**) in a “pure-translation” way;

STEP 2: the optical heads of the three Keyence® sensors are adjusted manually to the position for which:
(a) the *intensity of the signal received (after reflection on the sphere surface) is maximized* (see Figure 3.4 in section 3.2.2) and
(b) the distances read were as close as possible to the absolute zeros of the sensors³⁰;

STEP 3: Using MODEL 2, the end-effector moves, still in a “pure-translation” way, from the nominal position of the centre of rotation (example: **(1.6 1.6 1.6 0 0 0)**) to its real position (example: **(1.567340 1.646350 1.593450 0 0 0)**), for which the readings of the three Keyence® are exactly zero (within the resolution of the laser sensors).

The exact position (X Y Z) of the centre of rotation (which depends, of course, on the position of the Keyence® sensors) **is therefore known and could be recovered at any time** (if the sensors stay at the same place in respect to the robot).

²⁸ Y-axis: model LC-2420, X and Z-axes: model LC-2430. See Table 3.3 of section 3.2.2 for the properties of these two models.

²⁹ The sphere was made of steel.

³⁰ The three laser Keyence® laser sensors perform measurements in an absolute mode. Therefore, there is a target distance (10 mm for model LC-2420 and 30 mm for model LC-2430 – see Table 3.3) for which the reading of the sensors is zero. See Figure A.2 of Appendix A for the illustration of the basic operating principle of these sensors.

This “manual adjustment” of the optical heads to the reference positions of the sensors was typically within $\pm 20 \mu\text{m}$.

The measurements could then start. For each centre of rotation, the measurements occurred as follows:

■ **PART 1: using MODEL 2** (“pure-translations”), the end-effector moved from the robot reference position $(0 \ 0 \ 0 \ 0 \ 0 \ 0)$ to the absolute zeros of the three laser sensors in order to determine the translational coordinates of the centre of the sphere (future centre of rotation);

■ **PART 2: using MODEL 1**, the end-effector moved from the previous “pure-translational” pose (centre of the sphere) to a certain number of new angular poses.

The angular coordinates of these new poses are correct but their translational coordinates remain unknown. For each new pose, a closed-loop performed between the three sensors and the robot allowed these unknown translational coordinates to be set equal to those of the “pure-translational” position of PART 1.

Therefore, the centre of rotation around which the end-effector executed the different rotations always remains the same³¹ (centre of the sphere).

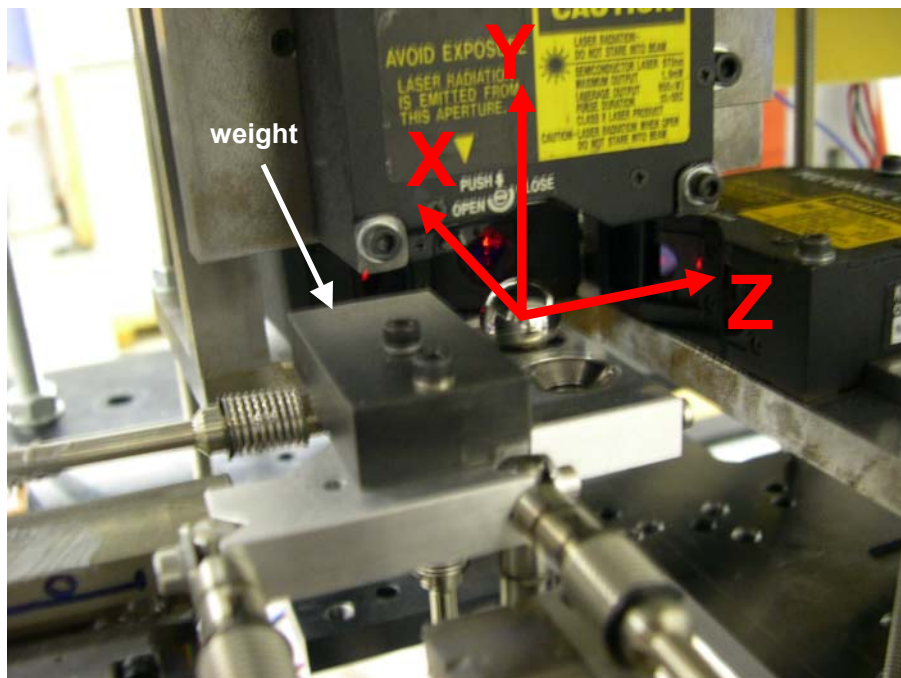


Figure 4.13 – Closed-loop of the type “rotations without translations” (phase 3 of the calibration procedure for the 6-DOF robot) performed with the help of the three Keyence® LC laser displacement sensors. In this phase, the robot performed rotations of corrected magnitude around the same centre of rotation imposed by the three sensors reading the relative displacements of the centre of the sphere.

This closed-loop therefore allows the collection of true 6D data (translations combined with rotations) in an indirect way.

The role of the weight is to keep the robot end-effector with the same load in the same centre of mass in respect to phases 1 and 2 (in which the mirror cube is mounted).

This Figure reports a frame X-Y-Z with the origin at the centre of the sphere. When the end-effector is in the robot reference position $(0 \ 0 \ 0 \ 0 \ 0 \ 0)$, this frame is actually the **absolute reference frame** in respect to which the 6D data was collected.

Section 4.3.2 clarifies the relationship between this frame and the frame reported in Figure 4.9.

Notice that all the points obtained in PART 2 are now combinations of translations and rotations. In fact, **for each centre of rotation, the translational coordinates are those of the position determined in PART 1, whereas the angular coordinates are those imposed in PART 2.**

³¹ It is very important to bear in mind that these sensors are NOT used for measuring translations (which are already measured and calibrated in phase 2). Their only task is to impose through a closed-loop action the sphere to stay always in the same position at which the readings of the three sensors indicate “zero” simultaneously. See section A.5 of Appendix A.

In the next lines, we report an algorithm summarizing the different actions performed in phase 3. For the sake of clarity, the following parameters are defined:

- **N** = number of centres of rotation;
- **M** = number of rotations to be executed around each centre of rotation;
- ϵ_{transl} = threshold below which translations are considered to be suppressed (normally we took $\epsilon_{\text{transl}} = 50$ nm).

Algorithm for obtaining translations combined with rotations

FOR i = 1 to N

STEP 0:

- The preliminary adjustments (as described previously) are performed in order to prepare the measurements and to define the future centre of rotation.
- Using MODEL 2, the end-effector moves from the robot reference position to the absolute zeros of the three laser sensors (centre of the sphere) in a “pure-translation” way. This “pure-translational” pose ($X_i \ Y_i \ Z_i \ 0 \ 0 \ 0$) is considered to be the real **centre of rotation** and its corresponding translations are recorded.

FOR j = 1 to M

STEP 1: Using MODEL 1, the end-effector moves to a new pose ($X_i \ Y_i \ Z_i \ \theta_{X,j} \ \theta_{Y,j} \ \theta_{Z,j}$) for which the angles are assumed to be correct.

STEP 2: The three sensors read the corresponding displacements ($X_{\text{residual}} \ Y_{\text{residual}} \ Z_{\text{residual}}$) experienced by the centre of the sphere relatively to the coordinates of the centre of rotation.

STEP 3: IF ($\|X_{\text{residual}}\| < \epsilon_{\text{transl}}$ and $\|Y_{\text{residual}}\| < \epsilon_{\text{transl}}$ and $\|Z_{\text{residual}}\| < \epsilon_{\text{transl}}$)

the coordinates of this pose are recorded.
(i.e. we consider that the rotation has been performed around the centre of rotation)

ELSE

the end-effector moves to a new pose:

($X_i - X_{\text{residual}} \ Y_i - Y_{\text{residual}} \ Z_i - Z_{\text{residual}} \ \theta_{X,j} \ \theta_{Y,j} \ \theta_{Z,j}$)

AND go to **STEP 2**

END $j = j + 1$ (i.e. go to **STEP 1**: different angles, same centre of rotation)

END $i = i + 1$ (i.e. go to **STEP 0**: different angles, different centre of rotation)

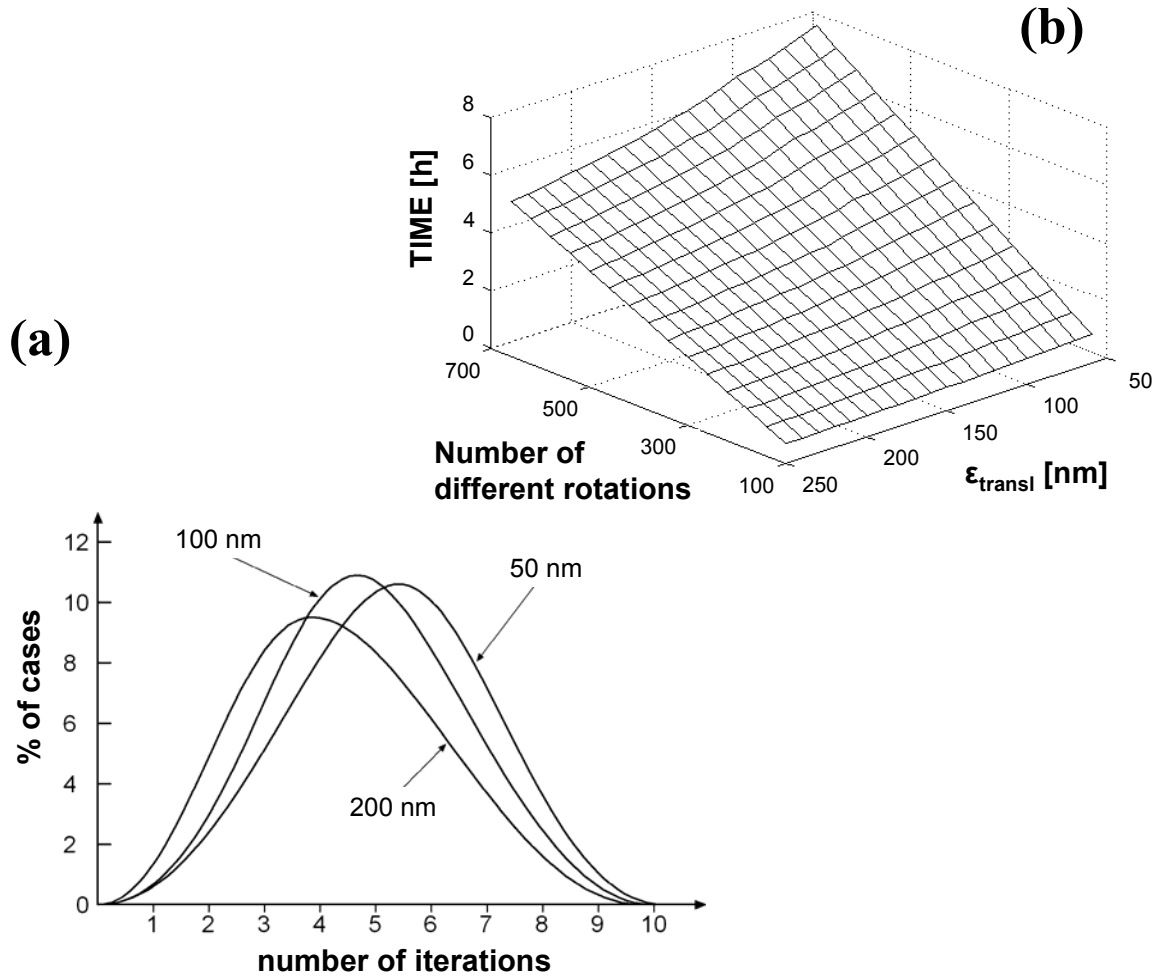


Figure 4.14 – Rotations around the same centre of rotation (RWT):

(a) – histogram of the number of iterations required to suppress residual translations for three different thresholds ϵ_{transl} : 50, 100 and 200 nm (the number of positions used to report these results was approx. 700 points);

(b) – total measuring time (corresponding to a single centre of rotation) as a function of the threshold ϵ_{transl} and the number of different rotations to be executed around the same centre of rotation.

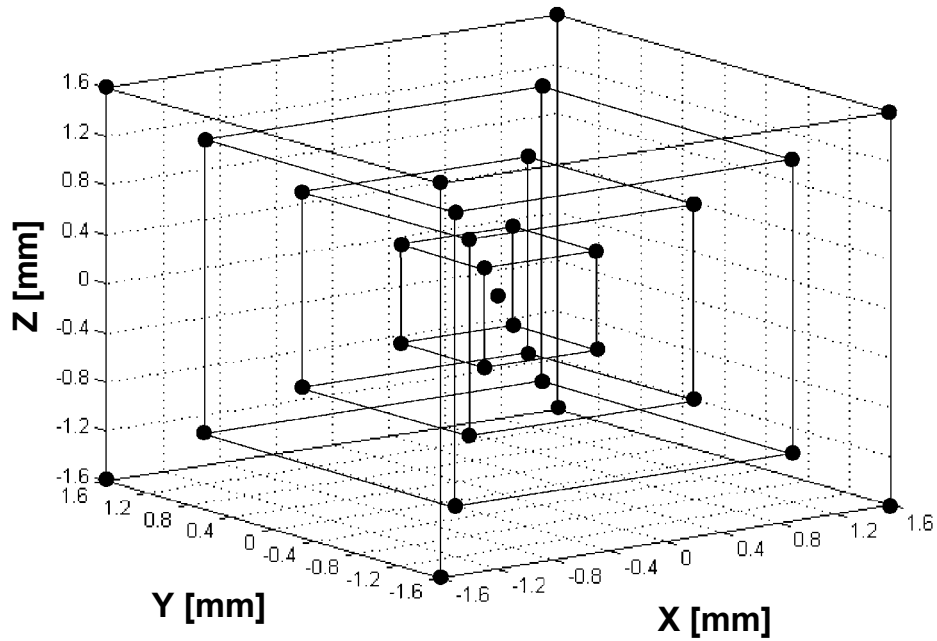


Figure 4.15 – Translational coordinates of the 33 different centres of rotation around which the rotations were executed (corresponding to the nominal positions of STEP 1 of the preliminary adjustments).

The number of different rotations performed around the same centre of rotation in a given measurement session was typically:

- in the case of “small angles”: $7 \times 7 \times 7 = 343$ rotations.

These positions corresponded to the following regular divisions for each angle (in arcseconds): ± 300 , ± 200 , ± 100 and 0;

- in the case of “large angles”: $3 \times 12 \times 3^2 = 324$ rotations.

These positions corresponded to only 1 “large angle” varying per time according to the following divisions³²:

$-3^\circ - 150''$	-3°	$-3^\circ + 150''$	$-1.5^\circ - 150''$	-1.5°	$-1.5^\circ + 150''$
$+1.5^\circ - 150''$	$+1.5^\circ$	$+1.5^\circ + 150''$	$+3^\circ - 150''$	$+3^\circ$	$+3^\circ + 150''$

while the two remaining angles remain at the following small values:
 ± 150 and $0''$.

Figures 4.14a and 4.14b report respectively the influence of the threshold ϵ_{rot} on the average number of iterations and the influence of this threshold and of the number of different rotations to be executed on the total measuring time. Notice that these 2 graphs correspond only to the case of “small angles”³³.

Up to 700 poses, **Figure 4.14b** shows that imposing strict correction thresholds ϵ_{transl} , for a fixed number of rotations around the same centre, does not have a major impact on the total measuring time.

Figure 4.15 represents the nominal coordinates of the 33 different centres of rotation measured in phase 3.

(d) – Summary of the 6D measuring protocol

In order to overcome the lack of direct 6D measuring instrumentation, an original measuring protocol was proposed to collect a full set of 6D data.

This protocol is actually an indirect measuring method making use of existing instrumentation.

The overall measuring protocol comprises in fact three different phases:

■ **PHASE 1: Calibration of the angles (3D calibration)**: the end-effector moves, according to the ideal IGM, over the full 6D workspace but only the orientations are measured. “Small angles” (within the range of the autocollimator: $\sim \pm 412$ arcsec) are measured directly on the surfaces of the mirror cube, whereas “large angles” (up to $\pm 3^\circ$) are measured on the faces of calibrated polygon prisms. At the end of this phase, the robot is able to move its end-effector over its workspace with correct angles.

■ **PHASE 2: Calibration of the translations (3D calibration)**: using either the results of the previous phase or a closed-loop with the two autocollimators, the angular variations are suppressed from the motions of the end-effector, so that the corresponding translations can be measured accurately. At the end of this phase, the robot is able to move its end-effector over its workspace in a “pure-translation” way.

³² In the next lines, we will use « 1'' » instead of « 1 arcsec » for the sake of clarity.

³³ The case of “large angles” required a particular measurement strategy. This strategy (and the reasons for its implementation) is presented in **paragraph b** of **section 4.3.3**.

■ **PHASE 3:** *Measurements of translations combined with rotations (full 6D data):* the robot, having a sphere mounted on its end-effector, is forced to execute M different rotations around the same centre of rotation, by means of a closed-loop with three *Keyence*[®] laser sensors. This operation is repeated for a certain number N of different centres of rotation spread over the translational workspace.

For each centre of rotation, the 6D data is then assembled having regard to the results of the previous phases:

- the translational coordinates are those of a “pure-translational” pose determined using the results of phase 2;
- the angular coordinates are determined using the results of phase 1.

Figure 4.16 summarizes the calibration procedure described previously.

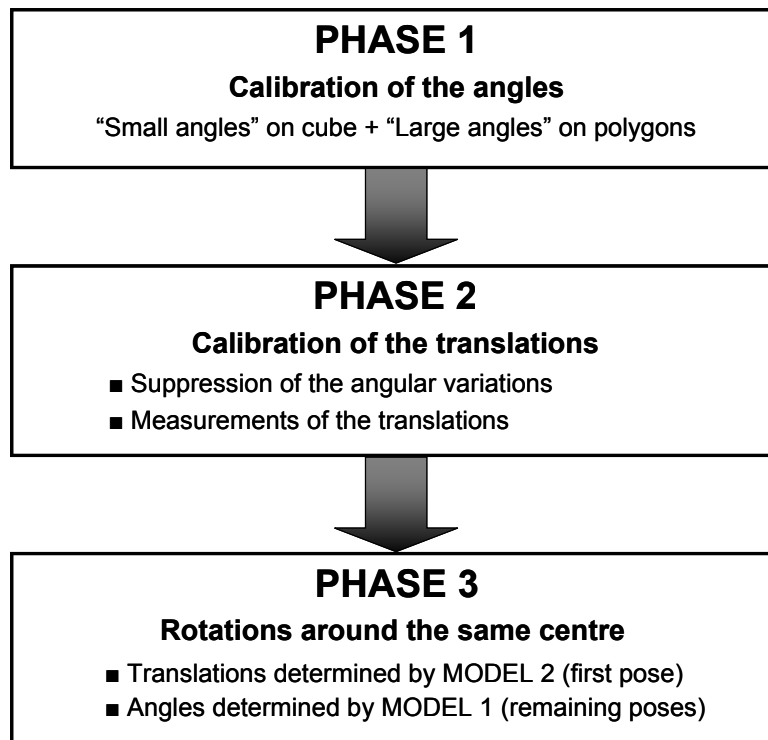


Figure 4.16 – 6D measuring protocol proposed in this section for collecting the data from the 6 DOF robot.

Remarks:

1. The major advantage of this procedure lies in its *modularity*. In fact, phases 1 and 2 are two separate 3D calibrations of the rotations and the translations, respectively. Depending on the application in which the robot is being used (positioning in translations or adjustment of absolute angles), one can perform one phase or the other independently without having to go through the entire 6D procedure.

2. The protocol of **Figure 4.16** is not unique. Using similar elementary phases, alternative measuring protocols (not presented in this document for the sake of clarity) can also be formulated.

(e) Limitations of the 6D measuring procedure proposed

The procedure described in this section suffers mainly from the following limitations:

■ Uncertainty propagation

The collection of the 6D data is an indirect procedure developed to overcome the lack of appropriate direct measuring instrumentation.

In particular, phase 3 assembles the 6D data from the two 3D calibrations assuming that the translational and angular motions coming, respectively, from MODELS 1 and 2 are without errors. In fact, these models always have a limited prediction capability: approx. ± 100 nm for translations, ± 0.3 arcsec for “small angles” and ± 2.7 arcsec for “large angles”. Therefore, a certain amount of noise may be added into the collected data.

In addition, the configuration in which the *Keyence*[®] sensors are used may also bring additional error in assembling the data since the reflection of the laser beam is performed on a spherical surface. Even if this is not of major importance since these sensors are only used as “zero detectors” (see detailed information on this issue in **section A.5** of **Appendix A**) and not for measuring distances, the influence of this effect is believed to be within the threshold ϵ_{transl} below which translations are considered to be suppressed (± 50 nm).

We believe that the only solution to this error propagation is to develop a new direct 6D measuring system (having the same accuracy in measuring translations and rotations as the interferometer and the autocollimator, respectively).

■ Angular range

Only a limited part of the robot angular workspace was covered in this work. Again, this is due to the limited performance of current measuring devices.

As mentioned above, only a new metrological development will overcome this limitation.

■ Measuring time

Among the three different phases of the procedure, phase 3 is certainly the most time-consuming³⁴. This is mainly due to the two following reasons:

1. as opposed to phases 1 and 2, *phase 3 is actually concerned with the 6 operational coordinates of the robot*. Therefore, its total measuring time is much higher, since this phase has to deal with a larger amount of possible data combinations;
2. the *necessity of different manual adjustments throughout the entire duration of the phase*. In fact, a new manual positioning of the optical heads was required each time a new centre of rotation had to be measured.
Consequently, each time a manual adjustment had to be performed, the thermal chamber was opened and a new temperature-regulation run had to be launched before the measurements corresponding to this new centre of rotation could actually start.

³⁴ The average time to accomplish the measurements of phases 1 and 2 (together) is less than 1 week while phase 3 requires between 2 and 3 weeks.

If phase 3 is fully automated (in particular, the adjustment of the three *Keyence*[®] sensors before the actual measurements), we believe that the total measuring time of phase 3 could be reduced to approximately 1 week.

A solution to the second problem could be the integration of a 3D motorized stage inside our measurement system. However, this would introduce a new heat source into the measuring environment.

4.3.2 – Absolute reference frame

Two different reference frames were reported in **Figures 4.9**³⁵ and **4.13**.

These frames have exactly the same directions but different origins: the reference frame used during phases 1 and 2 has an origin at the centre of the mirror cube O_C (see **Figure 4.9**), while the origin of the frame used in phase 3 is the centre of the sphere O_S (see **Figure 4.13**).

The reason for the existence of these two frames (represented in **Figure 4.17**) is related to practical constraints imposed by our method and instrumentation.

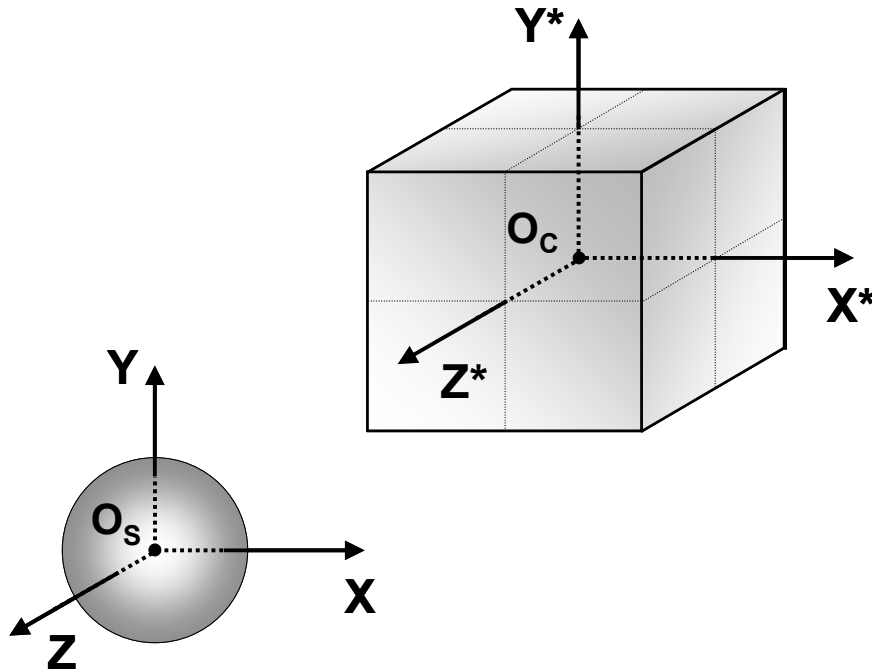


Figure 4.17 – The two different frames used during the different phases of the calibration of the 6-DOF robot (see Figures 4.9 and 4.13). These frames have the same directions but different origins. The **absolute reference frame** has its origin at the centre of the sphere (O_S).

■ During phase 1, only the magnitudes of the rotations are actually measured (without any concern about the centre of rotation). Since, from the practical point of view, these measurements had to be carried out on the surfaces of the mirror cube, we decided to use the surfaces of the cube to define the directions of the absolute frame when the robot is in its reference position $(0 \ 0 \ 0 \ 0 \ 0 \ 0)$.

In addition, since the interferometer operates in an incremental mode, only the directions of the absolute frame are required to actually measure the “pure-translational” motions. Consequently, the directions defined in the previous frame are also used in phase 2.

³⁵ The frame of **Figure 4.12** is the same of **Figure 4.9**.

The frame used for the measurements of phases 1 and 2 is then a virtual frame exclusively defined in respect to the mirror cube: the origin is the centre of the cube \mathbf{O}_C and the directions are defined by the three functional surfaces in the same way as in **section 4.2.1** (for the 3-DOF robot).

■ The assembly of the two 3D calibrations in order to obtain 6D poses (phase 3) requires, however, a frame with a new origin.

In fact, in view of the limitations of the current instrumentation, this assembly can only be achieved by means of *indirect measuring methods* and particular *conventions*:

- we used the reading of three *Keyence*[®] measuring the displacements of the centre of a sphere in order to “force” the rotations to occur around different centres of rotation, since this represents an **indirect way of actually dealing with the 6 degrees of freedom simultaneously**.
- in our case, we made use of the concept of centre of rotation in accordance with the convention of section 4.1.1 – paragraph (b).

According to what has been said, it is now clear that the origin of the frame used in phase 3 has to be the centre of the sphere. Consequently:

the **absolute reference frame** in respect to which the 6D data was collected is a **virtual frame** with the following characteristics:

- the **origin** is the centre of the sphere when the robot is in the reference position (0 0 0 0 0 0)
- the **directions** are those defined by the surfaces of the mirror cube, in the same way as for the case of the 3-DOF robot (see **section 4.2.1 – paragraph (a)**).

As in the case of the 3-DOF robot, this definition of the absolute frame was also the consequence of the fact that the measurements of the 6-DOF robot could not be performed in a *differential mode* (and, therefore, using an external reference frame), again due to the limitations of the instrumentation used.

Notice, finally, that our particular way of defining the absolute reference frame has important consequences if such calibration procedure has to be used in real 6D industrial operations. **Appendix C** provides an insightful discussion on this issue.

4.3.3 – Delicate aspects

In this section, the reader is alerted to some delicate points regarding the different phases of the calibration of the 6-DOF robot. Advice is provided on the basis of the acquired experience.

In addition to these specific points, the reader is also referred to **Chapter 3** in which general points related to the measurements of any high-precision flexure parallel robot were discussed.

(a) Delicate aspects during PHASES 1 and 2

■ Performing the TWR closed-loop using a single autocollimator

The TWR closed-loop of **phase 2** (paragraph b – section 3.6.1) can also be performed with a single autocollimator.

Figure 4.18 illustrates the method followed in this particular case. In **case (a)**, the autocollimator is mounted so that the beam can only read the variations of angles θ_x and θ_y . As the autocollimator will stay in its initial mount, additional mirrors have to be mounted in order to read variations of angle θ_z – **case (b)**. The use of a flag in two different positions allows a change in the measuring configuration.

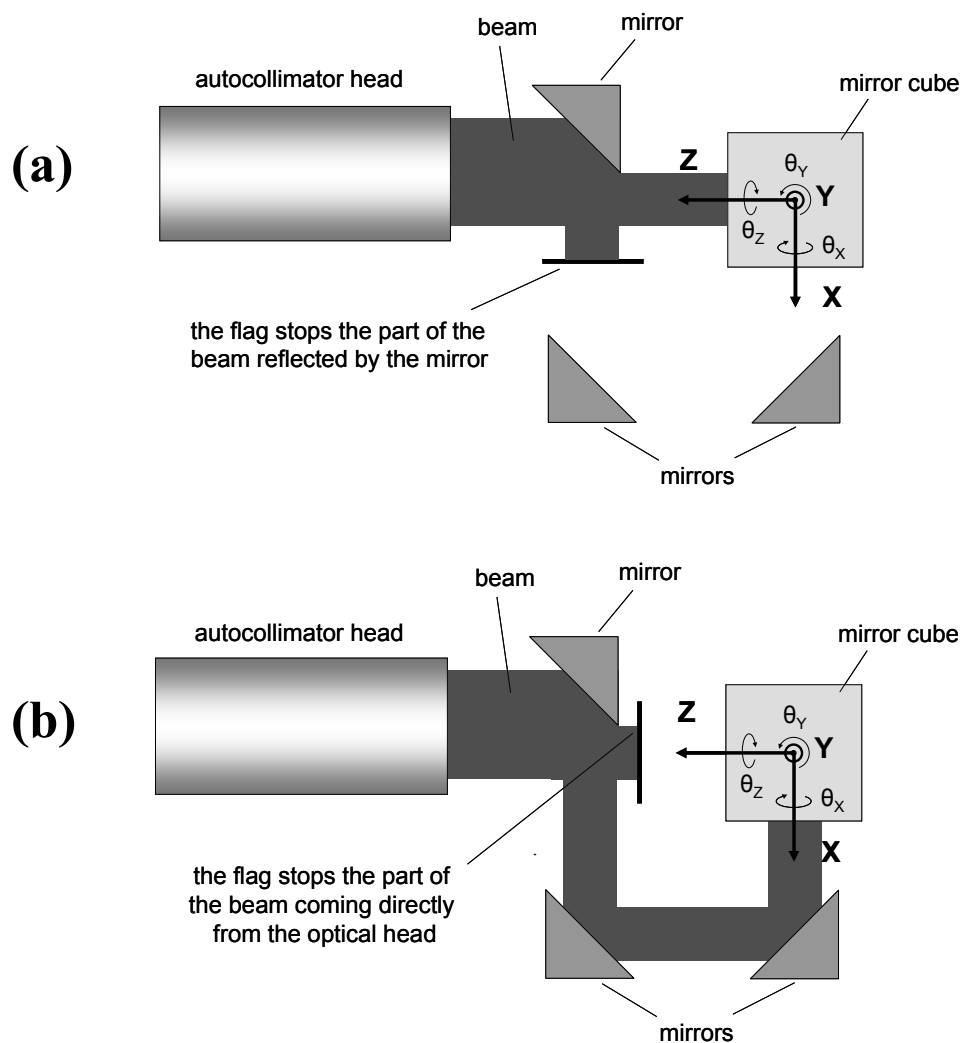


Figure 4.18 – Performing TWR closed-loop using a single autocollimator and a system of additional mirrors to complete the optical path. **Configuration (a)** is used to read θ_x and θ_y , while **configuration (b)** is used to read θ_y and θ_z .

However, this way of performing the measurements suffers from a few drawbacks:

- the motor used to control the position of the flag may produce additional heat that may influence significantly the stability of the various regulated temperatures;
- the number of reflections and the total length of the optical path in **case (b)** are much higher than in **case (a)**. These factors will increase the inaccuracy of the corresponding reading and will bring considerable drift³⁶ in the measurement;
- in both cases, only a part of the autocollimator's original beam is used for the actual measurement. This also decreases the accuracy of the corresponding measurement, as we have seen in **section 3.2.3 – paragraph (b)**.

■ “Beam break” during the measurements of “pure-translations”

As we have seen previously, in order to measure distances accurately with the laser interferometer, the mirror surface on which the laser is reflected has to remain as far as possible orthogonal to the beam.

In **paragraph (b)** of the previous section, we have proposed solutions to suppress the static angular variations of the positions for which the translations have to be measured by the interferometer.

However, when going from one “pure-translational” position to another, a “**beam break**” may occur due to the existence of dynamic angular variations between these two positions.

The following solutions can be adopted in order to avoid this problem:

- in cases in which the position regulation is performed at the motor coordinate level, the trajectories can be decomposed into the three elementary directions of the 3D space.
Example: $(-2, -2, -2) \rightarrow (-2, -2, +2) \rightarrow (-2, +2, +2) \rightarrow (+2, +2, +2)$ ³⁷
- *trajectory tracking* may be implemented using the model calibrated for angles (MODEL 1)

(b) Delicate aspects during PHASE 3

■ Performing the RWT closed-loop in the case of “large angles”

Phase 3 involves three laser sensors reading the position of a sphere mounted on the robot end-effector. In comparison with the interferometer, these sensors have a restricted measuring range (e.g. $\pm 200 \mu\text{m}$ for the model LC-2420).

Therefore, *the difficulty of performing the RWT closed-loop correction on positions having “large angles” lies in maintaining the signal within the range of the sensors.*

A solution to this problem could be to reach the desired angle in a “step-by-step way” (e.g.: $0^\circ \rightarrow 0.5^\circ \rightarrow 1^\circ \rightarrow 1.5^\circ \rightarrow 2^\circ \rightarrow 2.5^\circ \rightarrow 3^\circ$) and perform different intermediate closed-loop corrections for each position of the previous decomposition. In this way, the position of the sphere could always be read and corrected for at any time.

³⁶ We have detected drifts up to ± 10 arcsec over short periods of time.

³⁷ Actually, any order of decomposition along the different axes works.

4.3.4 – *Measurement results*

This section aims to provide a complete portrait of the accuracy of the 6-DOF robot before calibration on the basis of the data collected by means of the previous procedure.

(a) Angular errors

■ Case of the “pure-translational” poses

Figure 4.19 shows the histogram of the angular errors when the robot end-effector is asked to move in a “pure-translation” way, according to the ideal IGM.

These histograms report the results corresponding to the 729 positions uniformly spread over the robot translational workspace. It can be seen that these errors are up to ± 150 arcsec, which corresponds therefore to the accuracy of the ideal IGM used to control the robot.

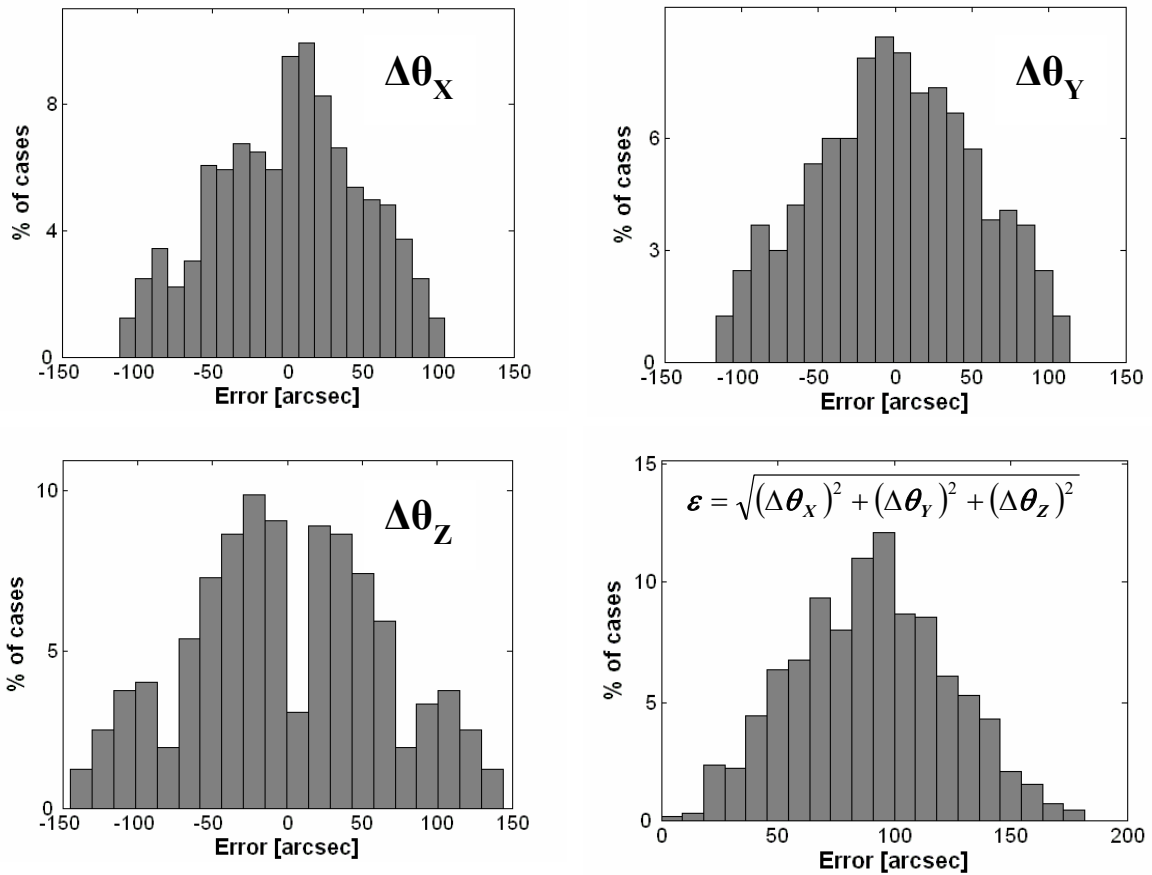


Figure 4.19 – Histogram of the errors in the angular motions when the 6-DOF robot is required to move its end-effector in a “pure-translation” way, according to the ideal IGM.

As for the 3-DOF robot, it is more convenient to represent the previous results in terms of *error isosurfaces* in order to relate them to the geometry of the robot. This representation is given in **Figure 4.20**.

In this Figure, the shape of the isosurfaces corresponding to the cases $\Delta\theta_x$, $\Delta\theta_y$ and $\Delta\theta_z$ reminds the results obtained for the 3-DOF robot (see **Figure 4.7** in **section 4.2.3**).

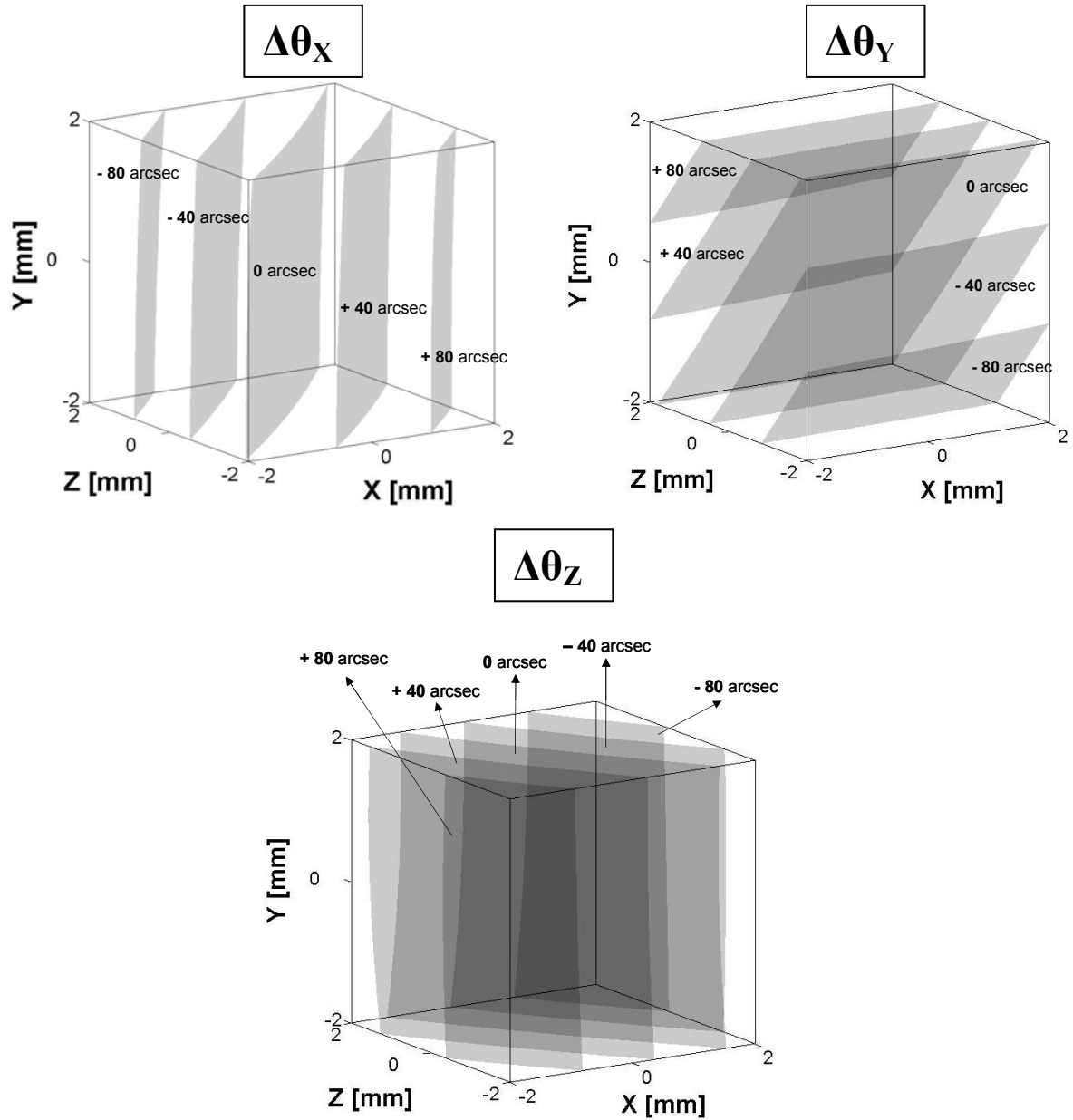


Figure 4.20 – Isosurface representation of the angular errors when the robot is asked to move its end-effector in a “pure-translational” way.

Table 4.1 summarizes the main observations that can be made from the graphs of **Figure 4.20** and for which we will provide an explanation in the following lines. For a proper understanding of the following explanations, the reader is invited to look periodically at **Figure 4.21** which gives a schematic representation of the robot kinematics.

■ When the end-effector is required to move exclusively along X-axis according to the ideal IGM (first row of **Table 4.1**):

- the angle θ_y remains almost constant: this is due to the fact that the translational stages of chains 4 and 6 (imposing the distances in X-axis) move with equal displacement steps (differences are in the nanometre range, thanks to the excellent relative accuracy of the *Heidenhain*[®] rules);

- the variation of angle θ_x is caused by a lack of parallelism between arms 3 and 5 during the X-motion;
- in a similar way, the variation of angle θ_z is the consequence of errors between arms 1, 3 and 5 during the X-motion.

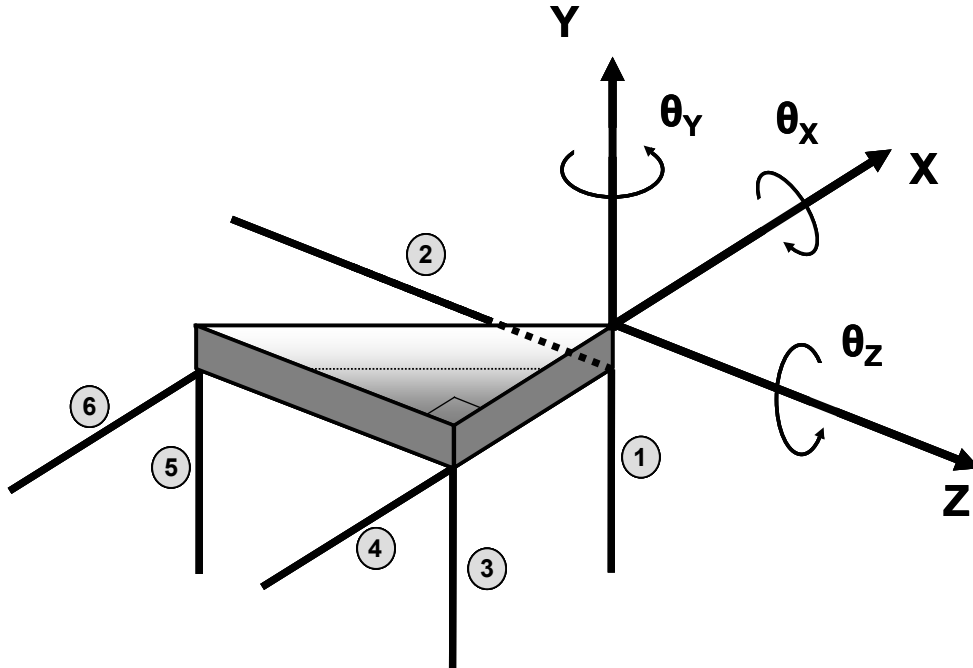


Figure 4.21 – Detailed view of the 6-DOF robot end-effector showing the axes convention used and the arrangement of the different kinematic chains connected to the end-effector in order to compose the full 6D motion.

■ When the end-effector is required to move exclusively along Y-axis according to the ideal IGM (second row of **Table 4.1**):

- the angles θ_x and θ_z remain almost constant: this is due to the fact that the relative motions of the translational stages of chains 1, 3 and 5 (used to impose the displacements along Y-axis) are equal at the nanometre range, thanks once more to the excellent accuracy of the *Heidenhain*[®] rules;
- the variation of angle θ_y is due to a lack of parallelism between arms 4 and 6 during the Y-motion.

■ When the end-effector is required to move exclusively along Z-axis according to the ideal IGM (third row of **Table 4.1**):

- the variation of angle θ_x is due to a lack of parallelism between arms 3 and 5 during the Z-motion;
- the variation of angle θ_y is due to a lack of parallelism between arms 4 and 6 during the Z-motion;
- the variation of angle θ_z is due to a lack of parallelism between arms 1 and 3 during the Z-motion.

	ANGULAR VARIATION detected			
AXIS along which the displacement is imposed		$\Delta\theta_x$	$\Delta\theta_y$	$\Delta\theta_z$
	X-axis	$\neq 0$	≈ 0	$\neq 0$
	Y-axis	≈ 0	$\neq 0$	≈ 0
	Z-axis	$\neq 0$	$\neq 0$	$\neq 0$

Table 4.1 – Summary of the main observations from graphs of Figure 4.20.

■ Case of a general 6D pose of the full measurable workspace

Figure 4.22 reports the angular errors around the different axes when the robot is asked (according to the ideal IGM) to execute different rotations over its full 6D measurable workspace.

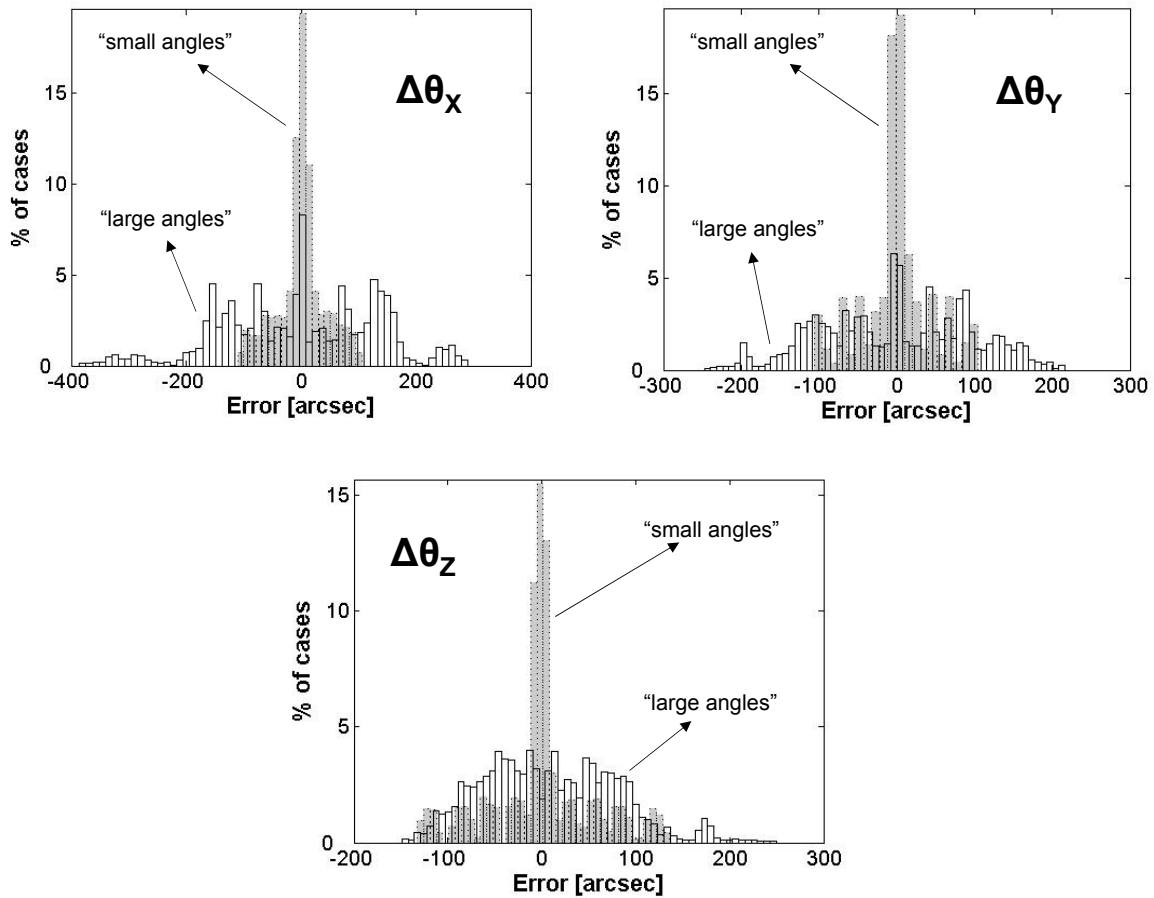


Figure 4.22 – Histogram of the errors (= measured operational coordinate – ideal operational coordinate according to the ideal IGM) in the angular motions of the 6-DOF robot over its workspace. The two cases “small angles” and “large angles” are reported.

For each axis, we reported the errors corresponding to the case of “small angles”, read on the surfaces of the mirror cube, and to the case of “large angles”, read on the surfaces of the polygon prisms.

From the observation of these histograms, one can see that the accuracy of the ideal IGM in predicting “large angles” is degraded when compared to that of “small angles”.

The main reason for this lies in the fact that the former requires a great number of flexures in the robot kinematics to adopt bending angles of significant magnitude (close to maximum stress profiles). We believe that this brings, from the modelling point of view, additional non-linear behaviour for which the IGM (which is based on the assumption that flexures act like perfect pivots) is incapable of providing accurate predictions as it would for poses located in more “central areas” of the robot workspace.

(b) Translational errors

■ **Figure 4.23** shows the histogram of the errors in the translational motions when the robot is required to act as a “pure-translator”, according to the ideal IGM.

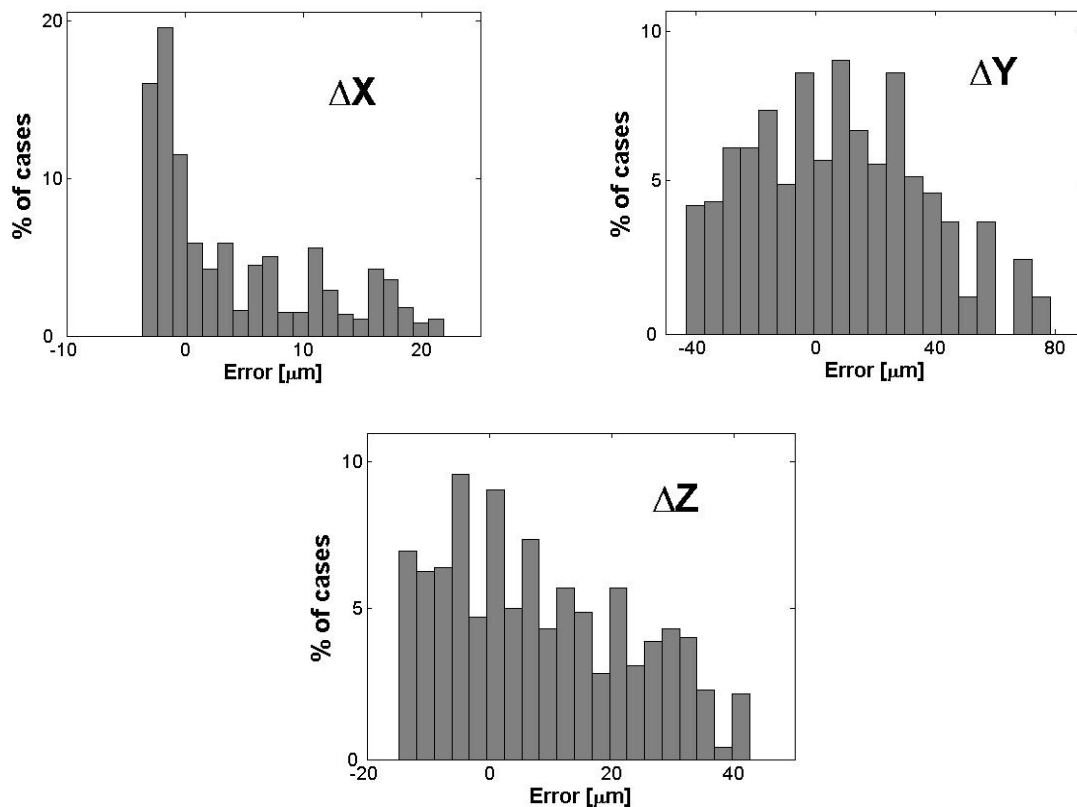


Figure 4.23 – Histogram of the errors (= measured operational coordinate – ideal operational coordinate) in the translational motions when the 6-DOF is asked to execute “pure-translational” motions, according to the ideal IGM.

These histograms present the results corresponding to the 729 poses uniformly distributed over the robot translational workspace, for which the angular variations were suppressed using the TWR algorithm described in **paragraph (b) of section 4.3.1**.

Therefore, the translational results presented in this section are free from any angular influence.

■ Notice that, in comparison to the graphs of the 3-DOF robot (**Figure 4.6**), we can see that the errors along the different axes have quite different variation ranges and are clearly not symmetric in respect to the origin, since the robot itself has an asymmetric kinematic structure (see **Figure 4.21**).

In particular, we can see that errors along Y-axis are higher than those along X- and Z-axes. A possible reason for this lies in the fact that through the entire translational workspace explored, Y-axis is the one for which the displacements imposed to the translational stages of the chains controlling the axis motion (chains 1, 3 and 5) undergo more frequent corrections coming from the TWR closed-loop in order to guarantee a proper suppression of angular variations.

■ **Figure 4.24** provides a 3D isosurface representation of the errors, necessary for relating the measurement results to the geometry of the robot.

In the case of the 6-DOF robot, as opposed to the case of the 3-DOF robot, it is much more difficult to provide clear explanations for these particular error profiles.

This difficulty arises mainly from the following issues:

- the structure of the robot is much more complex (there are 6 different kinematic chains, arranged in an asymmetric way, and interacting with each other in order to compose the 6D motion);
- the results presented here correspond only to “pure-translational” poses. Therefore, they are exclusively related to the behaviour of the robot in a particular subset of its full 6D workspace.

However, despite this complexity, and in our opinion, the following arguments, originally presented for the 3-DOF robot, can still be used to explain the profiles of **Figure 4.24**:

■ the error also remains unchanged in respect to displacements along the direction being measured (example: ΔX does not vary significantly in respect to X, ΔY in respect to Y and ΔZ in respect to Z).

This is due to the fact that, in this case, the accuracy of the motion is mainly determined by the excellent linear relative positioning accuracy of the *Heidenhain*[®] rules used to impose the displacements of the translational stages along the direction of interest;

■ the dependency of the error measured along one particular direction in respect to the displacements occurring in the directions not being measured is mainly the result of the fact that space parallelograms have initial orientations other than 0° when the robot is in its reference position (**0 0 0 0 0 0**) – [see the discussion and figures on pages 60 to 62](#).

In our case, Y-axis seems to be the most affected by this type of errors.

Notice that, in the case of the 6-DOF robot, this dependency is no longer linear at the first-order approximation (as is the case for the 3-DOF robot). This is probably due to the complexity of the interactions between the different kinematic chains of the robot composing the final operational motion (and probably also, in part, due to the displacement of the instantaneous centre of rotation of the flexures, which follows a second-degree polynomial law³⁸).

³⁸ According to the results reported by other researchers, e.g. Bacher [Bac03].

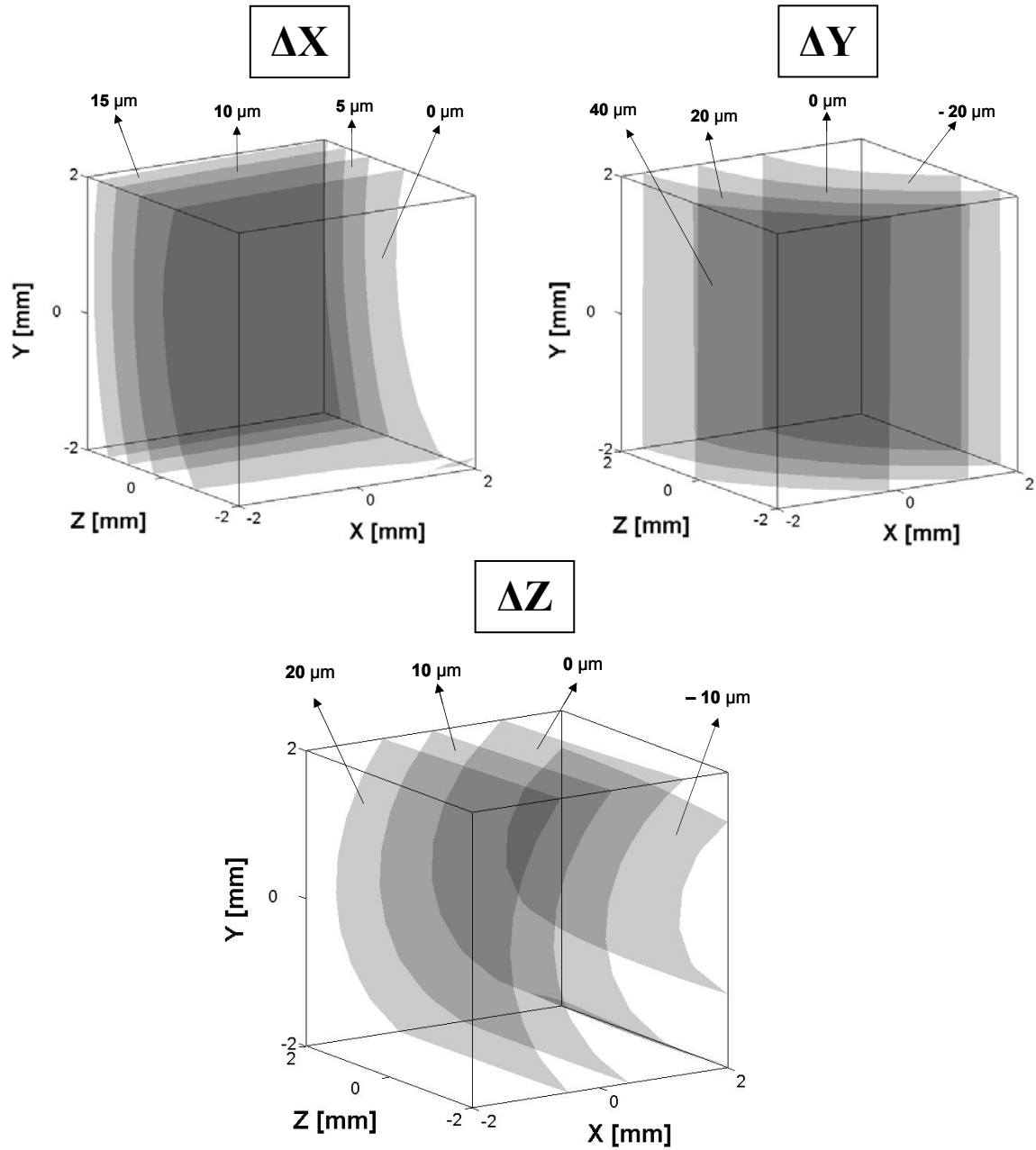


Figure 4.24 – Isosurface representation of the translational errors (= measured operational coordinate – ideal operational coordinate) corresponding to “pure-translational” poses spread over the robot workspace.

Notice finally that, as we have also mentioned for the 3-DOF robot, **the calibration of the 6-DOF robot can still be performed even in the absence of clear explanations for the error profiles reported in this section.**

4.4 – Conclusion

This chapter was devoted to the description of the measurements collected from a 3-DOF (3 translations) and a 6-DOF (3 translations + 3 rotations) robot.

■ In the case of the **3-DOF robot**, the measuring protocol consisted of imposing, for a certain number of positions, regular displacements in motor or operational coordinates (as predicted by the ideal IGM) and measuring (with the help of a laser interferometer) the real displacements experienced by the end-effector on which a precision mirror cube is mounted.

Since passive DOF (residual rotations) influence the calibration of the active DOF (translations), a slight readjustment of the robot assembly (in order to minimize the angular variations) was necessary before the calibration could start.

A typical readjustment can set these angular variations within the range of ± 10 arcsec. If the influence of such residual rotation (measured with the help of autocollimators) is not considered, then the reading of the interferometer could be corrupted up to ± 100 nm³⁹.

We have seen that the data collected from the 3-DOF robot indicates that the statistical distribution of the errors is roughly symmetric in respect to zero, which is in accordance with the kinematic symmetry of this robot.

For each direction, the differences between the measured operational coordinate and the corresponding value imposed by the ideal IGM could be up to ± 70 μ m. Even though this is not required to calibrate the robot, we have also tried to explain the error profiles on the basis of the configuration adopted by the space parallelograms at the robot reference position.

■ In the case of the **6-DOF robot**, as there is still a lack of existing instrumentation able to measure the 6 degrees of freedom simultaneously within the desired accuracy, an original measuring protocol had to be developed.

In this protocol, the 6D calibration problem was decoupled into two 3D calibrations: calibration of the rotations using autocollimators + calibration of the translations (after the rotations were actively suppressed) using a laser interferometer.

In order to merge these two 3D calibrations to actually obtain the full 6D data, an additional step was required in which the robot was “forced”, through a closed-loop action (in our case, we used three high-precision laser triangulation sensors mounted orthogonally), to execute rotations around different centres of rotation (with known coordinates).

The data collected from the 6-DOF robot showed that the angular errors before calibration could be up to ± 150 arcsec in the case of “pure-translational poses” and more than ± 200 arcsec in the case of a general 6D pose of the measurable workspace.

Translational errors (before calibration) could be up to ± 80 μ m. We have also seen that these errors in the translational motions (which are now⁴⁰ completely free of any angular influence since the angular variations are below ± 0.2 arcsec⁴¹ during the measurements of the translations) are no longer statistically distributed in a symmetric way in respect to zero since the kinematic structure of the robot itself is asymmetric.

³⁹ The influence of these residual rotations on the interferometer reading can be corrected according to the expressions proposed in **Appendix B**, as long as they can be measured.

⁴⁰ As opposed to the case of the 3-DOF robot.

⁴¹ The influence of an angular variation of ± 0.2 arcsec in the reading of a 2 mm translation is less than ± 2 nm.

DATA PROCESSING

Chapter 5

Model-based approach to pose correction

5.1 – Introduction

If a robot calibration is solved using a *model-based approach* it means that the correction of the errors in the robot pose is achieved using mathematical functions for which the analytical forms are used explicitly. A set of parameters calculated during the identification phase confer the desired approximation capability to the model.

The literature review in **Chapter 2** has shown that most of the existing model-based techniques rely on the use of models having a physical representation¹. This means that the parameters to be identified are directly related to the geometry of the robot being calibrated. For very simple manipulators with few DOF, the use of such models is straightforward.

However, in the case of multi-DOF manipulators with complex and/or difficult-to-model geometries, such as flexure parallel robots, the use of these models presents a few drawbacks. First, a very large number of parameters have to be used if one wishes to cover all the possible sources of inaccuracy that tackle accuracy levels in the nanoscale. This implies that a very dense system has to be solved during the identification phase.

Second, some of the sources of inaccuracy may be very difficult to model explicitly which results in a lack of model completeness and, thereby, in a loss of accuracy.

Third, even if a complete physical model is available for calibration, its non-linearity (arising from the coupling between DOF, which typically characterizes parallel mechanisms) will cause the parameter identification to be a very delicate problem. Standard non-linear optimization algorithms will most probably be trapped in a local minimum, so that the physical solution of the problem will always remain unknown.

The use of *behavioural models* is a reliable solution to overcome the previous difficulties.

In such models, the correspondence between the motor and the operational worlds is realized by means of a mathematical function whose “shape” is decided from the observation of the data collected on the robot. As opposed to physical models, the coefficients are completely free of any physical meaning and their values are calculated so that the resulting function best fits the desired input-output mapping.

Among the different functions typically used for regression tasks, this chapter makes use of *multi-variable polynomials*.

The structure of this chapter is as follows.

We start by motivating the use of polynomial functions for the calibration of high-precision flexure parallel robots (**Section 5.2**) and discuss briefly a few issues related to this application (**Section 5.3**).

We then present the calibration results of the 3 and 6-DOF robots measured in this thesis (**Sections 5.4 and 5.5**) and prove the effectiveness of our approach with the help of simulation data. As we will see in **Section 5.6**, the polynomial-approach reported here is a method that is now commonly employed by our industrial partner.

Finally, **Section 5.7** summarizes the main contributions and concludes the chapter.

¹ For the sake of language simplicity, these will be called “physical models”.

5.2 – Towards behavioural models

5.2.1 – The case of elementary flexures

The study of the kinematic behaviour of elementary flexures is not new.

In recent works, such as [Bac03], it has been demonstrated that flexure joints do not act like perfect pivots as assumed by standard geometric models.

In fact, Finite-Element simulations proved that the centre of rotation of a given flexure hinge seems to move in respect to the bending angle adopted by the joint and, thus, in respect to the displacement imposed on the moving part.

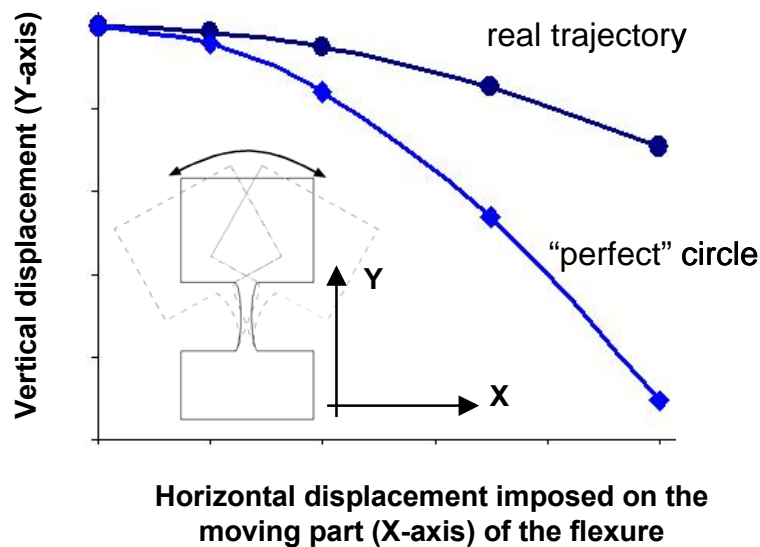


Figure 5.1 – Real trajectory followed by the moving part of a circular flexure hinge during the flexion process. The nominal dimension of the flexure seems to “expand” in respect to the ideal circular path adopted by a perfect pivot. This expansion can be interpreted as a displacement of the instantaneous centre of rotation.

For flexures of elliptical shape (of which circular and leaf-shaped flexures are particular cases), Bacher [Bac03] concluded that the displacement of this so-called “instantaneous centre of rotation” seems to obey to a 2nd order polynomial law in respect to the displacement imposed on the moving part.

Additional investigations carried out by Niarisiry [Nia06] demonstrated that this is still valid in the presence of different types of error such as geometry defaults, errors arising from temperature effects or those generated by external loads.

With the help of Finite-Element simulation models, this researcher also proved that joints (prismatic, cardanic, etc) obtained from the combination of several elementary flexures also exhibit smooth and low-order polynomial-shaped trajectories.

In order to provide an experimental confirmation of this result, we decided to investigate the case of a 4-hinge translational stage (see **Figure 1.3a** – page 3).

The experiment consisted of measuring, with the help of the *SIOS*[®] laser interferometer, the displacements of a motorized translational stage along the vertical direction of motion on a mirror cube placed on its end-effector (which defined the reference frame for the measurements).

Three different prototypes, having different geometric errors² imposed during the manufacturing process³, were measured.

Once the data had been collected, a polynomial regression was performed in respect to the displacements imposed along the axis of motion (active DOF).

The small residual errors (less than ± 20 nm within $U_{90\%}$) relatively to this 2nd order polynomial fit, represented in **Figure 5.2** below, provide the first experimental evidence of the smooth and low-order polynomial-shaped motions produced by flexure parallel mechanisms.

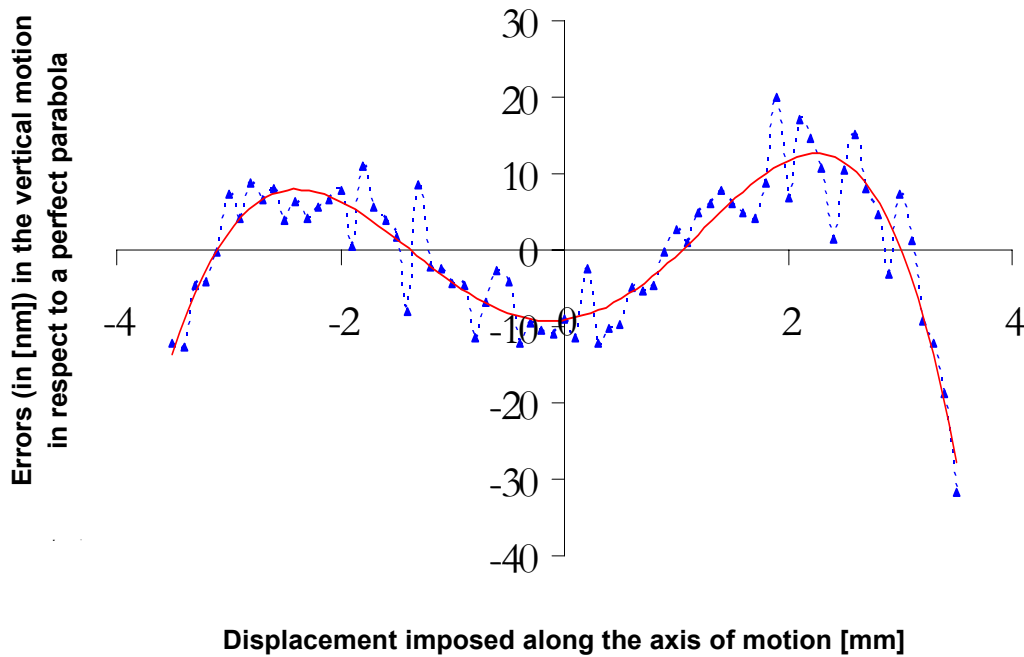


Figure 5.2 – Typical distribution of the errors in the vertical motion measured on a translational stage made of flexure joints in respect to the prediction of a 2nd order polynomial. We believe that the residual errors reported here are mainly attributable to the relative positioning accuracy of the *Heidenhain*[®] glass rules and/or the subsequent interpolation process.

5.2.2 – The case of the 3-DOF robot

A first glance at the error profiles corresponding to the data collected on the 3-DOF robot (see graphs of **Figure 4.7** – **section 4.2.3**) seems to reinforce the conclusion of the previous paragraph.

The goal of this section is to prove that multi-dimensional polynomial functions can also be used to calibrate a *full multi-DOF flexure mechanism*. In addition, we shall demonstrate through the case-study of the 3-DOF robot that these functions are even preferable to physical models (regarding the attainable accuracy) for the calibration of this particular class of robots.

The first calculations carried out on the 3-DOF robot only considered the data corresponding to a displacement (in end-effector coordinates) imposed by the IGM on the X-Y plane⁴ and letting $Z = 0$.

² The errors imposed corresponded, according to Niaritsiry's work, to configurations generating maximum deviations in respect to the nominal case.

³ These three prototypes were manufactured by *MECARTEX S.A.*: Z. I. Zandone CH-6616 Losone (TI), Switzerland.

⁴ The directions of the X, Y and Z axes mentioned in this section are those indicated in **Figure 4.1**.

Figure 5.3a reports (in a more detailed view than in **Figure 4.7**) the error along Y-axis between the displacement imposed by the IGM and the real displacement executed by the end-effector for different (X, Y) consigns.

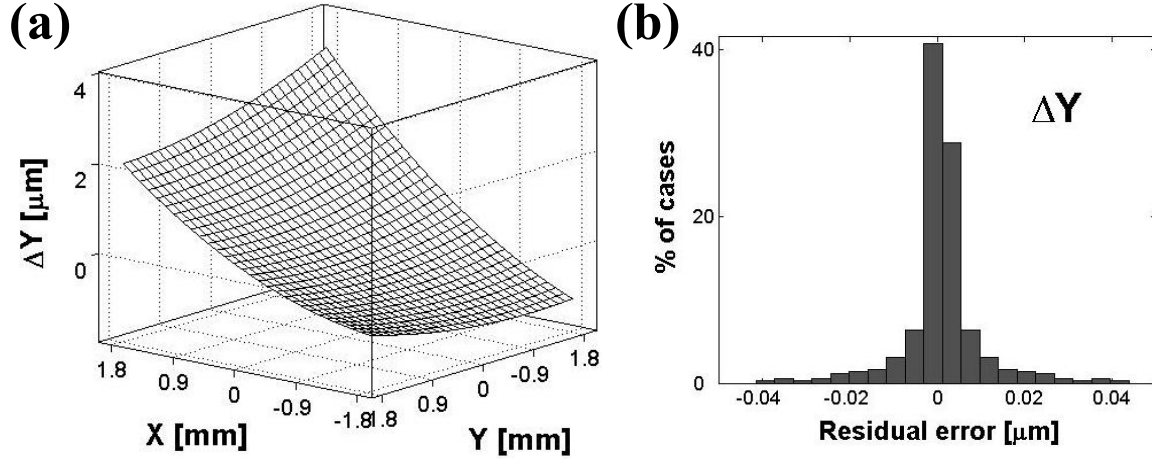


Figure 5.3 – (a): Error between the measured displacement along Y-axis and the corresponding consign imposed by the IGM. The figure corresponds to different points with different displacements along the X and Y directions and for which $Z = 0$. (b): Accuracy in the approximation of this error surface using a simple 2D polynomial regression based on model (5.1).

Following the ideas of the previous paragraph, we attempted to approximate this error surface by means of a simple 2D polynomial regression.

We found that the previous surface could be approximated within ± 15 nm ($U_{90\%}$) – see **Figure 5.3b**, with the use of the model:

$$\Delta Y(X, Y) = c_1 \cdot X + c_2 \cdot Y + c_3 \cdot X \cdot Y + c_4 \cdot X^2 + c_5 \cdot Y^2 \quad (\text{eq. 5.1})$$

A similar approach was then tested with a data set “mapping” the full workspace of the robot.

6’859 positions uniformly distributed over the robot workspace (the range of each axis being limited to ± 1.8 mm) were measured for this purpose and two different types of model were considered for data processing:

- on one hand, models having coefficients directly related to the geometry of the robot (*physical models*). For each kinematic chain of the robot, the parameters were the angular offsets of each space parallelogram at the robot reference position⁵ (represented by α and β in **Figure 4.8**) and the errors in the lengths of the arms and forearms;
- on the other hand, general 3D polynomial functions depending on the displacements imposed by the IGM (*behavioural models*). The parameters to be identified were simply the mathematical weights of these polynomials. Only the terms corresponding to orders⁶ 0, 1 and 2 were considered.

⁵ We believe that these angular offsets were the primary cause of the error profiles for this robot – see **section 4.2.3** for a detailed discussion of this issue.

⁶ The order of a given term of the polynomial corresponds here to the sum of the exponents of the different variables forming this term. Example: $X \cdot Y$ and X^2 are both 2nd order terms.

The approximation capabilities of these two models were investigated. In order to make a “fair” comparison, only the errors provided by models having the same number of parameters were considered for benchmark purposes.

Table 5.1 reports the best accuracy that can be expected from physical and behavioural models with 6, 9 and 12 parameters for the calibration of the 3-DOF robot.

Number of model parameters	Physical models	Generalized polynomial models
6 (2 per axis)	$\Delta X: 4.83, \Delta Y: 5.35, \Delta Z: 2.49$	$\Delta X: 0.59, \Delta Y: 1.61, \Delta Z: 1.70$
9 (3 per axis)	$\Delta X: 4.63, \Delta Y: 4.72, \Delta Z: 0.77$	$\Delta X: 0.49, \Delta Y: 0.75, \Delta Z: 0.92$
12 (4 per axis)	$\Delta X: 4.62, \Delta Y: 4.71, \Delta Z: 0.76$	$\Delta X: 0.42, \Delta Y: 0.42, \Delta Z: 0.70$

Table 5.1 – Accuracies provided by physical and behavioural models with different numbers of identifiable parameters.

Looking at the accuracy of the robot before calibration ($\Delta X: \pm 51 \mu\text{m}$, $\Delta Y: \pm 31 \mu\text{m}$, $\Delta Z: \pm 27 \mu\text{m}$ – within $U_{90\%}$), we can claim that both models are able to correct the majority of the pose errors for each direction.

However, a comparison between the two models emphasizes the clear advantage in the use of simple polynomial functions over classical physical models.

This advantage can be seen not only in the fact that the former are able to correct the errors within higher accuracies (between 3 and 7 times higher than the latter) but also because this performance continues to increase in respect to the number of parameters used (which is not the case for physical models⁷).

Lastly, a major advantage lies in the *linearity* of the parameter identification problem when working with polynomial models. It significantly alleviates the degree of difficulty and solvability inherent to the *non-linear* calculations that often have to be carried out if physical models are used.

For these reasons, we decided to adopt **exclusively multi-dimensional polynomial functions for the model-based calibration of high-precision flexure parallel robots.**

⁷ We believe that there are two reasons for this:

First, the *real* sources of inaccuracy of the robot are very difficult to model and their confirmation (i.e. measuring the dimensions of the robot parts in order to evaluate the *true* geometric errors and other defects) can only be achieved at highly prohibitive costs. A second and probably more important reason lies (as already mentioned in the discussion of **Section 4.2.3**) in the fact that it is impossible to determine which part of measured errors is due to a mismatch between the internal frame (impossible to define) and the frame used for calibration and which part is attributable to the physical sources of inaccuracy in which we are really interested.

5.3 – Using polynomial functions for pose correction

5.3.1 – Literature review

Despite the common use of multi-variable polynomial functions in standard linear and non-linear regression tasks over a wide range of engineering problems, these functions have so far had much less popularity than classical physical models in the robot calibration literature.

As far as we know, the work of Payannet [Pay85] was the first to consider the use of polynomials for robot calibration. The major conclusion of this author was that the choice of the functions, the coupling between the different polynomial variables and the maximum order that has to be used can only be determined through experimentation.

Similar conclusions were reported by Shamma [Sha87], Kozakiewicz [Koz90] and Flury [Flu94]. However, the major difference between these authors relatively to Payannet's work lies in the fact that polynomial functions were used for correcting the motor consign values provided by the nominal IGM of the robot – **Figure 5.4**.

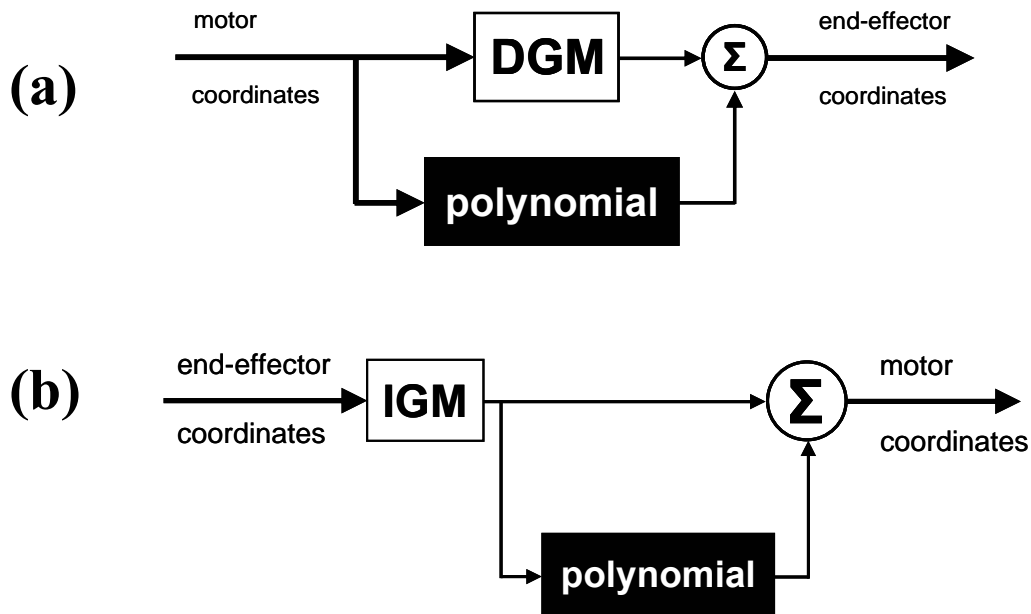


Figure 5.4 – (a): Configuration employed by Payannet [Pay85] in the context of a “forward” calibration procedure, **(b):** “Inverse” error-compensation schemes used by Shamma [Wat92], Kozakiewicz [Koz90] and Flury [Flu94] for calibration procedures.

Polynomial functions have also been applied for correcting the errors of machine tools such as in [Jan92].

Notice that other types of behavioural models can also be found in the literature for calibration purposes. Weighted sums of sines and cosines, also known as *trigonometric polynomials*, were also used by Flury [Flu94] for the calibration of a surgical manipulator.

5.3.2 – Using multi-variable polynomials for pose correction

(a) Generalization

In standard approximation problems, a given function (or model) is said to *generalize* well when the input-output mapping reproduced is correct (or nearly so) for test data never used for the calculation of the parameters of the function.

If the model used for approximation tasks is too complex, it may ultimately attempt to predict a feature (due to noise, for example) that is present in the data used for the calculation of the model coefficients but not true of the underlying function that is to be modelled. Such a phenomenon is usually referred to as *overfitting*.

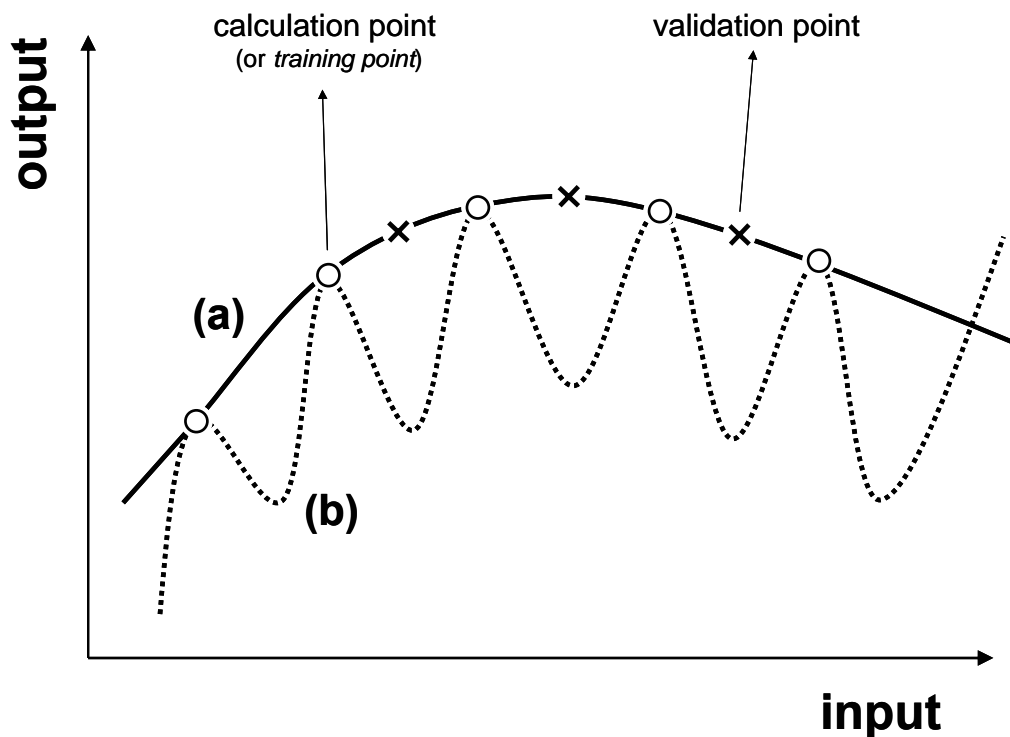


Figure 5.5 – Simple 1D example of (a): properly fitted data (good generalization) versus (b): overfitted data (poor generalization).

The best way to prevent overfitting and, thus, to guarantee a good generalization capability lies in a proper choice of the model used for the approximation process – **Figure 5.5**.

As we have seen in **section 5.2**, in the case of high-precision flexure parallel robots typical error surfaces present a quite *smooth* aspect for which low-order polynomials may perform an accurate approximation.

A model selection criterion, commonly known as *Ockham's razor*, states that unnecessarily complex models should not be preferred to simpler ones. In the context of our discussion, the simplest function means the smoothest function that performs the approximation within a desired error.

In addition, overfitting may be identified through the use of *cross-validation* techniques [Sto74], in which the available data is split into two different subsets. The first subset is used to calculate the model coefficients while the second contains new samples for the evaluation of the actual generalization performance of the model obtained.

(b) Correction configurations

Different configurations can be adopted for the calibration of a given robot using multi-variable polynomials. The origin of these configurations lies mainly in the following issues:

- 1) the IGM of the robot is easily available or difficult to compute (in the case of very complex kinematic structures in which there is a strong coupling between DOF);
- 2) the error compensation has to be performed in the motor or operational domain.

We will retain the 6 different configurations of **Figure 5.6**.

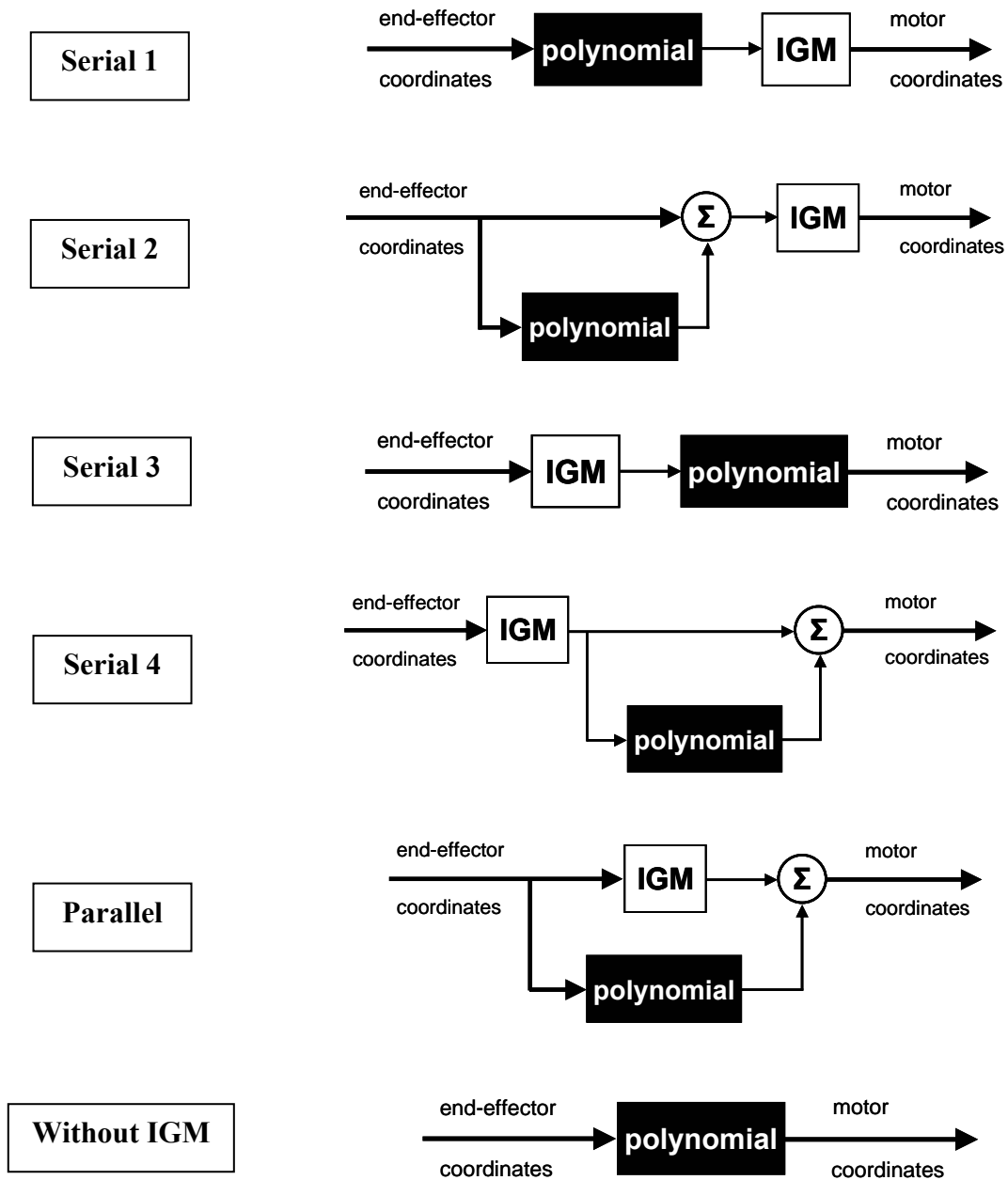


Figure 5.6 – Different correction configurations considered for data processing tasks for the calibration of a given robot. In the first 5 cases, notice that the polynomial function is interacting with the IGM. In the last configuration, the robot IGM is not used (which means that no information is given concerning the robot nominal structure) so that the problem of finding the correct relationship between the motor and the operational coordinates is fully “delegated” to the polynomial used.

Important remark: Notice that some of the configurations considered in the previous figure may be equivalent from a *strict mathematical point of view*.

However, all these different configurations will be considered in **sections 5.4** and **5.5** of this chapter as well as in **sections 6.4** and **6.5** of the next chapter. Our only motivation in doing so is simply to prove that it is always possible to find a polynomial function (chapter 5), or a neural network (chapter 6), able to provide a satisfactory accuracy irrespective of the complexity of the function to be approximated in the calibration of a given high-precision flexure parallel robot.

(c) Choice of the “best” polynomial function

For each output variable, the different polynomial candidates are generated in a step-by-step way, according to the following rules:

Rule 1: All the terms of a given order have to be considered and the corresponding models have to be evaluated before “exploring” an upper order.

Rule 2: In each order, only the terms that increase the quality of the fit are retained.

Table 5.2 below reports the different terms corresponding to orders 1, 2 and 3 considered for model evaluation purposes during the calibration of the 3-DOF robot.

These terms were actually considered in the configurations “Serial 1”, “Serial 2”, “Parallel” and “Without IGM” reported in **Figure 5.6**.

Order 0	c_0
Order 1	$c_1 \cdot X + c_2 \cdot Y + c_3 \cdot Z$
Order 2	$c_4 \cdot X^2 + c_5 \cdot Y^2 + c_6 \cdot Z^2 + c_7 \cdot X \cdot Y + c_8 \cdot X \cdot Z + c_9 \cdot Y \cdot Z$
Order 3	$c_{10} \cdot X^3 + c_{11} \cdot X^2 \cdot Y + c_{12} \cdot X^2 \cdot Z + c_{13} \cdot X \cdot Y^2 + c_{14} \cdot Y^3 + c_{15} \cdot Y^2 \cdot Z$ $+ c_{16} \cdot X \cdot Z^2 + c_{17} \cdot Y \cdot Z^2 + c_{18} \cdot Z^3$

Table 5.2 – Polynomial terms corresponding to orders 0, 1, 2 and 3 studied during the calibration of the 3-DOF robot.

The calculation of the different polynomial coefficients was performed using a standard least-squares regression in the framework of the *Optimization Toolbox*[®] of *MatLab*[®] [Col06].

A simple cross-validation is performed on the original data in order to obtain 3 different subsets (each one being representative of the whole data “diversity”).

The first one (called *calculation set*), composed of 80 % of the original data, is used to perform the least-squares estimate of the model coefficients. The second subset (called *validation set*) comprises 16 % of the original samples and is used to evaluate the performance of the different terms of the polynomial in order to decide if a given term will be kept or rejected. The last subset (called *test set*) is used to display the final calibration results.

The following sections present the calibration results of the 3 and 6 DOF robots measured in this thesis obtained when polynomial functions are used for processing the data.

5.4 – Correcting the pose of the 3-DOF robot

This section presents the results obtained for the calibration of the 3-DOF robot measured in this thesis using multi-variable polynomial functions for data processing.

The **first paragraph** reports the results obtained with the real data collected on the robot.

The **second paragraph** proves the robustness of this polynomial-based approach. Several issues are investigated in order to provide an answer to the following questions:

How is the accuracy of the model affected by *measurement noise* on the data used to calculate the coefficients?

Can the model deal with *modifications in the geometric dimensions* of the robot coming from manufacturing tolerances?

How does the accuracy of the model vary with the *number of points* used to calculate the coefficients?

5.4.1 – Working with measurement data

(a) Results obtained “off-line”

Following the approach described in the **paragraph (c)** of **Section 5.3.2**, we tried to find the functions able to predict the data collected on the 3-DOF robot within the highest accuracy.

The different configurations listed in **Figure 5.6** were considered for this purpose. First, the five configurations in which there is an interaction with the IGM of the robot: *Serial 1*, *Serial 2*, *Serial 3*, *Serial 4* and *Parallel*; second, the configuration in which the polynomial function has to predict by itself the full articular-operational mapping without the help of the IGM (*Without IGM*).

The data set used for the calculation of the model coefficients contained $19^3 = 6'859$ points uniformly distributed over the robot workspace (3D regular grid with the following coordinates in each axis [mm]: $\pm 1.8, \pm 1.6, \pm 1.4, \pm 1.2, \pm 1, \pm 0.8, \pm 0.6, \pm 0.4, \pm 0.2$ and 0).

For each of the 6 error correction configurations, a full evaluation of the different polynomial functions was performed up to the 3rd order and the best results found for each order are reported in **Table 5.3**. Notice that the values in this table are the errors corresponding to the predictions for the new points in the test set after the coefficients of the polynomials had been identified (“off-line” situation).

Several important conclusions can be drawn from the results of **Table 5.3**:

- multi-variable polynomial functions can always approximate the desired input-output mapping for the calibration of this 3-DOF robot up to accuracies close to the resolution of the robot. This conclusion is valid for different configurations that may be used for data processing tasks (see **Figure 5.6**);
- in particular, it is possible to approximate the direct correspondence between the motor and the operational coordinates of the robot in the absence of the IGM (case “Without IGM” in **Figure 5.6**). We believe that this result is of prime importance since it means that it is possible to calibrate this robot even if the sources of inaccuracy cannot be modelled (because they have

not been directly identified or because they are difficult to model), and also if the nominal geometry of the robot remains unknown.

Notice that the “complexity” of the polynomial dealing with the “Without IGM” configuration is much higher than in the remaining configurations.

This is due to the fact that, in the former, the function has to learn not only the fine corrections in respect to the IGM, but also the approximate positioning of the robot (task previously “delegated” to the IGM).

Therefore, we can see that 2nd order polynomials are adequate if the aim is to obtain errors below ± 100 nm for the 5 configurations using the information provided by the IGM whereas 3rd order terms have to be considered if a similar accuracy is sought in a “pure-polynomial” approach.

Configuration	Best off-line error at ORDER 1 ($U_{90\%}$) [nm]	Best off-line error at ORDER 2 ($U_{90\%}$) [nm]	Best off-line error at ORDER 3 ($U_{90\%}$) [nm]
<i>Serial 1</i>	± 991	± 41	± 22
<i>Serial 2</i>	± 991	± 41	± 25
<i>Serial 3</i>	± 702	± 30	± 23
<i>Serial 4</i>	± 702	± 30	± 24
<i>Parallel</i>	± 562	± 32	± 19
<i>Without-IGM</i>	$\pm 32'800$	± 633	± 27

Table 5.3 – Prediction capabilities of the best (over the 3 directions) multi-variable polynomials found (for each order) for the calibration of the 3-DOF robot using real data. The errors displayed were obtained exclusively from **off-line calculations**.

(b) Results obtained “in-line”

In order to evaluate the accuracy obtained after the calibration of this robot *in real experimental conditions* (“in-line” situation), the “best” polynomial functions calculated previously were implemented in the robot controller and their prediction for new points never seen during calibration was compared to the corresponding reading of the laser interferometer.

The errors were found to be within approximately ± 50 nm ($U_{90\%}$) when the interferometer was verifying an axis for which the optical head had not to be re-mounted in respect to the measurements taken for calibration, and ± 100 nm ($U_{90\%}$) otherwise.

On the one hand, the difference between the errors obtained *off-line* and those obtained *in-line* is mainly due to the limited accuracy of the measuring system and to a slight difference between the environmental conditions corresponding to the measurements taken *during* the calibration session and those performed *after* the calibration, for the purpose of validation.

On the other hand, we believe that the discrepancy between the ± 50 nm and ± 100 nm for the *in-line* case is mainly due to the tolerance (estimated to be within ± 1 mm) with which the beam of the interferometer can be centered on the surface of the cube over successive adjustments. In fact, the influence of the residual passive rotations experienced by the robot end-effector on the interferometer reading takes place *via* this tolerance (see **Section 4.2.2** and **Appendix B**).

5.4.2 – Working with simulation data

(a) Data sets, conditions and assumptions of the simulations

The aim of this section is to prove the effectiveness of the polynomial-based approach to the calibration of this robot.

For this purpose, the original function to be modelled had to be known beforehand. We chose to use the IGM to generate a set of operational coordinates-motor coordinates pairs, assumed to fully represent the behaviour of a 3-DOF robot being calibrated.

The data set generated by the IGM was distributed as follows:

- **DATA SET:** 3D regular grid with the 11 following coordinates in each axis [mm]: $\pm 2, \pm 1.8, \pm 1.6, \pm 1.4, \pm 1.2, \pm 1, \pm 0.8, \pm 0.6, \pm 0.4, \pm 0.2$ and $0 \rightarrow 21^3 = 9'261$ points.

We found that the best 3rd order polynomial could approximate the previous data within less than ± 28 nm of error ($U_{90\%}$).

(b) Sensitivity to measurement noise

In order to study the effect that measurement noise had in the data collected from a robot being calibrated on the corresponding calibration results, a zero-mean Gaussian signal was added to the end-effector coordinates of the previous data set.

Three different noise amplitudes were considered for this study: 25 nm, 50 nm and 100 nm.

Table 5.4 reports, for these three cases, the errors (relatively to the output of the IGM) in the prediction of new points when the polynomial coefficients are calculated with the help of the noisy data.

Noise amplitude [nm]	Prediction error ($U_{90\%}$) [nm]
<i>0 (nominal case)</i>	± 28
<i>25</i>	± 33
<i>50</i>	± 53
<i>100</i>	± 84

Table 5.4 – Simulation of the effect of a measurement noise in the calibration of the 3-DOF robot.

From the results of this table, we can see that the error attainable in the prediction is limited by the measurement noise in the data used to identify the coefficients of the polynomial. This agrees with logical expectations.

(c) Sensitivity to modifications in the robot geometry

The robustness of a given method used for data processing tasks in the calibration of a given robot also lies in the ability to correct for slight modifications in the robot geometry due to tolerances in the manufacturing process.

In order to investigate this issue, the nominal values of the geometric parameters of the IGM were modified by $\pm 10 \mu\text{m}$ (typical range of manufacturing errors).

The modifications considered were the following:

- *modification 1*: lengths of all the robot arms = nominal length + $10 \mu\text{m}$;
- *modification 2*: lengths of all the robot forearms = nominal length + $10 \mu\text{m}$;
- *modification 3*: lengths of all the robot arms = nominal length + $10 \mu\text{m}$
AND
lengths of all the robot forearms = nominal length + $10 \mu\text{m}$.

Table 5.5 reports, for each case, the errors (relatively to the modified IGM) in the prediction of new points when the model coefficients are calculated with the help of the modified data.

Geometric modification	Prediction error ($U_{90\%}$) [nm]
<i>0 (nominal case)</i>	± 28
<i>Modification 1</i>	± 29
<i>Modification 2</i>	± 28
<i>Modification 3</i>	± 28

Table 5.5 – Effect of modifications in the robot geometry coming from manufacturing errors in the calibration of the 3-DOF robot.

It can be seen that the polynomial is still able to compensate for the effect of the simulated modifications within the same accuracy of the nominal case, which again proves the effectiveness of this approach.

(d) Sensitivity to the number of calculation points

Finally, focus was given to the effect of the number of points used for the calculation of the polynomial coefficients on the accuracy of the corresponding model.

Of the different cases in **Figure 5.6**, only the configurations “Parallel” and “Without IGM” were considered, since they are the most commonly used and/or the most easy to implement from a practical point of view.

In order to perform a simulation as close as possible to a real calibration experiment, we used the data collected from the 3-DOF robot (6'859 points) to identify, for each configuration, the coefficients of the model that was subsequently used to generate the data for the simulations⁸.

⁸ Unlike paragraphs (b) and (c), in which the *nominal IGM* was used to generate the data for the simulations.

After the models had been identified for each configuration, three different data sets were generated. These were regular grids covering the full workspace of the robot and having the following divisions in each axis (in [mm]):

- **Set 1:** $\pm 2, \pm 1$ and 0 $\rightarrow 5^3 = 125$ points
- **Set 2:** $\pm 2, \pm 1.5, \pm 1, \pm 0.5$ and 0 $\rightarrow 9^3 = 729$ points
- **Set 3:** $\pm 2, \pm 1.6, \pm 1.2, \pm 0.8, \pm 0.4$ and 0 $\rightarrow 11^3 = 1'331$ points

For each configuration, three new different models were identified from each previous data set and the responses of these new models were compared, for a set of new positions, to the corresponding prediction given by the model identified using the real robot data. The resulting errors are reported in **Table 5.6**.

Configuration	Prediction error ($U_{90\%}$) obtained for different data sets used to identify the polynomial coefficients [nm]		
	Set 1 (125 points)	Set 2 (729 points)	Set 3 (1'331 points)
<i>Parallel</i>	± 106	± 21	± 17
<i>Without-IGM</i>	± 80	± 37	± 21

Table 5.6 – Effect of the number of points used for a realistic calibration of the 3-DOF robot.

A major conclusion that can be drawn from the results of this Table is that 125 points are already enough for obtaining the desired accuracy in the calibration of this robot, not only if the polynomial has to compensate for the errors of the IGM (case “Parallel”), but also if it has to predict by itself the “full” articular-operational mapping of the robot (case “Without-IGM”).

5.5 – Correcting the pose of the 6-DOF robot

This section focuses on the calibration of the 6-DOF robot measured in this thesis, using multi-variable polynomials for error correction purposes.

The **first part** presents the results with the real data collected from the robot. Since the measuring procedure of this robot comprises three different phases (see **section 4.3.1**), results are reported and discussed separately for each phase.

The **second part** investigates through simulation the effectiveness of this polynomial-based method following the same approach of the previous paragraph.

5.5.1 – Working with measurement data

(a) Results obtained for phase 1 (angles)

In phase 1, two different data sets were considered for data processing purposes.

■ The first set comprised only “**small angles**” (within the primary range of the autocollimators and measured directly on the mirror cube).

The poses measured in this set had the following operational coordinates, according to the IGM: $(X, Y, Z, \theta_X, \theta_Y, \theta_Z)$ for which:

- the *translations* X, Y, Z = origin $(0\ 0\ 0)$ + vertexes of the cubes at $\pm 1.6\text{ mm}$, $\pm 1.2\text{ mm}$, $\pm 0.8\text{ mm}$ and $\pm 0.4\text{ mm}$ (33 centres of rotation⁹);
- the *rotations* $\theta_X, \theta_Y, \theta_Z$ had the values of ± 300 , ± 200 , ± 100 and 0 arcsec .

The total number of points of this set was therefore $33 \times 7^3 = 11'319$.

■ The second set was composed of poses having “**large angles**” (measured on the faces of the polygon prisms) + the poses of the first set. The new poses were distributed as follows:

- *translations* X, Y, Z = origin $(0\ 0\ 0)$ + vertexes of the cubes at $\pm 1.6\text{ mm}$, $\pm 1.2\text{ mm}$, $\pm 0.8\text{ mm}$ and $\pm 0.4\text{ mm}$ (33 centres of rotation);
- *rotations* $\theta_X, \theta_Y, \theta_Z$ = only 1 “large angle” varying per time as follows:

$-3^\circ - 150\text{ arcsec}$	-3°	$-3^\circ + 150\text{ arcsec}$
$-1.5^\circ - 150\text{ arcsec}$	-1.5°	$-1.5^\circ + 150\text{ arcsec}$
$+1.5^\circ - 150\text{ arcsec}$	$+1.5^\circ$	$+1.5^\circ + 150\text{ arcsec}$
$+3^\circ - 150\text{ arcsec}$	$+3^\circ$	$+3^\circ + 150\text{ arcsec}$

while the two remaining angles could take the values: 0 and $\pm 150\text{ arcsec}$.

The effective number of poses involving “large angles” is then $33 \times (3 \times 12 \times 3^2) = 29'700$ which brings the total number of different poses of the second set to approx. $41'000$ points

a.1 – Results obtained “off-line”

Following the approach reported in **paragraph (c) of Section 5.3.2**, we attempted to approximate the second data set (which covers a larger part of the workspace of this robot than the first set) using multi-variable polynomials.

⁹ The spatial distribution of these centres of rotation is illustrated in **Figure 4.15 of Section 4.3.1**.

All the configurations of **Figure 5.6** were considered for this purpose: five configurations in which the approximating function has an interaction with the IGM (*Serial 1*, *Serial 2*, *Serial 3*, *Serial 4* and *Parallel*) and the case dealing with the full motor-operational mapping without the help of the IGM (*Without-IGM*).

For each configuration, the evaluation of the prediction capability of the different polynomial candidates was performed up to *order 4*. The best results obtained for each order in these “off-line” calculations are reported in **Table 5.7** below.

Configuration	Best off-line error at ORDER 1 (U _{90%}) [arcsec]	Best off-line error at ORDER 2 (U _{90%}) [arcsec]	Best off-line error at ORDER 3 (U _{90%}) [arcsec]	Best off-line error at ORDER 4 (U _{90%}) [arcsec]
<i>Serial 1</i>	± 3.3	± 0.86	± 0.43	± 0.32
<i>Serial 2</i>	± 3.2	± 0.86	± 0.43	± 0.32
<i>Serial 3</i>	± 3.3	± 0.82	± 0.78	± 0.31
<i>Serial 4</i>	± 3.3	± 0.82	± 0.56	± 0.29
<i>Parallel</i>	± 3	± 0.86	± 0.43	± 0.34
<i>Without-IGM</i>	± 5.5	± 1.12	± 0.43	± 0.33

Table 5.7 – Prediction capabilities of the best (over the 3 directions) multi-variable polynomials found (for each order) for the calibration of the *angular* motions of the 6-DOF robot (phase 1). The errors displayed were obtained exclusively from **off-line** calculations.

A careful observation of the results of this table yields the following conclusions:

- multi-variable polynomial functions are well-adapted for the calibration of the angular coordinates of this robot. In fact, it is always possible to find a polynomial that approximates the desired input-output mapping no matter which configuration is used for data processing tasks. Notice, however, that 4th order terms have to be considered in order to reach prediction errors close to the accuracy of the autocollimator (approx. ± 0.2 arcsec), instead of the 3rd order terms in the case of the 3-DOF robot (see **Table 5.3**). Of course, this is due to a higher coupling between DOF arising from the higher “structural complexity” of the 6-DOF robot relatively to the 3-DOF mechanism.
- as for the 3-DOF robot, the direct correspondence between the motor and operational coordinates (only angles in this phase) can be approximated without the help of the IGM, which means that the angles of this robot can be calibrated even if the nominal geometry of the manipulator remains unknown.

a.2 – Results obtained “in-line”

The previous polynomials were then implemented in the robot controller in order to evaluate *in real experimental conditions* (or “in-line”) the accuracy of the calibrated angles.

The robot was then set to poses not seen during calibration for which the prediction of the model was compared with the reading of the autocollimator. In cases involving exclusively “small angles” we found that the prediction errors were within ± **0.36 arcsec** (U_{90%}) and when “large angles” were verified, the error was up to ± **3 arcsec** (U_{90%}).

The reason for this difference lies in the fact that the measuring area used to read the “large angles” (surfaces of the polygon prisms) is more restricted (approx. by a factor of 10) than the one corresponding to the case of “small angles” (surfaces of the mirror cube). A complete evaluation of this effect has been presented in **paragraph (b)** of **Section 3.2.3** (see in particular **Figure 3.7**). Furthermore, the reflecting surfaces of the polygons are of poorer quality (flatness and reflectivity) than those of the mirror cube, thereby causing additional inaccuracy.

(b) Results obtained for phase 2 (translations)

b.1 – Results obtained “off-line”

The same work was carried out with the data collected in phase 2 (“pure-translational” poses).

The data set collected in this phase was composed of $21^3 = 9'261$ points uniformly spread over the robot translational workspace (with the following coordinates in each axis [mm]: $\pm 2, \pm 1.8, \pm 1.6, \pm 1.4, \pm 1.2, \pm 1, \pm 0.8, \pm 0.6, \pm 0.4, \pm 0.2$ and 0).

For each configuration of **Figure 5.6**, the best results obtained for the approximation of the data collected on the robot are reported in **Table 5.8**.

Configuration	Best off-line error at ORDER 1 ($U_{90\%}$)		Best off-line error at ORDER 2 ($U_{90\%}$)		Best off-line error at ORDER 3 ($U_{90\%}$)		Best off-line error at ORDER 4 ($U_{90\%}$)	
	transl. [nm]	rot. [arcsec]	transl. [nm]	rot. [arcsec]	transl. [nm]	rot. [arcsec]	transl. [nm]	rot. [arcsec]
<i>Serial 1</i>	$\pm 10'164$	± 3.37	± 185	± 0.61	± 133	± 0.49	± 42	± 0.27
<i>Serial 2</i>	$\pm 10'164$	± 3.40	± 185	± 0.61	± 120	± 0.49	± 48	± 0.29
<i>Serial 3</i>	$\pm 9'421$	± 3.31	± 179	± 0.59	± 126	± 0.61	± 51	± 0.28
<i>Serial 4</i>	$\pm 9'421$	± 3.31	± 180	± 0.61	± 134	± 0.56	± 44	± 0.29
<i>Parallel</i>	$\pm 9'750$	± 2.93	± 184	± 0.62	± 122	± 0.54	± 56	± 0.31
<i>Without-IGM</i>	$\pm 27'026$	± 3.31	± 480	± 1.51	± 135	± 0.55	± 54	± 0.29

Table 5.8 – Prediction capabilities of the best (over the 3 directions) multi-variable polynomials found (for each order) for the calibration of the *translational* motions of the 6-DOF robot (phase 2). The errors displayed were obtained exclusively from **off-line** calculations.

As for the previous paragraph, we can see that multi-variable polynomial functions can provide very good accuracies for the calibration of the translations of this robot. The “goodness” of these results can be seen not only in the accuracy of the translations but also in the angular accuracy at which the robot can execute new “pure-translational” motions.

The downside of this polynomial-approach is that 4th order terms have to be used if sub-100 nm accuracies are sought. This is again due to the “structural complexity” of this robot.

In comparison to the case of the 3-DOF robot, we can see that the off-line accuracy of the calibrated translations is slightly worse. We believe that this is the consequence of the limited accuracy of the corresponding measurements, certainly due to a measuring loop much longer for the 6-DOF robot than that of the 3-DOF robot (see **Figures 3.15** and **3.18**).

Lastly, note that the translations of this robot can also be calibrated without the help of the IGM.

b.2 – Results obtained “in-line”

An “in-line” evaluation of the previous results was carried out.

For each configuration, the responses of the best functions found previously were compared, for new “pure-translational” poses, to the corresponding reading given by the measuring devices (autocollimator and interferometer).

We found that the angular residues in these new “pure-translational” poses were within ± 0.3 arcsec ($U_{90\%}$) while, for translations, errors were within approximately ± 120 nm ($U_{90\%}$). As opposed to the 3-DOF robot, it should be noticed that unmounting and re-mounting the interferometer’s optical head for verification purposes does not affect the results in this case since the distances measured are now free of significant angular variations.

Finally, the reason for which the translational errors obtained here are higher than those obtained for the 3-DOF robot (in the situation without head removal) lies in a much longer measuring loop (resulting in poorer measuring accuracy).

(c) Results obtained for phase 3 (translations combined with rotations)

Finally, calculations were conducted with the full 6D data. For all the configurations of **Figure 5.6**, we found that the best polynomials comprising terms up to the 4th order were able to provide a “good” prediction accuracy for angles (same as in the previous phases) but poor accuracies for translations (approx. ± 400 nm within $U_{90\%}$).

We believe that there are two main reasons that may possibly explain the poor results obtained for translations:

- phase 3 utilizes three *Keyence*[®] laser sensors reading the position of a sphere. As mentioned in **section 3.2.2 of Chapter 3** and **section A.5 of Appendix A**, this configuration cannot be used for accurate distance measurements. It is in fact only valid for setting the position of the sphere always to the “zeros” of the three sensors simultaneously. However, thanks to residual temperature variations and to the limited threshold ϵ_{transl} adopted in the closed-loop, the accuracy of the “pure-translational” pose determined for each centre of rotation of phase 3 (and for which the three sensors read “zero” simultaneously at the beginning of the measurements) will slightly degrade as time progresses¹⁰;
- as mentioned in **paragraph (e) of section 4.3.1**, the main limitation of our 6D measuring procedure lies in the inevitable *uncertainty propagation* that takes place in the final phase, due to the use of models obtained at the end of phases 1 and 2 and which have a finite accuracy.

A simple test was carried out in order to evaluate the first effect and, therefore, to determine which accuracy could be expected after a calibration performed with these sensors. For this purpose, a set of data was collected from the robot using the three *Keyence*[®] sensors on which the end-effector was only allowed to turn around the same point in space¹¹ with different angular consigns (having unknown values).

¹⁰ As opposed to the measuring configurations in phases 1 and 2, residual thermal drifts in this phase cannot be cancelled simply through periodic returns to a reference position. The reason for this is the fact that the *Keyence*[®] sensors cannot be used to measure (and, therefore, to correct) distances since the laser beam is reflected on a spherical surface (see **section A.5 of Appendix A**). In the future, a possible solution to this problem could be a modification of the algorithm of phase 3 (described in page 71 of Chapter 4) in order to include several centres of rotation over the measurements made for each manual adjustment of the sensor’s optical heads. This solution was not implemented in our case since it would result in very large overall measuring times.

¹¹ In this test, we decided to use a position near the robot reference position (0 0 0 0 0 0).

We then tried to process this data in order to find a polynomial that would permit the robot to turn around the same centre of rotation but with new (unknown) angular consigns. We found that the best polynomial (4th order) could only achieve new rotations around the previous centre within an error in residual translations ± 200 nm ($U_{90\%}$).

The results of this section prove that we are only limited by the accuracy of the measurement procedure used to collect the data from the robot and not by the method used for processing this data.

In other words, the calibration of the translations and rotations of this robot within the desired accuracy was, in our case, only possible if these degrees of freedom were taken separately (3D calibrations).

5.5.2 – Working with simulation data

(a) Data sets, conditions and hypothesis of the simulations

The aim of this section is to demonstrate the effectiveness of our polynomial-based method for the calibration of the 6-DOF robot. In this section, we restrict ourselves to the case of the translations, since we believe this is enough for our purpose.

For the simulations reported in this section, we assumed that *the IGM represented the behaviour of a 6-DOF robot being calibrated*. The IGM was therefore used to generate the necessary data.

This data set was composed of the same points as those measured in phase 2 of the previous section: a 3D regular grid with the following divisions in each axis [mm]: $\pm 2, \pm 1.8, \pm 1.6, \pm 1.4, \pm 1.2, \pm 1, \pm 0.8, \pm 0.6, \pm 0.4, \pm 0.2$ and $0 \rightarrow 21^3 = 9'261$ points.

We found that a 3rd order polynomial was able to fit this data within less than ± 15 nm of error.

(b) Sensitivity to measurement noise

In order to simulate the effect of a measurement noise, a zero-mean Gaussian signal was added to the end-effector coordinates of the previous data set.

Three different noise amplitudes were considered for this study: 25 nm, 50 nm and 100 nm.

For each case, the coefficients of the previous polynomial were calculated from the corresponding noisy data set and the accuracy of the obtained models was compared to that of the nominal IGM, for a set of new positions. **Table 5.9** reports the results of this comparison.

Noise amplitude [nm]	Prediction error ($U_{90\%}$) [nm]
<i>0 (nominal case)</i>	± 15
<i>25</i>	± 20
<i>50</i>	± 41
<i>100</i>	± 76

Table 5.9 – Effect of a measurement noise on the calibration of the 6-DOF robot.

As for the 3-DOF robot, these results once more prove that the attainable errors in the calibration are limited by the amount of noise in the data used to process the model.

(c) Sensitivity to modifications in the robot geometry

Focus was given to the influence of a modification in the geometry of the robot coming from manufacturing tolerances.

This effect was simulated by modifying the nominal values of the IGM parameters. The data used for the calculations of the polynomial coefficients was then re-generated from the modified model.

Three different modifications were considered:

- *modification 1*: lengths of all the robot arms = nominal length + 10 μm ;
- *modification 2*: lengths of all the robot forearms = nominal length + 10 μm ;
- *modification 3*: lengths of all the robot arms = nominal length + 10 μm
AND
lengths of all the robot forearms = nominal length + 10 μm .

For each case, the coefficients of the polynomial were calculated from these data sets and the response of the corresponding model was compared, for a set of new positions, with that of the model used to generate the corresponding data set. Results are reported in **Table 5.10**.

Geometric modification	Prediction error ($U_{90\%}$) [nm]
<i>0 (nominal case)</i>	± 15
<i>Modification 1</i>	± 21
<i>Modification 2</i>	± 18
<i>Modification 3</i>	± 19

Table 5.10 – Illustration of the effect of a modification in the robot geometry in the calibration of the 6-DOF.

We can establish from these results that the model used can also account for modifications in the geometry of the robot being calibrated, which again proves its effectiveness.

(d) Sensitivity to the number of calculation points

Finally, attention was paid to the effect of the size of the data set (number of points) used to calculate the polynomial coefficients in the accuracy of the corresponding model.

We decide to focus exclusively on the configurations “Parallel” and “Without-IGM” among the different schemes of **Figure 5.6**. In fact, from the practical point of view, these are the most interesting cases to study.

In order to perform a simulation close to the reality of the calibration of this robot, we used the real data collected on the robot (*phase 2*), rather than the IGM, to identify the model that would then be used to generate the data for the simulations.

Three different data sets were generated for each configuration (having the following divisions in each axis, in [mm]):

- **Set 1:** $\pm 2, \pm 1$ and 0 $\rightarrow 5^3 = 125$ points
- **Set 2:** $\pm 2, \pm 1.5, \pm 1, \pm 0.5$ and 0 $\rightarrow 9^3 = 729$ points
- **Set 3:** $\pm 2, \pm 1.6, \pm 1.2, \pm 0.8, \pm 0.4$ and 0 $\rightarrow 11^3 = 1'331$ points

For each configuration, the coefficients of the polynomial were then re-calculated from the previous data sets and the output of the corresponding models was compared, for a set of new positions, to the output of the model identified with the help of the real robot data. The resulting errors are reported in **Table 5.11**.

Configuration	Prediction error ($U_{90\%}$) obtained for different data sets used to identify the polynomial coefficients [nm]		
	Set 1 (125 points)	Set 2 (729 points)	Set 3 (1'331 points)
<i>Parallel</i>	± 92	± 48	± 32
<i>Without-IGM</i>	± 108	± 67	± 42

Table 5.11 – Illustration of the effect of the number of points in a realistic calibration of the 6-DOF robot.

These results principally show that, even if the prediction capability of the polynomial used for calibration depends on the number of points used to calculate the coefficients, 125 points are in general sufficient for obtaining accuracies within ± 100 nm.

This is valid not only for a case where the polynomial only compensates the errors of the IGM (“Parallel” configuration) but also if it has to deal with the full articular-operational mapping (“Without-IGM” configuration).

5.6 – Industrial success of the model-based approach

The effectiveness of the model-based approach presented in this thesis for the calibration of high-precision flexure parallel robots can be seen not only from the results reported in **Sections 5.4** and **5.5** of this report but also from the success of its implementation on genuine industrial flexure parallel robots.

In fact, the use of multi-variable polynomial functions is now a common and well-established method employed by our industrial partner¹² for the calibration of recent prototypes of the 3-DOF robot studied in this thesis (**Figure 5.7**). These robots are now being commercialized by AGIE S.A. as new μ -EDM machines able to provide unprecedented accuracies (at the sub- μ m scale) over limited ranges (up to 10 mm).

Thanks to this approach, results similar to those presented in **Section 5.4.1** have recently been obtained over successive calibration experiments conducted with the two robots depicted in **Figure 5.7**.

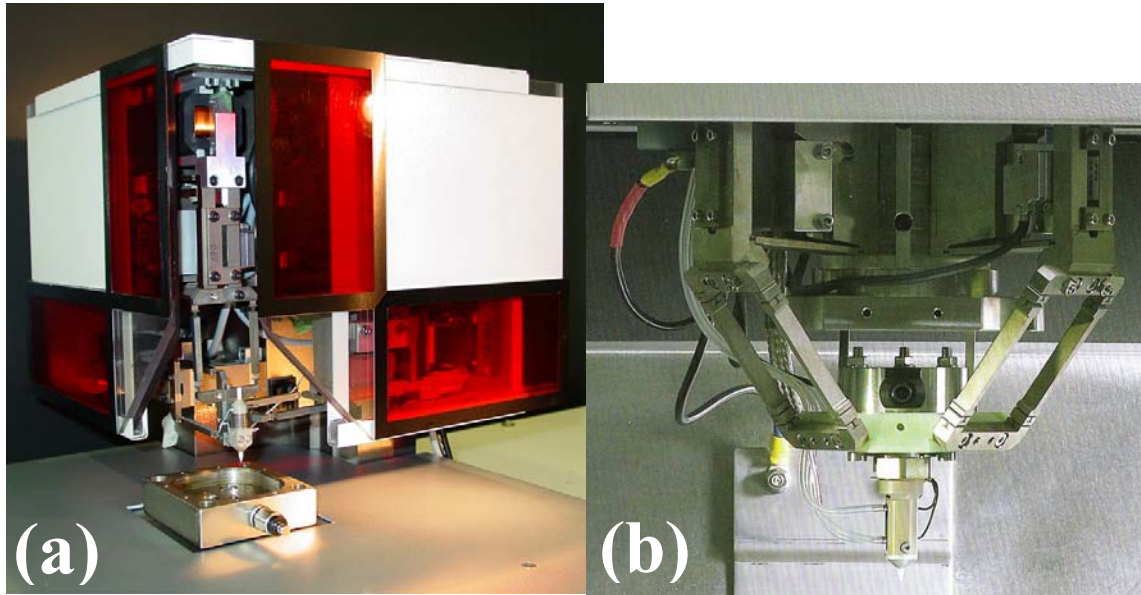


Figure 5.7 – Recent prototypes of the 3-DOF “Delta Cube” high-precision flexure parallel robot ((a): *Delta Cube 3* and (b): *Delta Cube 4*) currently used and marketed by AGIE S.A. as new μ -EDM machines offering sub- μ m accuracies over a limited range.

¹² AGIE S.A. – Via dei Pioppi 2, CH-6616 Losone (TI), Switzerland

5.7 – Conclusion

This chapter provided a model-based approach for processing the data in order to correct the pose errors in a robot calibration procedure.

The relevant points of this chapter are the following:

- We show that behavioural models are preferable to physical models for the calibration of a given multi-DOF high-precision flexure parallel robot. In particular, *multi-variable polynomial functions* are able to meet the desired accuracy requirements for the calibration of these robots. This presents the major advantage of not requiring a direct modelling of the different physical sources of inaccuracy of the robot being calibrated.

- The downside in the use of polynomial fitting in function approximation problems is that the solution is highly oscillatory (*overfitting*), especially if high-order models are employed. This problem can be avoided through a proper model choice and a continuous monitoring of its generalization capability on the basis of a *cross-validation* performed on the available data.

- It is possible to approximate, for the two robots measured in this thesis, the full motor-operational mapping within the desired accuracy (and not only the errors between the real robot and the IGM). This means that the calibration of a given multi-DOF flexure parallel robot can still be carried out even if the nominal geometry of the robot remains unknown.

- The active degrees of freedom of the 3-DOF were calibrated within ± 100 nm. When taken separately, the translational motions of the 6-DOF robot were calibrated within ± 120 nm and the angular motions within ± 0.36 arcsec (case of “small angles”) and ± 3 arcsec (case of “large angles”).

The accuracy of translations worsens (up to ± 400 nm) if we work directly with the 6D data assembled. This is due to the uncertainty propagation involved in the final phase of the 6-DOF calibration procedure as well as to issues related to the use of the three *Keyence*[®] laser sensors in that phase (limited closed-loop threshold and no compensation of the residual thermal drift).

- The effectiveness of our polynomial-based calibration method is proved with the help of simulation data. We tested in particular the effects of measurement noise, the number of points used for the calculation of the model coefficients and the errors in the geometry of the robot due to manufacturing tolerances.

Chapter 6 – Model-free approach to pose correction

6.1 – Introduction

In the case of a robot calibration problem solved by means of a *model-free* approach, the correction of the robot pose errors is performed in a “black-box” way. No knowledge (physical or behavioural-related) is provided on the sources of inaccuracy affecting the robot being calibrated.

Neural Networks (NN) are a common and widely used tool in standard black-box modelling problems.

This chapter deals with the use of NN in robot calibration.

Despite the fact that NN have already been applied in robot calibration problems by previous researchers, this thesis proposes new contributions in respect to published work:

- we propose an algorithm, based on a decision-tree scheme, for determining systematically the architecture of a network able to perform the approximation of a given input-output mapping within the desired accuracy and, therefore, able to correct the errors in the pose of any robot (not necessarily a high-precision flexure parallel robot);
- we prove through case-studies that it is possible to calibrate any high-precision flexure parallel robot even if its nominal geometry remains unknown. This result contradicts the conclusions of previous researchers [Gue88, Taw89 and Gar91].

We believe that this second result is a key contribution for robot calibration problems and hope that it will open new perspectives in this field.

The structure of this chapter is as follows. **Section 6.2** recalls some mathematical foundations of NN. **Section 6.3** provides some insight on how can NN be used for the calibration of a given robot.

Sections 6.4 and 6.5 report the calibration results of the 3 and 6-DOF robots measured in this thesis using NN-based techniques. Furthermore, the robustness of our approach is emphasized using simulation data.

Section 6.6 proves the universality of our neural calibration method by presenting the results of calculations performed with the data collected on robots other than those measured in this work. Finally, **section 6.7** summarizes the main results and concludes the chapter.

6.2 – What is a Neural Network?

6.2.1 – A brief reminder on the theory of Neural Networks

The human brain can be seen as a highly complex, non-linear and parallel computer. It has the capability to organize its structural constituents known as *neurons* (**Figure 6.1**) so as to perform certain computations many times faster than the fastest digital computer in existence today.

*Artificial Neural Networks*¹ (ANN) have been developed in order to mimic the way in which the brain works. The recent developments in ANN and their use in many engineering domains are mainly due to their computing power (based on a massively parallel distributed structure) and their ability to learn and generalize and, hence, the capacity to solve complex (large-scale) problems.

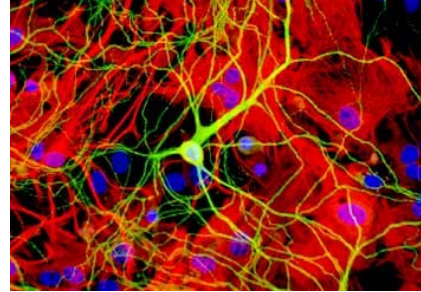


Figure 6.1 – Image of a human neuron.

Several definitions can be assigned to Neural Networks. We will adopt the general definition proposed by Haykin [Hay99]:

“A Neural Network is a machine that is designed to model the way in which the brain performs a particular task or function of interest”.

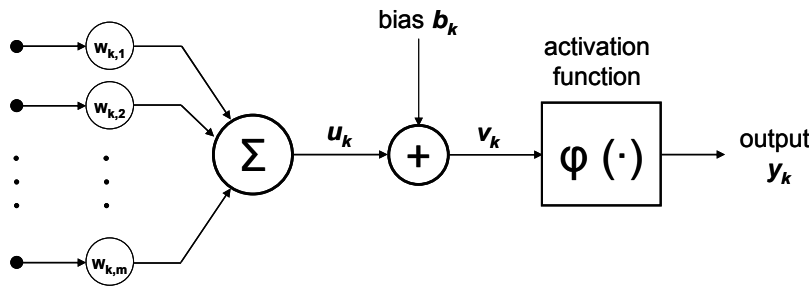


Figure 6.2 – Mathematical model of a neuron.

A *neuron* is the basic information-processing unit used to build Neural Networks.

It is composed of three main elements:

1. a set of **synapses** or connecting links, each of which is characterized by a **weight** or strength of its own. Specifically, a signal x_j at the input of synapse j connected to neuron k is multiplied by the synaptic weight $w_{k,j}$;
2. an **adder** for summing the input signal, weighted by the respective synapses of the neuron;
3. an **activation** or **transfer function** for limiting the amplitude of the neuron's output. The **bias** has the effect of increasing or lowering the network input of the activation function, depending on whether it is positive or negative, respectively.

¹ For the sake of clarity, the term “Artificial Neural Network” (ANN) will be replaced by “Neural Network” (NN).

In mathematical terms, a neuron (**Figure 6.2**) can be described by the following pair of equations:

$$u_k = \sum_{j=1}^m w_{k,j} x_j \quad \text{and} \quad y_k = \varphi(u_k + b_k) \quad (\text{eq. 6.1})$$

where

- $\{x_i\}_{1 \leq i \leq m}$ are the input signals;
- $\{w_{k,j}\}_{1 \leq j \leq m}$ are the synaptic weights of the neuron k ;
- u_k is the linear combiner output of the input signals;
- b_k is the bias;
- $\varphi(\cdot)$ is the activation function;
- y_k is the output signal of the neuron.

The use of the bias has the effect of applying an affine transformation to the output u_k of the linear combiner in the model in **Figure 6.2**, as shown by:

$$v_k = u_k + b_k \quad (\text{eq. 6.2})$$

A *Neural Network* (NN) is a group of neurons connected in an appropriate way forming different *layers* (**Figure 6.3**). The layers between the input and output layers are called *hidden layers*.

The role of the hidden neurons is to give the network the possibility of extracting high-order statistics.

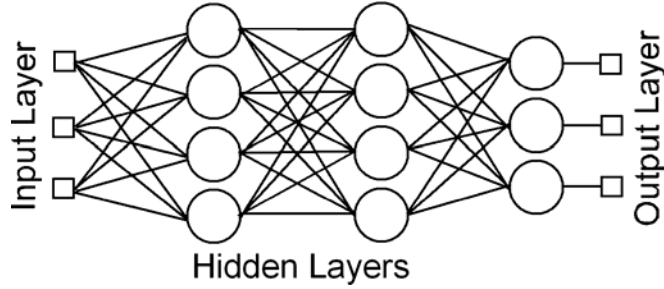


Figure 6.3 – Representation of a [4 4 3] feedforward NN.

This characteristic is particularly valuable when the size of the input layer is large.

In this work, we shall restrict ourselves to the case of *feedforward* NN. In such networks, the information moves in only 1 direction, forward, from the input nodes, through the hidden nodes and up to the output nodes. There are no cycles or loops.

One of the most important properties of a NN is the ability to learn from its environment.

In order to give the network good prediction capability, it has to go through a *training phase* in which a *learning algorithm* is used.

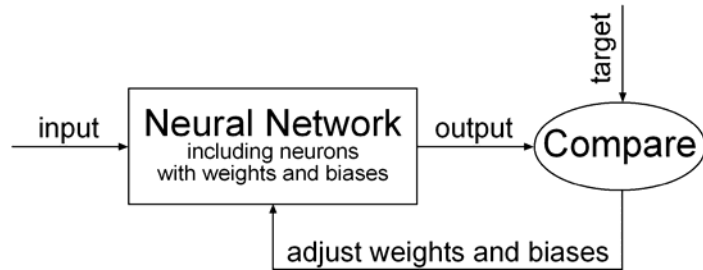


Figure 6.4 – Training of a feedforward neural network.

During this process, the free parameters of the network (the weights $w_{k,j}$ and the biases b_k of equation 6.1) are adapted iteratively through optimization schemes by comparing the network output to the target that has to be predicted (**Figure 6.4**).

The most commonly used training scheme is the *back-propagation algorithm* proposed by Rumelhart [Rum86] in which the network coefficients are adjusted by error-derivative vectors propagated backwards through the network, from the output nodes to the inner nodes.

Convention:

Throughout this work, we will adopt the same convention as that of the *Neural Network Toolbox*[®] of *MatLab*[®] [Dem06] for representing the architecture of a given network:

[number of neurons in the 1st hidden layer; number of neurons in the 2nd hidden layer; ; number of neurons of the output layer].

According to this convention, the architecture represented in **Figure 6.3** is therefore that of a [4 4 3] feedforward NN.

Because of their ability to learn the correspondence between input-output data, NN have been widely used in function approximation problems over the past 20 years.

6.2.2 – Using Neural Networks in function approximation problems

(a) Universal approximation capability

■ In recent years, the question of the approximation of real-valued functions using feedforward NN has been addressed by a variety of researchers [Fun89, Hor89 and Hor91] (this list is by no means complete!).

Funahashi's work [Fun89] proved that feedforward networks with as little as one hidden layer are capable of approximating any continuous real-valued function if sigmoid² functions are used in the hidden units and linear activation functions are used in the input and output layers.

Later, Hornik [Hor91] extended this result and proved that multilayer feedforward networks are universal approximators under very weak assumptions on the activation functions.

This author concluded that it is not the specific choice of the activation function, but rather the multilayer feedforward architecture itself which gives NN the potential for being universal learning machines.

■ Despite the existence of a variety of theoretical evidence establishing this universal approximation capability, very little attention has been paid so far to the practical aspects of the NN-based approximation process.

In particular, networks with a single hidden layer suffer from the fact that the neurons therein tend to interact with each other globally in such a way that, in approximation problems, it is difficult to improve the approximation at one point without worsening it at some other point [Che90]. Consequently, it is well recognized that working with networks with at least 2 hidden layers makes the approximation process more manageable from a practical computational point of view.

² The exact definition of the term “sigmoid” varies from author to author. In Funahashi's paper [Fun89], a *sigmoid* is considered to be a bounded and monotonic increasing differentiable function.

Moreover, networks whose existence is guaranteed by theorems may require a prohibitively long time to compute, or worse, they may not be computable at all.

In practice, since it is extremely difficult to know which network architecture should be employed for a given problem, networks that have to approximate some desired input-output mapping are built using either *constructive* or *pruning* procedures [Kwo95].

In the former, a small network is trained and then additional hidden units and weights are added *ad libitum* until a satisfactory solution is found. In the latter, a very large network is trained and, once an acceptable solution is found, hidden units or weights are removed if they are no longer actively used.

In general, no procedure dominates the others over all potential target functions.

Finally, a proper and accurate approximation also has to counter overfitting issues.

Remark: The universal approximation capability of feedforward NN includes, in particular, the possibility of predicting discontinuities or hysteretic behaviour which may occur in standard robot calibration problems as well as in other engineering applications.

(b) Overfitting and underfitting

■ A critical issue in the use of NN in function approximation problems lies in the *generalization* capability: how well will the network make predictions for samples that are not in the training set?

As for other nonlinear regression methods, such as multi-variable polynomial functions (see **section 5.3.2**), NN can suffer from either underfitting or overfitting.

A network that is not sufficiently complex can fail to fully detect the signal in a complicated data set, leading to *underfitting*. A network that is too complex may fit the noise, not just the signal, leading to *overfitting*³.

Overfitting is especially dangerous because it can easily lead to predictions that are far beyond the range of the training data. It can also produce wild predictions in multilayer networks, even with noise-free data – see **Figure 5.5** in **section 5.3.2**.

■ The best method for improving network generalization is to use a network that is just large enough to provide an adequate fit.

In fact, the larger the network is, the more complex the functions that it can create. If a small enough network is used, it will not have enough “power” to overfit the data.

Unfortunately, it is very difficult to know beforehand how large a network should be for a specific application.

There are 2 other methods for improving generalization: *early-stopping* and *regularization*.

³ Overfitting is generally recognized to be a violation of *Ockham's razor*. The latter is a principle that states that unnecessarily complex models should not be preferred to simpler ones.

1) Early-Stopping:

The use of an early-stopping method involves dividing the available data into 3 subsets.

The first subset, called the *training set*, is used for updating the network weights and biases during the training process.

The second subset is the *validation set*. The error in the validation set is monitored during the training session: the validation error normally decreases during the initial phase of training (as does the training set error); however, when the network begins to overfit the data, the error in the validation set typically begins to rise – at that time the training is stopped.

The third subset, called the *test set*, is used to actually display the results after training, as it contains truly unseen samples.

This situation is depicted in **Figure 6.5**.

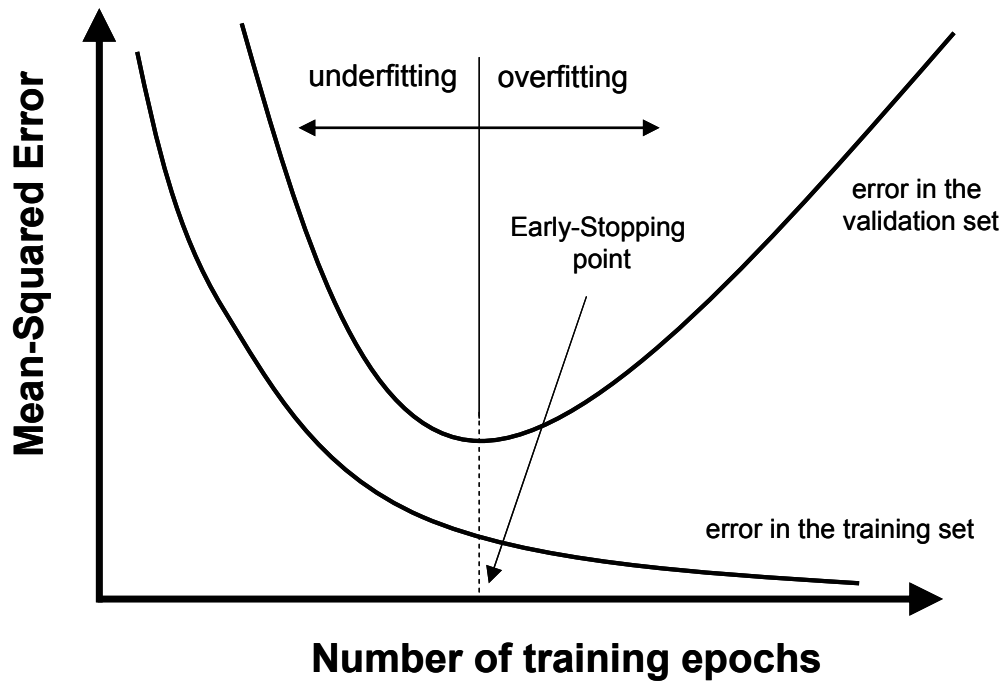


Figure 6.5 – Monitoring the network’s generalization capability using an **Early-Stopping** criterion. The training session is stopped at the minimum of the validation set error curve and the corresponding network weights and biases are recorded.

Remark: As we have mentioned in **section 5.3.2**, this technique of partitioning the original data into different subsets is commonly known as *cross-validation*.

The literature distinguishes different variants of this technique (especially when there is a scarcity of training samples, which is not our case). However, in this work, we will adopt the simplest type (hold-out cross-validation).

Our only requirements in the data division are therefore:

1. to use the majority of the data for training (at least two thirds) and
 2. to ensure that each subset is representative of the diversity of the original data.
-

2) Regularization:

A regularization method requires the modification of the cost function⁴, which is normally chosen to be the sum of squares of the network errors in the training set:

$$\mathbf{F} = \mathbf{E}_d = \frac{1}{N} \cdot \sum_{i=1}^N (\mathbf{e}_i)^2 \quad (\text{eq. 6.3})$$

It is possible to improve generalization if the previous cost function \mathbf{F} is modified by adding a term \mathbf{E}_w that consists of the mean of the sum of squares of the network weights and biases:

$$\mathbf{F} = \beta \cdot \mathbf{E}_d + \alpha \cdot \mathbf{E}_w \quad (\text{eq. 6.4})$$

Using this cost function causes the network to have smaller weights and biases, which forces the network response to be smoother and less likely to overfit.

The determination of the optimal values of these parameters α and β is a very complex and delicate problem for which a common approach used in engineering applications is the Bayesian framework of MacKay⁵ [McK, McK92 and references therein].

Remark: Originally proposed by Tikhonov [Tik63], the basic idea of regularization is to stabilize the solution by incorporating a certain prior knowledge into it.

In our case, the information provided lies in the assumption that the input-output mapping to be modelled is *smooth*. As we have seen in **section 5.2**, this assumption is in perfect accord with the reality of our robots.

Benchmark of these two methods, conducted in recent papers [Dem06 and Doa04], has shown that the Bayesian regularization approach performs better than early-stopping in most of the cases.

⁴ The *cost function* (also known as *objective* or *performance function*) is the function to be minimized during the training.

⁵ A detailed discussion of MacKay's Bayesian regularization method is beyond the scope of this work.

6.3 – Using Neural Networks in robot calibration

6.3.1 – Literature review

Although the era of NN started more than 60 years ago with the pioneering work of McCulloch and Pitts [MCu43], their use in robot calibration is less than 20 years old.

A literature review has shown 4 main methods of using feedforward NN for robot calibration tasks.

(a) – Learning the robot inverse model

In the earliest applications of NN in robot calibration, several researchers attempted to learn the IGM of robots using multilayered networks [Gue88, Taw89 and Gar91].

The major conclusion of these works was that the networks were able to reproduce the model only within quite limited accuracy (maximum with 1 % of the robot stroke).

(b) – Using networks combined with the nominal IGM

Seeing that networks were not able to predict as accurately as desired the direct mapping between the joint and world coordinates, other authors proposed to combine the use of NN with the nominal IGM of the robot. In this way, the network had only to learn the residual corrections to be made in order to reach the desired position.

This method is certainly the most commonly used in the literature [Jos87, Tak90, Koz90, Ren91, Wat92, Xu94, Lew94 and Zho94c].

However, different variants can be found, mainly depending on whether the error compensation occurs in the joint or in the operational space. **Figure 6.6** represents 4 different configurations used by previous researchers.

(c) – Using networks combined with previously identified analytical models

A third category of researchers [Mya92, Flu94, Tib03 and Wan05] extended the previous method by considering NN combined with realistic kinematic analytical models (instead of the nominal IGM). The parameters of these models had previously been identified using standard optimization algorithms in a separate preliminary calibration experiment.

The major advantage of this method lies in the fact that the network's approximation capability is now exclusively used for the correction (and suppression) of unmodelled error sources (usually of a non-geometric nature since, they are much more difficult to model than geometric errors). The calibration results are then expected to be better than in the previous approach. This has in fact been confirmed by the above authors.

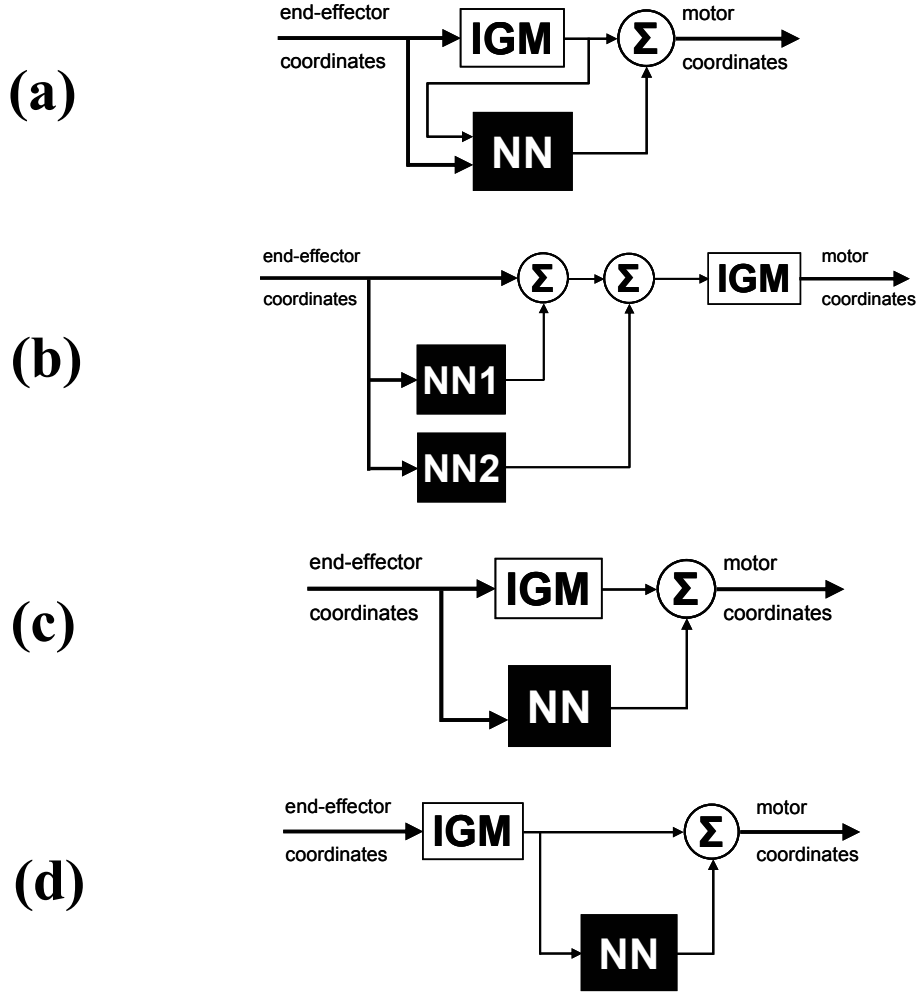


Figure 6.6 – Examples of different variants in which a NN is being used to correct the errors of the nominal IGM of the robot being calibrated. **(a)**: configuration used by Josin [Jos87], **(b)**: configuration adopted by Watanabe [Wat92] and Xu [Xu94], **(c)**: configuration used by Zhong [Zho94c] and **(d)**: configuration used by Takanashi [Tak90] and Lewis [Lew94].

(d) – Other approaches

The literature review revealed the existence of “exotic” approaches that could not be categorized with the above methods. We will present three of them.

As a follow-up of a previous paper, Zhong et al. [Zho94b] used NN (instead of standard linear or non-linear optimization algorithms) for the numerical identification of the D-H parameters in the kinematic model of the robot under calibration.

Dreiseitl [Dre97] presented a method for calibrating a robot composed of revolute joints only. The method consisted in “mapping” the kinematic equations of the robot into a NN representation. For this purpose, the robot kinematic equations were pre-processed through symbolic computation in order to be converted into a specific format (sum of sines) that was then implemented in a 2-layer feedforward NN with sinusoidal units.

Finally, Young [You99] used a *Fuzzy Cerebellar Model Articulation Controller* (FCMAC) learning algorithm for the implementation of a variable D-H kinematic model. The CMAC [Alb75 and Alb75b] is a primary form of a NN generally considered less sensitive to data paucity.

The goal of Young's work was to overcome the common problem of the local validity of the calibrated error parameters (CEP), so that different sets of CEP were calculated for different areas of the robot workspace in such a way that a better overall accuracy could be obtained.

(e) – Conclusions

A literature survey on the use of NN in robot calibration problems has led to the following conclusions:

- NN can only learn the IGM of a given robot within a very limited accuracy (maximum 1 % of the full stroke) which is in general not acceptable for calibration⁶;
- most researchers utilize NN for correcting errors of the nominal IGM. There are different variants of this correction corresponding to different input-output pairs to be learned by the network – however, the basic principle remains the same;
- there is no systematic or preferred method for determining of the architecture of a NN to be used in the calibration of a given robot. In general, the network architecture is determined on a “trial basis” by increasing either the number of neurons in a given hidden layer or the number of hidden layers until a satisfactory solution is found;
- most of the mechanisms studied are serial robots. The application of NN for the calibration of parallel kinematic machines has only been considered in quite recent studies [Yu05, Faz06 and Kuh06].

6.3.2 – Using Neural Networks in robot calibration

In this section, we will present the way in which NN have been used in this work for robot calibration.

Our contribution in respect to existing work lies exclusively in the implementation of an efficient **heuristic for the determination of the architecture** of a network able to provide a satisfactory accuracy for a given calibration problem.

The robustness of this heuristic, based on a decision-tree scheme, will be demonstrated in **sections 6.4** and **6.5** in which all the configurations reported in **Figure 5.6** will be considered for data processing (corresponding to different variants for the calibration of the same robot).

(a) – General properties of the networks used and training issues

The development, training and implementation of the different NN used in this thesis were performed in the framework of the *Neural Network Toolbox*[®] of *MatLab*[®] [Dem06].

The networks used were exclusively of the “feedforward” type having hyperbolic tangent activation functions (*MatLab*[®] function “tansig”) in all the hidden neurons and linear functions (*MatLab*[®] function ‘purelin’) in the input and output layers.

For training the networks, a particular version of the back-propagation algorithm was used.

⁶ The results presented in this thesis will actually contradict this conclusion.

This version, implemented in the *MatLab*[®] function “trainbr”, uses MacKay’s Bayesian regularization in combination with a Levenberg-Marquardt algorithm in order to update iteratively the network weights and biases. A detailed mathematical discussion of the method implemented in the function “trainbr” can be found in [For97].

In addition to this, a simple hold-out cross-validation was performed on the original data in order to obtain 3 different subsets (each one being representative of the whole data “diversity”). The “training set” was composed of 80 % of the original data, while the “validation” and “test set” were composed of the remaining 16 % and 4 %, respectively.

The prediction errors in these different sets were evaluated continuously during the entire duration of the training session so that the network generalization capability was monitored at every stage⁷.

(b) – Determination of the network architecture

As we have already seen, the difficulty in the use of NN for robot calibration tasks lies mainly in the fact that there is no systematic method for determining the architecture of networks able to approximate the data within the desired accuracy.

Since an exhaustive search by testing all possible network architectures is computationally prohibitive, in the next lines we propose a computation-effective method for the systematic determination of networks able to provide a satisfactory accuracy for a given function approximation problem.

Heuristic scheme based on a decision-tree search

The research always starts from a very simple NN. This network, called *Father Network*, is a network having only 1 hidden layer with the same number of neurons as the output layer. The number of layers in the output layer corresponds to the number of DOF of the robot or the number of joint coordinates to be predicted.

Starting from this network, the algorithm is as follows:

1. Generating the Children Networks from the Father Network: there are 2 different rules for this creation:

- *rule 1:* add a neuron in each hidden layer (one layer per time);
- *rule 2:* duplicate a given layer and insert this new layer before or after the layer from which it has been copied.

Example: From the Father Network [8 6], network [9 6] can be generated using *rule 1* and networks [8 8 6] and [8 6 6] using *rule 2*.

2. Training of all the Children Networks: all the children generated in the previous iteration are trained for a certain number of epochs. After a large number of tests, we decided to adopt

⁷ Despite the fact that, in general, regularization techniques are able to handle overfitting by themselves, an early-stopping criterion is still used as a “control mechanism”.

2'000 epochs for the training of the networks since, in most of the cases, the prediction error did not experience significant improvement beyond this number.

3. Choice of the new Father Network: all the children that have been generated and which have not yet become fathers will be compared. The one providing the best results will become the father of the next iteration.

Therefore, the tree is expanded until a certain level, for which:

$$\begin{aligned} & \text{Maximum number of neurons in any layer} \\ &= \text{Number of iterations} + \text{Number of neurons in the output layer} \end{aligned} \quad (1)$$

$$\text{Maximum number of iterations} + 2 = \text{Maximum number of layers} \quad (2)$$

Example:

A simple example is presented below in order to illustrate the way in which the algorithm performs the search.

In **Figures 6.7** to **6.10**, the *score* of the network corresponds to the *absolute value of the prediction error* (within a 90 % confidence interval) for a data set not seen during the training (test set error). It is the measure used to assess the prediction capability of the networks trained.

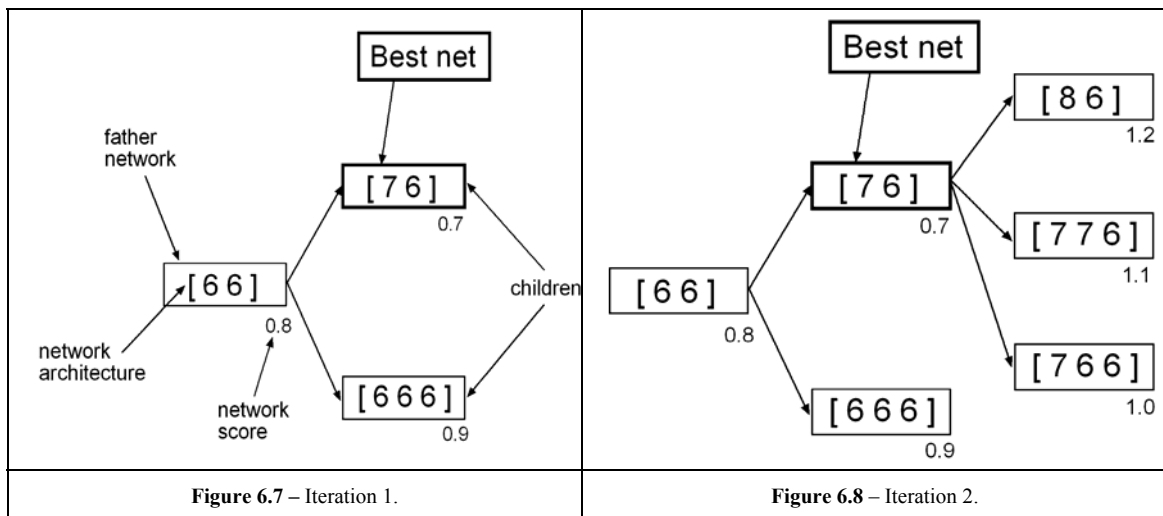
■ **Iteration 1:** Starting from the Father Network [6 6], the 2 children [7 6] and [6 6 6] are generated (**Figure 6.7**).

These networks are then trained and the one having the best score is chosen to become the father of the next iteration: in this case, it is the network [7 6].

■ **Iteration 2:** In this iteration, the network [7 6] generates 3 children: the networks [8 6], [7 7 6] and [7 6 6] – see **Figure 6.8**.

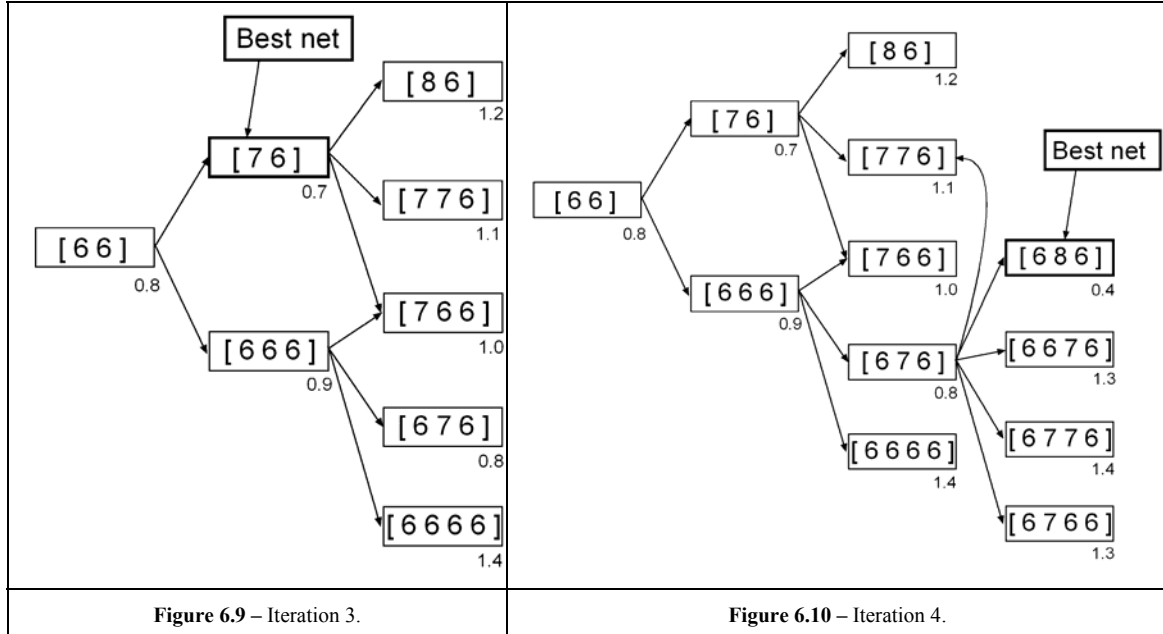
As before, these 3 networks are trained and their corresponding scores are compared. However, the network having the best score is still [7 6], which has already been a father previously.

Therefore, the next Father Network for the next iteration will be the one that has the best score and has not been father previously: [6 6 6].



■ **Iteration 3:** The father [6 6 6] now generates the networks [7 6 6], [6 7 6] and [6 6 6 6] (**Figure 6.9**). Note that [7 6 6] has already been generated in iteration 2, so this time it will not be trained.

We can see that the network [7 6] is still the one with the best overall score. Once more, the next father will be the one that has the best score and has not yet been a father: [6 7 6].



■ **Iteration 4:** In this last iteration, [6 7 6] generates the networks [7 7 6], [6 8 6], [6 6 7 6], [6 7 7 6] and [6 7 6 6] (**Figure 6.10**).

Since the maximum number of iterations is now reached, the performances of all the different networks trained so far are compared and the network with the best overall score will finally be adopted for calibration: [6 8 6].

Remarks:

1. Note that this algorithm is not of the “best-path” type: if the search stops because the maximum number of iterations has been reached, the network chosen for calibration will still be the one that has the best overall prediction capability, even if a large number of candidates have been evaluated afterwards.

2. The reader must bear in mind that this algorithm does not provide an “optimal solution” from the *mathematical point of view* but only a “satisfactory solution” (from the practical point of view) for a given accuracy request⁸.

It is believed [Hay99] that this is related to the presence of local minima (in addition to global minima) in the error surface, at which back-propagation algorithms can typically get stuck during the training process.

⁸ In fact, an “optimal solution” would also be dependent on the use of optimization algorithms able to find systematically a global optimal set of weights and biases in the training of a network with arbitrary architecture (i.e. with arbitrary complexity).

3. A major advantage of this algorithm lies in the fact that it preferentially looks for networks having small architectures.

This is an additional way of improving the generalization performance since, as we have mentioned previously, small networks are less prone to overfit the data presented for training. This heuristic is therefore in accordance with *Ockham's razor*.

(c) – Implementation in the robot controller

Three methods can be used to implement a NN-based correction model in a given robot controller.

(1) Using the original analytical expressions

As we have seen, from the mathematical point of view, neurons are simply elementary units that perform a given input-output transformation described by a given mathematical function. Therefore, a NN model can simply be implemented by computing its overall transfer function⁹. However, the drawback of this method lies in its large computational cost, since the complexity of the transfer function increases exponentially with the network size.

(2) Using a DLL created in MatLab

In the framework of *MatLab*[®], a given NN model can be exported from the *Neural Network Toolbox*[®] into a different environment in the form of a DLL. This DLL can be created using the function 'comtool'.

(3) Using dedicated electronic chips

Lastly, the mathematical operations performed by the network can be directly implemented in a dedicated electronic circuit.

As opposed to the two previous software-based methods, this implementation is performed at the hardware level. Examples of such hardware realizations using VLSI architectures can be found in [Ham93a and Ham93b].

We believe that this solution will probably be the fastest of the three different methods¹⁰.

Throughout this work, we have always used the second method which is, for *MatLab*[®] users, the best compromise between implementation time and computational speed.

The improvement of the computational speed between methods 2 and 3 is left to future investigations.

⁹ This would correspond to transforming this model-free approach into a model-based approach (in the sense intended in this thesis). Note, however, that this transformation would be performed after the model coefficients have been determined, as opposed to a "true" model-based approach.

¹⁰ A direct extension of this approach would be to actually use a NN-based strategy for robot control, such as in [Kwa95].

6.3.3 – Directions for future investigations

(a) Building up a network with the desired prediction capability

The heuristic presented in **section 6.3.2** is the basis used in this thesis for the NN-based calibration of our robots.

However, this algorithm is certainly not the only way to solve the problem. In fact, as we have mentioned in **paragraph (a)** of **section 6.2.2**, there is no procedure that dominates over the others in the determination of a network able to approximate a given input-output mapping within a desired accuracy.

From the practical point of view, some search procedures may be more attractive than others, especially as regards the time required to find a satisfactory solution.

In the future, a time comparison between different constructive or pruning-based search schemes would be a point of major interest. Additional improvements relatively to the procedure proposed in this thesis may certainly be obtained.

(b) Other machine learning tools

In this thesis, we have made use of standard feedforward NN for the purpose of calibration, which is a typical multi-dimensional function approximation problem.

This choice was motivated by the fact that they are well-established tools in the Artificial Intelligence and Machine Learning fields.

In the future, alternative machine learning tools may be applied to solve typical calibration problems. In particular, the following tools should be considered:

- **radial-basis function networks** (RBFN) having a single hidden layer with RBF activation units (typically Gaussian functions), instead of the traditional sigmoid functions used in this work.

The major advantage of these networks lies in the fact that they are also capable of universal approximation ([Par91]).

However, as Haykin [Hay99] pointed out, the drawback is that RBFN usually construct *local* approximations to non-linear input-output mapping, as opposed to the *global* approximation provided by standard sigmoidal networks. Therefore, RBFN may require a higher number of parameters for the approximation of a given non-linear input-output mapping than sigmoidal networks for the same degree of accuracy.

The use of these networks has been considered in a recent dissertation [Jen00].

- **Support Vector Machines** (SVM), recently developed by Vapnik [Vap98], which are another category of universal feedforward networks.

Besides the fact that SVM are also universal approximators [Ham03], an important advantage in the use of this machine learning tool is that it appears to be guaranteed to find a global extremum of the error surface during the training process [Hay99].

The downside lies in the fact that SVM are currently slower than other NN for a similar generalization performance.

6.4 – Correcting the pose of the 3-DOF robot

In this section, we report the results obtained for the calibration of the 3-DOF robot measured in this thesis using NN for data processing.

The **first paragraph** deals with work accomplished using the real data collected on the robot. The **second paragraph** proves the effectiveness of our neural approach using simulation data. Several situations are investigated for this purpose. First, a zero-mean Gaussian signal is added in order to simulate a given measurement noise. Second, the effect of a modification in the geometry of the robot is simulated. And finally, the influence of the number of points used to train the network is considered.

6.4.1 – Working with measurement data

(a) Results obtained “off-line”

For each of the 6 configurations of **Figure 5.6**, the algorithm described in **section 6.3.2** was run for a total of 30 iterations in order to evaluate the prediction capability of the different network candidates in the approximation of the data collected on the 3-DOF robot.

The data set used for training the different networks was composed of $19^3 = 6'859$ points uniformly spread over the robot workspace (with the following coordinates in each axis [mm]: $\pm 1.8, \pm 1.6, \pm 1.4, \pm 1.2, \pm 1, \pm 0.8, \pm 0.6, \pm 0.4, \pm 0.2$ and 0).

After a few iterations, the prediction capability of the networks (evaluated on samples not seen during training) seemed to remain constant, indicating therefore that an acceptable solution had been found for the approximation problem.

The architectures of the networks found for the different configurations of **Figure 5.6** are reported in **Table 6.1**, together with the minimum number of search iterations required to find these networks and the corresponding prediction capabilities evaluated “off-line”.

Configuration	Architecture of the network found	Minimum number of iterations required to find the network	Prediction error ($U_{90\%}$) obtained OFF-LINE [nm]
<i>Serial 1</i>	[7 5 6 3]	8	± 25
<i>Serial 2</i>	[4 4 4 5 3]	6	± 27
<i>Serial 3</i>	[6 7 7 3]	8	± 18
<i>Serial 4</i>	[4 4 4 4 3]	5	± 19
<i>Parallel</i>	[5 5 4 3]	6	± 18
<i>Without-IGM</i>	[6 6 6 7 3]	8	± 26

Table 6.1 – Networks found for the calibration of the 3-DOF robot and their corresponding prediction capabilities evaluated off-line.

Similar conclusions to those obtained for the model-based approach (see **Section 5.4.1**) can be formulated from the results of this Table:

- using the algorithm of **Section 6.3.2**, we were successful in finding a network able to approximate the desired input-output mapping for the calibration of the 3-DOF robot within accuracies close to the resolution of the robot.

This conclusion is valid for all the error compensation schemes of **Figure 5.6**, which ascertains the efficiency of the algorithm used to determine the architecture of the networks.

- in particular, we found a network able to approximate the direct correspondence between the motor and the operational coordinates of the robot in the absence of the IGM (configuration “Without IGM” in **Figure 5.6**). **Figure 6.11** below illustrates the architecture of this network.

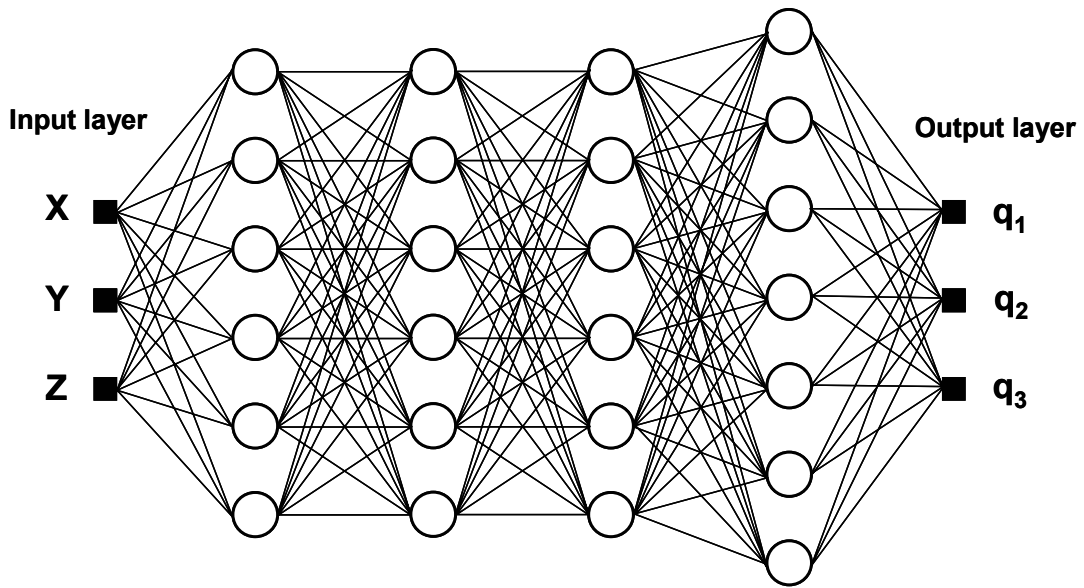


Figure 6.11 – Representation of the architecture of the [6 6 6 7 3] feedforward NN used for the calibration of the 3-DOF robot in the configuration “Without IGM”.

Note that the prediction capability obtained for this particular configuration was within the same range as those of the remaining cases.

To the best of our knowledge, this is a completely new result, which contradicts the conclusions of previous researchers (see **section 6.3.1**). It means that this robot can be calibrated even if the nominal geometry of the robot remains unknown.

(b) Results obtained “in-line”

The networks of **Table 6.1** were then implemented in the robot controller and the prediction for positions not seen during the calibration was compared to the corresponding reading of the laser interferometer (“in-line” implementation).

As in the case of the model-based approach, the errors were found to be within $\pm 50 \text{ nm}$ ($U_{90\%}$) when the interferometer was verifying an axis for which the optical head did not have to be re-mounted in respect to the measurements taken for the calibration, and approximately $\pm 100 \text{ nm}$ ($U_{90\%}$) otherwise. Reasons for the discrepancy between these two in-line values, on one hand, and for the difference between the in-line and off-line situations, on the other hand, have already been discussed in **Section 5.4.1**.

6.4.2 – Working with simulation data

(a) Data sets, conditions and hypothesis of the simulations

The aim of this section is to demonstrate the effectiveness of the NN-based approach for the calibration of the 3-DOF robot.

For this purpose, the function that the NN is to learn through training has to be previously known. We decided to use the IGM to generate a set of end-effector coordinates – motor coordinates pairs – this means that, for the simulations reported here, it was assumed that *the IGM represents exactly the behaviour of the 3-DOF robot being calibrated*.

The IGM was then used to generate the following data set:

- **DATA SET:** regular grid with the following coordinates in each axis: ± 2 mm, ± 1.8 mm, ± 1.6 mm, ± 1.4 mm, ± 1.2 mm, ± 1 mm, ± 0.8 mm, ± 0.6 mm, ± 0.4 mm, ± 0.2 mm and 0 [mm] $\rightarrow 21^3 = 9'261$ points;

We found that the network [6 6 5 5 3] was able to fit this data with an error less than ± 21 nm ($U_{90\%}$).

(b) Sensitivity to measurement noise

In order to simulate the effect of measurement noise, a zero-mean Gaussian signal was added to the operational coordinates of the previous data set. Three cases corresponding to three different noise amplitudes were considered: 25 nm, 50 nm and 100 nm.

Table 6.4 reports, for each case, the errors (relatively to the output of the IGM) when the network [6 6 5 5 3] is asked to predict new points if the training was performed with noisy data.

Noise amplitude [nm]	Prediction error ($U_{90\%}$) [nm]
<i>0 (nominal case)</i>	± 21
<i>25</i>	± 49
<i>50</i>	± 66
<i>100</i>	± 120

Table 6.4 - Simulation of the effect of a measurement noise on the calibration results for the 3-DOF robot.

As expected, we can see from the results of this Table that the error attainable after calibration is limited by the measurement noise corrupting the data used to train the network.

(c) Sensitivity to modifications in the robot geometry

A key issue in determining the effectiveness of the neural approach lies in the ability of the network to learn slight modifications in the robot geometry arising from manufacturing tolerances.

This issue was investigated by training the network with different sets of data generated by a modified IGM. The modifications considered were the following:

- *modification 1*: lengths of all the robot arms = nominal length + 10 μm ;
- *modification 2*: lengths of all the robot forearms = nominal length + 10 μm ;
- *modification 3*: lengths of all the robot arms = nominal length + 10 μm
AND
lengths of all the robot forearms = nominal length + 10 μm .

Table 6.5 presents, for each case, the errors (relatively to the output of the modified IGM) in the response of the network [6 6 5 5 3] for new points when the network is trained with the modified data.

Geometric modification	Prediction error ($U_{90\%}$) [nm]
<i>0 (nominal case)</i>	± 21
<i>Modification 1</i>	± 26
<i>Modification 2</i>	± 8
<i>Modification 3</i>	± 22

Table 6.5 - Simulation of the effect of modifications on the robot geometry in the calibration results of the 3-DOF robot.

As we can see, the prediction errors in the different cases remain in the same order of magnitude. This means that the network found for a given case is robust enough to correct effects of slight modifications in the geometry of the robot due to manufacturing tolerances.

(d) Sensitivity to the number of training points

Lastly, a realistic simulation was conducted in order to evaluate the effect of the number of training points on the prediction capability of the network.

Of the different cases in **Figure 5.6**, only the configurations “Parallel” and “Without IGM” were studied, since they are the most commonly used and/or the easiest to implement from a practical point of view.

Instead of using the nominal IGM to generate the data for the simulations (as in the previous paragraphs), we decided to use the two networks indicated in **Table 6.1** ([5 5 4 3] and [6 6 6 7 3]) trained with the real data collected on the robot.

The data generated was a regular grid of points uniformly spread over the robot workspace with the following coordinates on each axis (in [mm]):

- **Set 1:** $\pm 2, \pm 1$ and 0 $\rightarrow 5^3 = 125$ points
- **Set 2:** $\pm 2, \pm 1.5, \pm 1, \pm 0.5$ and 0 $\rightarrow 9^3 = 729$ points
- **Set 3:** $\pm 2, \pm 1.6, \pm 1.2, \pm 0.8, \pm 0.4$ and 0 $\rightarrow 11^3 = 1'331$ points

The two networks were then trained once more from the beginning with the sets 1, 2 and 3 and their responses were compared, for a set of new points, with the prediction given by the networks used to generate the data.

The resulting errors are reported in **Table 6.6**.

Configuration	Prediction error ($U_{90\%}$) obtained for different data sets used for training the networks [nm]		
	Set 1 (125 points)	Set 2 (729 points)	Set 3 (1'331 points)
<i>Parallel</i>	± 15	± 13	± 12
<i>Without-IGM</i>	$\pm 1'300'050$	± 19	± 17

Table 6.6 – Effect of the number of points used for the real calibration of the 3-DOF robot (configuration “Without IGM”).

As we can see, if a “Parallel” configuration is used for calibration, 125 points are enough to obtain the desired level of accuracy. However, if the calibration is conducted in a “pure neural” way, then 729 points have to be used for the same accuracy.

The reason for this lies in the number of network coefficients (weights and biases) that have to be adjusted through training. The network used in the “Parallel” configuration has “only” 92 coefficients while the “Without IGM” network utilizes 178 coefficients.

6.5 – Correcting the pose of the 6-DOF robot

This section presents the results obtained for the calibration of the 6-DOF robot measured in this thesis if NN are used for data processing tasks.

The **first paragraph** discusses the results obtained with the real data collected from the robot and corresponding to the three different phases of the calibration (see **section 4.3.1**).

The **second paragraph** emphasizes the effectiveness of this neural approach with the help of simulation data.

6.5.1 – Working with measurement data

(a) Results obtained for phase 1 (angles)

Phase 1 makes use of two different data sets for data processing purposes.

■ The first set comprises only “**small angles**” (within the primary range of the autocollimators and measured directly on the mirror cube).

The poses measured in this set have the following operational coordinates, according to the IGM: $(X, Y, Z, \theta_X, \theta_Y, \theta_Z)$ for which:

- the *translations* X, Y, Z = origin $(0\ 0\ 0)$ + vertexes of the cubes at ± 1.6 mm, ± 1.2 mm, ± 0.8 mm and ± 0.4 mm (33 centres of rotation¹¹);
- the *rotations* $\theta_X, \theta_Y, \theta_Z$ with the following possible values $\pm 300, \pm 200, \pm 100$ and 0 arcsec.

The total number of points in this set is therefore $33 \times 7^3 = 11'319$.

■ The second set comprises poses presenting “**large angles**” (measured on the faces of the polygon prisms) + the poses of the first set. These new poses are the following:

- *translations* X, Y, Z = origin $(0\ 0\ 0)$ + vertexes of the cubes at ± 1.6 mm, ± 1.2 mm, ± 0.8 mm and ± 0.4 mm (33 centres of rotation);
- *rotations* $\theta_X, \theta_Y, \theta_Z$ = only 1 “large angle” varying per time as follows:

$-3^\circ - 150$ arcsec	-3°	$-3^\circ + 150$ arcsec
$-1.5^\circ - 150$ arcsec	-1.5°	$-1.5^\circ + 150$ arcsec
$+1.5^\circ - 150$ arcsec	$+1.5^\circ$	$+1.5^\circ + 150$ arcsec
$+3^\circ - 150$ arcsec	$+3^\circ$	$+3^\circ + 150$ arcsec

while the two remaining angles could take the values: 0 and ± 150 arcsec.

The effective number of poses having “large angles” is then $33 \times (3 \times 12 \times 3^2) = 29'700$ which brings the total number of different poses in the second data set to approx. $41'000$ points.

a.1 – Results obtained “off-line”

For each configuration of **Figure 5.6**, the algorithm described in **section 6.3.2** was run for a total of 30 iterations in order to search for a network able to approximate the corresponding input-output mapping with the highest accuracy.

¹¹ The spatial distribution of these centres of rotation is given in **Figure 4.15** of **section 4.3.1**.

After a few iterations, we were able to find networks presenting a satisfactory accuracy for the different approximation problems.

Table 6.6 reports the architectures of these networks, the minimum number of iterations required to find them, as well as their corresponding prediction capabilities obtained *off-line* and evaluated in poses never seen during the training of the network.

Configuration	Architecture of the network found	Minimum number of iterations required to find the network	Prediction error ($U_{90\%}$) obtained OFF-LINE [arcsec]
<i>Serial 1</i>	[8 7 7 7 3]	6	± 0.29
<i>Serial 2</i>	[6 8 8 8 3]	6	± 0.29
<i>Serial 3</i>	[10 10 9 10 6]	8	± 0.63
<i>Serial 4</i>	[6 7 8 6]	5	± 0.77
<i>Parallel</i>	[6 6 6 6]	3	± 0.90
<i>Without-IGM</i>	[9 11 11 9 7 6]	10	± 0.80

Table 6.6 – Networks found for the calibration of the *angular* motions of the 6-DOF robot (phase 1) and their corresponding prediction capabilities evaluated *off-line*.

The following conclusions can be drawn from the results of this table:

- NN are able to correct the errors in the angular motions of the 6-DOF robot with accuracies in the sub-arcsec range. This occurs independently of the configuration adopted for correction purposes (at least those represented in **Figure 5.6**).

Note that, in general, these networks present more complex architectures (i.e. with a larger number of hidden layers and/or a larger number of hidden neurons) than the networks found for the 3-DOF robot (see **Table 6.1**). This is of course due to the presence of a higher number of DOF (causing a higher-order coupling) in the mechanism being calibrated;

- in particular, and as for the 3-DOF robot, the direct articular-operational mapping was approximated with satisfactory accuracy without the help of the IGM. This means that the angles of the 6-DOF robot can be calibrated even if the nominal geometry of the manipulator remains unknown.

a.2 – Results obtained “in-line”

In order to evaluate the accuracy of the calibrated angular coordinates *in real experimental conditions* (or “in-line”), the best network found previously was implemented in the robot controller.

The prediction of the neural model was then compared to the reading of the autocollimator for a set of new poses. If these new poses involved “small angles”, prediction errors were found to be within ± 0.33 arcsec ($U_{90\%}$) and, when “large angles” were verified, the error increased to ± 2.70 arcsec ($U_{90\%}$). A reason for this difference has already been discussed in **section 5.5.1 – paragraph a.2**.

(b) Results obtained for phase 2 (translations)

b.1 – Results obtained “off-line”

The same work was carried out with the data collected in phase 2 (“pure-translational” poses).

The data set used to train the networks was composed of $21^3 = 9'261$ points uniformly distributed over the robot workspace (with the following coordinates in each axis [mm]: $\pm 2, \pm 1.8, \pm 1.6, \pm 1.4, \pm 1.2, \pm 1, \pm 0.8, \pm 0.6, \pm 0.4, \pm 0.2$ and 0).

Once more, we were able to find networks capable of approximating with sub-100 nm accuracies the data corresponding to the different configurations of **Figure 5.6**.

In particular, a network presenting a satisfactory accuracy for the configuration “Without IGM” was found. This means that the translations of this robot can also be calibrated in the absence of any information on the (nominal or real) geometry of the robot.

The architectures of these networks, the minimum number of iterations required to find them, as well as their prediction capabilities are shown in **Table 6.7**.

Configuration	Architecture of the network found	Minimum number of iterations required to find the network	Prediction error ($U_{90\%}$) obtained OFF-LINE	
			transl. [nm]	rot. [arcsec]
<i>Serial 1</i>	[7 8 10 10 9 8 6]	10	± 50	± 0.26
<i>Serial 2</i>	[7 9 9 12 9 6]	11	± 57	± 0.25
<i>Serial 3</i>	[12 17 6]	13	± 45	± 0.23
<i>Serial 4</i>	[9 9 11 9 8 9 6]	11	± 42	± 0.24
<i>Parallel</i>	[7 7 6 7 10 7 6]	10	± 43	± 0.27
<i>Without IGM</i>	[6 9 10 10 10 6]	9	± 51	± 0.30

Table 6.7 – Networks found for the calibration of the *translational* motions of the 6-DOF robot (phase 2) and their corresponding prediction capabilities evaluated **off-line**.

Note that the *translational errors* obtained “off-line” for this robot are not as good as those of the 3-DOF robot. As mentioned in the previous chapter, this is the consequence of a greater inaccuracy in the corresponding measurements arising from a longer measuring loop (see **Figures 3.15** and **3.18**).

Angular errors are, however, close to the accuracy of the autocollimator (approx. ± 0.2 arcsec).

b.2 – Results obtained “in-line”

An “in-line” evaluation of the results of the previous paragraph was then performed.

For this purpose, the networks reported in **Table 6.7** were implemented in the robot controller and their accuracy was evaluated *in real experimental conditions* by comparing their prediction,

for new “pure-translational” poses, to the corresponding reading provided by the measuring devices (interferometer and autocollimator).

We found that the residual angular errors were within ± 0.27 arcsec ($U_{90\%}$), which is of the same order of magnitude as the results obtained for phase 1, while translational errors were found to be within ± 120 nm ($U_{90\%}$).

As opposed to the 3-DOF robot, note that the translational errors are not longer dependent on the mounting of the interferometer’s optical head since angular contributions are now negligible.

Lastly, note that the translational errors are higher when compared to those of the 3-DOF robot since the measuring loop is now longer introducing thus a higher amount of inaccuracy in the measurements

(c) Results obtained for phase 3 (translations combined with rotations)

Data processing was then conducted with the full 6D poses collected in phase 3.

After 30 search iterations and for all the cases of **Figure 5.6**, we were only able to find networks having “good” accuracies for angles (same order of magnitude as phases 1 and 2) but “poor” accuracies for translations (approximately ± 600 nm within $U_{90\%}$).

In order to improve this result, we split the global $IR^6 \rightarrow IR^6$ problem into 6 different $IR^6 \rightarrow IR^l$ problems¹² and searched for a network for each of these elementary cases. This approach was only conducted for the configuration “Without IGM” because of the enormous amount of computation time. Using this approach, we found that the error for the translations could be reduced at best by a factor of 2.

Reasons for “poor” results in predicting translational motions in the 6D assembled data were already extensively discussed in **paragraph (c) of Section 5.5.1**.

6.5.2 – Working with simulation data

(a) Data sets, conditions and hypothesis of the simulations

The goal of this section is to demonstrate the robustness of the NN-based calibration method for the case of the 6-DOF robot. We only consider the case of the translations since we believe this is enough for our purpose.

We assumed that *the IGM represents the behaviour of a real 6-DOF robot being calibrated*. Therefore, this model was used to generate the data for the simulations described below.

The data set generated contained 9’261 points uniformly spread over the translational workspace of the robot (a 3D regular grid with the following divisions in each axis [mm]: ± 2 , ± 1.8 , ± 1.6 , ± 1.4 , ± 1.2 , ± 1 , ± 0.8 , ± 0.6 , ± 0.4 , ± 0.2 and 0).

As for the 3-DOF robot, the first step of the simulation was to find a network able to fit the IGM of the robot.

¹² In this way, we eliminated residual errors due to a “compromise” in the determination of the different coefficients (weights and biases) during the training of the network. This now corresponds to a functionally equivalent situation to the one reported in Chapter 5.

We found that the network [7 7 6 6] could fit the nominal IGM with less than ± 8 nm of error (only for “pure-translational” poses).

This network was then used to perform the simulations described in the next paragraphs.

(b) Sensitivity to measurement noise

In order to simulate the effect of measurement noise, a zero-mean Gaussian signal was added to the operational coordinates of the previous data set.

Three different noise amplitudes were considered for this study: 25 nm, 50 nm and 100 nm.

Tables 6.10 and 6.11 report the prediction errors (= network response – IGM output) evaluated in new samples when the network [7 7 6 6] is trained with the noisy data.

Noise amplitude [nm]	Prediction error ($U_{90\%}$) [nm]
0 (nominal case)	± 8
25	± 48
50	± 63
100	± 107

Table 6.10 – Effect of a measurement noise in the calibration of the 6-DOF robot.

Like for the 3-DOF robot, these results prove that the attainable limit during calibration is limited by the amount of noise corrupting the measurement data.

(c) Sensitivity to modifications in the robot geometry

Finally, we tested the ability of the network to correct for slight modifications in the geometry of the robot, coming from manufacturing tolerances.

This was achieved by modifying the nominal values of the IGM parameters within the typical tolerances of the manufacturing process (we took ± 10 μm). Then, the previous data set was re-generated from this modified model.

Three different modifications were considered:

- *modification 1*: lengths of all the robot arms = nominal length + 10 μm ;
- *modification 2*: lengths of all the robot forearms = nominal length + 10 μm ;
- *modification 3*: lengths of all the robot arms = nominal length + 10 μm
AND
lengths of all the robot forearms = nominal length + 10 μm .

For each of these modifications, the network [7 7 6 6] was trained from the beginning and its response was compared to the output of the modified IGM used to generate the training data. Results of this comparison are reported in **Table 6.11**.

Geometric modification	Prediction error ($U_{90\%}$) [nm]
<i>0 (nominal case)</i>	± 8
<i>Modification 1</i>	± 11
<i>Modification 2</i>	± 9
<i>Modification 3</i>	± 10

Table 6.11 – Effect of a modification geometry on the calibration of the 6-DOF robot.

As we can see from the results in this Table, the errors obtained in all these cases remain within the same order of magnitude. This proves that the network can also handle modifications in the geometry of the robot arising from tolerances in the manufacturing process.

(d) Sensitivity to the number of training points

Last but not least, the effect of the number of training samples on the network's prediction capability was investigated.

We decided to consider only the configurations “Parallel” and “Without-IGM” among the different variants of **Figure 5.6**, since they are in fact the most common cases from the practical point of view.

In order to render the simulations reported in this section as close as possible to a real calibration experiment, the real data collected on the robot (*phase 2*) was used to train the two corresponding networks ([7 7 6 7 10 7 6] for the configuration “Parallel” and [6 9 10 10 10 6] for the case “Without IGM”).

Once the networks had been trained, they were used to generate the following data sets (with the following divisions in each axis [mm]):

- **Set 1:** $\pm 2, \pm 1$ and 0 $\rightarrow 5^3 = 125$ points
- **Set 2:** $\pm 2, \pm 1.5, \pm 1, \pm 0.5$ and 0 $\rightarrow 9^3 = 729$ points
- **Set 3:** $\pm 2, \pm 1.6, \pm 1.2, \pm 0.8, \pm 0.4$ and 0 $\rightarrow 11^3 = 1'331$ points

For each configuration, the networks were then trained again using these data sets and their response was compared, for a set of new positions, to the response of the network trained with the real robot data. The resulting errors are reported in **Table 6.12**.

Configuration	Prediction error ($U_{90\%}$) obtained for different data sets used for training the networks [nm]		
	Set 1 (125 points)	Set 2 (729 points)	Set 3 (1'331 points)
<i>Parallel</i>	$\pm 8'570$	± 18	± 16
<i>Without-IGM</i>	$\pm 302'040$	± 15	± 13

Table 6.12 – Effect of the number of points on a realistic calibration of the 6-DOF robot.

The results of this table indicate that 729 points are apparently necessary for an accurate calibration of the translations of this robot in both configurations (“Parallel” and “Without-IGM”). The reason for this lies in the number of parameters (between 400 and 500) that have to be identified in the networks involved in these calculations.

6.6 – Universality of the proposed method

This section presents the results of the application of our NN-based technique for the calibration of two robots measured by other researchers.

For each case, the algorithm described in **paragraph (b) of section 6.3.2** was used to determine the architecture of a network able to accomplish the error compensation with the highest accuracy for a certain amount of data presented for training.

We believe that our algorithm is largely applicable since the data processing is simply regarded as a function approximation problem. It is therefore reasonable to expect that our method may be applied for the calibration of *any* robot.

6.6.1 – Test with another flexure parallel robot

A few tests were carried out using the measurement data collected on a recent prototype of the 3-DOF “Delta Cube” robot¹³, currently used by our industrial partner as a new μ -EDM machine – the **Delta Cube 4** (see **Figure 5.7b**).

We found, by letting our decision-tree algorithm run for a total of 30 iterations, that the network [6 6 6 5 3] performed the error compensation within the highest accuracy. As for the two robots studied in this thesis, the training of networks was performed for 2’000 epochs using the *MatLab*[®] function “trainbr”. The data set used for training comprised 125 points collected from the robot.

This network could predict new points (not seen during training) within errors in the same range as those corresponding to the polynomial models ($\epsilon < \pm 100$ nm) described in **Chapter 5**.

6.6.2 – Test with a “non-flexure” parallel robot

In addition to the previous robot, calculations were also conducted using data collected on a new 5-DOF machine-tool with parallel geometry¹⁴ (called *Hita-STT*) recently designed in our lab [Thu04].

We found that the network [4 6 7 8 5 6 4 4] was able to compensate the errors of this robot within less than ± 5 μ m, which is markedly below the original requirements for the calibration of this machine (± 10 μ m). This result was obtained with a training set of approximately 300 measurement points¹⁵.

This result seems to indicate that our neural approach may also be applied for the calibration of non-flexure parallel robots.

Of course, additional tests should be carried out on a larger number of different kinematics in order to establish this universal applicability firmly and unequivocally. This point is left to future investigations.

¹³ The data used to perform these tests was kindly provided by Dr. Ivano Beltrami, Head of research department at AGIE S.A.

¹⁴ The calibration of this machine is being studied in the framework of a different dissertation [Fra06].

¹⁵ The data used to perform these tests was kindly provided by Mrs. Hélène Frayssinet-Mazerolle, research assistant at the LSRO.

6.7 – Conclusion

This chapter presented a “black-box” approach for processing the data in robot calibration problems.

The following points were demonstrated in the chapter:

- NN are well-established powerful tools widely used over the last decades in function approximation problems. A literature review has shown that NN have already been applied for robot calibration tasks. However, the majority of the published works deal only with serial manipulators.

- The robot calibration literature has shown the lack of a clear and systematic methodology for determining the architecture (number of hidden layers and number of neurons in each hidden layer) of a network able to approximate the data presented for training with a desired accuracy. In this chapter, we propose a computation-effective heuristic for solving this problem, based on a decision-tree search.

- The effectiveness of the above-mentioned algorithm is established from the fact that it always provides an acceptable solution irrespectively of the configuration used for data processing tasks (errors summed to the output of the IGM, to the input of the IGM ...).

In particular, we show that it is possible to calibrate the two robots measured in this thesis without the use of the IGM – this means that NN can be used to calibrate multi-DOF flexure parallel robots even if the geometry of the robot being calibrated remains unknown.

- It is claimed that the neural approach presented here is applicable to any robot. This universality is illustrated from the results of calculations performed on two robots other than those measured in this thesis.

- We proved that the active degrees of freedom of the 3-DOF robot can be calibrated with an accuracy below $\pm 100 \text{ nm}$. When taken separately, the translational motions of the 6-DOF robot can be calibrated within less than $\pm 120 \text{ nm}$ and the angular motions within $\pm 0.33 \text{ arcsec}$ (case of “small angles”) and $\pm 2.70 \text{ arcsec}$ (case of “large angles”).

- The robustness of our neural calibration method was demonstrated with the help of simulation data. We tested in particular the effects of measurement noise, the number of points used for training and the errors in the geometry of the robot due to manufacturing tolerances.

QUALITY CONTROL

Chapter 7 – Indentation as a verification tool

The aim of this chapter is to demonstrate the feasibility of the use of *indentation* (a technique commonly used for material characterization) to assess the accuracy (at the sub- μm range) of the calibrated translational DOF of a given high-precision flexure parallel robot.

After a brief description of the principle and the instrumentation used in classical indentation experiments for material testing, we describe some issues related to the implementation of this technique for our specific application. Results are then reported and the limitations of this method are discussed.

7.1 – A technique traditionally used for material testing

Over the last 30 years, *indentation* has become one of the most popular techniques for determining the mechanical properties of different types of materials [Bak01 and Voo98].

Conventional indentation tests involve pushing a hard tip of known geometry into the sample surface using a fixed peak load. The area of the corresponding footprint (called *indent*) created in the substrate is then measured, and the mechanical properties, in particular its hardness, are calculated from the peak load and the indentation area.

As shown schematically in **Figure 7.1**, equipment for performing instrumented indentation tests [Hay00] consists of three basic components: **(a)** an indenter of specific geometry usually mounted on a rigid column through which the force is transmitted, **(b)** an actuator for applying the force and **(c)** a sensor for measuring the indenter displacements.

Indenters are preferably made of diamond because of its high hardness and elastic modulus that minimize the interference of the tip over the measurement.

A variety of tip shapes can be used. Three main categories of indenter geometries are commonly used in the literature: pyramidal, spherical and conical indenters. **Figure 7.2** illustrates the shapes of some typical pyramidal indenters.

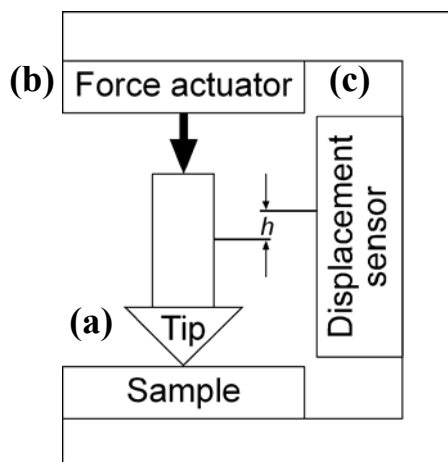


Figure 7.1 – Typical equipment used in an Instrumented Indentation Testing experiment.

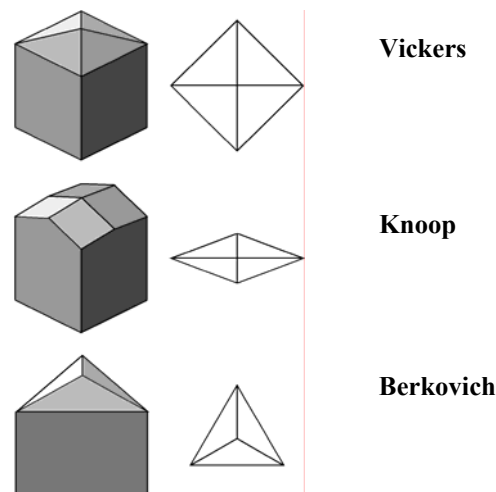


Figure 7.2 – Geometric shapes of different pyramidal indenters (*Berkovich*, *Vickers* and *Knoop* types) and their corresponding footprints.

7.2 – The indentation experiment

This section investigates the feasibility of using indentation as a procedure to validate the calibration of flexure parallel robots. Due to a certain number of constraints, only the translational DOF of the calibrated 6-DOF robot are studied.

The goal was to print a certain number of indents distributed according to a given pattern imposed by the robot on a temperature-stable substrate taken as reference (as in a real machining operation). The measurements (performed in a different institution) of the positions of the centres of these indents in a local frame defined on the substrate surface could then be used to evaluate the accuracy of the DOF (translations) used to print the indents.

The set-up used for our experiments is represented schematically in **Figures 7.3a and 7.3b**. A Vickers-type diamond indenter¹ was mounted on the end-effector of our calibrated 6-DOF robot and was used to indent a mirror-polished *Invar*[®] substrate – **Figure 7.4**.

The robot was used as a displacement sensor in the experiment, while the force sensing was achieved using a *Sensotec*[®] load-cell (model **31** – range: 10 N). The load-cell signal conditioner electronics allowed a force resolution of approximately 1 mN.

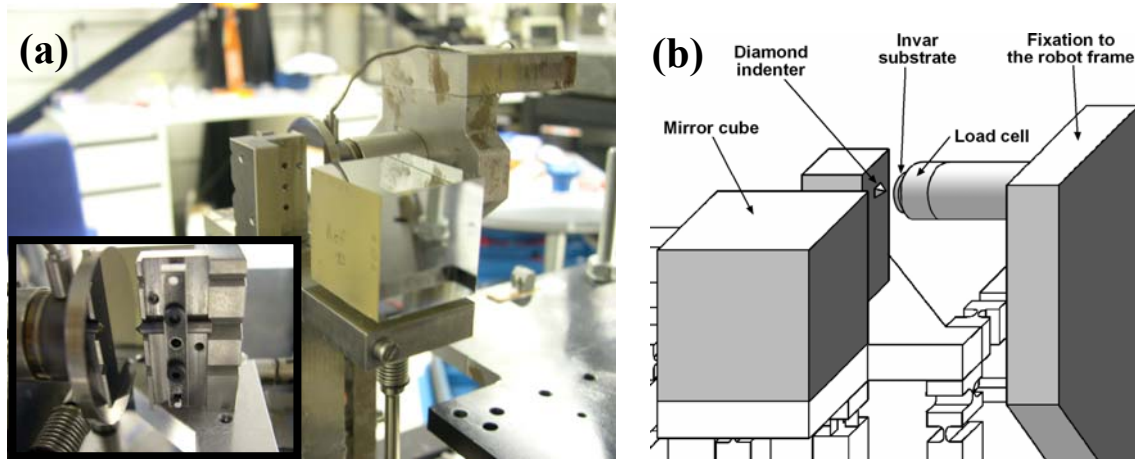


Figure 7.3 – (a): Photographic view of our indentation set-up with a detailed view of the indenter mounted on its support (b): Schematic view of the main functional parts mounted on the robot end-effector.

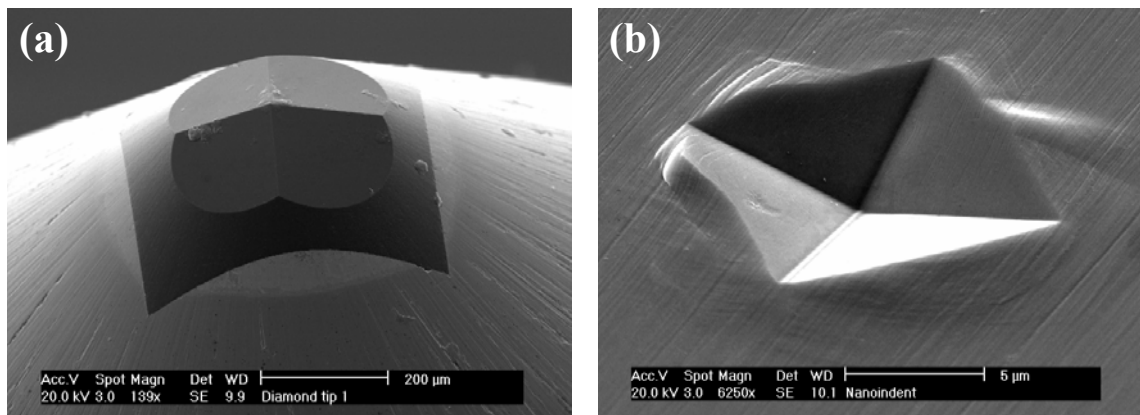


Figure 7.4 – SEM 3D views of indenter tip used for our experiments (a) and its corresponding footprint on an *Invar*[®] substrate (b)

¹ We chose to use a Vickers indenter since in this case the determination of the centre of the indent footprint (cross) is believed to be easier in this case (intersection of two lines).

A **closed-loop** was performed between the robot and the load-cell so that the maximum load applied during the indentation process was limited to approximately 10 mN (~ 1 gf).

As for the measurements during the calibration of the robot, the indentation was also performed in an automatic way and occurred inside the thermal chamber.

Once all the hardware had been mounted and the temperatures were stable, *a new local frame was defined on the indentation substrate* using the information corresponding to three “touches”, as at the beginning of any typical machining operation.

The indentation procedure then consisted of imprinting the substrate surface with a certain number of indents arranged in a previously determined pattern (imposed by the calibrated robot).

Remarks:

■ We decided to keep the mirror cube and the indenter support permanently attached to the robot end-effector (as shown in **Figure 7.3**) since we had observed that, in situations involving mounting/unmounting operations, the accuracy was highly degraded (deviations of the positions of the indent centres in respect to their nominal values were up to 800 – 900 nm at the borders of the indentation reticle).

Therefore, *we strongly encourage the use of end-effector mounts that avoid any manipulation on the robot between the calibration and the actual utilization period*, particularly during the phases in which high levels of accuracy (< 400 nm) are sought over the entire workspace.

■ We decided to use a threshold of 10 mN since in this situation the static and the dynamic behaviour of the robot (as seen by the interferometer and the autocollimators on the mirror cube) remain almost unchanged in relation to a typical calibration session.

Moreover, once the indenter was less than 10 μm from the surface to be indented, the robot end-effector moved by steps of 250 nm until the load threshold was reached in the “touch” (as indicated by the load-cell).

7.3 – Measuring the position of the indents

Once the indents have been properly printed on the substrate, the central point of this verification procedure lies in the *ability to measure with the maximum accuracy the $X - Y$ coordinates of the positions of the centres of the indents*.

At the beginning of the project, we planned to measure the position of the indents at METAS where a system based on an optical microscope is used, with the help of digital image processing methods (allowing sub-pixel accuracy), to find the positions of the centres of the indents. However, this system needed indents having large diagonals (at least 100 μm) in order to obtain reliable results in the determination of the centres of the indents.

Indents with such dimensions could not be produced in a temperature-stable material such as *Invar*[®] by our robot since it would require high indentation forces (that would radically influence the end-effector position within the μm range²).

² The diagonal of an indent printed on an *Invar*[®] substrate is approximately 8 μm . Indents having diagonals of 100 μm in the same material would require a load of at least 2 N. However, seeing that the nominal value of the robot structural stiffness is $2 \text{ N} \cdot \mu\text{m}^{-1}$, the previous load would induce a deformation of the robot end-effector of approximately 1 μm .

Therefore, we decided to perform the measurements at the *Sensors, Actuators and Microsystems Laboratory*³ (SAMLAB) on a **RAITH 150** [RAI], a machine commonly used for electron beam nanolithography and 2D nanometrology tasks.

The clear advantage of this machine over the METAS system lies in the fact that the optical microscope is now replaced by an electron microscope, with which high-resolution and high-magnification images can be obtained.

Therefore, the identification of the centre of the indent could be achieved *directly* on the observed SEM image with an uncertainty less than ± 50 nm, on the basis of a visual inspection with the help of appropriate cursors – **Figure 7.5**.

Note that (as in the case of METAS) the actual measurements on the RAITH 150 were performed by 2 interferometers measuring the 2D positions of the translational stage on which the sample was fixed.

In order to guarantee the accuracy of the 2D measurements performed by the 2 interferometers⁴ of the RAITH 150, we decided to use a **standard cross reticle**⁵ to calibrate this machine before measuring our indents – see **Figure 7.6**.

This standard, specifically designed for our application, was manufactured by *IMT Masken und Teilungen AG*⁶ using recent lithography techniques in such a way that it could be observed using both optical and electron microscopes.

The standard was a 10 mm x 10 mm x 2.28 mm quartz plate on which the 4 mm x 4 mm central area was covered by a reflecting Cr layer. In this area, a reticle of crosses was placed at fixed positions and lines made of Cr guaranteed a good optical contrast. This contrast is necessary to METAS since, as mentioned previously, their calibration system employs an optical microscope for the observation of the structures.

The X-Y coordinates of the different crosses of this standard were precisely determined by METAS with an accuracy of ± 20 nm on a frame defined on the standard.

The functional parts of this standard are represented schematically in **Figure 7.6**.

³ The *Sensors, Actuators and Microsystems Laboratory* (SAMLAB) – Institute of Microtechnology, University of Neuchâtel. Rue Jaquet-Droz 1 – case postale 526, CH-2002 Neuchâtel, Switzerland.

⁴ The RAITH interferometer stages can cover a measuring range of 150 mm x 150 mm.

Since the dimensions used during our application are quite restricted (3 mm x 3 mm) in respect to this range, the principal reason for using a standard for the calibration of this machine was the possible existence of an error in the orthogonality between the X and Y measurement axes.

If we were only interested in performing 1D measurements (rather than 2D) still within such a restricted range, this standard would be unnecessary. This statement has been verified experimentally.

⁵ Called hereafter “standard” for language simplification purposes.

⁶ *IMT Masken und Teilungen AG*: Im Langacher CH-8606 Greifensee, Switzerland.

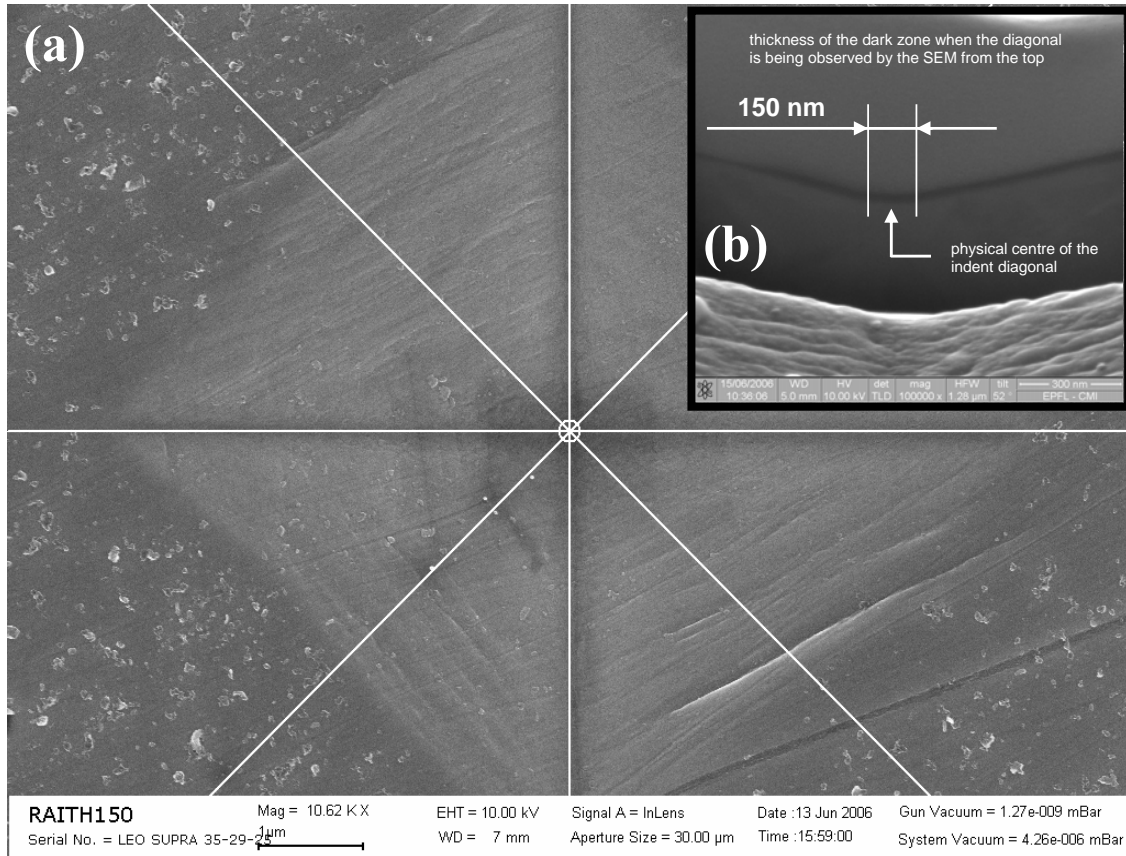


Figure 7.5 – (a): High-resolution SEM image of a typical indent (diagonal size of approx. 8 µm) printed by the 6-DOF robot (acting as a “pure-translator”) on an *Invar*[®] substrate with a load of approximately 10 mN. The selection of the indent centre (for measuring purposes) was performed by aligning the machine cursors with the 2 indent diagonals. We estimate the uncertainty of this way of proceeding to be less than ± 50 nm. **(b):** FIB cross section of an indent diagonal to which a cursor was aligned in order to define the centre of the indent.

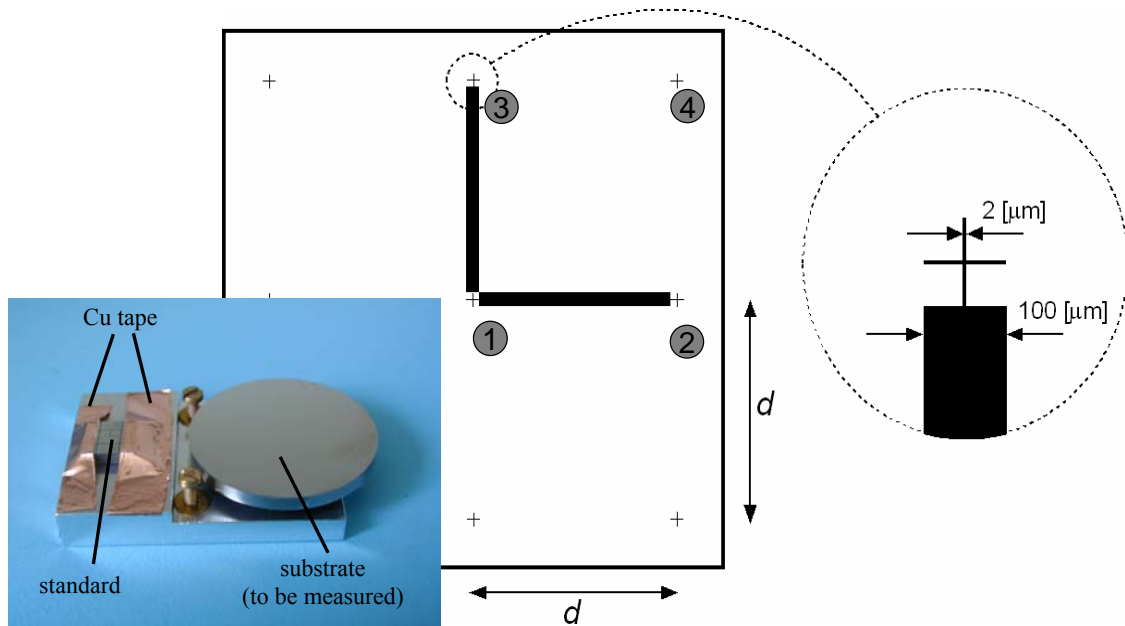


Figure 7.6 – Main scheme: Functional parts of the standard ($d = 1800 \pm 0.5 \mu\text{m}$) and previously calibrated by METAS. Crosses 1, 2 and 3 were used to define the absolute reference frame (calibration of the RAITH 150), whereas cross 4 was used for verification purposes. **Left corner:** photographic view of the standard (left) and the reticle to be measured (right) mounted on a carefully manufactured *Invar*[®] support (the copper tape was used to increase the electrical conductivity of the standard, for the SEM).

7.3.1 – Measurement procedure

The procedure used to measure the positions of the indents was as follows:

STEP 1 – The centres of the crosses 1, 2 and 3 on the standard (see **Figure 7.6**) were used to define an absolute coordinate frame in respect to which the indents were to be measured.

In order to increase the accuracy when selecting the centre of a given cross, we used cursors aligned with the two borders of the cross in each direction. Then, a very small ($\varnothing < 50$ nm) *contamination dot* was created by the SEM in order to “mark” the selected centre – **Figure 7.7**.

STEP 2 – In order to verify the accuracy of the calibrated RAITH 150, the coordinates of the centre of cross 4 (as indicated in the METAS certificate) were measured in respect to the previous frame. The average value of the deviation between the METAS position and the position indicated by the two interferometers of the RAITH 150 was within ± 15 nm.

STEP 3 – The positions of all the indent centres (in the frame on STEP 1) were then recorded.

STEP 4 – At the end of these measurements, the temperature drift was evaluated from the position of the contamination dot created in STEP 1 – **Figure 7.7b**.

Depending on the machine stabilization time⁷, this drift was typically between 50 and 100 nm.

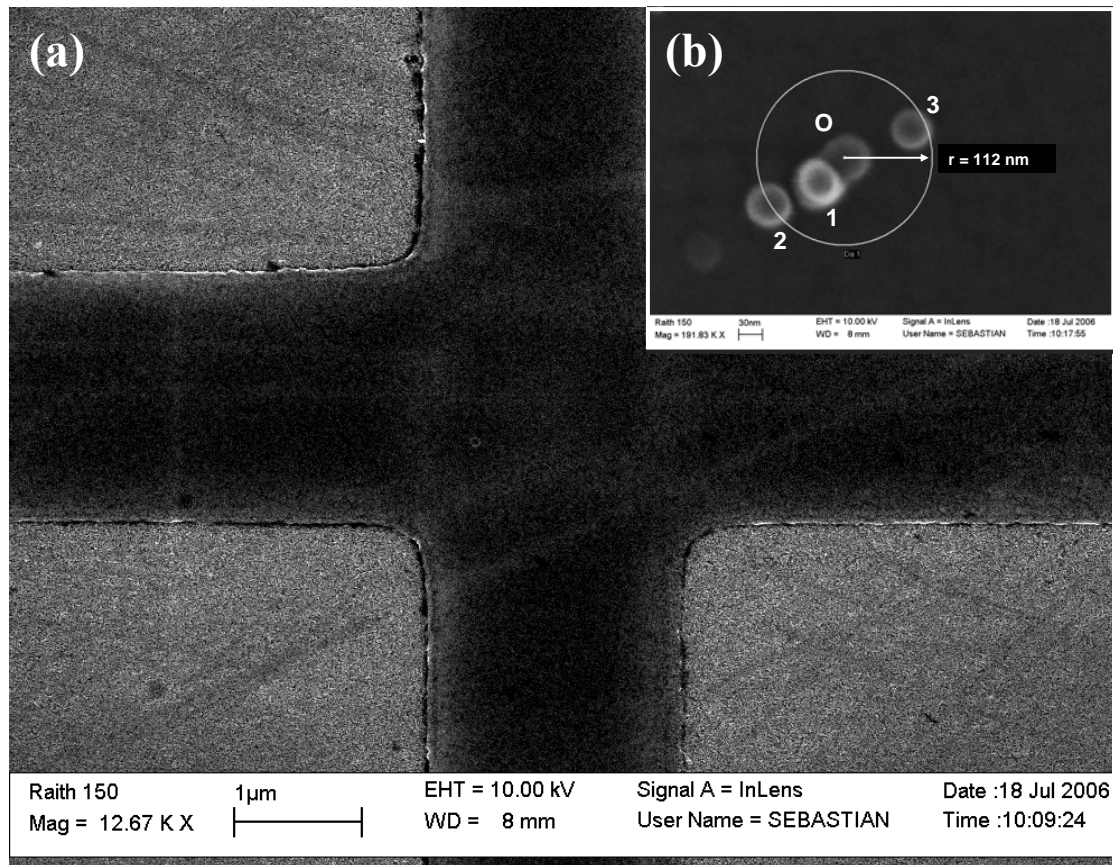


Figure 7.7 – (a): High-resolution SEM image of the standard central cross (used to define the origin of the absolute frame). The centre of the cross was determined with the help of cursors (not represented in this figure for clarity purposes) aligned with the two borders of the cross in each direction. (b): At the centre of the cross, very small *contamination dots* ($\varnothing < 50$ nm) were created in order to evaluate the thermal drift at the end of the measurement session. For example, dot O was used to define the origin of the absolute frame, whereas dots 1, 2 and 3 correspond to the ends of different measurement sessions.

⁷ Classical stabilization times of 1 h corresponded to drifts between 50 and 100 nm. The smallest drift ever obtained was 32 nm during a 45-minute measurement period, after 4 h of machine stabilization time.

7.3.2 – Uncertainty budget and estimation of the measurement accuracy

We believe that different error sources contribute to the overall measuring uncertainty of this method according to the following budget:

- *uncertainty in the calibration of the standard (METAS value)* = $\pm 20 \text{ nm}$
- *uncertainty in the appreciation of the centres of the standard crosses* used to calibrate the RAITH 150 interferometer stages: $\pm 50 \text{ nm}$
- *uncertainty in the appreciation of the centre of the indents*⁸: $\pm 50 \text{ nm}$
- *uncertainty due to thermal drift during measurements of the indents* (depends on the number of indents to be measured and the machine stabilization time): $\pm 100 \text{ nm}$
- *uncertainty due a misalignment between the surfaces of the standard and that of the substrate to be measured* due to manufacturing tolerances (cosine effect): $\pm 20 \text{ nm}$
- *systematic error due to the fact that the indents were produced at 25 °C and measured at 20 °C* (standard metrological temperature), over the 3 mm range: $\pm 15 \text{ nm}$

Since these error sources are independent from each other and according to the previous budget, the **global average uncertainty of this indentation-based verification method lies within**
 $15 + \sqrt{20^2 + 50^2 + 50^2 + 100^2 + 20^2} \approx 140 \text{ nm}$

This value could still be improved in the future if the measurements of the positions of the indents were directly performed by METAS (without intermediate steps). This entails the use of substrates made of appropriate materials having both low hardness⁹ (in order to obtain very large indents with very small loads) and very small thermal expansion coefficients¹⁰.

7.4 – Measurement results

7.4.1 – 1D comparison before/after calibration

In order to compare the accuracy of the robot before and after calibration, we decided in both cases to print a few indents along a line covering a large part (75 %) of the calibrated translational range (and making use of the two planar DOF simultaneously).

The X – Y coordinates were then measured in respect to the frame defined by the standard according to the procedure described previously. We then determined the line corresponding to

⁸ The determination of the centre of the indent could also be performed using **contrast algorithms** (after the SEM image had been acquired). The difference between the position of the centre of the indent determined using a contrast analysis and the same position obtained by means of visual appreciation (with the help of cursors) was observed to be less than $\pm 20 \text{ nm}$. It was decided not to use the contrast-based procedure since it was more time-consuming (therefore generating higher thermal drifts at the end of the measurements).

⁹ Matching low hardness and good surface polishing of the substrate to be indented is also suitable for optimal results.

¹⁰ In the future, the correction of the systematic error due to the difference between the temperatures at which indents are produced and measured could also be introduced, especially if indentation substrates are made of common materials (such as aluminium) having high thermal expansion coefficients.

In this case, residual systematic errors are only due to the uncertainty in the estimation of the absolute value of the temperature.

the best linear fit¹¹ of the coordinates of the indents for both situations (before and after calibration).

It was observed that the maximum deviation of a given indent centre to this line was **up to 5 μm** in the case of the **non-calibrated robot** and **only 63 nm** for the **calibrated robot**.

7.4.2 – 2D errors in the indent positions for the calibrated robot

In order to verify the calibration of the robot translations simultaneously along several directions, a grid of indents was printed on the substrate, according to the geometry represented in **Figure 7.8**.

Once the coordinates of the centres of these indents had been measured by the RAITH 150 in the absolute coordinate frame defined by the standard, these positions had to be processed in order to evaluate the deviations in respect to the nominal coordinates imposed by the robot.

This was performed by defining a new local Cartesian coordinate frame in which the position errors of the indents' centres in respect to their nominal value were minimized. Once this new frame had been defined, the positions of the indents were then expressed in this frame by means of a classical planar coordinate transformation.

Lastly, the errors in respect to the nominal positions imposed by the robot during the indentation session were finally computed for the new coordinates. **Figure 7.9** shows these errors in the X and Y coordinates for the geometry represented in **Figure 7.8**.

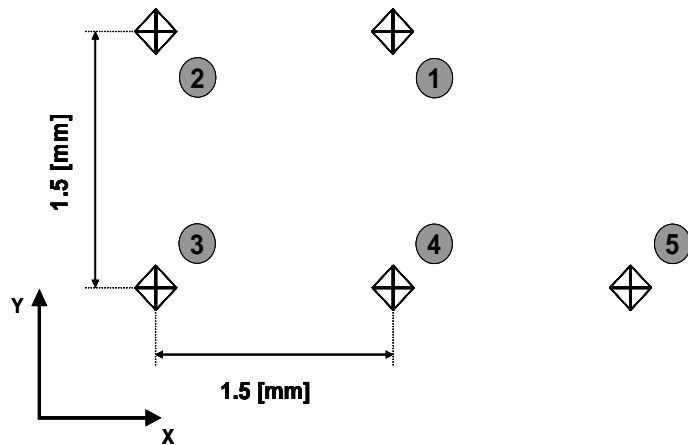


Figure 7.8 – Schematic representation of the arrangement of the different indents imprinted by the robot in order to evaluate the positioning accuracy along several calibrated translational degrees of freedom at the same time.

Figure 7.9 shows errors up to $\pm 300 \text{ nm}$, whereas the same errors after the primary (optical) calibration of the robot were only up to $\pm 100 \text{ nm}$ ($U_{90\%}$).

We believe that this discrepancy is mainly due to the following reasons:

- as opposed to the optical calibration methods, *the effect of the thermal drift* cannot be corrected throughout the entire indentation time¹², which may influence significantly the results;
- as opposed to the optical calibration methods, *the oscillations due to robot position regulation* cannot be averaged, which may also influence the results (up to 100 nm in our case);
- the accuracy of the indentation method is 10 times worse than that of the optical method since it involves several measuring steps before a final value is obtained.

¹¹ The aim of this procedure (which is essentially a form of averaging) is to make the position errors of the indents comparable to the results of the classical optical-based calibration of the robot.

¹² The indentation time in our case was approximately 5 minutes per indent.

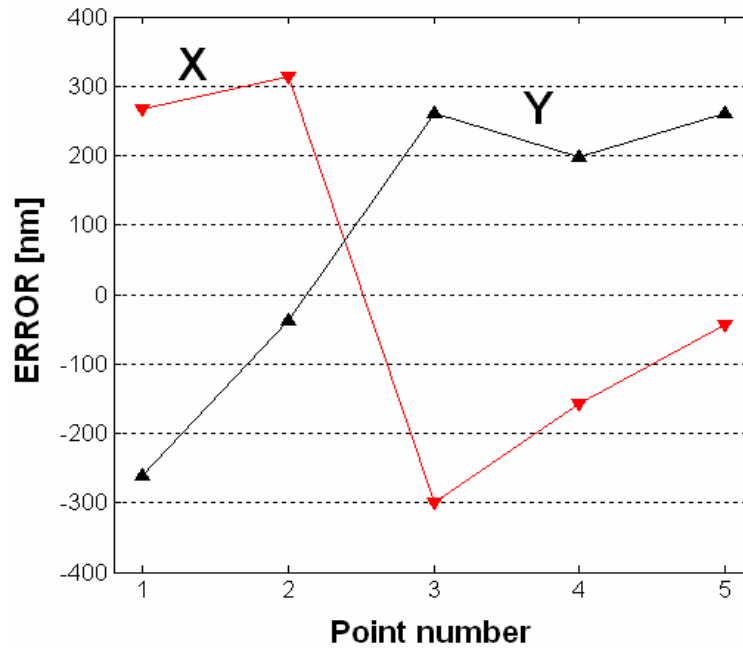


Figure 7.9 – Errors measured in the X and Y positions of the centres of the indents represented in Figure 7.8 relative to the corresponding nominal coordinates imposed by the calibrated robot.

7.4.3 – “Indirect” verification of the 3rd translational DOF

In **sections 7.4.1** and **7.4.2** we presented the results of the errors along two translational DOF of the robot measured directly with the help of an external measuring system (the RAITH 150).

Even if the errors occurring along the third translational DOF (i.e. the one corresponding to the direction of indentation) cannot be evaluated in such a direct way due to the nature of the indentation technique, it is still possible to perform an *indirect evaluation* of these errors using the reading of the end-effector operational coordinates at the exact moment of “touch”, for which the load remains always approximately at the same value (~ 10 mN).

For this purpose we took the information collected during the experiment described in **section 7.4.1** (line of indents).

We then determined the best linear¹³ fit that contained, for each indent, the operational coordinate along the direction of indentation at the peak load.

The errors along this third translational DOF were calculated from the deviations of these operational coordinates from the previous line. This was only possible because of the excellent flatness and roughness of our mirror-polished substrates (supposed¹⁴ to be better than 200 nm (peak-to-valley) over the 3 mm range used to print and measure the indents).

It was observed that these deviations were **up to 6 μm** in the case of the **non-calibrated robot**.

For the **calibrated robot**, these errors could only be estimated with an uncertainty of ± 250 nm since, as mentioned previously, the end-effector was moved by minimal steps of 250 nm during indentation (for time purposes). Despite this “poor” resolution, it was observed that the errors in

¹³ This line corresponded to the orientation of the substrate in respect to the frame in respect to which the robot had been calibrated.

¹⁴ The flatness and roughness were not actually measured, but the value indicated here corresponds to a “reasonable” estimation over the 3 mm range, according to the polishing operator.

the third translational DOF were within the previous resolution interval and, thus, **smaller than ± 250 nm**.

The reader should note however that these results correspond only to a rough experiment in order to demonstrate the feasibility of this indirect evaluation.

In fact, an accurate evaluation (i.e. within the nanometre range) would require:

- a precise “mapping” of the flatness and roughness of the substrate’s indentation zone (3 mm x 3 mm). Only in this way, would the exact contribution of the indentation surface quality be known precisely;
- the use of more accurate load-cells (resolution in the μN range) so that the non-linear deformations occurring during the tip-surface contact are minimized;
- the end-effector should be moved within steps corresponding to the actual robot resolution (10 nm) and a real-time reading of the load during indentation should preferably be adopted (dynamic closed-loop, which was not our case).

Under these conditions¹⁵, we believe that accuracies close to the resolution of the robot should be obtained straightforwardly.

7.5 – Conclusion

In this chapter, we have demonstrated the feasibility of using indentation procedures for verifying the absolute accuracy of calibrated high-precision flexure parallel robots at the sub- μm range. *We chose this technique because the robot is required to execute similar motions to those involved in a machining operation* for which industrial high-precision flexure parallel robots may be used¹⁶, e.g. $\mu\text{-EDM}$ [Jos05].

For the reasons set out in **section 7.4.2**, we believe that, as a primary calibration method, the optical methods described in Chapter 4 are still preferable to indentation techniques.

However, despite the technical limitations of this verification method, indentation procedures have the advantage of providing real physical samples on which the promised accuracy can be verified at any time by any well-equipped metrological institution.

We believe that this fact is of major commercial potential for industries employing high-precision flexure parallel robots on their production lines since, as we have seen in the previous chapters, carrying out optical measurements for the calibration of these robots may be a delicate and time-consuming task (especially in the case of the 6-DOF robot).

If performed periodically, indentation could therefore be used as an industrial “accuracy indicator” defining the ideal¹⁷ time between two consecutive robot calibration operations.

As a final remark, we would like to point out that indentation procedures should be regarded only as a *first* reliable step for verifying the accuracy (with uncertainties in the sub- μm scale) of the translational DOF of industrial calibrated high-precision flexure parallel robots.

In the future, if higher accuracies (similar to that of the interferometer) are sought in these verifications, further techniques should be developed based exclusively on *non-contact methods* (see **paragraph 8.2.2 (c)**).

¹⁵ Such procedure would now be a true *nano-indentation* experiment.

¹⁶ If a high-precision flexure parallel robot has to be used for a given industrial operation, the choice and implementation of the verification method has to be done in close relation to this operation.

¹⁷ In this context, “ideal” means ideal in terms of cost optimization.

Chapter 8 – General conclusion

The work related to this thesis can be seen as a “building-block” contributing to the research on high-precision flexure parallel robots.

The first contributions in this field at the LSRO dealt with the design of flexure parallel robots [Hen00] and with the integration of dynamics and control-related issues during the design phase [Bac03]. A recent work [Nia06] was dedicated to the minimization, through design improvement, of the residual passive DOF in the case of high-precision flexure parallel robots of the “Delta Cube” family.

Despite a careful robot design (after which the passive DOF are minimized), the use of ultra-high resolution actuators and an efficient control strategy, calibration is **always** necessary in order to reach ultra-high absolute accuracies (in the same order of magnitude as resolution), especially when dealing with nanoscale dimensions.

The goal of this thesis was to establish the theoretical and experimental basis for the calibration of multi-DOF high-precision flexure parallel robots¹ at the sub- μm accuracy range.

However, the work presented in this thesis was restricted to the static and load-invariant cases.

8.1 – Summary

A successful calibration of a given high-precision flexure parallel robot is the result of work conducted on three different fronts: **measurements**, **data processing** and **validation procedures**. In this work, solutions were presented for all these three aspects.

This section summarizes the relevant points developed in this thesis as regards these three phases. The reader is also referred to **Appendix D** in which a schematic view of the overall calibration procedure is given, together with the important points to be considered in each elementary phase.

8.1.1 – *Measurements*

Throughout this thesis, it has been observed that collecting measurements within absolute accuracies in the nanometre range is certainly the most challenging and delicate phase in the calibration of a given high-precision flexure parallel robot.

Our “technological goal” was to obtain absolute accuracies after calibration better than ± 100 nm for translations and less than ± 1 arcsec for rotations. This means that the corresponding measuring accuracies have to be at least ± 20 nm and ± 0.2 arcsec.

¹ In cases in which passive DOF influence the reading of the active DOF of the robot (as for the 3-DOF robot studied in this thesis), the engineer is encouraged to consider the solutions and methods recently proposed by Niaritsiry [Nia06] at the design stage, before going through any calibration procedure.

(a) Choice of the measuring devices and/or protocols

To the best of our knowledge, only non-contact devices, in particular optical-based instruments, can guarantee accuracies on the nanometre scale if measuring ranges are a few mm for distances and a few degrees for rotations.

■ If the DOF being calibrated are only *rotations*, angular interferometers and autocollimators can be used. The inconvenience of the latter lies however in their often limited range and/or poor linearity.

■ If the DOF to be calibrated involve *translations*, laser interferometers can be used. However, in this case, rotations ideally have to be suppressed as they corrupt the reading of the translations.

If these rotations are passive DOF, their suppression can only be achieved through re-design or re-assembly of the robot parts; otherwise, the suppression has to be accomplished during the actual measuring procedure by means of closed-loops with external measuring devices.

The 3 and the 6-DOF robots studied in this thesis are examples of the first and second situation, respectively².

A major difficulty encountered during this work lies in the fact that there are no standard high-precision measuring devices able to read the 6 DOF (translations combined with rotations) simultaneously.

This motivated the development of an original 6D measuring protocol. In this protocol, the 6D problem was divided into two separate 3D problems (translations + rotations), for which standard measuring devices are available on the market. An additional step was required at the end of these two 3D calibrations in order to obtain the full 6D data.

In comparison to a 3D calibration, a full 6D calibration is a very complex and time-consuming procedure³. We believe that the “passage 3D → 6D” increases the complexity⁴ and costs by a factor much higher than 2, despite the fact that the number of DOF involved is “only” doubled.

(b) Choice of the absolute reference frame

The choice of the absolute reference frame is crucial for calibration since the data collected will be reported in respect to this frame. Since we are dealing with measurements with sub- μ m accuracy, precisely-manufactured objects (with previously calibrated dimensions) should be used to define the frame.

Precision mirror cubes (like those employed in this thesis) are examples of such objects.

Ideally, the object defining the reference frame should be firmly attached to a heavy support made of a temperature-stable material (such as *Invar*[®]) to which the robot parts should also be attached. This frame should be considered at the robot design stage as a function of the application for which the robot is to be used.

² See **Figure D.2** of **Appendix D**.

³ Measuring time may be reduced in the future by the use of systems able to measure three translations simultaneously (by means of three interferometers), such as the *NanoPositioning and NanoMeasuring Machine* from *SIOS[®] Messtechnik* [Man05 and SIO] or the μ -Coordinate Measuring Machine recently developed by METAS [Mel05 and MET].

⁴ In the case of the 6-DOF robot studied in this thesis, the complexity is mainly due to the existence of several measuring phases and, sometimes, different open and closed-loop configurations in each phase – see **section 4.3**.

(c) Regulation of the measuring environment

We have seen that in order to guarantee an **absolute**⁵ accuracy in the sub- μm range, the regulation of the measuring environment (in particular, the stabilization of the temperatures of the robot and the measuring loop) is of major importance not only to ensure that the data collected is reliable (i.e. truly representative of the robot being calibrated) during the *calibration phase*, but also for the calibration to be effective over the entire *operational period* of the robot.

In this thesis, the measuring environment was protected against mechanical and thermal disturbances by working inside a *thermal chamber*. The temperatures were regulated with the help of Peltier cells according to the information provided by several differential resistor temperature sensors placed in different parts of the robot and the measuring loop.

Implementation of the following solutions, in addition to the use of a temperature regulation system, may help in the future to decrease the effect of temperature variations in the accuracy of the robot during calibration:

- use of *materials with very similar thermal expansion coefficients* (or preferably the same material) in the measuring loop, in order to guarantee homogeneous thermal behaviour (so that temperature drifts will be easier to predict and, thus, to correct for);
- use of *short measuring loops*, so that the overall expansion due to temperature variations is decreased;
- even if this solution is never sufficient at the nanometre range, a “*smart*” *robot design* can also suppress some part of the robot thermal drift [Nia06].

(d) Data collection

The data acquisition procedure must be automated as far as possible so that:

- the related costs can be decreased;
- random errors coming from human operators are suppressed;
- “large” data sets can be collected;
- the actual measurements used for data processing can be collected during periods of minimum external disturbances (nights or week-ends).

Moreover, in order to optimize the measuring accuracy, particular attention has to be paid to the following:

- the temperature drift experienced by the measuring loop can be cancelled through periodic returns to the robot reference position;
- the oscillations in the robot position regulation have to be averaged by using sampling frequencies over the Nyquist limit;
- the robot end-effector must remain with the same load in the same centre of mass. In addition, manipulations or mechanical contacts with the robot parts should be avoided as far as possible, both during and after calibration.

⁵ At the nanometre scale, all objects are constantly moving in respect to one another. Therefore, **absolute frames** do not exist in this scale. Our technological goal is to minimize the magnitude of these relative motions.

In particular, if the robot is to be used for a specific operation, the corresponding end-effector mount should be designed in accordance with this requirement.

8.1.2 – Data processing

Two different methods have been presented for data processing tasks.

■ The first method was called the *model-based approach* and made use of an analytical model relating the motor coordinates of the robot to the operational coordinates of its end-effector.

In most of the cases, this model sought to provide an accurate description of the robot geometry (*physical model*). The parameters to be identified are thus directly related to the dimensions of the robot being calibrated.

Alternatively, general mathematical functions may also be used (*behavioural models*). In this case, the model coefficients are free of any physical meaning and are identified so that the model approximates a given input-output relationship as closely as possible. Polynomial fitting is one of the oldest techniques used to solve general approximation problems.

In the case of high-precision flexure parallel robots, we show that simple polynomial functions can provide better accuracy after calibration than any classical physical model.

■ In the second method, called the *model-free approach*, the input-output relationship is fully or partly approximated in a “black-box” way.

As opposed to a model-based technique, no direct information has to be supplied as regards the form of the correction function that is to be used for obtaining a given accuracy after calibration. In this work, a model-free approach was implemented using *Artificial Neural Networks*, a recent tool originally inspired by biological processes.

In the future, other well-established tools commonly used in function approximation problems, such as B-splines [Hüg05 and Bla06], may also be used to perform this model-free calibration.

When “properly” used, these two approaches provide similar prediction capabilities⁶. Their only difference lies in the amount of data required for the calculation of the model coefficients. In general, for a given accuracy requirement, NN usually require a higher number of training samples than a polynomial function.

In addition, the NN prediction capability seems to be slightly worse than that of a polynomial function when the training data is corrupted with measurement noise⁷.

For both approaches, we show that it is possible to find appropriate models not only for correcting the errors of the IGM but also for predicting the direct relationship between motor coordinates and the corresponding operational coordinates, i.e. even if the geometry of the robot being calibrated remains unknown.

Therefore, the computation of the robot IGM is not necessary from a strict “data processing point of view”.

However, the IGM may be interesting from a “measurement point of view”. For example, in the calibration of the 6-DOF robot, we have seen that the measurement procedure may involve a closed-loop for suppressing the rotations in the motions of the end-effector⁸ (for the purpose of calibrating the translational motions of this robot).

The corrections to be made during this closed-loop can only be accomplished if the end-effector’s primary angular motions are within the measuring range of the autocollimators.

⁶ This conclusion has also been reported by previous researchers [Koz90 and Flu94].

⁷ It is quite difficult to provide a clear explanation to this effect since the differences are relatively small.

⁸ See the “TWR algorithm” of **section 4.3.1 – paragraph (b)**.

8.1.3 – *Verification procedures*

Guaranteeing an absolute accuracy of ± 100 nm in the operations of an industrial high-precision flexure parallel robot represents an enormous challenge today. For this reason, engineers are often faced with the skepticism of customers. Therefore, the possibility of performing different verifications should be available so that the accuracy of a robot calibrated by means of a given method can be verified using one or several alternative measuring methods.

Unfortunately, in the sub- μm accuracy range, the choice of the verification method is as limited as the choice of the measuring instruments able to meet such accuracy requirements.

In this work, we have chosen to use indentation to evaluate the accuracy of the calibrated translational DOF of the robot.

This technique consists of imprinting a mirror-polished surface with a certain number of footprints (or *indents*). The tool is a diamond tip mounted on the end-effector of the calibrated robot and the imprints follow an imposed pattern. Very small peak loads are used (typically in the order of 10 mN) in order to suppress as much as possible the static and dynamic deformations suffered by the robot end-effector during the process⁹ (relative to the original calibration of the robot, performed in a “non-contact” mode).

The measurements of the relative distances between the centres of the different indents can then be used to assess calibration conformity.

So far, the accuracy of this method (± 140 nm) is less satisfactory than the accuracy of the optical method (interferometry) used to collect the data for the primary calibration of the robots.

However, there are two major advantages which make this particular verification technique interesting from an industrial point of view:

- the robot is asked to execute similar motions to those involved in a real machining operation, such as $\mu\text{-EDM}$ [Jos05];
- it provides real physical samples in which the promised accuracy can be verified at any time by any well-equipped metrological institution.

8.2 – Suggestions for future research

In this section, new ideas are outlined concerning open issues that could be investigated in the future in order to improve or extend the methods described in this thesis.

We have chosen to divide this section into two paragraphs. The first paragraph is devoted to the study of totally new research concepts that still require feasibility studies and, therefore, are only suitable for long-term (> 10 years) industrial implementation. The second paragraph focuses on issues related to short-term (< 5 years) industrial implementation.

8.2.1 – *New research challenges*

(a) Development of direct 6D nano-metrology systems

We have seen throughout this report that acquiring reliable measurements with sub- μm accuracy is a very difficult task. It involves expensive instrumentation and highly-skilled operators.

⁹ The indentation process is a quasi-static operation. However, since we are using this technique to evaluate the robot's accuracy, care should also be paid to the minimization of dynamic oscillations (e.g. control).

In particular, we have seen that there is still no standard solution on the market that is capable of performing 6D measurements within nanometre accuracy. It is still the object of fundamental research by different metrology laboratories worldwide.

We believe that specific research has to be done exclusively in this field in order to develop new 6D direct¹⁰ ultra-accurate metrology systems with measuring accuracies better than ± 10 nm and ± 0.1 arcsec over a range of, at least, 10 mm and 10° for translations and rotations, respectively.

Besides the lack of a metrological concept potentially able to fulfil the above technological requirements, the difficulty in reaching such levels of accuracy lies mainly in two issues:

■ First, we believe that such performances can only be obtained by a system having the best solutions for:

- *robot design*: the robot probably has to be designed monolithically if the calibration is to be effective over a long period of time;
- *robot position regulation*: oscillations in the position regulation should not exceed ± 5 nm around the desired motor consign values;
- *environmental regulation*: stabilization of the temperature and relative humidity in the range of $\pm 0.001^\circ\text{C}$ [Law00] and $\pm 1\%$ are probably necessary to really guarantee absolute accuracy at the nanometre scale in the collected data¹¹;
- *mechanical insulation*: efficient vibration damping platforms should be used not only for the data collection during calibration but also for the actual robot operations.

■ Second, perfect control of all the domains that might influence the calibration is of prime importance. In fact, calibration is a procedure that is applied at the end of a product's development. Consequently, the results that can be attained in this phase are always influenced by errors or imperfections occurring in the earlier stages of product development¹². In order to get optimal results at the end of a given calibration procedure, one has to be aware of all the possible errors over the different development stages.

(b) Dynamic calibration

The work reported in this thesis could be naturally extended in order to predict the dynamic behaviour of the robot.

Again, the major obstacle one has to overcome in order to perform a reliable dynamic calibration is the lack of metrological equipment. For example, current interferometers are limited in terms of tolerated scanning rates for fringe counting (in the case of the *SIOS*[®] interferometer, this threshold is $600\text{ mm}\cdot\text{s}^{-1}$ – see **Table 3.1** in **section 3.2.1**).

Only a specialised specific metrological development will permit reliable dynamic calibrations.

¹⁰ The term “direct” means that all the 6 degrees of freedom have to be measured at the same time, without having to suppress some degrees of freedom in order to measure the others (which was the case for the calibration of the translations in this work – see **section 4.3.1**).

Working with direct measuring systems may contribute to reduce the overall measuring time in a 6D calibration.

¹¹ In an ideal situation, these requirements are to be kept not only during the calibration but also during the actual operations for which the robot has to be used. This would of course need additional technology.

¹² For example, in this work we have “suffered” from the parasitic angular variations experienced by the end-effector of the 3-DOF robot. The magnitude of these variations can only be controlled through careful design.

8.2.2 – *Towards industrial implementation*

We believe that short-term investigations should consider adapting our calibration procedures in industry. A successful adaptation would help to maintain in real industrial environments the sub- μm accuracies typically obtained in classical calibration experiments carried out in laboratory conditions.

It is quite difficult to provide an exhaustive list of these adaptations since they are highly dependent on the application for which the robot is to be used. However, this section discusses some adaptations which deserve particular attention.

(a) Real-time correction of external disturbances during measurements

The methods reported in this thesis could be extended in order to deal with the following effects:

- static external loads on the robot end-effector, with varying magnitudes and centres of mass;
- the influence of variations in environmental conditions, such as temperature and humidity variations in the environment in which the robot is being calibrated (or used).

A load-dependent calibration can probably be achieved straightforwardly by measuring a number of different (magnitude, centre of mass) configurations of the end-effector using integrated load-cells and by approximating the collected data using a NN-based approach (or a behavioural deformation model if less measuring points are sought).

In order to accomplish reliable calibration within the nanometre range without having to regulate the measuring environment, two different aspects should be considered:

- the *drift of the reference position* over time, due to expansions of the materials in the measuring loop (expansion of the dead path, in the case of the interferometer);
- the *modification of the robot's geometric dimensions*, which in turn will cause a slight modification in the robot kinematic behaviour.

In order to show the feasibility of this so-called “thermal calibration”, a simple test was made in which we attempted to predict the drift of the reference position measured during the initial period of a given temperature regulation run (during which “large” temperature variations took place) as a function of the temperature variations suffered by the different parts of the measuring loop.

The graph in **Figure 8.1** shows the raw data of this experiment and its corresponding prediction using a NN determined with the help of the algorithm presented in **section 6.3.2**.

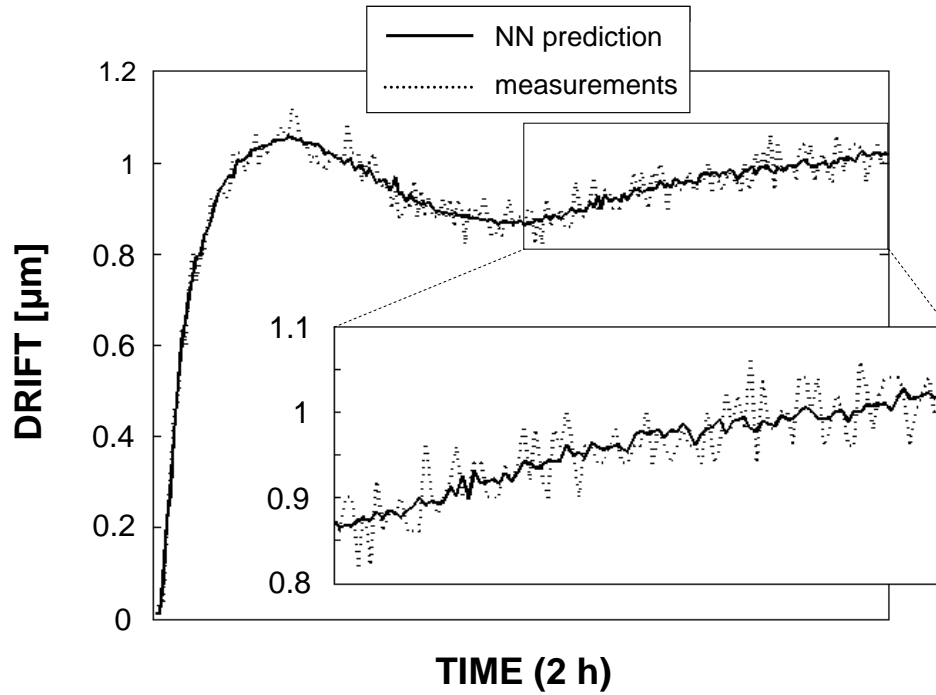


Figure 8.1 – Prediction of the drift experienced by the reference position as a function of the temperature variations in the different parts of the measuring loop, over a period of 2 hours in which large temperature variations take place.

The results of this graph prove that the thermal drift experienced by the reference position can be predicted (within a few tens of nanometres) as a function of the temperature variations occurring in the measuring loop.

In this way, it will be possible to extract from the overall measurement signal (robot + measuring loop), and in “real-time”, the thermal expansions suffered exclusively by the robot if the latter operates in unsteady industrial environments.

As a result, the total measuring time can be reduced, since periodic returns to the reference position therefore become unnecessary.

Despite this preliminary finding, a large amount of work is still necessary to perform a reliable “thermal calibration” with nanometre accuracy¹³.

In particular, the following issues need to be clarified:

- What should be the minimum number of thermal sensors for the optimal “thermal calibration” of a given robot? What is the exact contribution coming from the measuring loop?
- Where should these sensors optimally be placed¹⁴?

Unfortunately, due to a large number of heat (and humidity) sources, performing a successful absolute calibration in the nanometre accuracy range without temperature regulation in “normal” rapidly and highly-varying environments will be a task of tremendous difficulty.

¹³ The idea of correcting deformations due to temperature variations has been already considered in the literature but only in the context of machine tools, at the micrometer scale. Examples of such works in which NN are used for data processing tasks are [Hat96, Sri96, Yan96, Che97, Van97 and Tse02].

However, and to the best of our knowledge, no author performed yet a “thermal calibration” in the nanoscale accuracy domain.

¹⁴ The answer to this question would allow corrections in the position in terms of the temperature variations measured exclusively at these critical locations.

Therefore, we believe that the best solution for robots operating in industrial environments probably lies in a compromise between: (1) working in a thermal chamber inside which only very small temperature variations are allowed and (2) aiming to correct in real-time a robot having its mechanical structure fully exposed to external disturbances.

A cost-effective solution to this compromise could result in a concept in which the robot mobile structure is protected against fast temperature variations occurring in the working environment¹⁵ (protection against large gradients) and the temperature effects over long periods of time are corrected as a function of the readings provided by suitable temperature sensors placed on the robot (correction of small gradients).

(b) Use of an external absolute reference frame

As mentioned previously, the best way to perform the measurements in an “absolute way” would be to work with an **external reference frame** firmly attached to the working support of the robot.

This frame would act as an “absolute frame”. During the calibration of the robot, the operational coordinates would then be measured in a moving frame (internal reference frame) attached to the end-effector in respect to this absolute external frame.

Figure 8.2 below illustrates this scenario in case of distance measurements.

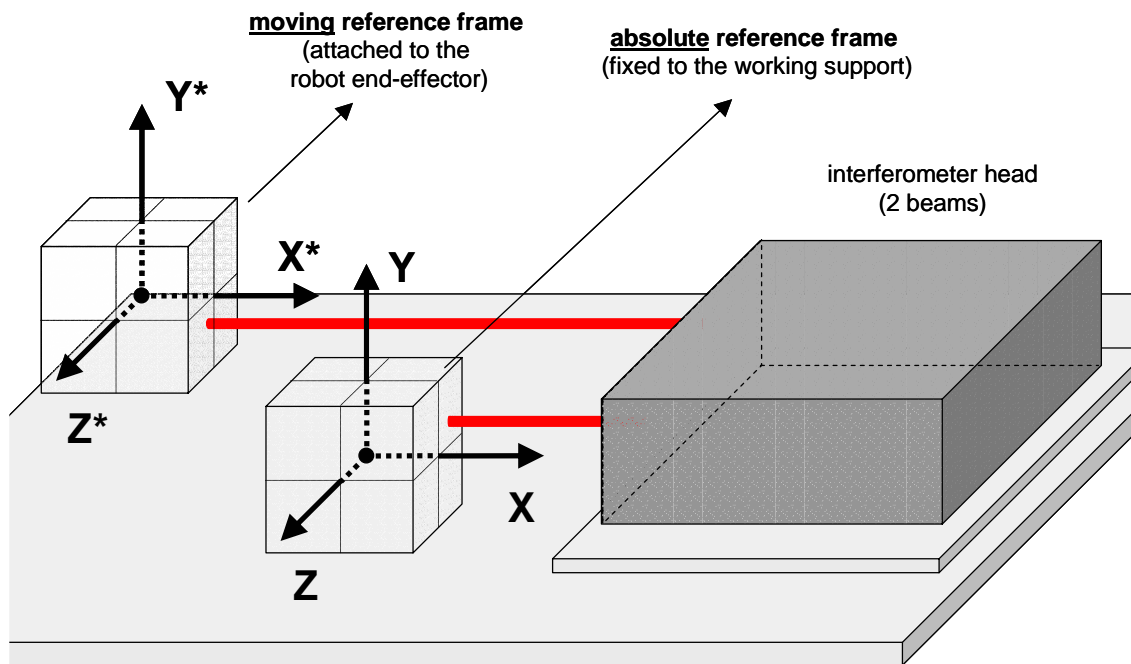


Figure 8.2 – Measuring distances in a differential mode with a 2-beam interferometer.

¹⁵ Mechanical solutions for protecting the robot mobile structure against large gradients are presented in [Nia06] in the case of “Delta Cube” robots.

The major advantage in working with an external absolute frame of this type lies in the fact that the thermal drift experienced by the measuring loop during the measuring period could be cancelled straightforwardly.

Unfortunately, costs of developing multi-dimensional (3D/6D) high-precision measuring systems making use of such differential operating mode are highly prohibitive.

Last but not least, particular attention should also be paid to the fixation of the tool in the end-effector. In fact, in the case of a given industrial operation making use of the 6 DOF simultaneously, the accuracy with which the distance between the functional tool and the position of the robot end-effector that was considered for calibration is known may have a critical influence. **Appendix C** provides an insightful and complete discussion of this issue.

(c) Implementation of new methods for verifying calibration conformity

In this work, we proved that indentation can be used to assess the accuracy of the translational motions of a given high-precision flexure parallel robot within sub- μm accuracy. Even if small loads ($\sim 10\text{ mN}$) were applied to the robot end-effector, this technique still remains a contact-based method and, therefore, will have a finite accuracy.

We suggest the use of **non-contact methods** in the future since the robot itself has to be calibrated also in a non-contact way. *2D grid encoders*, like those marketed by *Heidenhain*[®] GmbH for machine-tools (**Figure 8.3**), could be used for this purpose.

Unfortunately, at the time this thesis was being written, such systems were still largely beyond our accuracy requirements.

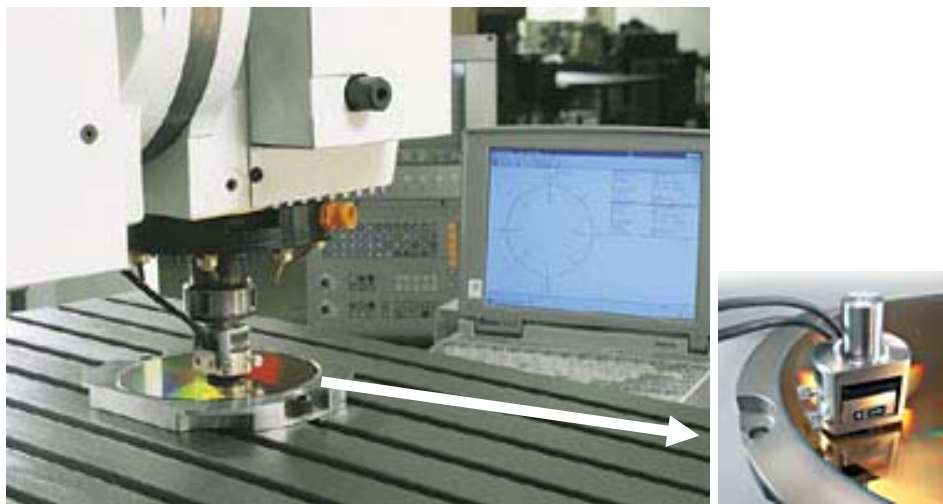


Figure 8.3 – Photographic view of the 2 D grid encoder (model KG182) from *Heidenhain*[®] GmbH.

Finally, in the particular case of a robot being used for machining tasks (e.g. $\mu\text{-EDM}$ [Jos05]), note that the implementation of such a non-contact verification method would have the major advantage of separating the accuracy of the motions executed by the calibrated robot from the accuracy of the manufacturing process itself.

8.3 – Concluding remark

Measuring within accuracies in the nanometre range is far from being an easy task, even for metrologists. In order to illustrate such level of difficulty, we would like to conclude this report by reporting the result of a recent investigation in the field of nano-metrology.

In order to evaluate the global comparability of length calibrations by metrology institutes on high-quality line scales, an international comparison (called NANO3 [Bos03] and completed in 2003) was recently conducted in which 13 institutes took part¹⁶.

The transfer standards used were two line scales with graduated lengths of 280 mm fabricated by *Heidenhain*[®] GmbH (Germany) from the temperature-stable substrate materials *Zerodur*[®] and quartz using the most recent lithography techniques.

The measuring uncertainties evaluated by the participants over the full 280 mm graduation¹⁷ showed variations ranging from ± 30 nm to ± 300 nm.

In the period between 1999 and 2002, similar international comparisons have also been conducted in order to evaluate the traceability of step height (NANO2 [Koe03]) and 1D pitch (NANO4 [Mel01]) measurements at the nanoscale.

¹⁶ The laboratory that served as pilot for this comparison was the German National Metrology Institute (PTB) in Braunschweig. METAS was among the participants.

¹⁷ If the measuring range was restricted to the one of this thesis (4 mm), the smallest uncertainty (with a 95% confidence interval) among the participants would be approximately **6 nm**.

APPENDICES

Appendix A

Measuring instrumentation

Abstract – This appendix should be regarded as a supplement to **Section 3.2**. We provide a brief description of the operating principles of the three measuring devices used in this thesis (SIOS[®] laser interferometer, Keyence[®] laser displacements sensors and Newport[®] electronic autocollimators). In addition, two essential metrological concepts (linearity and sampling frequency) related to the use of any measuring device are illustrated. Finally, we discuss an important issue related to the use of the Keyence[®] sensors in this thesis.

A.1 – SIOS[®] SP 2000 laser interferometer

Figure A.1 shows the basic operating principle of the homodyne laser interferometer.

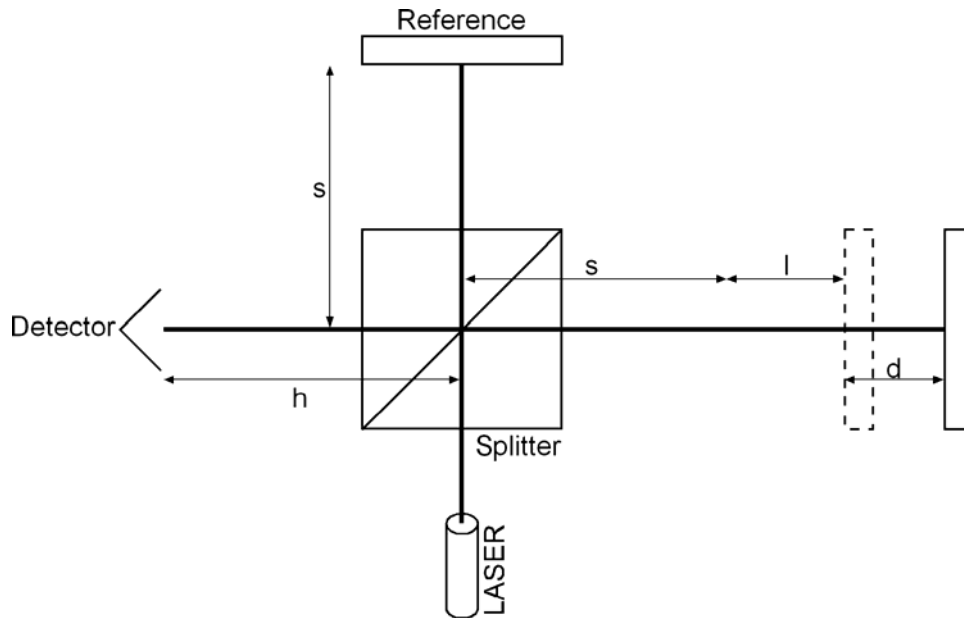


Figure A.1 – Basic operating principle of the laser interferometer, showing the trajectory of the measuring beam during a typical measurement. The distance l is often called the **dead-path** while d is the distance to be measured.

A laser beam coming from the optical head is split into 2 different beams: a first beam is directly reflected by the measurand while the second is reflected by a reference mirror. These 2 beams *interfere* when they return to the splitter. The information of the distance measured is “contained” in the interference pattern and is observed in a detector.

General mathematical formulas

■ Electromagnetic waves

The **power** vector of the electromagnetic wave is given by:

$$\underline{\mathbf{S}} = \underline{\mathbf{E}} \times \underline{\mathbf{H}} = \underline{\mathbf{S}}_0 \cdot \mathbf{e}^{j(\omega t - \mathbf{q} \cdot \mathbf{x})} \quad (\text{A1})$$

where $\omega = 2\pi \cdot f$, $q = \frac{2\pi}{\lambda}$, t is the time, x is the traveled path, f is the frequency of the electromagnetic wave and λ is the wavelength.

The intensity of the electromagnetic wave is simply:

$$\mathbf{I} = \underline{\mathbf{S}}^T \cdot \underline{\mathbf{S}} = |\underline{\mathbf{S}}|^2 \quad (\text{A2})$$

■ Interference between the 2 waves

First wave (reflected by the measurand mirror):

$$\underline{\mathbf{S}}_M = \underline{\mathbf{S}}_0 \cdot e^{j[\omega t - q \cdot (2s + 2l + 2d + h)]} \quad (\text{A3})$$

Second wave (reflected by the reference mirror):

$$\underline{\mathbf{S}}_R = \underline{\mathbf{S}}_0 \cdot e^{j[\omega t - q \cdot (2s + h)]} \quad (\text{A4})$$

Interference wave:

$$\underline{\mathbf{S}} = \underline{\mathbf{S}}_M + \underline{\mathbf{S}}_R = \underline{\mathbf{S}}_0 \cdot e^{j[\omega t - q \cdot (2s + h)]} \cdot [1 + e^{-2jq \cdot (l + d)}] \quad (\text{A5})$$

According to **equation A2**, the intensity of the interference wave is then:

$$\mathbf{I} = \underline{\mathbf{S}}^T \cdot \underline{\mathbf{S}} = |\underline{\mathbf{S}}_0|^2 \cdot [1 + e^{-2jq \cdot (l + d)}] \cdot [1 + e^{2jq \cdot (l + d)}] = 2 \cdot \mathbf{I}_0 \cdot [1 + \cos\left(4\pi \cdot \frac{d + l}{\lambda}\right)] \quad (\text{A6})$$

if we let $\mathbf{I}_0 = |\underline{\mathbf{S}}_0|^2$

■ Displacement reading

Intensity period: $\frac{\lambda}{2}$

Maximum at: $d_{\max, i} = \frac{\lambda}{2} \cdot i - l$

Quantification: $d = \frac{\lambda}{2 \cdot z} \cdot k - l$ with z = number of quantification intervals and k = number of fringe counts

During a given measurement, the displayed reading Δd is calculated from Δk :

$$\begin{aligned} k &= \frac{2 \cdot z}{\lambda} \cdot (d + l) \Rightarrow \Delta k = k - k_0 = \frac{2 \cdot z}{\lambda} \cdot (d + l) - \frac{2 \cdot z}{\lambda_0} \cdot (d_0 + l_0) \Rightarrow \\ d &= \frac{\lambda}{2 \cdot z} \cdot \Delta k + \frac{\lambda}{\lambda_0} \cdot (d_0 + l_0) - l \Rightarrow \boxed{\Delta d = \frac{\lambda}{2 \cdot z} \cdot \Delta k + \frac{\lambda}{\lambda_0} \cdot (d_0 + l_0) - l - d_0} \end{aligned} \quad (\text{A7})$$

A.2 – Keyence® LC 2420/2430 laser displacement sensors

Figure A.2 shows the operating principle (**laser triangulation**) of the Keyence® LC 2420/2430 laser displacement sensors [KEY].

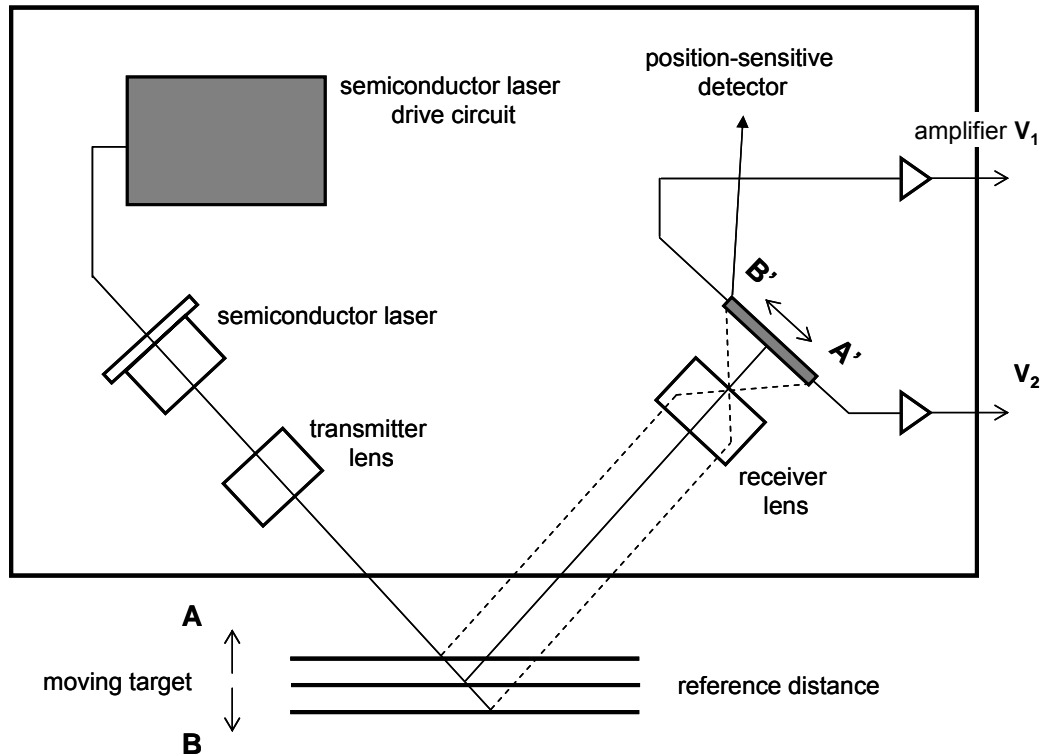


Figure A.2 – Scheme of the operating principle of the Keyence® LC 2420/2430 laser displacement sensors.

When a target moves between **A** and **B** in the above figure, the semiconductor laser beam moves accordingly between **A'** and **B'** in the position-sensitive detector of the sensor head. The electric signal generated by the beam displacement is then converted into a digital signal. After data processing, the measurement results are displayed and output.

A.3 – NewPort® LDS 1000 electronic autocollimator

Figure A.3 shows the basic principle of autocollimation [LDS].

■ A **classical autocollimator** uses a back illuminated cross light reticle **A**, located at the back of the focal plane of a collimating lens **B**. The consequent image is projected to infinity to be reflected back to the instrument with a plane reflecting mirror **C**.

The reflected image is focused on the back of the focal plane of the collimating lens. A beam splitter **D** is used to recover 50 % of the returned light to form the source reticle. The “autocollimated” image can be observed with a measuring eyepiece (position sensing device) **E**. For each angular movement of the mirror **C**, a lateral displacement can be seen for the image

reflected on the back of the focal plane of the collimated lens. If the value of the focal length of the collimated lens is “F”, then the lateral displacement will be

$$\Delta Y = F \cdot \tan(2 \cdot \Delta\theta) \quad (\text{A8})$$

where $\Delta\theta$ is the angular displacement of the mirror.

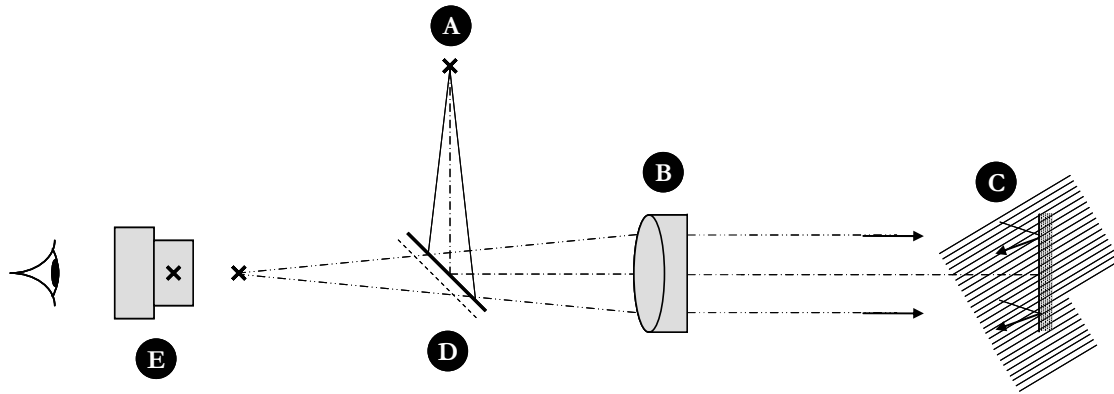


Figure A.3 – Basic principle of the classical autocollimation, according to reference [LDS].

■ In the case of an **electronic autocollimator** it is possible to perform measurements in an automatic way. In fact, the measuring eyepiece (E in **Figure A.3**) is now replaced by a **position-sensitive device** (PSD). Moreover, the source reticle is a **laser diode**.

The PSD is an electronic device that delivers analog signals proportional to the displacement of the spot light position. These two analog signals are then converted into digital signals. Those values are the ΔY of equation A8. At this point it is possible to calculate the angular displacements.

A.4 – On the concepts of linearity and sampling frequency

(a) – Linearity

The concept of **linearity** of a given measuring device is illustrated in **Figure A.4**. This term is often employed by manufacturers of measuring instruments, instead of “accuracy”¹.

Ideally, the reading of a given measurement device would be identical to the physical parameter to be measured, and the relationship between the reading and that physical value would be represented by a straight line.

Actual measurements, however, deviate slightly from the ideal line. The tolerance range in relation to this ideal line is called *linearity*.

(b) – Sampling frequency

When a given measurement device is reading the variation of some physical parameter, the **sampling frequency** is defined as the number of measured samples taken per second.

¹ In fact, the term “accuracy”, as employed throughout this thesis, includes linearity (as defined here), among other errors (approximation capability of the model used for data processing, temperature effects, ...)

In our case, the adjustment of this parameter is essential in order to ensure maximum accuracy in the data collected.

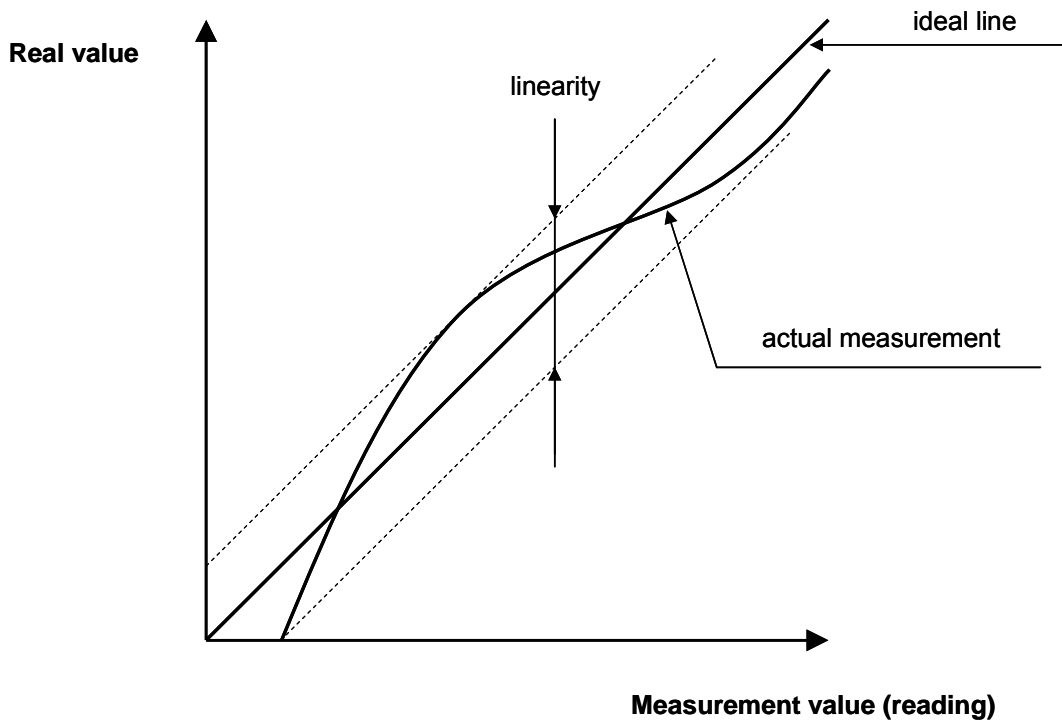


Figure A.4 – Schematic illustration of **linearity** of a measuring device used to read the variation of a given physical parameter.

In fact, the robot controller position regulator sets the different displacements read in the *Heidenhain*[®] rules to given consign static values. However, in reality, dynamic oscillations take place around this consign. These oscillations in motor coordinates will, in turn, cause similar oscillations in the operational coordinates of the robot end-effector. It is therefore desirable to suppress the influence of these oscillations during the measurement in order to collect data that is truly representative of the robot static behaviour, without loss of information.

A fundamental rule in signal processing – the **Nyquist principle**, states that the sampling rate must be at least twice the frequency of the signal to be sampled. If the sampling rate is insufficient, then higher-frequency components are “undersampled” and appear shifted to lower frequencies². These frequency-shifted components are called *aliases*.

A common method for suppressing the influence of dynamic oscillations on a given measurement is, therefore, to use sampling frequencies higher than the Nyquist limit.

As it may not always be possible to employ this solution, an alternative method is to use well-dimensioned **anti-aliasing filters**. These are lowpass filters acting before the A/D conversion.

² In our case, **undersampling** implies that the mean measurement value recorded will not reflect the actual behaviour of the robot. The consequence of an undersampled measurement would be a loss of accuracy in the calibration procedure.

A.5 – On the use of the Keyence[®] sensors in our 6D measuring procedure

In **Chapter 4**, we proposed a novel indirect measuring procedure capable of collecting 6D data (translations combined with rotations) with sub- μm accuracy. This procedure comprises, in particular, a phase in which three Keyence[®] LC laser sensors are used to force (through a closed-loop action) the robot end-effector to execute rotations around a fixed centre of rotation.

It is of prime importance for the reader to understand that **these sensors are NOT used to measure any distance but rather for repeatability purposes i.e. set the sphere mounted on the robot end-effector always to a position for which the readings of the three sensors indicate “zero” simultaneously.**

The goal of this section is to prove mathematically that, **for each fixed position of these sensors, there is only one geometrical position in the space for which the sensors indicate “zero” simultaneously.**

As a consequence of this, the RWT closed-loop required in our 6D measuring procedure guarantees to find always the solution that is physically relevant which unequivocally ascertains the effectiveness of the 6D measuring protocol proposed in this thesis.

(a) – Errors in the use of three Keyence[®] sensors reading the position of a sphere

As indicated in **Section A.2** of this appendix, the Keyence[®] sensors operate according to the principle of laser triangulation (see **Figure A.2**).

However, due to the particular configuration in which they are used in this work (reflection on a spherical surface), their reading will be corrupted by parasitic motions.

Therefore, a careful geometric analysis is required in order to quantify the different contributions to the signal measured by the sensor.

Two different situations can occur.

■ Displacement of the sphere along the direction of interest³

Suppose that the sphere moves of **D** along the direction of interest (see **Figure A.5**).

In this case, the reading of the Keyence[®] will be made of a principal component (as if the reflective surface was a perfectly flat plane) and a parasitic component.

- The *principal component* is simply:

$$r_{\text{principal}} = \frac{D}{\cos(\theta)} \quad (\text{A8})$$

where θ is half of the angle formed by transmitted and received beams of the sensor.

³ In this context, the “direction of interest” is the direction along which the sensor is mounted.

- The *parasitic component* is given by:

$$r_{\text{parasitic}} = \tan(2 \cdot \alpha) \cdot \frac{L}{\cos(\theta)} \quad (\text{A9})$$

where:

$$\alpha = \arcsin\left(\frac{D \cdot \tan(\theta)}{R}\right) \quad (\text{A10})$$

R is the radius of the sphere and L is the working distance (to moving target).

When the sphere physically moves of D along the direction of interest, the *Keyence*[®] will thus read:

$$R_{\text{principal}} = \frac{D}{\cos(\theta)} + \tan\left(2 \cdot \arcsin\left(\frac{D \cdot \tan(\theta)}{R}\right)\right) \cdot \frac{L}{\cos(\theta)} \quad (\text{A11})$$

■ Displacement of the sphere along a lateral direction

Suppose that the sphere moves of T along a direction that is orthogonal to that along which the *Keyence*[®] is mounted (see **Figure A.6**).

In this case, the sensor reading will only be the result of a *parasitic motion* whose magnitude is:

$$r_{\text{parasitic}} = \tan(2 \cdot \alpha) \cdot \frac{L}{\cos(\theta)} + \frac{R \left(1 - \cos\left(\frac{T}{R}\right)\right)}{\cos(\theta)} \quad (\text{A12})$$

where:

$$\alpha = \arcsin\left(\frac{T + R \cdot \tan(\theta) \cdot \left(1 - \cos\left(\frac{T}{R}\right)\right)}{R}\right) \quad (\text{A13})$$

Therefore:

$$R_{\text{lateral}} = r_{\text{parasitic}} = \tan\left(2 \cdot \arcsin\left(\frac{T}{R} + \tan(\theta) \cdot \left(1 - \cos\left(\frac{T}{R}\right)\right)\right)\right) \cdot \frac{L}{\cos(\theta)} + \frac{R}{\cos(\theta)} \cdot \left(1 - \cos\left(\frac{T}{R}\right)\right) \quad (\text{A14})$$

Important remark: attending to the dimension of our sphere ($R = 7.5$ mm) and considering the intrinsic properties of our sensors (values of L and θ), expressions **A11** and **A14** can be approximated (within errors below 30 nm) by linear functions in respect to D and T

respectively, providing that the sphere remains close ($< 1 \mu\text{m}$) to the absolute zeros of the sensors.

This implies that:

$$\begin{cases} \frac{\mathbf{R}_{\text{principal}}}{\mathbf{D}} \cong \mathbf{K}_1 \\ \frac{\mathbf{R}_{\text{lateral}}}{\mathbf{T}} \cong \mathbf{K}_2 \end{cases} \quad (\text{A15})$$

where \mathbf{K}_1 and \mathbf{K}_2 are constant values.

■ Numerical values in the case of our sensors

- In the case of the model LC-2420, we have $\theta = 31.5^\circ$ and $L = 10 \text{ mm}$, which yields:

$$\begin{cases} \mathbf{K}_1 \cong 3.09 \\ \mathbf{K}_2 \cong 3.13 \end{cases}$$

- For the model LC-2430, we have $\theta = 22.5^\circ$ and $L = 30 \text{ mm}$, which yields:

$$\begin{cases} \mathbf{K}_1^* \cong 4.67 \\ \mathbf{K}_2^* \cong 8.66 \end{cases}$$

(b) – Using the three *Keyence*[®] sensors for “zero detection” purposes

According to the above-mentioned, for a real displacement $(\mathbf{X} \ \mathbf{Y} \ \mathbf{Z})^T$ of the sphere, the corresponding sensor's readings $(\mathbf{X}_{\text{reading}} \ \mathbf{Y}_{\text{reading}} \ \mathbf{Z}_{\text{reading}})^T$ can be written as follows:

$$\begin{bmatrix} \mathbf{X}_{\text{reading}} \\ \mathbf{Y}_{\text{reading}} \\ \mathbf{Z}_{\text{reading}} \end{bmatrix} = \underbrace{\begin{bmatrix} \mathbf{K}_1^* & \mathbf{K}_2^* & \mathbf{K}_2^* \\ \mathbf{K}_2 & \mathbf{K}_1 & \mathbf{K}_2 \\ \mathbf{K}_2^* & \mathbf{K}_2 & \mathbf{K}_1 \end{bmatrix}}_{\mathbf{A}} \cdot \begin{bmatrix} \mathbf{X} \\ \mathbf{Y} \\ \mathbf{Z} \end{bmatrix}$$

Attending to the values of the coefficients of our sensors, we can see that:

$$\det(\mathbf{A}) \neq 0$$

Therefore, only one position in space will correspond to the situation for which the readings of the three *Keyence*[®] sensors are at “zero” **simultaneously**, i.e.

$$\begin{bmatrix} \mathbf{X}_{\text{reading}} \\ \mathbf{Y}_{\text{reading}} \\ \mathbf{Z}_{\text{reading}} \end{bmatrix} = \begin{bmatrix} 0 \\ 0 \\ 0 \end{bmatrix} \Rightarrow \begin{bmatrix} \mathbf{X} \\ \mathbf{Y} \\ \mathbf{Z} \end{bmatrix} = \begin{bmatrix} 0 \\ 0 \\ 0 \end{bmatrix}$$

QUOD ERAT DEMONSTRATUM

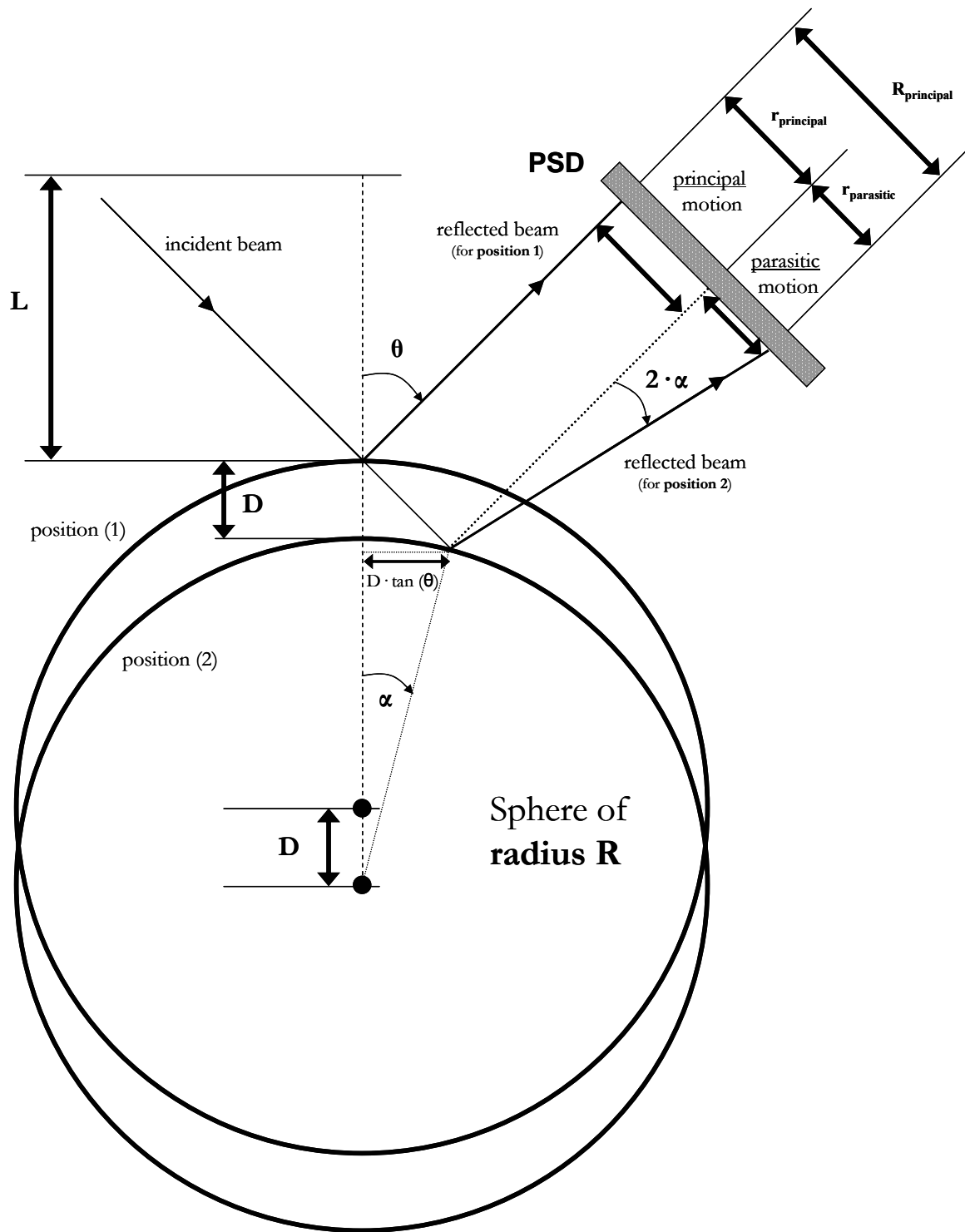


Figure A.5 – Different contributions to the reading of a Keyence® triangulation laser sensor for a given displacement executed by the sphere along the direction of interest.

In this case, contributions are either from the principal motion or from parasitic motions (due to the spherical shape of the reflective surface).

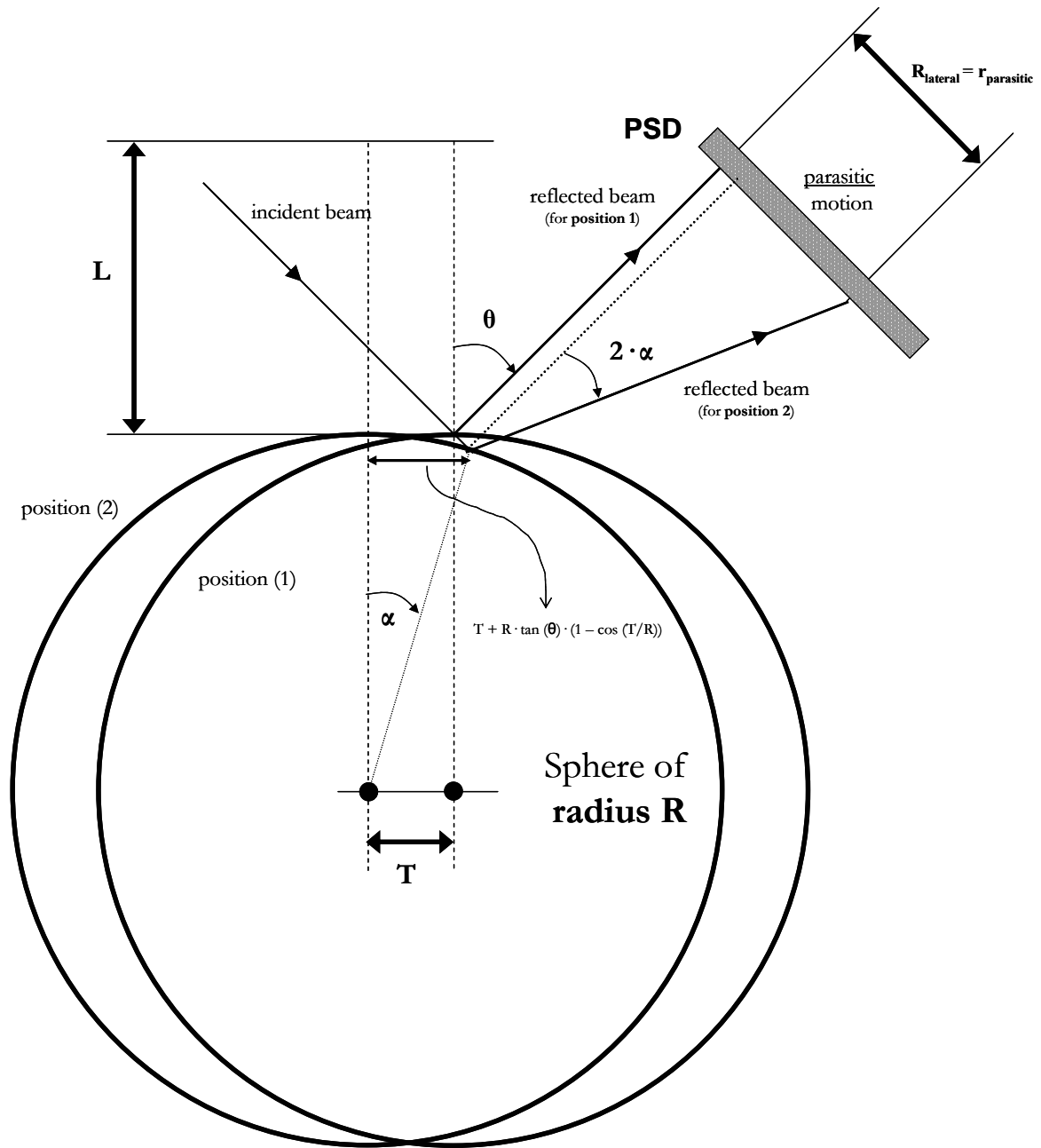


Figure A.6 – Different contributions to the reading of a Keyence® triangulation laser sensor for a given displacement executed by the sphere along a lateral direction.
In this case, contributions are exclusively the result of parasitic motions (due to the spherical shape of the reflective surface).

Appendix B

Effect of the residual passive angular variations on the calibration of the active DOF of the 3-DOF robot

Abstract – As mentioned in **section 4.2**, the calibration of the 3-DOF robot was performed by defining an absolute reference frame with an origin at the centre of the mirror cube. It was observed experimentally that the robot end-effector experienced residual passive angular variations throughout its workspace (which cannot be corrected). This section presents a rigorous analysis of the effect of these angular variations on the reading of the translations of the centre of the cube (functional point to be calibrated). A sensitivity study is performed on the basis of the analytical relations derived.

B.1 – Preliminary analysis in the 2D case

Let us consider in this section the situation in **Figure B.1**. This figure illustrates a case in which the laser interferometer is reading a translation along the Y-axis (as defined by the cube) experienced by the robot end-effector.

An angular variation (whose magnitude has been exaggerated in the figure for clarity purposes) around Z-axis, θ , is corrupting the interferometer reading Y_m .

The goal is to find the relationship between the translation Y experienced by the centre of the cube and the reading Y_m , i.e. when the reading surface goes from position 1 to position 2.

α is the angle that quantifies the error in the orthogonality between the surface of the cube being used for this measurement and the one taken as reference (value indicated by the manufacturer). e_x is an Abbe offset that indicates how centered the laser measuring spot is in respect to the centre of the cube (in X direction).

C_1 is the centre of the cube corresponding to the position of the surface in position 1. C_2 corresponds to position 2.

(a) Derivation using basic trigonometry

From **Figure B.1**, we have:

$$\delta = \tan(\theta) \cdot \left[\mathbf{a}_2 + \mathbf{r} \cdot \frac{1 - \cos(\theta)}{\sin(\theta)} - \mathbf{e}_x \right] \quad (\text{B1})$$

and

$$Y_m = \mathbf{a}_1 - \delta \quad (\text{B2})$$

Seeing that

$$\begin{cases} \mathbf{a}_1 = \mathbf{Y} \cdot \cos(\alpha) - \mathbf{X} \cdot \sin(\alpha) \\ \mathbf{a}_2 = \mathbf{Y} \cdot \cos(\alpha) + \mathbf{X} \cdot \sin(\alpha) \end{cases} \quad (\text{B3})$$

we have:

$$Y_m = \mathbf{Y} \cdot \cos(\alpha) - \mathbf{X} \cdot \sin(\alpha) - \tan(\theta) \cdot \left[\mathbf{Y} \cdot \cos(\alpha) + \mathbf{X} \cdot \sin(\alpha) + \mathbf{r} \cdot \frac{1 - \cos(\theta)}{\sin(\theta)} - \mathbf{e}_x \right] \quad (\text{B4})$$

(b) Derivation using a coordinate transformation approach

Let us consider an initial Cartesian frame having the origin at \mathbf{M}_0 and oriented in the same way as the surface of the cube corresponding to position 1.

- In order to go from point \mathbf{M}_0 to point \mathbf{M}_1 , the **translation** $\mathbf{A}_1 = \mathbf{T}(\vec{\mathbf{u}} = (-\mathbf{e}_x \ 0 \ 0))$ is needed.
- From point \mathbf{M}_1 to point \mathbf{C}_1 , we need the **translation** $\mathbf{A}_2 = \mathbf{T}(\vec{\mathbf{v}} = (0 \ \mathbf{r} \ 0))$.
- From point \mathbf{C}_1 to point \mathbf{C}_2 , the **rotation** $\mathbf{A}_3 = \mathbf{R}(-\alpha, \mathbf{Z})$ followed by the **translation** $\mathbf{A}_4 = \mathbf{T}(\vec{\mathbf{w}} = (\mathbf{X} \ \mathbf{Y} \ 0))$ are required.
- In order to go from the point \mathbf{C}_2 to point \mathbf{P} , the **rotation** $\mathbf{A}_5 = \mathbf{R}(\alpha + \theta, \mathbf{Z})$ followed by the **translation** $\mathbf{A}_6 = \mathbf{T}(\vec{\mathbf{b}} = (0 \ -\mathbf{r} \ 0))$ are needed.

The coordinates of P relative to the initial frame are determined by multiplying the above matrices:

$$\begin{cases} \mathbf{x}(\mathbf{P}) = \mathbf{X} \cdot \cos(\alpha) + \mathbf{Y} \cdot \sin(\alpha) + \mathbf{r} \cdot \sin(\theta) - \mathbf{e}_x \\ \mathbf{y}(\mathbf{P}) = \mathbf{r} \cdot [1 - \cos(\theta)] + \mathbf{Y} \cdot \cos(\alpha) - \mathbf{X} \cdot \sin(\alpha) \\ \mathbf{z}(\mathbf{P}) = 0 \end{cases} \quad (\text{B5})$$

The surface of the mirror in position 2 can be modelled by the following linear law:

$$\mathbf{y} = \tan(\theta) \cdot \mathbf{x} + \mathbf{Y}_m \quad (\text{B6})$$

The combination of equations (B.5) and (B.6) yields the desired relationship relating the reading of the interferometer to the real displacement at the centre of the cube:

$$\mathbf{Y}_m = \sec(\theta) \cdot \{ \mathbf{r} \cdot [\cos(\theta) - 1] + \mathbf{Y} \cdot \cos(\theta + \alpha) - \mathbf{X} \cdot \sin(\theta + \alpha) + \sin(\theta) \cdot \mathbf{e}_x \} \quad (\text{B7})$$

The verification of the equivalence between expressions (B.4) and (B.7) can be performed easily with the help of standard algebraic computation software such as *Mathematica*[®].

B.2 – General case in 3D

The extension of the previous 2D expressions to the general 3D case is straightforward if coordinate transformations are used.

For the sake of clarity, only the **final 3D general expressions** are given below, leaving their step-by-step derivation as a simple mathematical exercise for the reader:

$$\begin{aligned} \mathbf{X}_m = & \mathbf{Y} \cdot \sin(\alpha_Z) - \mathbf{e}_Z \cdot \sec(\theta_Z) \cdot \tan(\theta_Y) - \mathbf{r} + \sec(\theta_Z) \cdot \{ \mathbf{X} \cdot \cos(\alpha_Y) \cdot \cos(\alpha_Z + \theta_Z) + \\ & \mathbf{r} \cdot \sec(\theta_Y) - [\mathbf{Z} \cdot \cos(\alpha_Y) - \mathbf{Y} \cdot \sin(\alpha_Y)] \cdot \tan(\theta_Y) + \mathbf{Z} \cdot \sin(\alpha_Y) \cdot \sin(\alpha_Z) \cdot \tan(\theta_Z) \} - \\ & \mathbf{e}_Y \cdot \tan(\theta_Z) + \cos(\alpha_Z) \cdot [\mathbf{Y} \cdot \tan(\theta_Z) - \mathbf{Z} \cdot \sin(\alpha_Y)] \end{aligned} \quad (\text{B8})$$

$$\begin{aligned} \mathbf{Y}_m = & -\mathbf{X} \cdot \sin(\alpha_Z) - \mathbf{e}_Z \cdot \sec(\theta_Z) \cdot \tan(\theta_X) + \mathbf{r} + \sec(\theta_Z) \cdot \{\mathbf{Y} \cdot \cos(\alpha_X) \cdot \cos(\alpha_Z + \theta_Z) - \\ & \mathbf{r} \cdot \sec(\theta_X) + [\mathbf{Z} \cdot \cos(\alpha_X) - \mathbf{Y} \cdot \sin(\alpha_X)] \cdot \tan(\theta_X) - \mathbf{Z} \cdot \sin(\alpha_X) \cdot \sin(\alpha_Z) \cdot \tan(\theta_Z)\} + \\ & \mathbf{e}_X \cdot \tan(\theta_Z) + \cos(\alpha_Z) \cdot [-\mathbf{X} \cdot \tan(\theta_Z) + \mathbf{Z} \cdot \sin(\alpha_X)] \end{aligned} \quad (\text{B9})$$

$$\begin{aligned} \mathbf{Z}_m = & \mathbf{X} \cdot \sin(\alpha_Y) - \mathbf{e}_Y \cdot \sec(\theta_Y) \cdot \tan(\theta_X) + \mathbf{r} - \sec(\theta_Y) \cdot \{-\mathbf{Z} \cdot \cos(\alpha_X) \cdot \cos(\alpha_Y + \theta_Y) + \\ & \mathbf{r} \cdot \sec(\theta_X) + [\mathbf{Y} \cdot \cos(\alpha_X) + \mathbf{Z} \cdot \sin(\alpha_X)] \cdot \tan(\theta_X) + \mathbf{Y} \cdot \sin(\alpha_X) \cdot \sin(\alpha_Y) \cdot \tan(\theta_Y)\} - \\ & \mathbf{e}_X \cdot \tan(\theta_Y) + \cos(\alpha_Y) \cdot [\mathbf{X} \cdot \tan(\theta_Y) - \mathbf{Y} \cdot \sin(\alpha_X)] \end{aligned} \quad (\text{B10})$$

Since:

■ the normal to the surface of the cube along which measurements of the X-translations are performed defines the direction of the X-axis of the absolute frame (in respect to which the data is collected), which means that:

$$\alpha_Y = 0 \text{ and } \alpha_Z = 0 \text{ in the expression (B8)}$$

■ the angles involved have small values (between 10^{-4} and 10^{-5} rad) and, therefore:

$$\begin{cases} \cos(\theta) \approx 1 \\ \sec(\theta) \approx 1 \\ \sin(\theta) \approx \theta \\ \tan(\theta) \approx \theta \end{cases}$$

then equations (B8), (B9) and (B10) can be simplified as:

$$\mathbf{X}_m = \mathbf{X} - (\mathbf{Z} + \mathbf{e}_Z) \cdot \theta_Y + (\mathbf{Y} - \mathbf{e}_Y) \cdot \theta_Z \quad (\text{B8bis})$$

$$\begin{aligned} \mathbf{Y}_m = & \mathbf{Y} - \mathbf{X} \cdot \alpha_Z + (\mathbf{Z} - \mathbf{e}_Z) \cdot \theta_X + (-\mathbf{X} + \mathbf{e}_X) \cdot \theta_Z + \\ & \alpha_X \cdot (\mathbf{Z} - \mathbf{Y} \cdot \theta_X - \mathbf{Z} \cdot \alpha_X \cdot \theta_Z) \end{aligned} \quad (\text{B9bis})$$

$$\begin{aligned} \mathbf{Z}_m = & \mathbf{Z} + \mathbf{X} \cdot \alpha_Y - (\mathbf{Y} + \mathbf{e}_Y) \cdot \theta_X + (\mathbf{X} - \mathbf{e}_X) \cdot \theta_Y - \\ & \alpha_X \cdot (\mathbf{Y} + \mathbf{Z} \cdot \theta_X + \mathbf{Y} \cdot \alpha_Y \cdot \theta_Z) \end{aligned} \quad (\text{B10bis})$$

The derivation of the position (\mathbf{X} , \mathbf{Y} , \mathbf{Z}) of the centre of the cube (functional point) in respect to the interferometer readings (\mathbf{X}_m , \mathbf{Y}_m , \mathbf{Z}_m) is again left as a mathematical exercise for the reader.

B.3 – Sensitivity analysis

In this section, the effect of the different parameters involved on the formulas given in the previous section is studied numerically.

As a case-study, we consider the expression **(B9bis)** corresponding to the case of the Y-axis. We assume that the robot is set to a position on the border of its workspace (at least 1 operational coordinate has a value of ± 1.8 mm).

■ For studying the effect of the *orthogonality errors* between the different functional surfaces of the cube (parameters α_x and α_z , varying within ± 24 arcsec in our case) the remaining parameters (θ_x , θ_z , r , e_x and e_z) were set to zero (0).

→ The maximum error obtained in Y_m in respect to the nominal case is approximately **420 nm**

■ In order to study the effect of the *angular variations* (parameters θ_x and θ_z , varying within ± 10 arcsec for our robot) several scenarios were considered since they can influence the reading of the interferometer via one of the following parameters:

- e_x and e_z varied within ± 5.0 mm, while $r = r_{\text{nominal}} = 15$ mm and $\alpha_x = \alpha_z = 0$ arcsec

→ The maximum error obtained in Y_m in respect to the nominal case is approximately **660 nm**

- $r = r_{\text{nominal}} + 0.5 = 15.5$ mm, while $e_x = e_z = 0$ mm and $\alpha_x = \alpha_z = 0$ arcsec

→ The error obtained in Y_m in respect to the nominal case is negligible (not physically detectable).

- 183 -

Appendix C

Remarks on the application of our 6D calibration procedure for real industrial tasks

Abstract – After a brief résumé of geometric composition of 6D motions (translations + rotations), some ideas are outlined in order to guarantee a successful application of the procedure proposed in this thesis for the calibration of a 6-DOF robot that is to be used for real 6D industrial tasks.

This appendix should thus be regarded as a supplement to **section 4.3**.

C.1 – Preliminary: geometric decomposition of a 6D motion

Let us consider an object (cube) going from position A to position B. This displacement is composed of translations and rotations.

From the observer's point of view, an infinite number of geometric combinations can be used to describe this displacement.

Figure C.1 reports examples of three different combinations:

- *1st possibility*: rotation of angle α_1 around the centre C_1 ;
- *2nd possibility*: translation ($u_1 \ u_2$) followed by a rotation of angle α_2 around the centre C_B ;
- *3rd possibility*: translation ($u_3 \ u_4$) followed by a rotation of angle α_3 around the centre C_2 .

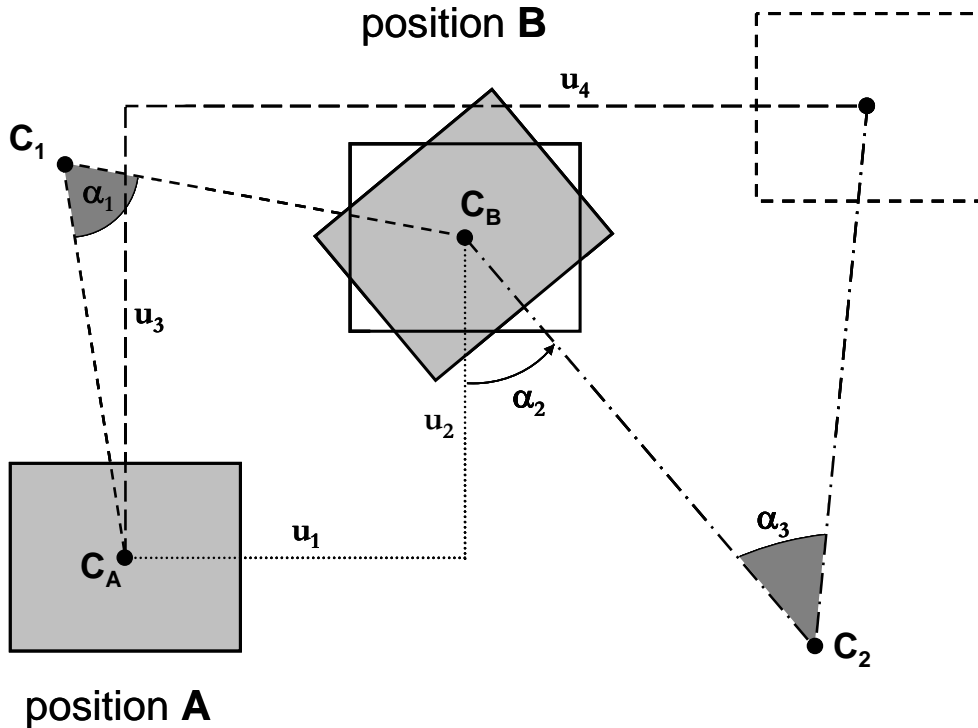


Figure C.1 – Example of three possible geometric combinations for describing a motion from position A to position B.

An accurate geometric modelling (for the purpose of calibration) can only be achieved with the use of a particular **convention**.

The purpose of this convention is to provide an unambiguous answer to the following questions:

1. what are the directions and origin of the *absolute reference frame* in respect to which the motions are reported?
2. what is the *actual calibrated position* on the robot end-effector?
3. what is the *order of the composition of motions* (translations combined with rotations)?

For the calibration of the 6-DOF robot (**section 4.3**), we calibrated the pose of the centre of a sphere mounted on the end-effector. The absolute reference frame was a virtual frame with an origin at the centre of the sphere (when the robot was at the reference pose) and having the directions defined by the surfaces of the mirror cube (see **section 4.3.2**).

The convention used for composing the motions considered that the rotations were always performed after the translations and were executed around the translated centre of the sphere (see **section 4.1.1**).

*Our convention corresponds therefore to the 2nd possibility of **Figure C.1**.*

C.2 – *Remarks on the use of our 6D calibration protocol in future 6D industrial applications*

Despite the necessity of adopting a given convention for modelling purposes, note that **motions imposed according to a particular convention can be converted into motions according to a different convention¹**.

In order to move the functional tool (mounted in the robot end-effector and used for a given 6D operation) as accurately as the calibrated position of the end-effector, this property is of prime importance.

In the next lines, a few rules are reported concerning this issue.

RULE 1: If translations or rotations have to be used in a separate way (3D operations) then the distance between the tool and the centre of the absolute frame does NOT need to be known. The tool can thus be installed in any position relative to the frame used during the calibration of the robot.

RULE 2: If the 6 degrees-of-freedom have to be used simultaneously (i.e. rotations around different centres of rotation) then the distance between the tool and the centre of the absolute frame used during the calibration must be determined accurately.

¹ In other words, a rotation around any given centre of rotation (1st and 3rd possibilities of **Figure C.1**) is equivalent to a translation in respect to a fixed frame followed by a rotation around the translated origin (2nd possibility of **Figure C.1**).

Examples: let us consider the situation in **Figure C.1**. Assume that C_A is the position of the end-effector for which the poses are accurately known after calibration (calibrated position). Suppose now that, during a given operation, the robot is asked to execute a rotation of $\alpha_1 = 3^\circ$ around C_1 (functional tool). Ideally, the tool has to stay in the same physical position after the rotation has been completed.

- if the distance between C_A and C_1 is known within $\pm 5 \mu\text{m}$ then the residual translational errors in the execution of this rotation can be up to $5 \cdot \sin(\alpha_1) \approx \pm 0.26 \mu\text{m} = \pm 260 \text{ nm}$.
- if we let the distance between C_A and C_1 be 20 mm and if the error Δ in the calibration of α_1 is $\pm 3 \text{ arcsec}$, then the residual translational errors in the execution of this rotation can be up to: $20\,000 \cdot \sin(\Delta) \approx \pm 0.29 \mu\text{m} = \pm 290 \text{ nm}$.

RULE 3: Suppose that the rotations $(\theta_x \ \theta_y \ \theta_z)$ have to be accomplished around a given centre of rotation C_R . Let $(X \ Y \ Z)$ be the translational coordinates of C_R in respect to the absolute reference frame used for the calibration of the robot.

- if the position $(X \ Y \ Z)$ is inside the calibrated translational workspace of the robot, then the latter may execute this rotation by moving directly to $(X \ Y \ Z \ \theta_x \ \theta_y \ \theta_z)$, according to our convention used for geometric modelling (**section 4.1.1 – paragraph (b)**);

- otherwise, the motion has to be recomposed.

The robot end-effector may then perform this rotation by moving to the pose $(X^* \ Y^* \ Z^* \ \theta_x \ \theta_y \ \theta_z)$. According to our convention, this pose must correspond to the “physical result” of the original motion (**example:** passing from the 1st to the 2nd possibility of the previous paragraph). $(X^* \ Y^* \ Z^*)$ are the coordinates of a virtual centre of rotation (inside the translational workspace) used by the robot to perform this rotation.

Figure C.2 above illustrates the second situation of RULE 3.

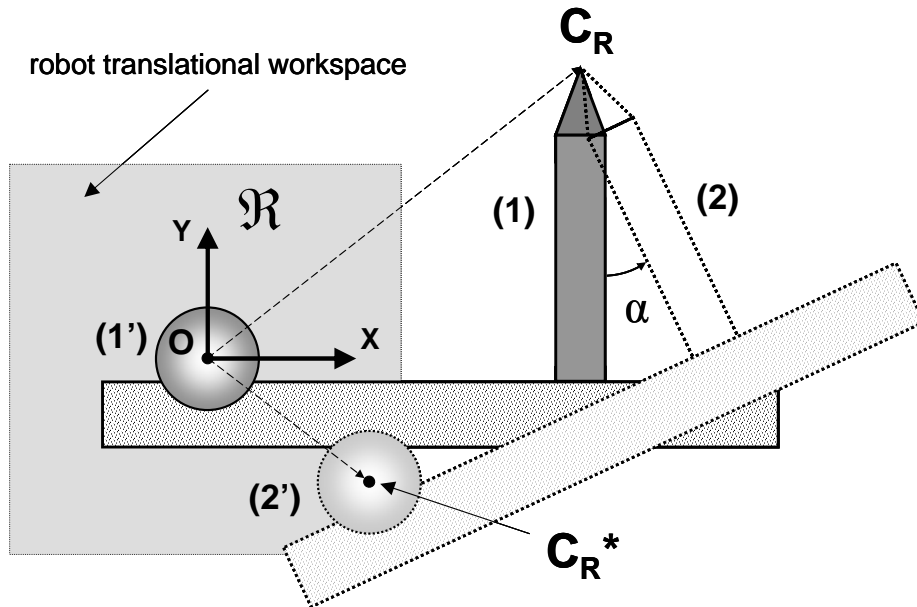


Figure C.2 – Example of a real operation in which a rotation of magnitude α has to be executed around the tip of a tool mounted on the robot end-effector.

Since the centre of rotation is located outside the robot translational workspace, the rotation has to be recomposed on the basis of the coordinates of the centre of rotation in the absolute reference frame \mathcal{R} used during the calibration of the robot.

As a result of this recomposition, the rotation of the tool around the desired centre of rotation C_R : (1) \rightarrow (2) corresponds to a translation of the calibrated position: (1') \rightarrow (2') followed by a rotation around the translated centre of rotation C_R^* .

Appendix D

Calibration of High-Precision Flexure Parallel Robots: View of the different phases of the procedure

Abstract – *This Appendix presents a general view of the work reported in this thesis. The aim is to show, by means of flow-charts, the main issues to be addressed and the correct questions to be answered for a given multi-DOF high-precision flexure parallel robot to be calibrated properly. This appendix should then be regarded as a supplement to **section 8.1**.*

D.1 – General overview

The calibration of a given multi-DOF high-precision flexure parallel robot within accuracies in the sub- μm range is a complex and delicate procedure that comprises a certain number of phases.

Figure D.1 presents a general view of the entire procedure and shows the different elementary steps. These steps will be detailed in the next sections of this Appendix.

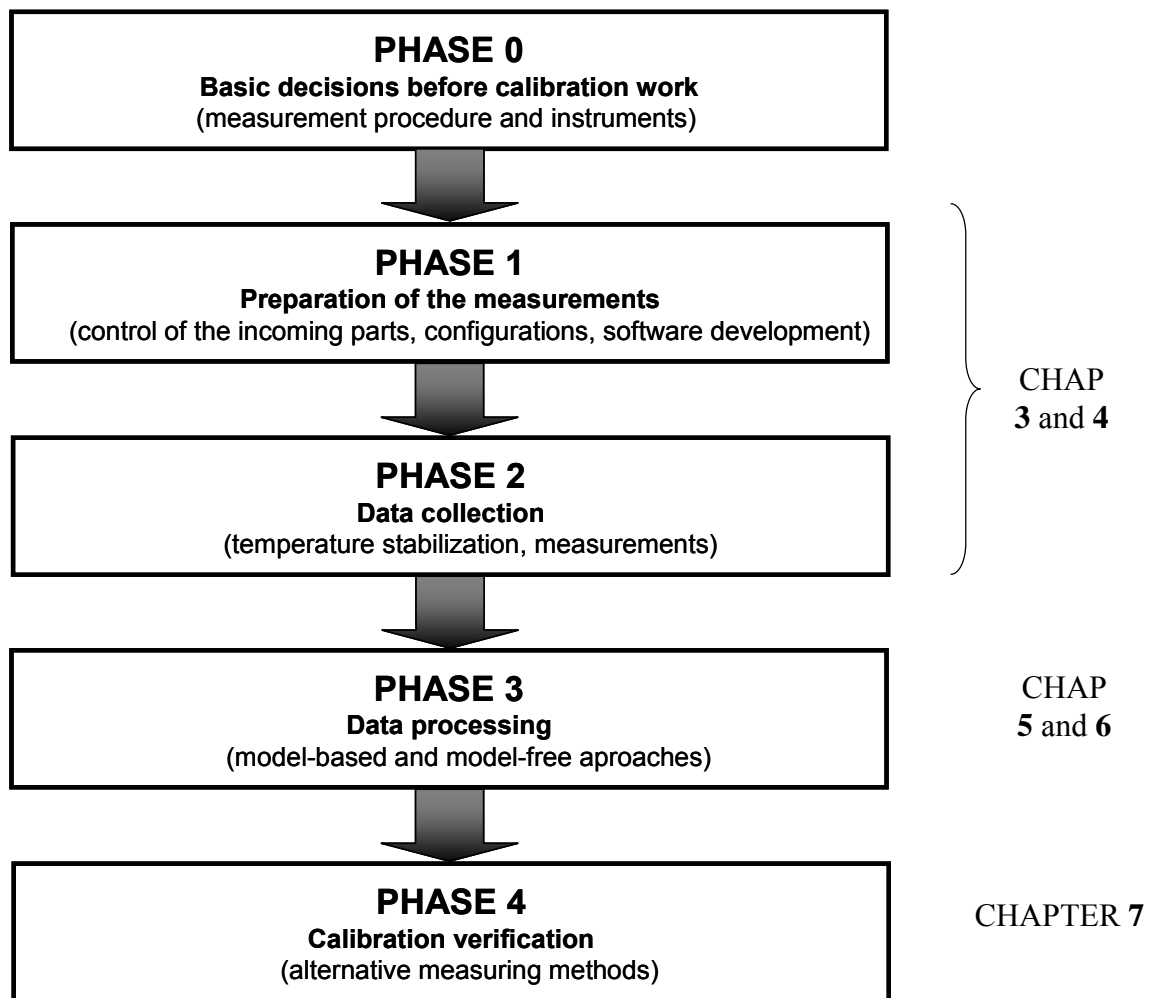


Figure D.1 – General overview of the different phases of the calibration of a given multi-DOF high-precision flexure parallel robot.

D.2 – Phase 0: basic decisions before calibration

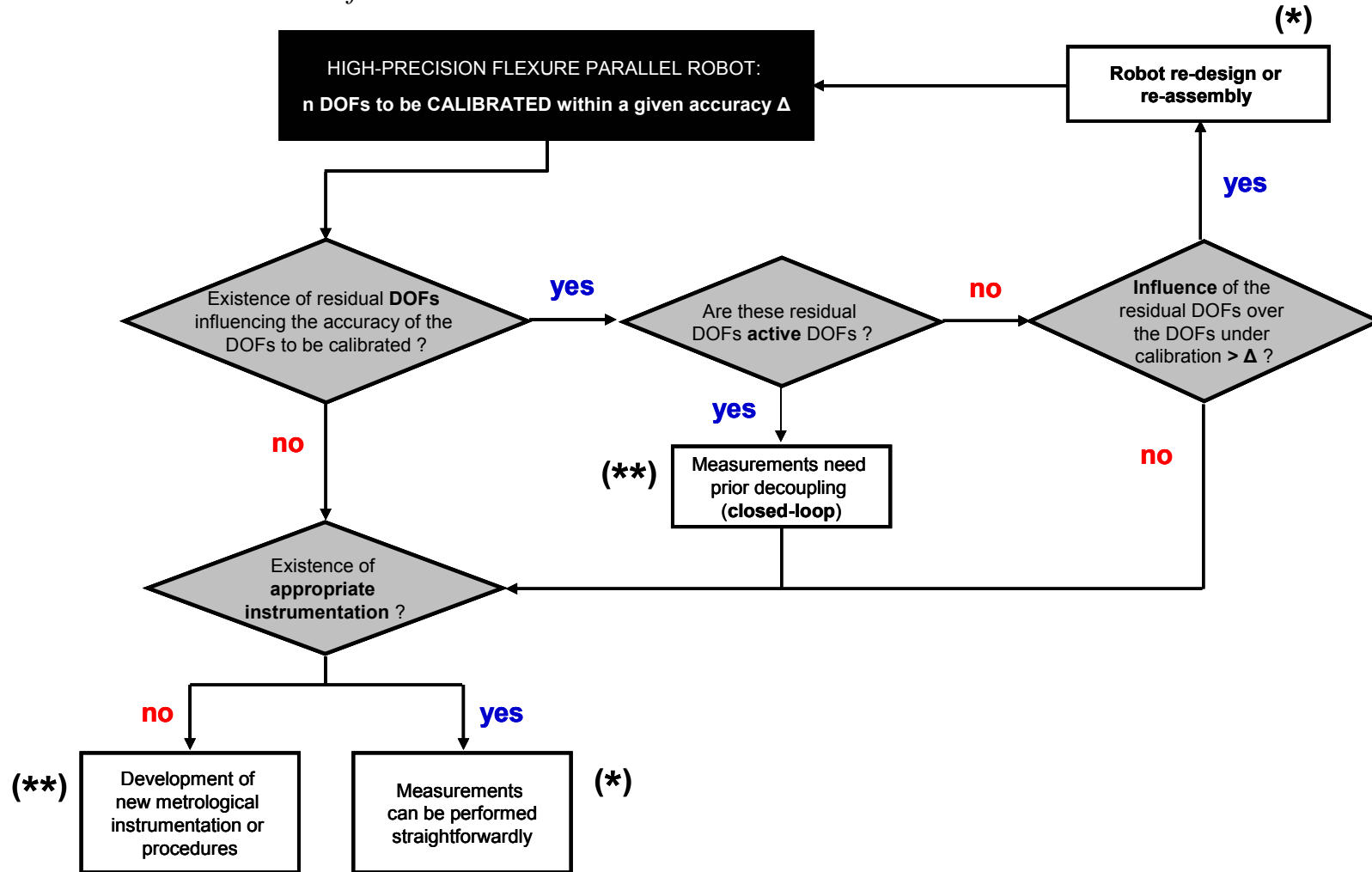


Figure D.2 – Phase 0 of the calibration procedure. This phase comprises a certain number of key questions for which the answers provide some indications about the strategy to be adopted for the measurement procedure (the most difficult part of the calibration work). (*) and (**) correspond, respectively, to the case of the 3-DOF and the 6-DOF treated in this thesis.

D.3 – Phase 1: preparation of the measurements

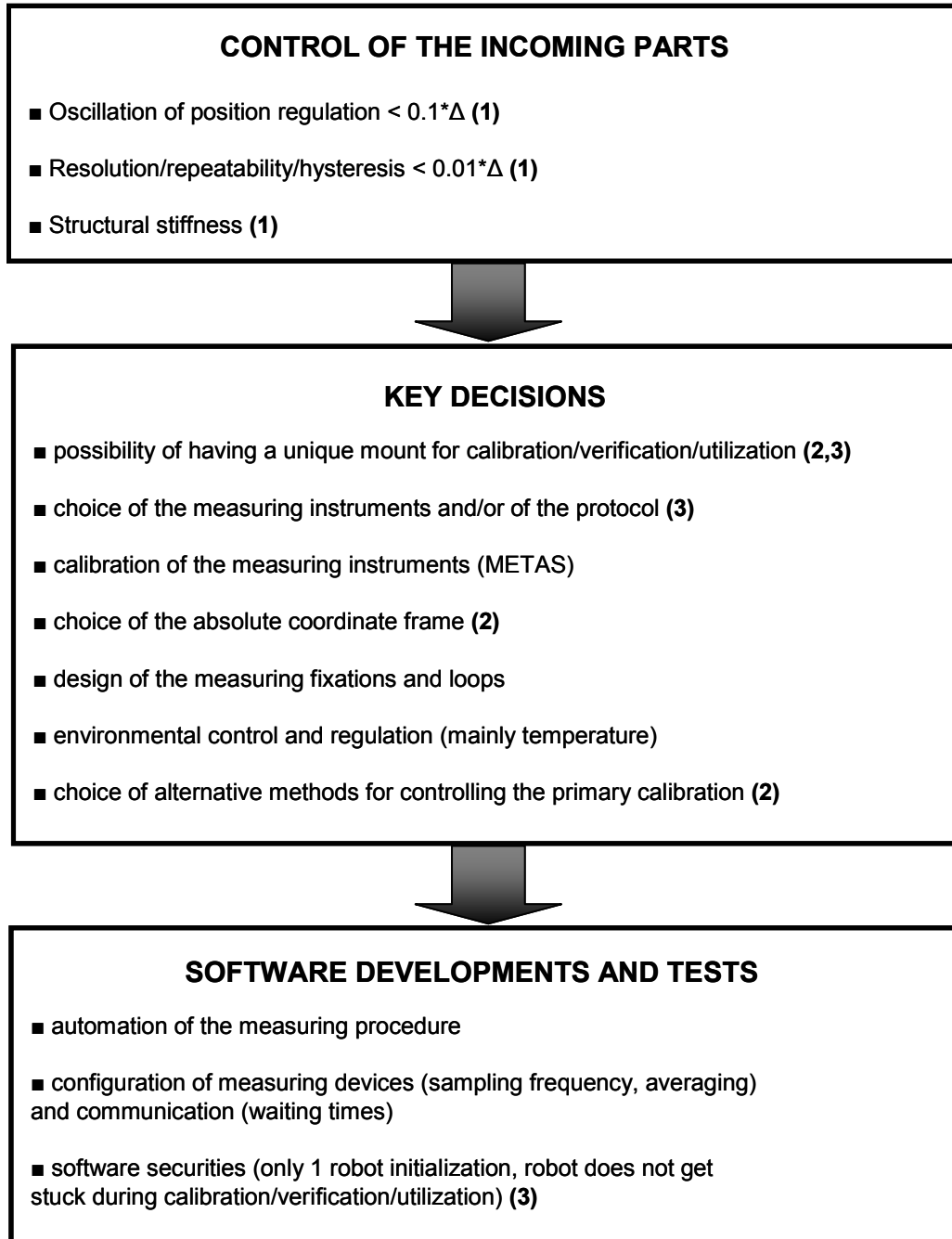


Figure D.3 – Phase 1 of the calibration procedure. This phase involves the development of the complete measurement system, once the direction has been defined (phase 0).

Remarks

- (1): to be checked for all the positions of the robot workspace that will be measured during calibration;
- (2): to be decided in relationship with the industrial application for which the robot will be used;
- (3): as far as possible, avoid mechanical contact with the robot during calibration/verification/utilization (mounting/unmounting operations).

D.4 – Phase 2: data collection

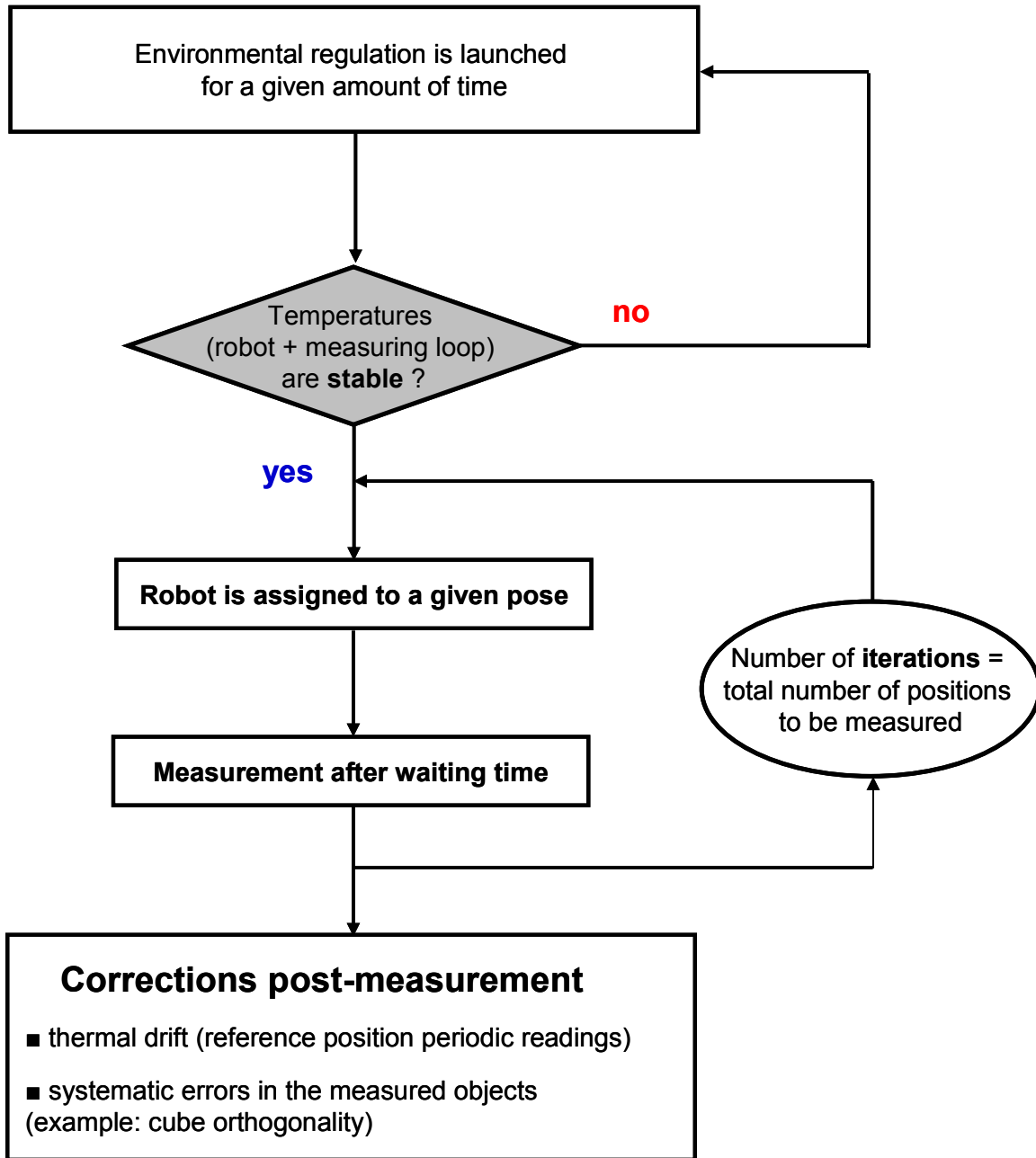


Figure D.3 – Phase 2 of the calibration procedure. This phase consists of the acquisition of a complete set of measurement data from the robot, using the system developed in phase 1.

D.5 – Phase 3: data processing

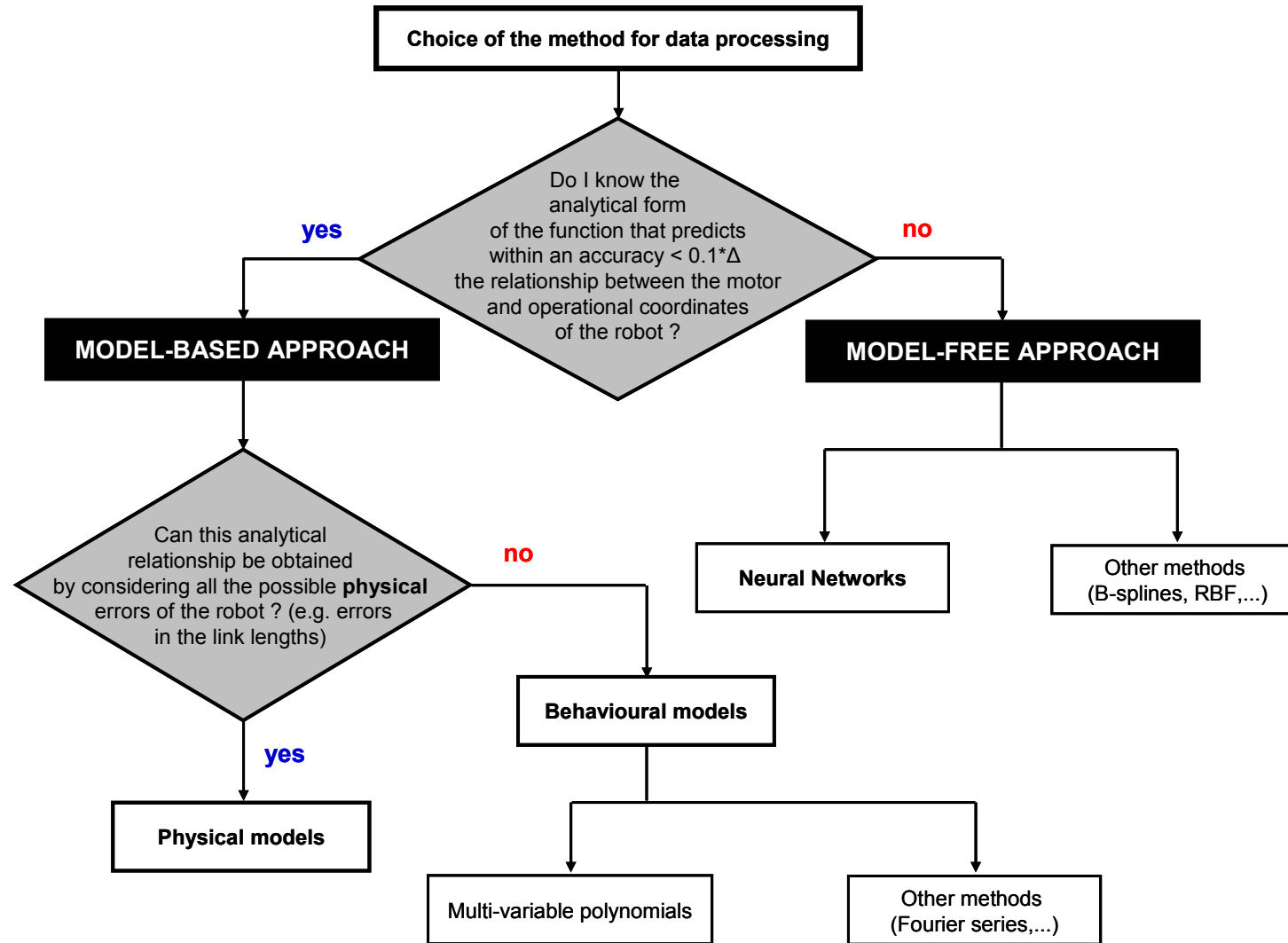


Figure D.5 – Phase 3 of the calibration procedure. In this phase, the data collected from the robot being calibrated is processed in order to actually correct the errors of the robot pose. Two different techniques can be applied for this purpose: a *model-based* or a *model-free* approach. Hybrid approaches can also be imagined.

The choice between a model-based and model-free approach is the result of a compromise, since each method offers interesting features while suffering from some limitations at the same time. The Table below summarizes the advantages and drawbacks of each method.

TYPE OF APPROACH		ADVANTAGES	DRAWBACKS
MODEL-BASED APPROACH	<i>Physical models</i>	<ul style="list-style-type: none"> ■ possibility of interacting with robot design (parameter sensitivity analysis); ■ possibility of implementing methods requiring incomplete measurements (e.g.: extract 3D data by measuring only along 1 or 2 directions, instead of 3). 	<ul style="list-style-type: none"> ■ models have limited accuracies (match between representation and reality); ■ models are generally highly non-linear → parameters very difficult to identify (even if identified often do not correspond to the physical solution...).
	<i>Behavioural models</i>	<ul style="list-style-type: none"> ■ The determination of the model coefficients is basically solving a dense system of linear equations; ■ universal approximation capability; ■ knowledge of the sources of inaccuracy, or even of the robot structure, not required; ■ possibility of accurate extrapolation; ■ no need of large data sets for calculation of the model coefficients. 	<ul style="list-style-type: none"> ■ highly oscillatory solutions → overfitting; ■ necessity of finding the model with the best prediction capability.
MODEL-FREE APPROACH	<i>General</i>	<ul style="list-style-type: none"> ■ knowledge of the sources of inaccuracy, or even of the robot nominal structure, not required. 	<ul style="list-style-type: none"> ■ need for a large amount of data (“mapping” the entire robot workspace).
	<i>Neural Network – based method</i>	<ul style="list-style-type: none"> ■ does not require previous observation of the data to be approximated; ■ great capability for generalizing and predicting non-linear behaviour (universal approximation) 	<ul style="list-style-type: none"> ■ the architecture of the network has to be determined; ■ overfitting; ■ poor accuracy for extrapolation.

D.6 – *Phase 4: verification of the calibration conformity*

The choice of the method to be used in this phase has to be in accordance with the following requirements:

- the method must not perturb the calibrated robot statically or dynamically (**example 1**: care is required if a mounting/unmounting operation is involved between primary calibration and verification, **example 2**: if the verification method is a contact-based method, check whether the “touch” induces vibrations larger than the accuracy to be verified);
- the accuracy of the method must be within the same range as that of the method used to perform the primary calibration of the robot;
- the method should preferably be “inspired” by (or in accordance with) the application for which the robot will be used;
- the method should preferably provide samples that can be measured in a different institution (properly equipped metrology institute) from the one on which the primary calibration was performed.

Glossary

REMARKS

In this glossary, the reader may find the definition of a few terms used in this thesis.

- the definitions given here are adapted to the context in which the terms are employed.
- the french correspondence is provided for each term defined (in brackets).

Abbe error

(fr: *erreur d'Abbe*)

displacement caused by an angular error together with an offset (called *Abbe offset*) between the axis of motion and the axis being used to measure that motion. It characterizes every device used for distance measurements.

Accuracy

(fr: *précision*)

difference (distance or angle) between a target pose (never taught before) and the pose attained in reality.

Activation function

(fr: *fonction d'activation*)

see *transfer function*.

Architecture

(fr: *architecture*)

description of the number of layers and the number of neurons in each layer of a given neural network. The representation of the architecture is generally performed in accordance with a specific convention. In this thesis, we adopt the convention of *MatLab*[®].

Approximation

(fr: *approximation*)

problem that consists in extracting a certain deterministic mathematical behaviour. In the context of function approximation, the goal is to be able to reproduce the response of the function being approximated for samples never seen during the calculation of the model coefficients.

Articular coordinates

(fr: *coordonnées articulaires*)

set of coordinates corresponding to the motions (angles or distances) imposed by the actuators to the active joints of the kinematic chains composing the structure of the robot in order to obtain a certain pose at the end-effector.

Autocollimator

(fr: *autocollimateur*)

optical instrument for measuring angles in a non-contact mode.

Backlash

(fr: *erreur d'inversion*)

amount of lost motion due to clearance when movement is reversed and contact is re-established.

Back-propagation

(fr: *rétro-propagation*)

learning rule in which the weights and biases of a given neural network are adjusted by propagating the errors backwards. It is the commonly used method for training multilayer feedforward networks.

Behavioural model

(fr: *modèle de comportement*)

model used for the calibration of a given robot in which the parameters that have to be identified are coefficients of a general mathematical function. Unlike *physical models*, these parameters are then free from any physical meaning or, in other words, they are not related directly to the geometry of the robot being calibrated. A multi-variable polynomial function is an example of a behavioural model.

Bias

(fr: *seuil*)

parameter characterizing a given neuron that is summed with the neuron's weighted inputs and passed through the neuron's transfer function in order to generate the output of that neuron.

Calibration

(fr: *étalonnage*)

the art of accuracy improvement. It is a technique that consists of suppressing the systematic errors of a system being calibrated, so that the response of the system can be predicted within a certain acceptable error.

Closed-loop

(fr: *boucle fermée ou asservissement*)

configuration in which the output of a given system is being controlled according to the information provided by another system.

Cosine error

(fr: *erreur de cosinus*)

measurement error caused by an angular misalignment between the axis of motion and the axis being used to measure that motion. It characterizes every device used for distance measurements.

Cross-validation

(fr: *validation croisée*)

statistical practice of partitioning a quantity of data into different subsets such that the analysis is initially performed on a single subset, while the other subset(s) is (are) retained for subsequent use in confirming and validating the initial analysis.

Dead-path

(fr: *chemin mort*)

part of the trajectory of an interferometer's measuring beam which is the difference between the distance splitter – reference mirror and the distance splitter – external reflector.

Early-Stopping¹

(fr: *arrêt anticipé*)

method used to monitor continuously the generalization capability of a given network. It consists of dividing the original data set into three subsets (see also *cross-validation*). The first subset is the training set used for updating the weights and biases of the network. The second subset is the validation set. When the validation error increases for a specified number of iterations, the training is stopped and the weights and biases at the minimum of the validation error are returned and used to produce the subsequent network response. The third subset is the test set. It is typically used to display the results.

Epoch

(fr: *époque*)

presentation of the data set used for training to a network and the calculation of new weights and biases.

End-effector

(fr: *organe terminal*)

part of the robot structure used to perform some desired task.

Feedforward

(fr: *unidirectionnel*)

term used to describe a network in which each layer only receives inputs from the previous layers.

Flexure

(fr: *articulation flexible*)

joint that operates using the elastic property of matter and whose motions are thus free of dry friction or backlash.

Generalization

(fr: *généralisation*)

attribute of a given model or network whose output for a new input tends to be close to outputs for similar inputs in the data set used to calculate the model coefficients or train the network. In general, reliable calibration models or networks have to present good generalization capabilities.

Heuristic

(fr: *heuristique*)

technique designed to solve a problem that ignores if the solution can be proven to be correct, but which usually produces a good solution or solves a simpler problem that contains or intersects with the solution or the more complex problem.

Hidden

(fr: *caché(e)*)

term used to describe the layers (or the neurons of these layers) located between the input and output layers of a given neural network.

In-line

(fr: *en ligne*)

refers to a certain number of operations when a given model (for which the performances were previously evaluated *off-line*) is implemented in robot controller in order to test its accuracy in real experimental conditions. When dealing with accuracies at the

¹ As opposed to “cross-validation”, the term “Early-Stopping” is exclusively used in the context of Neural Networks.

nanoscale, the errors obtained during an *in-line* implementation are generally worse than the corresponding *off-line* evaluations.

Indentation

(fr: *indentation*)

technique traditionally employed for the characterization or determination of the mechanical properties of different materials. It consists of pushing a hard tip of known geometry (indenter) into the sample surface (substrate) using a fixed peak load. The resulting footprint created in the substrate is called indent.

Interferometer

(fr: *interféromètre*)

optical instrument based on the principle of wave interference and traditionally used to measure distances within nm or even sub-nm resolution.

Inverse Geometric Model

(fr: *modèle géométrique inverse*)

Model describing the geometry of a given robot in which the coordinates of the robot end-effector (input) are given as a function of its articular coordinates (output). The function that performs the opposite transformation is called the Direct Geometric Model (DGM).

Isosurfaces

(fr: *isosurfaces*)

surface that represents points of a constant value within a volume of space. It is the 3D analog of an isocontour.

Layer

(fr: *couche*)

group of neurons having connections to the same inputs and sending output signals to the same destinations.

Learning

(fr: *apprentissage*)

process in which the weights and biases of a given neural network are adjusted in order to obtain some desired behaviour (example: approximate a given input-output relationship).

Linearity

(fr: *linéarité*)

term traditionally employed by manufacturers of measuring instruments to refer to the *accuracy* of a given device.

Joint coordinates

(fr: *coordonnées des jointures*)

see *articular coordinates*.

Metrology

(fr: *métrologie*)

the science of measurement.

Model-based approach

(fr: *approche basée sur un modèle*)

method for processing the data for the purpose of calibrating a given robot in which a model having a full analytical formulation is used. This model can be obtained either from a physical description of the robot (*physical model*) or from the observation of the measurement data collected from the robot (*behavioural model*).

Model-free approach

(fr: *approche non basée sur un modèle ou approche « boîte noire »*)

method for processing the data for the purpose of calibrating a given robot in which the input-output mapping is approximated using a “black-box” approach. *Neural Networks* and B-splines are examples of mathematical tools used in model-free approaches.

Motor coordinates

(fr: *coordonnées moteur*)

see *articular coordinates*.

Neural Network²

(fr: *réseaux de neurones*)

group of neurons organized in different layers and relating an input vector to an output one. It is a mathematical tool used to perform some task or function of interest, such as the approximation of a given input-output mapping (regression).

Neuron²

(fr: *neurone*)

basic processing unit of a neural network. From the mathematical point of view, it includes weights and bias, a summing junction and an output transfer function.

Off-line

(fr: *hors-ligne*)

refers to a certain number of data processing operations performed in order to test the accuracy of a given model when *not* implemented in the robot controller. It is the opposite of *in-line*.

Open-loop

(fr: *boucle ouverte*)

the opposite of *closed-loop*.

Operational coordinates

(fr: *coordonnées opérationnelles*)

set of coordinates characterizing the position (3D) or pose (6D) of the robot end-effector with respect to a given frame.

Overfitting

(fr: *sur-approximation*)

situation in which a model or network provides an accurate fit at points used for the calculation of the model coefficients or the training of the network but presents a poor response (i.e. not representative of the function to be approximated) for new points.

² In this thesis, the terms “neuron” and “neural network” are in fact used to replace the terms “artificial neuron” and “artificial neural network” respectively. They refer to abstractions of *biological neurons* and *biological neural networks*.

Parallel robot

(fr: *robot parallèle*)

closed-loop mechanism in which the mobile platform is connected to the base by at least 2 serial kinematic chains (legs).

Physical model

(fr: *modèle physique*)

model used for the calibration of a given robot in which the parameters that have to be identified are related directly to the geometry of the robot (examples: lengths of the arms or forearms, joint offsets...). The term “physical models” was originally derived from the fact that these models are obtained on the basis of a physical representation of the robot being calibrated. They are the most widely used models in the robot calibration literature.

Pose

(fr: *pose*)

set of coordinates describing the location (X, Y, Z) and orientation (θ_x , θ_y , θ_z) of some object in respect to a given Cartesian frame.

Position

(fr: *position*)

set of coordinates describing the location (X, Y, Z) of some point of interest in respect to a given Cartesian frame.

Precision

refers to the positioning capabilities of a given robot. Since the exact meaning of this term varies from author to author, we prefer instead the use of the terms *accuracy* and *repeatability*.

Pruning

removal of “excess” items from a budget. Here, it refers to a class of methods for building up a network by successively removing hidden neurons that are no longer playing a “positive role” in improving the approximation capability of the network being used to predict a given input-output mapping.

Random

(fr: *aléatoire*)

attribute of a given variable or process which cannot be described in a deterministic way.

Regression

(fr: *régression*)

method of approximating a given curve which uses least-squares estimations.

Regularization

(fr: *régularisation*)

method used to improve the generalization capability of a given network in which the cost function to be minimized during the training session, normally chosen to be the sum of squares of the network errors in the training set, is modified by adding a term related to the squares of the network weights.

Repeatability

(fr: *répétabilité* ou *répétitivité*)

capability of returning to a previously taught pose.

Resolution

(fr: *résolution*)

smallest incremental motion that can be achieved.

Robot

(fr: *robot*)

manipulator with several degrees of freedom which is controlled and programmable in order to accomplish some operation of interest.

Sampling frequency

(fr: *fréquence d'échantillonnage*)

frequency at which a given measuring device is sampling (or reading) a given physical parameter to be measured.

Sigmoid

(fr: *sigmoïde*)

monotonic S-shaped function that maps numbers in the interval $(-\infty, +\infty)$ to a finite interval such as $(-1, +1)$ or $(0, 1)$.

Smoothness

(fr: *degré de lissage*)

measure of the oscillatory nature of a function. A function is said to be smoother than another function if it is less oscillatory. In other words, the smoother a function is, the smaller its high-frequency content will be.

Standard

(fr: *étalon*)

object with accurately known dimensions in relation to which the dimensions of another object (being calibrated) are compared during a calibration procedure.

Systematic

(fr: *systématique*)

attribute of a given variable or process which can be described using deterministic models.

Traceability

(fr: *traçabilité*)

refers to an unbroken chain of measurements relating an instrument's measurements to a known standard.

Training

(fr: *entraînement*)

procedure by which a network acquires the ability to perform a particular job, such as the approximation of given input-output mapping.

Transfer function

(fr: *fonction de transfert*)

function that converts a neuron's input vector into its actual output.

Uncertainty

(fr: *incertitude*)

see *accuracy*.

Underfitting

(fr: *sous-approximation*)

situation in which a model or network does not have sufficient “power” or complexity to fully extract the behaviour of the function to be approximated.

References

- [Abd00] M. Abderrahim and A. R. Whittaker, “Kinematic model identification of industrial manipulators”, *Robotics and Computer-Integrated Manufacturing* Vol. 16, pp 1 – 8, 2000.
- [Ack85] D. S. Ackerson and D. R. Harry, “Theory, experimental results and recommended standards regarding the static positioning and orienting precision of industrial robots”, *Robotics and Computer-Integrated-Manufacturing*, Vol. 2, No. 3/4, pp 247 – 259, 1985.
- [Afz89] N. V. Afzulpurkar and G. R. Dunlop, “A novel antenna mount for orbital satellite tracking and marine communications”, *Proceedings of the 5th National Space Engineering Symposium*, Canberra (Australia), pp 92 – 96, November – December 1989.
- [Alb75] J. S. Albus, “A new approach to manipulator control: The Cerebellar Model Articulation Controller (CMAC)”, *ASME Journal of Dynamic Systems, Measurement and Control*, Vol. 97, Issue 3, pp 220 – 227, 1975.
- [Alb75b] J. S. Albus, “Data storage in the Cerebellar Model Articulation Controller (CMAC)”, *ASME Journal of Dynamic Systems, Measurement and Control*, Vol. 97, Issue 3, pp 228 – 233, 1975.
- [Ali03] G. Alici and B. Shirinzadeh, “Laser Interferometry Based Robot Position Error Modelling for Kinematic Calibration”, *Proceedings of the IEEE International Conference on Intelligent Robots and Systems*, Las Vegas – Nevada (USA), pp 3588 – 3593, October 2003.
- [Bac01] J.-Ph. Bacher, S. Bottinelli, J.-M. Breguet and R. Clavel “Delta³: A New Ultra-High Precision Micro-robot”, *Journal Européen des Systèmes Automatisés*, Vol. 36, No. 9, pp 1263 – 1275, 2002.
- [Bac02] J.-Ph. Bacher, C. Joseph and R. Clavel, “Flexures for high precision robotics”, *Industrial robot*, Vol. 9, No. 4, pp 349 – 353, 2002.
- [Bac03] J.-Ph. Bacher, “Conception de robots de très haute précision à articulations flexibles: interaction dynamique – commande”, *Thèse N° 2907* (PhD dissertation), École Polytechnique Fédérale de Lausanne, 2003.
- [Bai03b] Y. Bai, H. Zhuang and Z. S. Roth “Experiment Study of PUMA Robot Calibration Using a Laser Tracking System”, *Proceedings of the IEEE International Workshop on Soft Computing in Industrial Applications*, Binghamton – New York (USA), pp 139 – 144, June 2003.
- [Bak01] S. P. Baker, “Nanoindentation Techniques”, In *Encyclopedia of Materials: Science and Technology* (ISBN 0-08-0431526), pp 5908 – 5916, Elsevier, 2001.
- [Ben91] D. J. Bennett and J. M. Hollerbach, “Autonomous Calibration of Single-Loop Closed Kinematic Chains Formed by Manipulators with Passive Endpoint Constraints”, *IEEE Transactions on Robotics and Automation*, Vol. 7, No. 5, pp 597 – 606, October 1991.
- [Ber93] R. Bernhardt and S. L. Albright, “Robot calibration”, *Kluwer Academic Publishers*, ISBN: 0412491400, 1993.
- [Ber93b] J. O. Berg, “Path and Orientation Accuracy of Industrial Robots”, *International Journal of Advanced Manufacturing Technology*, Vol. 8, pp 29 – 33, Springer – Verlag, 1993.
- [Bes99] S. Besnard and W. Khalil, “Calibration of parallel robots using two inclinometers”, *Proceedings of the IEEE International Conference on Robotics and Automation*, pp 1758 – 1763, Detroit – Michigan (USA), May 1999.
- [Bla06] O. Blanc, “Multi-dimensional Non-Uniform Interpolation and Approximation for Robot Calibration”, *Semester project* (co-supervised by N. Fazenda), Biomedical Imaging Group (EPFL), 2006.
- [Bor89] J.-H. Borm and C.-H. Menq, “Experimental study of observability of parameter errors in robot calibration”, *Proceedings of the IEEE International Conference on Robotics and Automation*, Vol. 1, pp 587 – 592, May 1989.

- [Bos03] H. Bosse, W. Hässler-Grohne, J. Flügge and R. Köning, “Final report on CCL-S3 supplementary line scale comparison Nano3”, *Metrologia*, Vol. 40 (Technical Supplement), 04002, 2003.
- [Cau96] P. Cauchick-Miguel, T. King and J. Davis, “CMM verification: a survey”, *Measurement*, Vol. 17, No. 1, pp 1 – 16, 1996.
- [Cha87] L. M. Chao and J. C. S. Yang, “Implementation of a scheme to improve the positioning accuracy of an articulate robot by using laser distance-measuring interferometry”, *Precision Engineering*, Vol. 9, No. 4, pp 210 – 217, October 1987.
- [Che90] D. L. Chester, “Why two hidden layers are better than one”, *Proceedings of the IEEE International Joint Conference on Neural Networks*, Vol. 1, pp 265 – 268, Washington DC (USA), 1990.
- [Che97] J.-S. Chen, “Fast calibration and modelling of thermally-induced machine tools errors in real machining”, *International Journal of Machine Tools and Manufacture*, Vol. 37, N° 2, pp 159 – 169, 1997.
- [Cla91] R. Clavel, “Conception d’un robot parallèle rapide à 4 degrés de liberté”, *Thèse N° 925* (PhD dissertation), École Polytechnique Fédérale de Lausanne, 1991.
- [Col06] T. F. Coleman and Y. Zhang, “Optimization Toolbox For Use with MatLab® – User’s guide”, *Version 3.1*, The MathWorks, September 2006.
- [Cul04] M. L. Culpepper and G. Anderson, “Design of a low-cost nano-manipulator which utilizes a monolithic, spatial and compliant mechanism”, *Journal of Precision Engineering*, Vol. 28, Issue 4, pp 469 – 482, 2004.
- [Cul04b] M. L. Culpepper, G. Anderson and P. Petri, “Hexflex: a planar mechanism for six-axis manipulation and alignment”, *Proceedings of the American Society for Precision Engineering (ASPE) 17th Annual Meeting*, St Louis (USA), pp 20 – 25, 2004.
- [Dan02] D. Daney, “Optimal Measurement Configurations for Gough Platform Calibration”, *Proceedings of the IEEE International Conference on Robotics and Automation*, Vol. 1, Washington DC (USA), May 2002, pp 147 – 152.
- [Dan05] D. Daney, Y. Papegay and B. Madeline, “Choosing Measurement Poses for Robot Calibration with the Local Convergence Method and Tabu Search”, *The International Journal of Robotics Research*, Vol. 24, No. 6, pp 501 – 518, June 2005.
- [Dem06] H. Demuth, M. Beale and M. Hagan, “Neural Network Toolbox For Use with MatLab® – User’s guide”, *Version 5*, The MathWorks, September 2006.
- [Den55] J. Denavit and R. S. Hartenberg, “A Kinematic Notation for a Lower-Pair Mechanisms Based on Matrices”, *ASME Journal of Applied Mechanics*, pp215 – 221, 1955.
- [Doa04] C. D. Doan and S.-Y. Liong, “Generalization for multilayer neural network: Bayesian regularization or Early-Stopping?”, *Proceedings of the 2nd Conference of the Asia Pacific Association of Hydrology and Water Resources (APHW)*, Singapore, July 2004.
- [Dor93] A. Doria, F. Angrilli and S. De Marchi, “Inverse Kinematics robot calibration by spline functions”, *Applied Mathematical Modelling*, Vol. 17, pp 492 – 498, September 1993.
- [Dre97] S. Dreiseitl, W. Jacak, T. Kubik and R. Muszynski, “Neural processing based robot kinematics modelling and calibration for pose control”, *Systems Science*, Vol. 23, No. 3, pp 61 – 68, 1997.
- [Dri90] M. R. Driels and U. S. Pathre, “Significance of Observation Strategy on the Design of Robot Calibration Experiments”, *Journal of Robotic Systems*, Vol. 7, No. 1, pp 197 – 223, February 1990.
- [Eve87] L. J. Everett, M. Driels and B. W. Mooring, “Kinematic Modelling for Robot Calibration”, *Proceedings of the IEEE International Conference on Robotics and Automation*, Vol. 1, pp 183 – 189, March 1987.
- [Eve88] L. J. Everett and T. W. Hsu, “The Theory of Kinematic Identification for Industrial Robots”, *Transaction of the ASME – Journal of Dynamic Systems, Measurement and Control*, Vol. 110, pp 96 – 100, 1988.

- [Eve88b] L. J. Everett and C. Y. Lin, "Kinematic Calibration of manipulator with closed-loop actuated joints", *Proceedings of the IEEE Conference on Robotics and Automation*, pp 792 – 797, Philadelphia – PA (USA), April 1988.
- [Eve93] L. J. Everett, "Models for diagnosing robot error sources", *Proceedings of the IEEE Conference on Robotics and Automation*, Vol. 2, pp 155 – 159, May 1993.
- [Eve93b] L. J. Everett and T. W. Ives, "A sensor used for measurements in the calibration of production robots", *Proceedings of the IEEE Conference on Robotics and Automation*, pp 174 – 179, Atlanta – Georgia (USA), May 1993.
- [Faz06] N. Fazenda, E. Lubrano, S. Rossopoulos and R. Clavel, "Calibration of the 6-DOF high-precision flexure parallel robot "Sigma 6" ", Keynote paper Calibration, *Proceedings of the 5th Chemnitz Parallel Kinematics Seminar* (PKS 2006), Chemnitz (Germany), pp 379 – 398, April 2006.
- [Fis03] Ch. Fischer, "Participation à l'élaboration d'un montage expérimental destiné au calibrage d'un robot de très haute précision (co-supervisé by N. Fazenda)", *Internship report*, Laboratory of Robotic Systems (EPFL), 2003.
- [Flu94] P. Flury, "Étude de la précision du système stéréotaxique robotisé Minerva", *Thèse N° 1236* (PhD dissertation), École Polytechnique Fédérale de Lausanne, 1994.
- [For97] F. D. Foresee and M. T. Hagan, "Gauss-Newton Approximation to Bayesian Learning", *Proceedings of the IEEE International Joint Conference on Neural Networks*, pp 1930 – 1935, 1997.
- [Fra06] H. Frayssinet-Mazerolle, "Méthode d'étalonnage d'une machine-outil à cinématique parallèle à 5 axes à grands angles d'inclinaison", *Thèse N° 3702* (PhD dissertation), École Polytechnique Fédérale de Lausanne, 2006.
- [Fra99] J. Frączek and Z. Buško, "Calibration of multi robot system without and under load using electronic theodolites", *Proceedings of the First IEEE International Workshop on Robot Motion and Control*, pp 71 – 75, 1999.
- [Fun89] K.-I. Funahashi, "On the Approximate Realization of Continuous Mappings by Neural Networks", *Neural Networks*, Vol. 2, pp 183 – 192, 1989.
- [Gar91] J. F. Gardner, A. Brandt and G. Luecke, "Applications of Neural Networks for Trajectory Control of Robots", *Proceedings of the IEEE International Conference on Advanced Robotics*, pp 487 – 492, Pisa (Italy), 1991.
- [Glö00] R. Glöss, "Hexapod parallel kinematics with sub-micrometer accuracy", *Proceedings of the 2nd Chemnitz Parallel Kinematics Seminar*, Chemnitz (Germany), pp 397 – 404, 2000.
- [Gos93] A. Goswami, A. Quaid and M. Peshkin, "Complete parameter identification of a robot from partial pose information", *Proceedings of the IEEE International Conference on Robotics and Automation*, pp 168 – 173, May 1993.
- [Gue88] A. Guez and Z. Ahmad, "Solution to the Inverse Kinematics Problem in Robotics by Neural Networks", *Proceedings of the IEEE International Conference on Neural Networks*, Vol. 2, pp 617 – 624, July 1988.
- [Ham03] B. Hammer and K. Gersmann, "A Note on the Universal Approximation Capability of Support Vector Machines", *Neural Processing Letters*, Vol. 17, Issue 1, pp 43 – 53, February 2003.
- [Ham93a] D. Hammerstrom, "Neural Networks at work", *IEEE Spectrum*, Vol. 30, No. 6, pp 26 – 32, 1993.
- [Ham93b] D. Hammerstrom, "Working with neural networks", *IEEE Spectrum*, Vol. 30, No. 7, pp 46 – 53, 1993.
- [Hat96] M. Hattori, H. Noguchi, S. Ito, T. Suto and H. Inoue, "Estimation of thermal-deformation in machine tools using neural network technique", *Journal of Materials Processing technology*, Vol. 56, pp 765 – 772, 1996.
- [Hay83] S. Hayati, "Robot Arm Geometric Link Parameter Estimation", *Proceedings of the 22nd Conference of the IEEE Control Systems Society, Decision and Control*, San Antonio – Texas (USA), Vol. 3, pp 1477 – 1483, December 1983.

- [Hay99] S. Haykin, "Neural Networks – A comprehensive foundation", Prentice-Hall, 1999.
- [Hay00] L. Hay and G. M. Pharr, "Instrumented Indentation Testing", In *Material Testing and Evaluation* (ASM handbook Volume 8: ISBN 0871703890), H. Kuhn and D. Medlin (editors), pp 232 – 243, 2000.
- [Hel06] P. Helmer, "Conception systématique de structures cinématiques orthogonales pour la microrobotique", *Thèse N° 3365* (PhD dissertation), École Polytechnique Fédérale de Lausanne, 2006.
- [Hen00] S. Henein, "Conception des structures articulées à guidages flexibles de haute précision", *Thèse N° 2194* (PhD dissertation), École Polytechnique Fédérale de Lausanne, 2000.
- [Hes95] J. Hesselbach and H. Kerle, "Structurally Adapted Kinematic Algorithms for Parallel Robots up to Six Degrees of Freedom", *Proceedings of the IFToMM "Theory of Machines and Mechanisms"*, pp 1930 – 1935, Milano (Italy), 1995.
- [Hol88] J. M. Hollerbach, "A Survey of Kinematic Calibration", In *Robotics Review*, O. Khatib, J. J. Craig and T. Lozano-Perez (editors), MIT Press, 1988.
- [Hol96] J. M. Hollerbach and C. W. Wampler, "The calibration index and taxonomy for robot kinematic calibration methods", *International Journal of Robotics Research*, Vol. 15, Issue 6, pp 573 – 591, 1996.
- [Hor89] K. Hornik, "Approximation Capabilities of Multilayer Feedforward Networks", *Neural Networks*, Vol. 4, pp 251 – 257, 1991.
- [Hor91] K. Hornik, M. Stinchcombe and H. White, "Multilayer Feedforward Networks are Universal Approximators", *Neural Networks*, Vol. 2, pp 359 – 366, 1989.
- [Hua03] T. Huang, J. Wang, D. G. Chetwynd and D. J. Whitehouse, "Identifiability of Geometric Parameters of 6-DOF PKM Systems using a Minimum Set of Pose Error Data", *Proceedings of the IEEE International Conference on Robotics and Automation*, Taipei – Taiwan, pp 1863 – 1868, September 2003.
- [Hüg05] N. Hügi, "Multi-dimensional Interpolation and Approximation for Robot Calibration", *Semester project* (co-supervised by N. Fazenda), Biomedical Imaging Group (EPFL), 2005.
- [Iur99] C. C. Iurascu and F. C. Park, "Geometric Algorithms for Closed Chain Kinematic Calibration", *Proceedings of the IEEE Internal Conference on Robotics and Automation*, Detroit – Michigan, pp 1752 – 1757, May 1999.
- [Jan92] H.-K. Jan, C. N. Chu and C. R. Liu, "A Configuration Independent Error Model of Machine Tools: Hyperpatch model and Metrology Pallet", *Robotics and Computer-Integrated Manufacturing*, Vol. 9, No. 3, pp 201 – 210, 1992.
- [Jen00] I. D. Jenkinson, "An application of neural networks to improve the accuracy of an industrial robot for off-line programming", PhD thesis, Liverpool John Moores University – Liverpool (UK), 2000.
- [Jeo98] J. W. Jeong, S. H. Kim, Y. K. Kwak and C. C. Smith, "Development of a parallel wire mechanism for measuring position and orientation of a robot end-effector", *Mechatronics*, Vol. 8, pp 845 – 861, 1998.
- [Jos87] G. Josin, D. Charney and D. White, "Robot Control using Neural Networks", *Proceedings of the IEEE International Conference on Neural Networks*, 1988, Vol. 2, pp 625 – 631, 1987.
- [Jos02] C. Joseph, J.-Ph. Bacher, J.-M. Breguet and R. Clavel, "Miniature Electro Discharge Machine for high precision micro-structurisation", *Third International Workshop on Microfactories (IWMF 2002)*, Minneapolis - Minnesota (USA), September 2002.
- [Jos05] C. Joseph, "Contribution à l'accroissement des performances du processus de µEDM par l'utilisation d'un robot à dynamique élevée et de haute précision", *Thèse N° 3281* (PhD dissertation), École Polytechnique Fédérale de Lausanne, 2005.
- [KEY] Keyence® LC series, user's manual.

- [Kha91] W. Khalil, M. Gauthier and Ch. Enguehard, "Identifiable parameters and optimum configurations for robots calibration", *Robotica*, Vol. 9, pp 63 – 70, 1991.
- [Koe03] L. Koenders, R. Bergmans, J. Garnaes, J. Haycocks, N. Korolev, T. Kurosawa, F. Meli, B. C. Park, G. S. Peng, G. B. Picotto, E. Prieto, S. Gao, B. Smereczynska, T. Vorburger and G. Wilkening "Comparison on nanometrology: Nano2 – Step-height ", *Metrologia*, Vol. 40 (Technical Supplement), 04001, 2003.
- [Kos98] Y. Koseki, T. Arai, K. Sugimoto, T. Takatiji and M. Goto, "Design and accuracy evaluation of high-speed precision parallel mechanism", *Proceedings of the IEEE International Conference on Robotics and Automation*, pp 1340 – 1345, Leuven (Belgium), May 1998.
- [Koz90] C. Kozakiewicz, T. Ogiso and N. Miyake, "Calibration Analysis of a direct drive robot", *Proceedings of the IEEE International Workshop on Intelligent Robots and Systems (IROS)*, pp 212 – 220, 1990.
- [Kuh06] B. Kuhfuss, C. Schenck and S. Allers, "Static Calibration of a Tripod by Neural Network Error Identification", *Proceedings of the 5th Chemnitz Parallel Kinematics Seminar (PKS 2006)*, pp 603 – 616, Chemnitz (Germany), April 2006.
- [Kwa95] C. M. Kwan, F. L. Lewis and Y. H. Kim, "Robust Neural Network Control of Flexible-Joint Robots", *Proceedings of the 34th Conference on Decision and Control*, New Orleans – LA (USA), pp 1296 – 1301, December 1995.
- [Kwo95] T.-Y. Kwok and D.-Y. Yeung, "Constructive Feedforward Neural Networks for Regression Problems: A Survey", *Technical Report HKUST-CS95-43*, Department of Computer Science – The Hong Kong University of Science and Technology, September 1995.
- [Kyl95] S. A. Kyle, "Optical methods for calibrating and inspecting robots", *Computing & Control Engineering Journal*, Vol. 6, Issue 4, pp 166 – 173, August 1995.
- [LDS] Newport[®] LDS-Vector autocollimator, user's manual.
- [Law00] K. Lawton and S. Patterson, "A high stability air temperature control system", *Precision Engineering*, Issue 24, pp 174 – 182, 2000.
- [Lew94] J. M. Lewis, X. L. Zhong and H. Rea, "A neural network approach to the robot inverse calibration problem", *Proceedings of the IEE International Conference on Intelligent Systems Engineering*, pp 342 – 347, September 1994.
- [Lub05] E. Lubrano, "Calibration of a 6-DOF high-precision parallel robot using artificial neural networks", *Master of Science thesis* (supervised by N. Fazenda), Laboratory of Robotic Systems (EPFL), July 2005.
- [Man05] E. Manske, R. Mastilo, T. Hausotte, N. Hofmann and G. Jäger, "Advances in Traceable Nanometrology with the Nanopositioning and Nanomeasuring Machine", In *Nanoscale Calibration Standards and Methods: Dimensional and Related Measurements in the Micro- and Nanometer Range*, G. Wilkening and L. Koenders (editors), Wiley-VCH Verlag, pp 47 – 59, 2005.
- [Mas93] O. Masory, J. Wang and H. Zhuang, "On the accuracy of a Stewart platform – Part II: Kinematic Calibration and Compensation", *Proceedings of the IEEE International Conference on Robotics and Automation*, pp 114 – 120, May 1993.
- [MCa79] H. McCallion and D. T. Pham, "The analysis of a six degree of freedom work station for mechanized assembly", *Proceedings of the 5th World Congress on Theory of Machines and Mechanisms*, pp 611 – 616, 1979.
- [McK92] D. J. C. MacKay, "A practical Bayesian framework for backprop nets", In J. E. Moody, S. J. Hanson and R. P. Lippmann (editors), *Advances in Neural Information Processing Systems*, pp 839 – 846, 1992.
- [McK] web-page: "http://www.inference.phy.cam.ac.uk/mackay/Bayes_FAQ.html".
- [MCu43] W. S. McCulloch and W. Pitts, "A logical calculus of the ideas immanent in nervous activity", *Bulletin of Mathematical Biophysics*, Vol. 5, pp 115 – 133, 1943.
- [Mel01] F. Meli, "International comparison in the field of nanometrology: pitch of 1D gratings (Nano4)", *Proceedings of the 2nd EUSPEN International Topical Conference*, Vol. 1, p 358, Turin (Italy), May 2001.

- [Mel03] F. Meli and M. Fracheboud, "High precision, low force 3D touch probe for measurements on small objects", *Proceedings of the EUSPEN Internal Topical Conference*, Vol. 2, Aachen (Germany), pp 411 – 414, May 2003.
- [Mel05] F. Meli, A. Küng and R. Thalmann, Optical Engineering and Instrumentation, Recent developments in traceable dimensional measurements III, *Proceedings of SPIE*, Vol. 5879 - 28, San Diego (USA), 2005.
- [Men88] C.-H. Menq and J.-H. Borm, "Statistical Measure and Characterization of Robot Errors", *Proceedings of the IEEE International Conference on Robotics and Automation*, Vol. 2, pp 926 – 931, April 1988.
- [ME76] R. H. McEntire, "Three Dimension Accuracy Measurement methods for Robots", *Industrial Robot*, pp 105 – 112, September 1976.
- [Mer00] J. P. Merlet, "Parallel robots", Kluwer Academic Publishers, 2000.
- [MET] **web-page:** "<http://www.metas.ch/de/labors/3/micro-cmm/index-e.html>".
- [Moo83] B. W. Mooring, "The Effect of Robot Joint Axis Misalignment on Robot Positioning Accuracy", *Proceedings of the ASME International Computers in Engineering Conference and Exhibit*, Illinois, pp 151 – 156, 1983.
- [Moo89] B. W. Mooring and S. S. Padavala, "The Effect of Kinematic Model Complexity on Manipulator Accuracy", *Proceedings of the IEEE International Conference on Robotics and Automation*, Vol. 1, pp 593 – 598, May 1989.
- [Moo91] B. W. Mooring, Z. S. Roth and M. Driels, "Fundamentals of Manipulator Calibration", *John Wiley & Sons*, 1991.
- [Mya92] T. Miyazaki, K. Maekawa and T. Bamba, "Compensation of Positioning Errors of Industrial Robot using Neural Networks", *Proceedings of the 23rd Industrial Symposium on Industrial Robotics (ISIR)*, pp 377 – 382, Barcelona (Spain), October 1992.
- [Nah94] A. Nahvi, J. M. Hollerbach and V. Hayward, "Calibration of a Parallel Robot Using Multiple Kinematic Closed Loops", *Proceedings of the IEEE International Conference Robotics and Automation (ICRA)*, Vol. 1, pp 407 – 412, May 1994.
- [New00] W. S. Newman, C. E. Birkhimer and R. J. Horning, "Calibration of a Motoman P8 Robot Based on Laser Tracking", *Proceedings of the IEEE International Conference on Robotics and Automation*, San Francisco – California (USA), Vol. 4, pp 3597 – 3602, April 2000.
- [Nia06] T. Niaritsiry, "Optimisation de la conception du robot parallèle Delta Cube de très haute précision", *Thèse N° 3567* (PhD dissertation), École Polytechnique Fédérale de Lausanne, 2006.
- [Not95] L. Notash and R. P. Podhorodeski, "Kinematic Calibration of Parallel Manipulators", *Proceedings of the IEEE International Conference on Systems, Man and Cybernetics*, Vol. 4, pp 3310 – 3315, October 1995.
- [Now88] A. Nowrouzi, Y. B. Kavina, H. Koçekali and R. A. Whitaker, "An overview of robot calibration techniques", *The Industrial Robot*, Vol. 15, Issue 4, pp 229 – 232, 1988.
- [Par87] G. A. Parker, "The present status of measurement techniques for robot calibration", *Proceedings of the IEE Colloquium on 'Robot Calibration and Performance Measurement'* (Digest No. 3), pp 1/1 – 5, 1987.
- [Par91] J. Park and I. W. Sandberg, "Universal approximation using radial-basis-function networks", *Neural Computation*, Vol. 3, Issue 2, pp 246 – 257, 1991.
- [Pay85] D. Payannet, "Modélisation et correction des erreurs statiques des robots manipulateurs", *Thèse de l'université des sciences et techniques du Languedoc*, Académie de Montpellier, 1985.
- [Per98] E. Pernette, "Robot de haute précision à 6 degrés-de-liberté pour l'assemblage des microsystèmes", *Thèse N° 1909* (PhD dissertation), École Polytechnique Fédérale de Lausanne, 1998.
- [RAI] **web-page:** "<http://www.raith.com/index.php?xml=solutions%7CLithography+%26+nanoengineering%7CRAITH150>"

- [Rat85] G. Rathbun, "A Stewart platform six-axis milling machine development", M.E. thesis, University of Canterbury, Christchurch (New Zealand), 1985.
- [Ren91] J.-M. Renders, J. Millán del R. and M. Becquet, "Non-geometrical parameters identification for robot kinematic calibration by use of neural network techniques", *Proceedings of the European Robotics and Intelligent Systems Conference*, Corfu (Greece), 1991.
- [Ros04] S. Rossopoulos, N. Fazenda and T. Niaritsiry, "Mesures angulaires et réglages du Delta Cube II", *Internal report*, LSRO – EPFL, April 2004.
- [Ros04b] S. Rossopoulos, T. Niaritsiry and N. Fazenda, "Mesures thermiques du Delta Cube II", *Internal report*, LSRO – EPFL, April 2004.
- [Ros05] S. Rossopoulos, N. Fazenda and T. Niaritsiry, "Concept de calibrage industriel", *Internal report*, LSRO – EPFL, December 2005.
- [Ros06] S. Rossopoulos, N. Fazenda and T. Niaritsiry, "Maîtrise des moyens de mesure", *Internal report*, LSRO – EPFL, March 2006.
- [Rot87] Z.S. Roth, B. W. Mooring and B. Ravani, "An Overview of Robot Calibration", *IEEE Journal of Robotics and Automation*, Vol. ra-3, No. 5, pp 377 – 385, October 1987.
- [Rum86] D. E. Rumelhart, G. E. Hinton and R. J. Williams, "Learning internal representations by error propagation", In *Parallel Data Processing – Vol. 1*, D. E. Rumelhart and J. L. McClelland (editors), Cambridge, Massachusetts: The M.I.T. Press, pp 318 – 362, 1986.
- [Ryu97] J. Ryu, D. G. Gweon and K. Moon, "Optimal design of a flexure hinge based $XY\theta$ wafer stage", *Precision Engineering*, Vol. 21, pp 18 – 28, 1997.
- [Sag04] M. Saglini, "Mise en oeuvre, gestion préventive de la mesure et calibrage statique du robot Delta Cube", *Master of Science thesis* (co-supervised by N. Fazenda), Laboratory of Robotic Systems (EPFL), 2004.
- [Sch93] K. Schröder, C. Ament, S. Patzelt and G. Goch, "Improving Machine Tool Accuracy by a Direct Position Measurement Using a New Approach of Laser Goniometry", *Proceedings of the European Society for Precision Engineering (EUSPEN) International Topical Conference*, pp 137 – 140, Aachen (Germany), May 2003.
- [Sha87] J. S. Shamma and D. E. Whitney, "A method for inverse robot calibration", *Journal of Dynamic Systems, Measurement and Control*, Vol. 109, pp 36 – 43, 1987.
- [SIO] **web-page:** "http://www.sios.de/ENGLISCH/PRODUKTE/NMM_E.HTM".
- [SIO2] SIOS® SP 2000 laser interferometer, user's manual.
- [Sri96] N. Srinivasa and J. C. Ziegert, "Automated measurement and compensation of thermally induced error maps in machine tools", *Precision Engineering*, Vol. 19, pp 112 – 132, 1996.
- [Ste65] D. Stewart, "A platform with six degrees of freedom", *Proceedings of the IMechE*, Vol. 180, pp 371 – 385, 1965.
- [Sti95] G. Stix, "Nice Legs", *Scientific American*, p 24, December 1995.
- [Sto74] M. Stone, "Cross-validatory choice and assessment of statistical predictions", *Journal of the Royal Statistical Society*, Vol. B36, pp 111 – 133, 1974.
- [Tak90] N. Takanashi, "6 D.O.F. manipulators absolute positioning accuracy improvement using a neural-network", *Proceedings of the IEEE International Workshop on Intelligent Robots and Systems*, pp 635 – 640, 1990.
- [Tan93] G.-R. Tang and L.-S. Liu, "Robot calibration using a single laser displacement meter", *Mechatronics*, Vol. 3, No. 4, pp 503 – 516, 1993.
- [Taw89] R. Tawel and A. Thakoor, "Neural Network Hardware Solution to the Inverse Kinematic Problem in Robotics", *Proceedings of the IEEE Third Annual Parallel Processing Symposium*, Fullerton – CA (USA), March 1989.

- [Thu04] M. Thurneysen, “Méthode systématique de conception de cinématiques parallèles”, *Thèse N° 3009* (PhD dissertation), École Polytechnique Fédérale de Lausanne, 2004.
- [Tib03] M. Tiboni, G. Legnani, P.L. Magnani and D. Tosi, “A closed-loop neuro-parametric methodology for the calibration of a 5 DOF measuring robot”, *Proceedings of the IEEE International Symposium on Computational Intelligence in Robotics and Automation*, pp 1482 – 1487, Kobe (Japan), 2003.
- [Tik63] A. N. Tikhonov, “On solving incorrectly posed problems and method of regularization”, *Doklady Akademii Nauk USSR*, Vol. 151, pp 501 – 504, 1963.
- [Tse02] P.-C. Tseng and S.-L. Chen, “The Neural-fuzzy Thermal Error Compensation Controller on CNC Machine Center”, *JSME International Journal (Series C)*, Vol. 45, N° 2, pp 470 – 478, 2002.
- [Van97] P. Vanherck, J. Dehaes and M. Nuttin, “Compensation of thermal deformations in machine tools with neural nets”, *Computers in Industry*, Vol. 33, pp 119 – 125, 1997.
- [Vap98] V. N. Vapnik, “Statistical learning theory”, Wiley, New York, 1998.
- [Vin94] M. Vincze, K. M. Filz, H. Gander, J. P. Prenninger and G. Zeichen, “A Systematic Approach to Model Arbitrary Non Geometric Kinematic Errors”, In *Advances in robot kinematics and computational geometry*, J. Lenarcic and B. Ravani (editors), pp 129 – 138, 1994.
- [Vin94b] M. Vincze, J. P. Prenninger and H. Gander, “A laser tracking system to measure position and orientation of robot end-effectors under motion”, *International Journal of Robotics Research*, Vol. 13, pp 305 – 314, 1994.
- [Vin96] M. Vincze, K. M. Filz, H. Gander and J. P. Prenninger, “A Systematic and Extendible Model for Arbitrary Axis Configurations”, *International Journal of Flexible Automation and Integrated-Manufacturing*, Vol. 2, Issue 2, pp 147 – 164, 1996.
- [Vin99] M. Vincze, S. Spiess, M. Parotidis and M. Götz, “Automatic Generation of Non-redundant and Complete Models for Geometric and Non Geometric Errors of Robots”, *International Journal of Modelling and Simulation*, Vol. 19, Issue 3, pp 236 – 243, 1999.
- [Vis96] P. Vischer, “Improving the accuracy of parallel robots”, *Thèse N° 1570* (PhD dissertation), École Polytechnique Fédérale de Lausanne, 1996.
- [Voo98] G. Vander Voot and G. M. Lucas, “Microindentation Hardness Testing”, *Advanced Materials & Processes*, Vol. 154, No.3, pp 21 – 25, September 1998.
- [Vuk95] M. Vukobratovic and B. Borovac, “Accuracy of the robot positioning and orientation assessed via its manufacturing tolerances”, *Mechanism and Machine Theory*, Vol. 30, No. 1, pp 11 – 32, 1995.
- [Wam95] C. W. Wampler, J. M. Hollerbach and T. Arai, “An Implicit Loop Method for Kinematic Calibration and Its Application to Closed-Chain Mechanisms”, *IEEE Transactions on Robotics and Automation*, Vol. 11, No. 5, pp 710 – 724, October 1995.
- [Wan05] D.-S. Wang, X.-G. Liu and X.-H. Xu, “Calibration of the arc-welding robot by neural networks”, *Proceedings of the Fourth IEEE International Conference on Machine Learning and Cybernetics*, pp 4064 – 4069, Guangzhou (China), August 2005.
- [Wat92] T. Watanabe, T. Hidekatsu, K. Kurokawa, A. Kawano, S. Kubo and K. Kenichi, “Calibration of position and orientation of robot manipulators using a neural network”, *Proceedings of the 1992 Japan – USA Symposium on Flexible Automation – Part 1*, San Francisco – California (USA), pp 219 – 225, 1992.
- [Whi86] D. E. Whitney, C. A. Lozinski and J. M. Rourke, “Industrial Robot Forward Calibration Method and Results”, *Journal of Dynamic Systems, Measurement and Control*, Vol. 108, pp 1 – 8, 1986.
- [SIO] web-page: “<http://www.wikipedia.org>”.
- [Xu94] W. L. Xu, K. H. Wurst, T. Watanabe and S. Q. Yang, “Calibrating a Modular Robotic Joint Using Neural Network Approach”, *Proceedings of the IEEE International Conference on Neural Networks*, Vol. 5, pp 2720 – 2725, July 1994.
- [Yan96] S. Yang, J. Yuan and J. Ni, “The improvement of thermal error modelling and compensation on machine tools by CMAC neural network”, *International Journal of Machine Tools and Manufacture*, Vol. 36, N° 4, pp 527 – 537, 1996.

- [Yi03] B. J. Yi, G. Chung, H. Na, W. Kim and I. Suh, "Design and experiment of a 3-DOF parallel micro-mechanism utilizing flexure hinges", *IEEE Transactions on Robotics and Automation*, Vol. 19, pp 604 – 612, 2003.
- [You99] K.-Y. Young and J.-J. Chen, "Implementation of a variable D-H Parameter Model for Robot Calibration Using an FCMAC Learning Algorithm", *Journal of Intelligent and Robotic Systems*, Vol. 24, pp 313 – 346, 1999.
- [Yu05] D.-Y. Yu, D.-C. Cong and J.-W. Han, "Parallel robots pose accuracy compensation using artificial neural networks", *Proceedings of the Fourth IEEE International Conference on Machine Learning and Cybernetics*, pp 3194 – 3198, Guangzhou (China), August 2005.
- [Zho94b] X. L. Zhong and J. M. Lewis, "Kinematic identification and compensation of robot manipulators using neural optimization networks", *Proceedings of the 3rd International Conference on Automation, Robotics and Computer Vision*, Singapore, Vol. 3, pp 1472 – 1476, 1994.
- [Zho94c] X. L. Zhong, J. M. Lewis and H. Rea, "Neuro-accuracy Compensator for Industrial Robots", *Proceedings of the IEEE International Conference on Neural Networks*, Vol. 5, pp 2797 – 2802, July 1994.
- [Zhu94] H. Zhuang and Z. S. Roth, "On Vision-Based Robot Calibration", *Proceedings of the IEEE Southcon Conference*, pp 104 – 109, March 1994.
- [Zhu95] H. Zhuang, O. Masory, J. Yan, "Kinematic Calibration of a Stewart Platform Using Pose Measurements Obtained by a Single Theodolite", *Proceedings of the IEEE/RSJ International conference on Intelligent Robots and Systems*, Vol. 2, pp 329 – 334, August 1995.
- [Zhu96] H. Zhuang, "Camera-Aided Robot Calibration", *CRC Press*, 1996.
- [Zhu97] H. Zhuang, "Self-calibration of parallel mechanisms with a case study on Stewart platforms", *IEEE Transactions on Robotics and Automation*, Vol. 13, No.3, pp 387 – 397, June 1997.
- [Zhu98] H. Zhuang, J. Yan and O. Masory, "Calibration of Stewart Platforms and Other Parallel Manipulators by Minimizing Inverse Kinematic Residuals", *Journal of Robotic Systems*, Vol. 15, Issue 7, pp 395 – 405, 1998.

Curriculum Vitæ

Nuno Ricardo FAZENDA CARRIÇO

born on March 22nd 1979 in Lisbon (P)

Portuguese citizen

EDUCATION

- 2003 – 2006: *PhD thesis* (supervisor: Prof. Dr Reymond Clavel)
EPFL, Laboratory of Robotic Systems (LSRO), Switzerland
- 1997 – 2002: *Physics engineer degree* (M.Sc.)
EPFL, Switzerland
- 1997: *European Baccalaureate*, European School of Luxembourg
Best overall average score (93.45 %)

PROFESSIONAL EXPERIENCE

- 2002 – 2004: *Project TOP NANO 21* (in collaboration with AGIE S.A. and METAS)
concerning the calibration of high-precision flexure parallel robots
- Since 2002: *Research assistant* at the LSRO – EPFL
Supervision of several student projects and teaching activities
- 2000: *Internship* at the LSRO
Numerical simulation modelling of an atomic force microscope (AFM)

PUBLICATIONS

A. Peer-refereed papers

Published

■ N. Fazenda, E. Lubrano, S. Rossopoulos and R. Clavel, **Calibration of the 6-DOF high-precision flexure parallel robot “Sigma 6”** – **KEYNOTE PAPER**, *Proceedings of the 5th Chemnitz Parallel Kinematics Seminar* (PKS 2006), Chemnitz (Germany), pp 379 – 398, April 2006.

■ T. Niaritsiry, N. Fazenda and R. Clavel, **Study of the sources of inaccuracy of a 3 DOF Flexure Hinge based Parallel Manipulator**, *Proceedings of the IEEE International Conference on Robotics and Automation* (ICRA 2004), New Orleans – LA (USA), Vol. 4, pp 4091 – 4096, April – May 2004.

- T. Niaritsiry, N. Fazenda and R. Clavel, **Simulation analysis of the sources of inaccuracy of a parallel manipulator**, *Proceedings of the IEEE International Conference on Robotics, Intelligent Systems and Signal Processing (RISSP 2003)*, Changsha (China), Vol. 1, pp 266 – 271, October 2003.

In preparation

- N. Fazenda, E. Lubrano and R. Clavel, **A Novel and Universal Model-free Approach for Data Processing Tasks in Robot Calibration Problems**.
- N. Fazenda, E. Lubrano and R. Clavel, **Improving the accuracy of a 6-DOF ultra-high precision robot using a novel indirect measuring procedure**.
- N. Fazenda, E. Lubrano, S. Rossopoulos and R. Clavel, **Calibrating the translational degrees-of-freedom of industrial flexure parallel robots with absolute accuracies in the sub- μm range: data collection, data processing and quality control issues**.
- T. Niaritsiry, N. Fazenda, C. Raminosoa, S. Rossopoulos and R. Clavel, **Improving the design of the 3-DOF “Delta Cube” high-precision flexure parallel robot as regards the suppression of passive DOF**.

B. Internal reports

- S. Rossopoulos, N. Fazenda and T. Niaritsiry, **Mesures angulaires et réglages du Delta Cube II**, *Internal report*, LSRO – EPFL, April 2004.
- S. Rossopoulos, T. Niaritsiry and N. Fazenda, **Mesures thermiques du Delta Cube II**, *Internal report*, LSRO – EPFL, April 2004.
- S. Rossopoulos, N. Fazenda and T. Niaritsiry, **Concept de calibrage industriel**, *Internal report*, LSRO – EPFL, December 2005.
- S. Rossopoulos, N. Fazenda and T. Niaritsiry, **Maîtrise des moyens de mesure**, *Internal report*, LSRO – EPFL, March 2006.

C. Others

- T. Niaritsiry and N. Fazenda, **Modélisation par éléments finis avec ANSYS® de robots parallèles ayant des structures flexibles**, *1^{er} Forum des utilisateurs ANSYS®*, EPFL, November 2004.